



**INVESTIGATION OF SURFACE QUALITY, METALLURGICAL DEFECTS
AND MECHANICAL PROPERTIES OF LASER POWDER BED FUSION
PROCESSED 316L STAINLESS STEEL AND Ti6Al4V TITANIUM ALLOYS**

A Thesis submitted to the School of Computing & Engineering
In the Partial Fulfilment of the Requirements
For the degree of Doctor of Philosophy
In the Department of Mechanical Engineering
University of Huddersfield

By

Shubhavardhan Ramadurga Narasimharaju
(*Shubha RN*)

Primary supervisors: Dr Shan Lou

Secondary Supervisor: Prof. Xiangqian (Jane) Jiang & Dr Wenhan Zeng

Copyright Statement

I, Shubhavardhan Ramadurga Narasimharaju, declare this Thesis entitled “Investigation of Surface Quality, Metallurgical defects and Mechanical Properties of Laser Powder Bed Fusion Processed 316L Stainless Steel and Ti6Al4V Titanium Alloys” is my research work produced by me as a result of conducting the original scientific investigation. And I confirm that:

i. This research work is carried out completely while in full-time candidature for a Doctor of Philosophy degree at the EPSRC Future Metrology Hub, University of Huddersfield;

ii. I have acknowledged wherever I have cited the published work and the online articles of others. The source of this referred work is provided.

iii. Any copyright in this thesis (including any appendices and/or schedules) is owned by the author, and that author has granted the University of Huddersfield permission to utilise that copyright for any administrative, or educational purposes of marketing, instruction, and/or teaching.

iv. Only in accordance with the University Library's rules may copies of this thesis, either in full or in excerpts, be made. You can ask the Librarian for further information about these rules. Any such copies must include a copy of this page.

v. The ownership of any patents, designs, trademarks, and any other types of intellectual property rights (collectively, "Intellectual Property Rights"), excluding copies of copyrighted works like graphs and photographs, tables ("Reproductions") that may be mentioned in this thesis may not be the author's property and may belong to other people. Without the owner(s) of the applicable Intellectual Property Rights and/or Reproductions' prior written consent, such Intellectual Property Rights and Reproductions cannot and must not be made available for use.

Abstract

Additive manufacturing (AM) is making a significant breakthrough including osseointegration implants used in biomedical applications and heat transfer-cooling channels used in aerospace applications. Most functional osseointegrated implants and cooling channels require a surface roughness of $0.5\text{ }\mu\text{m}$ - $1.5\text{ }\mu\text{m}$, with the current state-of-the-art of AM, it is non-viable to achieve this extent surface finish. However, early-stage research revealed that these implants' biocompatibility and load-bearing capabilities could be enhanced by designing/modifying and/or tailoring the surface roughness to greater than $4\text{ }\mu\text{m}$ (up to $100\text{ }\mu\text{m}$ in dental implants). Similar certain (higher) surface roughness induced by intentional porosities adds more benefits for extracting heat from cooling and maintaining the structural integrity of rocket engines and other aerospace-related applications. Additionally, the surface quality of acetabular and tibial knee augments ortho implant's external surface is different from internal surfaces. To design or tailor the desired roughness levels, it is imperative to understand the complex surface topography fingerprint that emerges on various external and internal AM surfaces. The laser powder bed fusion (LPBF) process is a type of metal AM process which uses a laser energy source to selectively melt the predefined contours of thousands of minuscule layers of the powder bed layer-by-layer; generating complex surface topography. This complex surface topography of metal AM presents a new challenge for conventional surface quality characterisation or surface texture metrology as the surface quality of AM surfaces is not trivial like conventional surfaces. The complex surface topography of various metal AM surfaces is formed by the virtue of diverse metallurgical defects and surface asperities, such as balling, porosities, cracks, staircase effect, spatters and adhered un-melted or partially melted particles which impart poor surface quality. As a result of this substandard final part quality, LPBF components fail to meet compliance with industrial standards. It is paramount to address the emergence of these defects and asperities, but very limited research is available addressing the emergence of metallurgical defects and surface asperities. Conventional surface texture metrology is predominantly focused to characterise the overall surface topographical asperities data of the whole measured region by a limited set of scalar values. R_a/S_a lacks characterising the diverse surface topographical features (metallurgical defects and surface asperities) and fails to interpret the functional performance. Also, the conventional texture parameters (R_a/S_a) are not intending to provide information about the individualities present on the surface nor the spatial distributions. Also, good practice to characterise and correlate the individual defect or asperity (including quantification of particle features) with a suitable surface texture parameter is clearly missing. More importantly, it is incomprehensible to

characterise and correlate this plethora of defects and anomalies with just one profile/areal surface texture height parameter (Ra/Sa). For example, a widely used Ra/Sa parameter is not suitable or applicable to characterise, correlate and or quantify the particle features (spatters, un-melted or partially melted particles) formed on various LPBF surfaces. Furthermore, the elaborate geometries of internal surfaces promote a significant challenge for measurement and characterisation, concurrently post-processing alone is not sufficient to improve the internal surface quality. Establishing an advanced surface texture characterisation tool for complex metal AM surfaces is a prerequisite.

The research developed within this thesis contributes to the novel characterisation and quantification of diverse metallurgical defects and various surface asperities which emerge on both external and internal surfaces of bespoke metal AM artefacts built with varying inclination angles. The individual surface defects and asperities are then correlated with an array of suitable areal surface texture parameters described in ISO 25178-2, and newly proposed particle analysis for quantifying the particle features. Based on the areal surface texture characterisation, height parameters Sa and Sq, and spatial parameter Sal were suitable to characterise the staircase effect, while hybrid parameters Sdq, Sdr, feature parameter Spd and functional parameter Vmp were appropriate to characterise the particle features (spatters, un-melted/partially melted particles). Particle analysis is applicable to quantify the particle features. The experimental investigation and prediction model established a strong correlation between final surface quality and varying inclination angles. The research also found that the location of AM part on the build platform and the laser incidence angle significantly influence the final surface quality. A comprehensive statistical analysis of variance (ANOVA) revealed the presence of a statistical significance of inclinations angles, build orientations and the type of surfaces on the resultant surface quality.

The critical LPBF parameters deemed mainly responsible for designing/optimising the final surface quality are laser power, hatch spacing, layer thickness, point distance, and exposure time. Therefore, sincere efforts have been made to design and optimise the critical parameters to achieve (tailor) lower or desired final surface quality by using the Taguchi design of experiments (TDOE). The impact (percentage contribution) of individual critical parameters on the resultant surface quality was examined by ANOVA. The results found that the hatch spacing and point distance were the main contributing factors to the top surface quality, while exposure time and point distance were the dominant factors responsible for the side surface quality. Confirmation experiments were conducted to validate the statistically predicted parametric combinations and compare them with the industrial default settings. The results

demonstrated that the lower or desired final surface quality can be achieved/tailored by optimising the critical parameters. Additionally, the diverse metallurgical defects and surface asperities that emerged on 25 different top and side surfaces were systematically characterised. To complement surface texture characterisation and TDOE optimisation, the influence of different build orientations on the surface quality, microstructure and mechanical properties was studied. Horizontally-oriented samples displayed higher tensile strength and superior fatigue life, due to refined microstructure and smaller defects whereas the presence of oxide inclusions, bigger defects and asperities in vertically-oriented samples resulted in poor performance under both static and dynamic loading conditions. This complimentary research investigation concluded that build orientations significantly influenced the surface quality and mechanical properties especially the tensile and fatigue performance of LPBF dog-bone samples.

Acknowledgements

I would like to take this opportunity to express my sincere gratitude to Lord Shiva, the Almighty God, and to everyone who has supported me directly or indirectly throughout this course of my journey while I have been conducting research for this PhD Thesis. First and foremost, I want to express my deep appreciation to my dear supervisors, Dr Shan Lou, Dame Professor Xiangqian (Jane) Jiang, and Dr Wenhan Zeng, for creating, offering me this position, and allowing me to conduct my PhD research under their invaluable guidance with total freedom. Throughout the entirety of my PhD path, I sincerely appreciate their unwavering support and insightful comments and feedback. I also want to thank Prof. Paul Scott, Dr Zicheng Zhu, and Dr Tian Long See for their review comments. I also like to thank the members of my progression committee, Prof. Fengshou Gu and Dr Graeme Greaves, for their support, constructive suggestions, and useful advice. Additionally, I appreciate the valuable support from my friends, colleagues and external contributors of the Centre for Precision Technologies (CPT), the Future Metrology Hub, 3M Buckley Innovation Centre, the Manufacturing Technology Centre (MTC), the Henry Royce Institute at the University of Sheffield, and the Advanced Forming Research Centre-National Manufacturing Institute of Scotland. My sincere thanks to Prof. Liam Blunt, Janine Downs, and Steve Knowles for their invaluable assistance while printing my samples. I also thank the support provided by Dr Vahid Nekouie from Henry Royce Institute for his assistance with post-process treatment, Philip Holdsworth in helping with tensile and fatigue testing, Chris Dawson for training optical measurement systems, Dr Anamul Haq Mir from MIAMI and Oliver Armitage for helping with the sample preparation and SEM. I would also like to remember my previous supervisors Prof. Sankunni Surendran (IIT Madras), and Prof. KA Venugopal (MCE-Hassan) for their guidance and encouragement. Last, but not least, I would sincerely recognise the contribution of my colleagues Weidong Liu, Xiao Chen, and Ronnie Ssebagala in helping with the measurement and data analysis.

Finally, I acknowledge the Engineering and Physical Sciences Research Council (EPSRC) of the UK for providing me with full PhD financial support. I also acknowledge the funding received from the Henry Royce Institute at the University of Sheffield for Hot-Iso-static Pressing post-processing treatment. I would also like to acknowledge the support received from EPSRC: New Investigator Award (EP/S000453/1), Catapult Researcher in Residence (EP/R513520/1), Future Advanced Metrology Hub (EP/P006930/1). 3M Buckley Innovation Centre: 3M BIC Fellowship.

Dedication

*I would like to dedicate this Thesis to my lovely wife **Pruthvirani Kakasuraiah**, for her unreserved support, especially in difficult times when things seemed overwhelming. You have always been selfless, sacrificing your life personally, and professionally to be my side to pursue my dream (PhD). I have to admit that personally, I wouldn't have done this for you. You are my great inspiration to be strong, and determined, no matter how significant the hurdles have been.*

*Also, to my beloved parents, **Shakunthala** and **Narasimharaju**, Indiramma and Kakasuraiah, my brother Harshavardhan, and sisters Sudha and Pooja, uncle Muniswamy, sister-in-law Saritha, brother-in-law Manojkumar, co-sister-in-law Anusha, nephew and niece Tejas and Shresta and my adorable newbies Shreynik and Krishang, and my best friend Vinay, and all the relatives, friends, and well-wishers., the reason for all the accomplishments that I achieved. Thank you for your unconditional love, continuous support and encouragement.*

*I am always grateful to **Lord Shiva** for providing me with everything in one or another form at the right time.*

List of publications

The work discussed in this PhD Thesis has been published in the following papers:

1. Narasimharaju, S. R., Zeng, W., See, T. L., Zhu, Z., Scott, P., Jiang, X., & Lou, S. (2022). A comprehensive review on laser powder bed fusion of steels: Processing, microstructure, defects and control methods, mechanical properties, current challenges and future trends. *Journal of Manufacturing Processes*, 75, 375-414.

My contribution: Major role in reviewing and writing completely, and providing suitable rebuttals for the Journal reviewers' comments till the final publication.

2. Narasimharaju, S. R., Liu, W., Zeng, W., See, T. L., Scott, P., Jiang, X. J., & Lou, S. (2021). Surface texture characterization of metal selective laser melted part with varying surface inclinations. *Journal of Tribology*, 143(5).

My contribution: Major role in planning the work, data analysis-interpretation, writing, and providing suitable rebuttals for the Journal reviewers' comments till the final publication.

3. S Ramadurga Narasimharaju, Weidong Liu, Wenhan Zeng, TianLong See, PJ Scott, X Jiang, Shan Lou (2022). Influence of critical process parameters on surface roughness and statistical optimization of LPBF 316L stainless steels (*Conference paper*). Summer Tropical Meeting: Advancing Precision in Additive Manufacturing. American Society for Precision Engineering, (ASPE). The University of Tennessee. Tennessee. U.S.A.

My contribution: Major role in planning the work, experimental work, measurement, data analysis-interpretation, writing, and providing suitable rebuttals for the Journal reviewers' comments till the final publication.

4. S Ramadurga Narasimharaju, Weidong Liu, Wenhan Zeng, TianLong See, PJ Scott, X Jiang, Shan Lou (2022). Investigating the surface texture of internal and external metal AM surfaces built with varying inclination angles (*Poster presentation*). *International Conference of Metrology and Properties of Surfaces*, University of Strathclyde, Glasgow.

My contribution: Major part in planning the work, measurement, data analysis-interpretation, writing, and providing suitable rebuttals for the Journal reviewers' comments till the final publication.

5. S Ramadurga Narasimharaju, Weidong Liu, Wenhan Zeng, TianLong See, PJ Scott, X Jiang, Shan Lou (2021). Surface irregularities of metal SLM part with different surface inclinations and their impact on surface texture characterization (*Poster presentation*). *Joint Special Interest Group meeting between euspen and ASPE Advancing Precision in Additive Manufacturing*. St. Gallen. Switzerland.

My contribution: Major role in planning the work, the experimental work, data analysis interpretation, writing, and providing suitable rebuttals for the Journal reviewers' comments till the final publication.

Table of Contents

Copyright Statement	ii
Abstract	iii
Acknowledgements	vi
Dedication	vii
List of publications	viii
List of abbreviations	xxi
Chapter 1 Introduction	1
1.1 Background and motivation	1
1.2 Identification of research knowledge gaps	3
1.3 Aim and objectives	5
1.4 Organisation of the thesis	6
1.5 Novelty and Originality of this PhD thesis	8
Chapter 2 Literature review	9
2.1 Additive manufacturing (AM)	9
2.1.1 Laser powder bed fusion (LPBF) process	10
2.1.2 Steels in AM/LPBF and their applications	13
2.2 Metal AM metallurgical defects and surface asperities	17
2.2.1 Balling	18
2.2.2 Porosity	19
2.2.3 Residual stress and cracking	22
2.2.4 Oxidation	25
2.2.5 Loss of alloying elements	27
2.2.6 Denudation	28
2.2.7 Environmental effects	29
2.2.8 Surface asperities responsible for poor surface quality	30
2.3 Importance of metal AM surface quality	34
2.3.1 Surface texture metrology	38
2.3.2 Areal surface texture parameters	41
2.3.3 Influence of process parameters on metal AM surface quality	47

2.3.4 Influence of scan strategies on metal AM surface quality.....	75
2.3.5 Tribological and corrosion properties of metal AM components.....	81
2.3.6. Surface quality prediction of metal AM surfaces built with varying inclination angles	85
2.3.7 Surface texture characterisation of metal AM surfaces with varying inclination angles	91
2.4 Metal AM critical process parameters optimisation	101
2.4.1 Taguchi design of experiments.....	106
2.4.2 Statistical analysis of variance (ANOVA).....	107
2.5 Microstructure, mechanical properties and post-processing treatments	108
2.5.1 Microstructure characteristics of metal AM components.....	108
2.5.2 Tensile properties of metal AM components	113
2.5.3 Fatigue properties of metal AM components	120
2.5.4 Impact of build orientations on metal AM surface quality and Fatigue life.....	123
2.5.5 Effect of post-process treatments on metal AM surface quality	126
2.6 Summary	134
Chapter 3. Surface texture characterisation of LPBF processed metal part built with varying surface inclinations	136
3.1 Research methodology.....	137
3.1.1 Truncheon artefact design and fabrication	137
3.1.2 Measurement strategy.....	140
3.1.3 Data acquisition and processing strategy.....	142
3.1.4 Areal surface texture parameters characterisation.....	142
3.2 Surface roughness prediction model.....	143
3.3 Results and discussions.....	144
3.3.1 Visual inspection of truncheon artefact	144
3.3.2 Height parameters.....	147
3.3.3 Spatial parameters.....	152
3.3.4 Hybrid parameters	154
3.3.5 Functional parameters.....	156
3.3.6 Feature parameters.....	157
3.3.7 Particle analysis	158
3.4 Summary	160

Chapter 4 Surface quality characterisation of external and internal surfaces of LPBF processed ball artefact built with varying inclination angles	162
4.1 Research methodology	163
4.1.1 Ball artefact design and fabrication	163
4.1.2 Measurement strategy	166
4.1.3 Data acquisition and processing	167
4.1.4 Areal surface texture parameters characterisation	169
4.2 Results and discussions	169
4.2.1 Visual inspection of longitudinal facet external up-skin surfaces	169
4.2.2 Visual inspection of longitudinal facet external down-skin surfaces	170
4.2.3 Visual inspection of longitudinal facet internal down-skin surfaces	174
4.2.4 Visual inspection of longitudinal facet internal up-skin surfaces	174
4.2.5 Visual inspection of latitudinal facet external and internal surfaces	177
4.3. Surface texture characterisation of longitudinal facets	182
4.3.2 Height parameters	183
4.3.3 Hybrid parameter (Sdr)	187
4.3.4 Particle analysis	188
4.3.5 Longitudinal facet particles descriptors analysis	191
4.4 Surface texture characterisation of latitudinal facets	195
4.4.1 Height parameters	195
4.4.2 Hybrid parameter (Sdr)	199
4.4.3 Particle analysis	200
4.4.4 Latitudinal facet particles descriptors analysis	201
4.5 Statistical analysis of variance (ANOVA)	207
4.5.1 Impact of inclination angles on resultant surface roughness	207
4.5.2 Statistical difference between up-skin and down-skin surfaces	208
4.5.3 Statistical difference between external and internal surfaces	209
4.6 Summary	210
Chapter 5. Statistical optimisation and impact of critical parameters on top and side surface quality of LPBF processed 316L SS hexagon artefacts	213
5.1 Hexagon artefacts design and fabrication	215
5.2 Measurement and data processing strategy	216

5.3 Taguchi design of experiments and ANOVA	217
5.4. Results and discussions.....	218
5.4.1 Taguchi DOE optimisation and ANOVA for top surface quality	220
5.4.2 Visual inspection of top surface quality	223
5.4.3 Surface texture characterisation of top surfaces	223
5.4.4 Interaction plot of critical LPBF parameters on top surface quality	225
5.5 Taguchi DOE optimisation and ANOVA for side surface quality	226
5.5.1 Visual inspection of side surface quality	229
5.5.2 Surface texture characterisation of side surfaces.....	231
5.5.3 Interaction plot of critical LPBF parameters on side surface quality	232
5.6 Verification experiments.....	234
5.7 Summary	236
Chapter 6. Impact of build orientation on surface quality, microstructure and mechanical properties of LPBF 316L SS parts	238
6.1. Research methodology.....	238
6.1.1 Dog-bones samples design and fabrication	238
6.1.2 Surface quality measurement strategy and data analysis.....	240
6.1.3 Microstructure analysis.....	241
6.1.4 Tensile testing.....	242
6.1.5 Fatigue testing.....	242
6.2. Results and discussions.....	243
6.2.1 Surface quality analysis of dog-bone samples.....	243
6.2.2 Microstructure and tensile property.....	247
6.2.3 Microstructure and fatigue life	254
6.3 Summary	259
Chapter 7 Conclusions and future work.....	261
7.1 Conclusions.....	261
7.2 Contributions to the field	268
7.3 Future work.....	269
References.....	270

List of Figures

Figure 2. 1 Forecast of AM Industry growth (Wohler's report 2020)	10
Figure 2. 2 (a) Categories, industrial sectors of AM applications as per Wohler's Report	11
Figure 2. 3 Schematic illustration of the LPBF process	12
Figure 2. 4 Various LPBF-produced metallic part applications;	13
Figure 2. 5 Taxonomy scheme for various Steels.....	15
Figure 2. 6 Correlation between Additive manufacturing key features and its advantages. ...	17
Figure 2. 7 Metallurgical defects and surface asperities that emerge in LPBF.	18
Figure 2. 8 Schematic illustration of balling phenomena	19
Figure 2. 9 SEM images of porosity defects observed in 316L LPBF samples	21
Figure 2. 10 Scanning electron microscope (SEM) image showing open porosity or voids ...	22
Figure 2. 11 Schematic of thermal gradient mechanism of residual stress in LPBF.	24
Figure 2. 12 Morphology of cracking (a) Liquation and (b) solidification cracking.....	25
Figure 2. 13 Light OM at different magnifications of the LPBF parts N ₂ atmosphere.	27
Figure 2. 14 Confocal height microscope image of denuded zones around melt tracks.	29
Figure 2. 15 X-ray images showing spatter counts for the same powder bed thickness.	30
Figure 2. 16 Context diagram of surface asperities form on inclined, curved AM surfaces. ...	32
Figure 2. 17 Schematic illustration of surface asperities.	33
Figure 2. 18 Schematic showing support remnants attached on the down-skin surface.....	34
Figure 2. 19 Schematic of AM components of a rocket engine in aerospace applications	35
Figure 2. 20 Metal AM biomedical applications	36
Figure 2. 21 schematic illustration of different porous AM spinal implants.	38
Figure 2. 22 schematic illustration of primary roughness and waviness profiles.....	39
Figure 2. 23 Roughness and waviness profiles extracted from the primary surface	40
Figure 2. 24 Schematic illustration of Sa	41
Figure 2. 25 Schematic illustration of Sq.....	42
Figure 2. 26 Schematic illustration of Ssk	42
Figure 2. 27 Schematic illustration of Sku.....	43
Figure 2. 28 Schematic illustration of autocorrelation length Sal	43
Figure 2. 29 Schematic illustration of (a) Sdq of scale limited surface.	45
Figure 2. 30 Schematic illustration of (a) Sdr of scale limited surface.....	45
Figure 2. 31 Schematic illustration of peak volume material Vmp of scale limited surface ...	46
Figure 2. 32 Schematic illustration of peak volume material Vmp of scale limited surface ..	47
Figure 2.33 Correlation between surface roughness, sloping angles and the parameters.....	50

Figure 2. 34 Correlation between contour parameters, surface quality of NDT methods	51
Figure 2. 35 Correlation between contour parameters and the fatigue life (a) SL, (b) XCT ...	51
Figure 2. 36 Correlation between surface texture and relative density/internal defects—.....	54
Figure 2. 37 Schematic illustration of optical microscope images for 40° up-skin surfaces....	55
Figure 2. 38 Schematic illustration of different Hatching angles used for IN625 AM.	76
Figure 2. 39 Schematic illustration of various scan strategies, and Sa results	77
Figure 2. 40 Schematic of various scan strategies, normal, concentric and hexagonal.....	78
Figure 2. 41 Roughness values for (a) top and (b) lateral surfaces for various scan strategies. 78	
Figure 2. 42 Stress-strain curve, UTS for top, lateral surfaces for various scan strategies.	79
Figure 2. 43 Schematic illustration of four different scan strategies used in LPBF process ...	80
Figure 2. 44 Tribological properties of LPBF under different scan strategies.	81
Figure 2. 45 Comparison of wear rate in dry wear test condition.....	82
Figure 2. 46 Schematic of cyclic polarisation curves (corrosion test)	82
Figure 2. 47 Building directions, COF and wear rate at different temperatures.....	83
Figure 2. 48 Schematic illustration of corrosion testing results.....	84
Figure 2. 49 schematic illustration of cusp geometry	85
Figure 2. 50 Schematic illustration of layer deposition patterns.	87
Figure 2. 51 Schematic of ANN and genetic algorithm to optimise AM surface quality.....	88
Figure 2. 52 Schematic illustration of AM artefact, surfaces identification	90
Figure 2. 53 Equated and real surface roughness values for various inclination angles	91
Figure 2. 54 Roughness profiles obtained for CSI, CONF, C-CONF and FV.	94
Figure 2. 55 Schematic of re-entrant features on up-skin and down-skin surfaces	96
Figure 2. 56 schematic of (a) artefact, (b) Sdr and Sdq for varying inclination angles	97
Figure 2. 57 Quantification of particle features on various build inclination angles [36]	98
Figure 2. 58 Schematic illustration of LPBF process critical parameters.....	103
Figure 2. 59 Illustration of hatch spacing vs melt track overlapping in LPBF process.....	103
Figure 2. 60 Label of LPBF processing windows and their impact on final part quality	106
Figure 2. 61 Microstructural evolutions of LPBF fabricated specimens:.....	109
Figure 2. 62 Schematic illustration of the typical LPBF microstructure of 316L SS.....	111
Figure 2. 63 Schematic illustration of overview of mechanical properties of metal LPBF... 114	
Figure 2. 64 SEM images taken from the tensile fracture surfaces of LPBF samples.	116
Figure 2. 65 Illustration of LPBF build directions and stress concentrations.....	122
Figure 2. 66 Schematic illustration of vertically oriented fracture surfaces.....	124
Figure 2. 67 Illustration of (a) vertically oriented fractured surface showing defects.....	125

Figure 2. 68 Schematic illustration of 3 building directions used in the metal AM process .	128
Figure 2. 69 Polar spectrum graphs of (a) as-built and post-processed.	129
Figure 2. 70 Ra values of different surfaces built with varying inclination angles.	131
Figure 2. 71 Fatigue properties of metal AM samples.....	132
Figure 2. 72 schematic illustration of tensile testing and fatigue results.	133
Figure 3. 1 SEM image showing 316L SS powder morphology.....	138
Figure 3. 2Truncheon artefact design drawing and measurement plan;	139
Figure 3. 3 Bruker Alicona focus varying measurement (FVM) system.....	141
Figure 3. 4 Extraction of the primary surface, staircase surface, and the particle surface. ...	142
Figure 3. 5 3D representation of prediction CAD model to show staircase computation.	144
Figure 3. 6 Six different truncheon surface topography transitions.....	145
Figure 3. 7 Surface transition between upskin and down-skin inclination angles	147
Figure 3. 8 Sa, Sq of the primary surface, staircase surface, and the predicted surface.	149
Figure 3. 9 3D view of surface topography at 90°:up-skin surface;down-skin surface.....	150
Figure 3. 10 Ssk and Sku of primary surface, staircase surface, and for predicted surface...	151
Figure 3. 11 Surface height distribution of three inclinations significance of Ssk, Sku.....	152
Figure 3. 12 Sal of the staircase surface, and the predicted surface.	153
Figure 3. 13 Schematic to illustrate the variation in staircase width.	153
Figure 3. 14 Str of the primary surface, particle surface, and the staircase surface	154
Figure 3. 15 Sdr of the primary surface, particle surface, and the staircase surface.....	155
Figure 3. 16 Sdq of the primary surface, particle surface, and the staircase surface.	156
Figure 3. 17 Vmp and Spd for the particle surface with respect to surface inclination.....	157
Figure 3. 18 Number of particles, particle coverage of the particle surface.	159
Figure 3. 19 Comparison of particle density and Spd of the particle surface	159
Figure 3. 20 Particles identification for six inclined surfaces.....	160
Figure 4.1SEM showing size distribution, morphology of grade of Ti powder.....	163
Figure 4. 2Schematic illustration of LPBF ball artefact.	165
Figure 4. 3 Focus variation measurement scheme.	167
Figure 4. 4 Illustration of particle analysis; raw data, waviness and particle surface.....	168
Figure 4. 5 Schematic illustration of longitudinal facet external surfaces.....	172
Figure 4. 6 Schematic illustration of rationale behind intermittent heat transfer	173
Figure 4. 7 Schematic illustration of longitudinal facet internal surfaces	176
Figure 4. 8 Schematic illustration of latitudinal external surfaces.....	180
Figure 4. 9 Schematic illustration of AM ball artifact position during fabrication	181

Figure 4. 10 Schematic of laser beam incidence angle, away from centre of build plate.....	181
Figure 4. 11 Schematic illustration of (a) front light and (b) back light	182
Figure 4. 12 Line graph for longitudinal external and internal Sa.....	184
Figure 4. 13 Line graph for longitudinal external and internal Sq.....	185
Figure 4. 14 Line graph for longitudinal external and internal Ssk	186
Figure 4. 15 Line graph for longitudinal external and internal Sku.....	187
Figure 4. 16 Line graph for longitudinal external and internal Sdr	188
Figure 4. 17 Line graph longitudinal external and internal surfaces particle numbers.....	190
Figure 4. 18 Longitudinal external and internal surfaces particles coverage ratio	191
Figure 4. 19 Longitudinal external particles descriptors and particles coverage ratio	193
Figure 4. Longitudinal internal particles descriptors and particles coverage ratio labels.....	194
Figure 4. 21 Polar plot for latitudinal full-turn external and internal Sa	196
Figure 4. 22 Polar plot for latitudinal full-turn external and internal Sq	196
Figure 4. 23 Polar plot illustrating full-turn external and internal Ssk	198
Figure 4. 24 Polar plot for latitudinal full-turn external and internal Sku	198
Figure 4. 25 Polar plot for latitudinal full-turn external and internal Sdr.....	199
Figure 4. 26 Polar plot for latitudinal facet full-turn external and internal particles	201
Figure 4. 27 Polar plot for latitudinal external and internal particles coverage ratio	202
Figure 4. 28 latitudinal external particles descriptors and particles coverage ratio.....	204
Figure 4. 29 (a-x). latitudinal internal particles and particles coverage ratio	206
Figure 5. 1 Flowchart of this research.....	215
Figure 5. 2 Dimensions, LPBF built 25 hexagon artefacts using Taguchi DOE.....	216
Figure 5. 3 Label of S/N ratio plots for LPBF critical parameters for top surface	221
Figure 5. 4 Percentage contribution of the control factors for top surfaces.....	222
Figure 5. 5 Visual inspection of the top surface from 25 artefacts	Error! Bookmark not defined.
Figure 5. 6 Experimentally obtained top surface Sa values for 25 hexagon artefacts	225
Figure 5. 7 Interaction plot for top surface quality from the critical LPBF parameters	226
Figure 5. 8 Label of S/N ratio plots for LPBF critical parameters for side surface quality...	228
Figure 5. 9 Percentage contribution of the control factors for side surfaces	229
Figure 5. 10 Visual inspection of the side surface from 25 artefacts.....	231
Figure 5. 11 Experimentally obtained side quality Sa values for 25 hexagon artefacts	232
Figure 5. 12 Interaction plot for side surface (Sa) from the critical LPBF parameters	233
Figure 5. 13 Visually inspected top and side surfaces with Renishaw default settings.....	236

Figure 6. 1 Dimension of dog-bone sample.....	239
Figure 6. 2Schematics of LPBF dog-bone samples built in four build orientations.....	239
Figure 6.3 LPBF printed samples in H,V,HI and VI orientations	240
Figure 6. 4 Tensile testing rig (ASTM E8 dog-bone) with extensometer	242
Figure 6. 5 Sa Sq plot for dog-bone samples for four different build orientations.....	244
Figure 6. 6 Sku Ssk plot for as-built processed samples for four build orientations	245
Figure 6. 7 Height map for as-built LPBF samples in four build orientations	246
Figure 6. 8 Topography of H,V,HI and VI orientations	247
Figure 6. 9 Stress-strain curves of LPBF dog-bone samples in four orientations	248
Figure 6. 10 SEM microstructure of as-built LPBF dog-bones in four orientations	249
Figure 6. 11 SEM-EDS of horizontal oriented sample showing alloying elements	251
Figure 6. 12 SEM-EDS of vertical oriented sample showing impurities oxide inclusions.	253
Figure 6. 13 S-N diagram for as-built dog-bone samples in four orientations	255
Figure 6. 14 SEM image of fractured interface of dog-bone samples in four orientations. ..	256
Figure 6. 15 Metallurgical defects and surface asperities observed in four orientations.....	258

List of Tables

Table 2. 1 Chemical composition and mechanical properties of a major class of steels	15
Table 2. 2 Summary of AM parameters influence on final surface quality from literature	56
Table 2. 3 Summary of AM parameters interrelation with surface quality from literature	75
Table 2. 4 Summary of surface texture measurement and characterisation from literature ..	100
Table 2. 5 Summary of surface quality for different fabricating conditions from literature .	100
Table 2. 6 Tensile and hardness properties of metal AM from different literature	119
Table 2. 7 Surface quality and fatigue properties of AM with different build orientations ..	126
Table 3. 1 Main LPBF process parameters adapted in this part of the research.....	138
Table 3. 2 Configuration of FV measurement.	141
Table 3. 3 Areal surface texture parameters explored in this research	143
Table 4.1 Main LPBF parameters adapted in this part of research.....	165
Table 4. 2 Focus variation measurement method configuration.....	166
Table 4. 3 Areal surface texture parameters explored in this research	169
Table 4. 4 ANOVA-Impact of inclination angles on external up-skin surfaces.....	207
Table 4. 5 ANOVA-Impact of inclination angles on external down-skin surfaces	208
Table 4. 6 Impact of inclination angles on internal down-skin surfaces	208
Table 4. 7 ANOVA-Impact of inclination angles on internal up-skin surfaces.....	208
Table 4. 8 ANOVA- statistical difference between external up-skin, down-skin surfaces ...	209
Table 4. 9 ANOVA- statistical difference between internal up-skin, down-skin surfaces....	209
Table 4. 10 ANOVA statistical difference between external and internal up-skin surfaces .	210
Table 4. 11 ANOVA-statistical difference between external, internal down-skin surfaces..	210
Table 5. 1 LPBF critical parameters used for parametric optimization.....	216
Table 5. 2 Focus variation measurement method configuration.....	217
Table 5. 3 L25 Orthogonal array by Taguchi and their resultant top surface Sa values.....	219
Table 5. 4 Taguchi response for S/N ratios for top surface-Smaller-the-better.....	221
Table 5. 5 Taguchi DOE predicted LPBF parameters for top surface quality.....	221
Table 5. 6 ANOVA for S/N ratios for top surface quality.....	222
Table 5. 7 L25 Orthogonal array by Taguchi and their resultant side surface quality Sa	227
Table 5. 8 Taguchi response for S/N ratios for side surface-Smaller-the-better	228
Table 5. 9 Taguchi DOE predicted LPBF parameters for side surface quality	228
Table 5. 10 ANOVA for S/N ratios for side surface quality,	229
Table 5. 11 Top surface Sa for default, best Sa achieved from Taguchi L25 array	235

Table 5. 12 Side surface Sa for default, best Sa achieved from Taguchi L25 array.....	235
Table 6. 1 FVM measurement configurations	241
Table 6. 2 Average Sa, Sq, Ssk and Sku for four build orientations	243
Table 6. 3 Tensile testing results for LPBF dog-bone samples in four orientations.....	247
Table 6. 4 Fatigue life of as-built dog-bone samples in four different orientations	254

List of abbreviations

RP	Rapid prototyping
AM	Additive manufacturing
LPBF	Laser Powder Bed Fusion
SLM	Selective laser melting
3D	Three-dimensional
CAD	Computer-aided-design
Nd:YAG	Neodymium-doped Yttrium Aluminum Garnet
LP	Laser power (W)
HS	Hatching spacing (μm)
LT	Layer thickness (μm)
PD	Point distance (μm)
ET	Exposure time (μs)
VED	Volumetric energy density (J/mm^3)
LSR	Laser re-melting
SS	Stainless steel
FGM	Functionally graded materials
FVM	Focus variation measurement
SEM	Scanning electron microscope
XCT	X-ray computed tomography
TEM	Transmission electron microscope
YS	Yield strength
UTS	Ultimate tensile strength
DOE	Design of experiments
TM	Taguchi method
ANOVA	Analysis of variance
COF	Coefficient of friction
ISO	International organisation for standardisation
ASTM	American society for testing and materials

Chapter 1 Introduction

This chapter is dedicated to briefly introducing the background and the motivation of this thesis. The main goal and the specific objectives are presented in this section. A part of this chapter is published as a review paper [1]

1.1 Background and motivation

The creation of a 3D object by layer-by-layer additive approach was first developed in the early 1980s under the name of Rapid Prototyping (RP). The primary purpose of RP development was a faster fabrication by layers consolidation of raw materials using a 3D computer-aided design (CAD) model [2-4]. In the initial stages, RP was used to create a model and prototype physical parts or an assembly, offering quick realisation for researchers and engineers of manufacturing novel complex objects they had envisioned [4]. The RP technique was one of the advanced fabrication processes that finally culminated in Additive Manufacturing which is adopted in this research for the production of 3D physical parts built in minuscule layers from a CAD model without using any supporting tools [4,5]. The essential advances of AM process are the design & development and production of intricate parts with a substantial reduction in both lead time and cost, which is facilitated by the increased human intervention and the process optimisation of the production cycle, thereby, ensuring the fabrication of any envisaged part which is otherwise highly unlikely to produce using other conventional processes [5,6]. AM enables the complimentary unsurpassed benefits like reducing feedstock materials by recycling, and conservation of the environment by creating eco-friendly products for lean manufacturing [7]. Recent research from major companies like Airbus, Boeing, General Electrics, and Siemens have implemented the actual use of AM to fabricate over 100 types of functional spare parts, including gas turbine components, with an estimated reduction in repair time close to 90% in certain instances [8]. Another collaborative study conducted by Airbus and other popular automotive and aerospace part manufacturers in the UK revealed that significant time and material can be saved. For example, the fabrication of the titanium bracket was completed in just 40 minutes by AM compared to the four hours needed in conventional machining, simultaneously reducing the cutting material usage by 50% [8].

AM is gaining more popularity as a fabrication method rather than just a prototyping technique among the industrial, research and academic fraternity because, in addition to a single material,

fabrication of the concurrent assemblage of multiple material parts presents new opportunities in the design and development of complex multi-range bionics, functionally graded materials, lightweight parts, cellular and lattice-type structures with improved efficiency and optimised topographies which are used in aerospace, electronics, biomedical, powerplant, and automotive industry applications [9-11]. Amongst all, one advantage that stands out from this complex design approach is the potential to create small internal geometry channels and passageways that are particularly useful for cooling in high-temperature heat flux applications such as liquid rocket engines, gas turbine aerofoils and electronics [1]. However, the higher benefits of AM present more challenges in terms of surface quality, microstructure, and mechanical properties, eventually affecting AM components' functional performance.

Despite possessing the vast advantages of indefinite geometrical freedom and minimal material wastage, AM is not completely established to meet compliance with industrial standards as it still suffers from substandard surface quality and poor dimensional tolerance. It is necessary to have a strong understanding of AM parameters' influence on the resultant surface quality [12]. A comprehensive knowledge of AM enables the fabrication of load-critical parts with enhanced surface integrity [13]. The surface quality of the load-bearing AM parts is crucial in certain biomedical and aerospace applications requiring surface roughness of $<1.5\mu\text{m}$ to avoid premature failure from the surface-initiated cracking under mechanical loading [14, 15]. However, it is difficult to improve the surface quality infinitely by optimising the metal AM process alone but early studies have shown that tailoring/modifying the surface roughness to greater than $4\mu\text{m}$ (up to $100\mu\text{m}$ in dentistry) enhances biocompatibility and load-bearing capacity of osseointegrated implants in biomedical applications. Likewise, certain higher roughness helped to extract heat from regenerative cooling in aerospace applications [14-16]. To design/tailor the desired roughness levels, it is imperative to understand the complex surface topography comprised of diverse metallurgical defects and surface irregularities, such as balling, porosities, cracks, staircase effect, spatters and adhered un-melted or partially-melted particles, which impart poor surface quality on various metal AM surfaces. Additionally, the build orientations, position of the AM part on the substrate, and laser beam incidence angle are other factors that strongly influence the final surface quality. It is important to note that very limited research is available addressing the emergence of metallurgical defects and surface asperities. Also, good practice to characterise and correlate the individual defect or asperity (including quantification of particle features) concerned

with suitable areal surface texture parameters is completely missing. More importantly, it is incomprehensible to characterise and correlate this plethora of defects and anomalies with just one profile/areal surface texture height parameter (Ra/Sa). For example, a widely used Ra/Sa parameter is unsuitable or applicable to characterise, correlate and quantify the particle features (spatters, un-melted or partially melted particles) formed on various metal AM surfaces. The complex geometry of internal surfaces is a major concern for measurement, characterisation, and post-processing. Hence, it is paramount to gain insights into internal AM surfaces. For example, the acetabular implant's external surface is different from the internal surface, same with tibial augments of knee implants: the internal surface is rougher while the external surface is smoother. Moreover, post-processing alone is not sufficient to improve internal geometrical surface quality.

1.2 Identification of research knowledge gaps

Despite AM being capable of building the most complicated dimensional parts, which in most cases are considered impossible in traditional processes, surface quality is one critical limitation or a key challenge that is highly worth overcoming for the rapid progress of the metal AM process [17]. In general, most of the properties of the materials are indeed considered the standard surface properties of mechanical products. For example, fatigue, cracking, friction and wear, oxidation, abrasion, adhesion and bonding, erosion etc., are all influenced by the surface properties, as surface quality plays a vital role in determining the final part quality and functional performance of many engineering applications including AM parts [17-21]. Some of the major contributors accountable for poor surface quality or rougher surface finish of metal AM parts are: firstly, the process itself induces higher surface roughness as it undergoes a very complex thermophysical mechanism and kinetic phenomena during the layer-by-layer building process; secondly, the proper selection amongst the diverse AM process parameters plays their part in imparting unique anisotropic fingerprint on surface features generating poor surface quality [18,22]; and finally, miscellaneous factors such as lower process resolution of building part/artefact and layering effects, supporting structures, feedstock materials quality, packing density, morphology, rheology contribute towards the substandard surface quality [18,22,23]. Therefore, the surface quality of AM parts is perceived to be unpredictable and uncontrollable. The individual or the combination of these three circumstances yields strong surface characteristics inherent to the metal AM process, which is usually dominated by the number of metallurgical defects (e.g., balling, porosities, cracks, denudation, etc.) and associated surface asperities (staircase effect, spatters, un-melted and

partially melted particles) or irregularities [1]. The formation of different types of process-related defects and/or surface asperities depends on the type of part/artefact being built, the laser angle of incidence relative to the build platform, and the kind of metal AM processes employed [2].

The metallurgical defects and asperities that form on the AM surface during the fabrication process tend to act as a nucleation site for crack initiation and corrosion, as they promote premature failure subjected to mechanical loading conditions, eventually restricting the AM applications of functional AM components [17,24]. Furthermore, the surface properties also contribute to the impact of the part aesthetics (shiny or matte), and other functional attributes such as sealing, lubrication, thermal conductivity and electrical conductivity, light reflection, fluid dynamics, and mating, etc. [7,25,26]. As a result of poor surface finish, AM components fail to fulfil the industrial standard, which is a major concern that needs to be resolved in a timely manner. The surface quality of AM components is regarded below par as compared to conventional processed parts [27]. The surface quality is one of the crucial properties that determine the part functionality. It is well acknowledged that surface quality contributes up to 10% of the part failure rate in conventionally processed parts [28]. However, this is estimated to be even higher in the case of AM-fabricated parts [29]. To overcome this surface quality deficiency and thereby, satisfy the industrial standard accuracy in terms of dimensional tolerance and near-net shape, AM-built components need to undergo one or the other form of surface finishing or additional post-processing treatments. Post-processing is usually expensive, labour-intensive, and time-consuming [27]. Improving surface quality not just saves money and time but also reduces the environmental impact [30].

To tailor or enhance the surface quality to the desired levels, it is paramount to understand the suitable existing metrology techniques and appropriate best practices applied for the precise measurement, characterisation and quantification of surface roughness to ensure compliance with functional hallmarks of industrial standards. Moreover, to gain insights into surface properties and ultimately achieve better final part quality, it is of utmost importance to peruse AM fabricated part's physical and chemical characteristics. Surface texture metrology is beneficial to tailor or achieve the desired surface quality by optimising the fabricating processes as well as the fabricated part functionality [31]. The lack of fundamental knowledge about the functional importance of various surface properties correlating with areal surface texture parameters is one of the essential issues that need to be addressed. The AM surface quality evaluation is considered a 3D analysis in

micro and nanoscales, which is functionally important. Many researchers in the widely available literature have used basic and standard procedures for surface quality characterisation, but are unable to fully address the characteristics of AM surfaces. A thorough investigation of the emergence of various surface asperities on different AM surfaces built with varying inclination angles is missing. Also, the characterisation and quantification of a plethora of defects, surface asperities, and the correlation of these individual defects, asperities with the suitable areal surface texture parameters are lacking. The previous research is mainly limited to height parameters while evaluating the surface quality of AM surfaces. However, it is essential to note that other parameters defined in ISO 25178-2 [32] provide the necessary information useful to understand the functional behaviour of AM surfaces in used in various aerospace, biomedical, transportation and marine applications. The research on the functional importance of asperities-induced surface quality is generally very limited. Areal surface texture analysis offers more opportunities than studying profiles.

In addition to external surface properties, the surface quality of AM components' internal geometries encompassing elaborate surfaces is paramount. The complex geometry of internal surfaces poses a significant challenge for post-processing. Also, post-processing alone is not sufficient to improve the surface quality, microstructure characteristics and mechanical properties of internal geometries [12,33]. There is a considerable amount of literature available pertaining to basic surface texture measurement and characterisation of external surfaces. Still, research specific to investigating the surface quality of AM internal surfaces is scarce. Many researchers in the public literature have fabricated only a few basic cubes and/or existing standard artefacts using a limited set of parameters while evaluating the surface characteristics prediction and statistical parametric optimisation of critical AM process parameters [34-38]. Additionally, minimal research is carried out to examine the influencing factors like varying build inclination angles, laser beam incidence angle, position on AM part on the build plate, build orientations, percentage contribution of individual critical process parameter, existence of statistical significance of different type of surfaces, various surface inclinations and orientations on the resultant surface quality.

1.3 Aim and objectives

This PhD research aim is to systematically characterise and quantify the diverse metallurgical defects and surface asperities that emerge on different LPBF external and internal surfaces and correlate them with the suitable areal surface texture parameters described in ISO-25178-2.

The main objective(s) of this PhD are:

1. To characterise the emergence of diverse metallurgical defects and surface asperities emerge on the LPBF flat, vertical and inclined surfaces built with varying inclination angles, and correlate them with the suitable array of areal surface texture height, spatial, hybrid, functional and feature parameters, including quantification of particle features using newly developed particle analysis as per ISO 25178-2.
2. To characterise and correlate the surface quality of both longitudinal and latitudinal external and internal surfaces with the array of areal surface texture height and hybrid parameters, and quantify feature-based particle analysis as per ISO 25178-2.
3. To investigate the importance of laser beam incidence angle, and location of AM part on the build platform relating to final surface quality. Also, examine the statistical significance of inclinations angles, build orientations and the type of surfaces on the resultant surface quality by using ANOVA.
4. To optimise the LPBF critical parameters by Taguchi DOE, and examine the impact of individual critical parameters by ANOVA, which can act as a design guideline to reduce or tailor metallurgical defects and surface asperities, thereby achieving lower or desired surface quality. The 25 different top and 25 different side surfaces were characterised.
5. Complimentary to the surface quality characterisation and process optimisation, the influence of different build orientations on the final surface quality, microstructure characteristics and the mechanical performance of LPBF components were studied.

1.4 Organisation of the thesis

Chapter 1 enlightens the background of AM, introduction to various aspects responsible for the metal AM final quality, identifies the research knowledge gaps, the motivation for this research and the main aims and objectives.

Chapter 2 is the literature review which is organised into six sub-sections: (i) the primary subsection 2.1 provides the fundamentals of AM and LPBF processes, Steels in AM/LPBF and their applications; (ii) sub-section 2.2 is devoted to a critical review of process-induced diverse metallurgical defects and surface asperities that are responsible for the substandard surface quality, microstructure and mechanical properties of metal AM components; (iii) sub-section 2.3 presents importance of metal AM surface quality, introduces to surface texture metrology, provides

comprehensive review of influencing factors such as critical process parameters, scan strategies, varying inclination angles, building orientations on the complex metal AM surface topographies, and explores the surface texture measurement and characterisation of various metal AM surface topographies, (iv) sub-section 2.4 is related to an in-depth review to gain insights into the metal AM process critical parametric optimization by statistical tools such as Taguchi DOE and ANOVA to achieve lower or desired top and side surface quality, (v) sub-section 2.5 is dedicated to understanding the microstructure characteristics, tensile and fatigue properties of metal AM components built with different building orientations, including the impact of various post-process treatments on metal AM surface quality. Finally, sub-section 2.6 presents the summary.

Chapter 3 provides the comprehensive details, including the rationale behind the emergence of diverse metallurgical defects and surface asperities on different up-skin and down-skin surfaces of the Truncheon artefact built with varying inclination angles. More importantly, the diverse defects and asperities are individually characterised and correlated with an appropriate array of areal surface texture (height, spatial, hybrid, functional, feature) parameters described in ISO 25178-2, including the newly developed particle analysis to quantify the particle features; balling, spatters, un-melted, partially melted particles.

Chapter 4 comprehensively characterises a plethora of metallurgical defects and surface asperities formed on the longitudinal and latitudinal facets of both external and internal up-skin and down-skin surfaces of an LPBF ball artefact, and correlate them with surface texture height parameters, hybrid parameters and feature-based particle analysis. A thorough examination was carried out to investigate the impact of the ball artefact position and laser beam incidence angle on the resultant surface quality. Finally, statistical ANOVA is presented to verify the existence of statistical significance between the latitudinal, longitudinal, external and internal up-skin and down-skin surfaces.

Chapter 5 presents the LPBF process critical parameters optimisation and surface quality prediction using Taguchi DOE. Laser power, hatch spacing, layer thickness, point distance and exposure time are deemed to be the critical parameters in LPBF process fabrication. Hence, selecting these 5 critical parameters at 5 levels contributed to the L25 orthogonal array in TDOE, and the ANOVA determines the percentage contribution of each individual critical parameter on the final surface quality of hexagon artefacts' top and side surfaces. The confirmation experiment results are ultimately verified to validate the predicted values and compared them with the default

industrial settings. The diverse surface topographical features that emerged on 25 different top and 25 side surfaces were systematically characterised.

The penultimate complimentary Chapter 6 explicitly dedicated to study the impact of various building orientations on the final surface quality, microstructure and mechanical performance of as-built LPBF dog bone samples.

Chapter 7 is dedicated to presenting the conclusions and highlights of future work.

1.5 Novelty and Originality of this PhD thesis

The novelty and original findings of this PhD thesis are as follows,

1. Developed a novel surface texture characterising toolbox to systematically characterise the diverse metallurgical defects and surface asperities that emerge on various metal AM external and internal surfaces built with varying inclination angles.
2. Established a new paradigm to correlate these individual defects and asperities with an appropriate array of areal surface texture parameters, including quantifying the feature-based particle analysis described in ISO-25178-2.
3. Ascertained a strong correlation between the different build inclination angles and the final surface quality of various LPBF external and internal surfaces.
4. Discovered the statistical significance of inclinations angles, build orientations and the type of surfaces on the resultant surface quality by using ANOVA.
5. Determined that the location of the AM part on the build platform and the laser beam incidence angle were strongly responsible for the final surface quality.
6. Demonstrated lower or desired surface quality could be achieved or tailored by optimising LPBF critical parameters using Taguchi DOE, and the impact (percentage contribution) of each critical parameter was quantified by ANOVA. Importantly, the diverse surface topographical features that emerged on 25 different top and 25 side surfaces were systematically characterised.
7. Finally, identified that different build orientations present significant impact on the final surface quality, microstructure and mechanical properties of metal AM components.

Chapter 2 Literature review

This chapter is assigned to report the in-depth literature review and the relevant current state-of-the-art applicable to this PhD research. The chapter is organized into six sub-sections: (i) the primary subsection 2.1 provides the fundamentals of AM and LPBF processes, Steels in AM/LPBF and their applications; (ii) sub-section 2.2 is devoted to a critical review of process-induced diverse metallurgical defects and surface asperities that are responsible for the substandard surface quality, microstructure and mechanical properties of metal AM components; (iii) sub-section 2.3 presents importance of metal AM surface quality, introduces to surface texture metrology, provides comprehensive review of influencing factors such as critical process parameters, scan strategies, varying inclination angles, building orientations on the complex metal AM surface topographies, and explores the surface texture measurement and characterisation of various metal AM surface topographies, (iv) sub-section 2.4 is related to an in-depth review to gain insights into the metal AM process critical parametric optimization by statistical tools such as Taguchi DOE and ANOVA to achieve lower or desired top and side surface quality, (v) sub-section 2.5 is dedicated to understanding the microstructure characteristics, tensile and fatigue properties of metal AM components built with different building orientations, including the impact of various post-process treatments on metal AM surface quality. Finally, sub-section 2.6 presents the summary.

The major part of this chapter has been published, by the first author SR Narasimharaju, titled “A comprehensive review on laser powder bed fusion of steels: Processing, microstructure, defects and control methods, mechanical properties, current challenges and future trends” [1].

2.1 Additive manufacturing (AM)

The AM process belongs to a group of technologies where the material is added rather than removed to create the finished product. Unlike the typical manufacturing process, which entails shaping or carving materials into the necessary end components by subtracting various elements from it [1]. In this context, AM is considered as the polar opposite; three-dimensional components are created directly from a 3D CAD file by the virtue an additive technique that involves depositing or melting consecutive layers of feedstock materials inside a closed chamber [1]. AM is considered as the direct manufacturing technology that gives freedom to fabricate parts from materials composed of metals, polymers, ceramics, and composites with complex features through external and internal layouts, in addition to reduced material consumption [39,40]. The feedstock materials used in AM process can be in the form of powder, wire, sheet, etc. [41,42]. AM process is often

described by other terms such as additive fabrication, additive technique, additive layer manufacturing, layer manufacturing, solid freeform fabrication and freeform fabrication [1,43]. According to SmarTech Publishing’s latest metal AM report “*Additive Manufacturing with Metal Powders 2018*”, LPBF technology is one of the most used and studied AM methods [44]. Forecasts of AM technologies have been constantly driving the industry revenues resulting from hardware, materials, and software. This revenue growth is predicted (by Wohler’s report 2020) to be worth \$US 25.5 billion in 2022, growing to \$US 40.8 billion in 2024. (see Figure 2.1) [45].

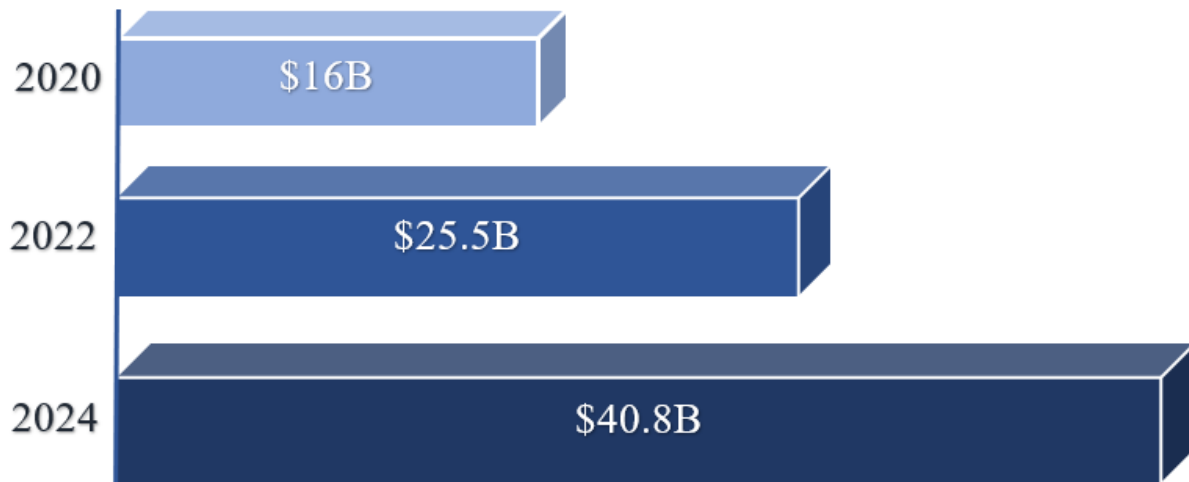


Figure 2. 1 Forecast of AM Industry growth (Wohler’s report 2020) [45]

Metal AM technology has attracted many researchers and industries because of its distinctive applications. In recent years metal AM is used to fabricate end-use products of medical devices (dental restorations, medical implants), aerospace and military applications, and automobile industries and consumer applications [46] (see Figures 2.2a & b). AM is also expanding its territory into the aircraft maintenance and transportation sector through the production of spare parts and refurbishing damaged components [47-50].

2.1.1 Laser powder bed fusion (LPBF) process

Out of many AM processes, the LPBF process is considered one of the most favoured and widely used metal AM techniques [51]. On the other hand, there are other metal AM technologies that are equally popular in recent times, such as electron beam melting, direct energy deposition, and laser-engineered net shaping [52]. The versatility of metal LPBF provides greater feasibility in both design and selection from the array of feedstock materials. Steels, titanium, aluminium, metal

matrix composites, nickel, and tungsten-based superalloys powders are particularly attractive in the metal AM process [7,17].

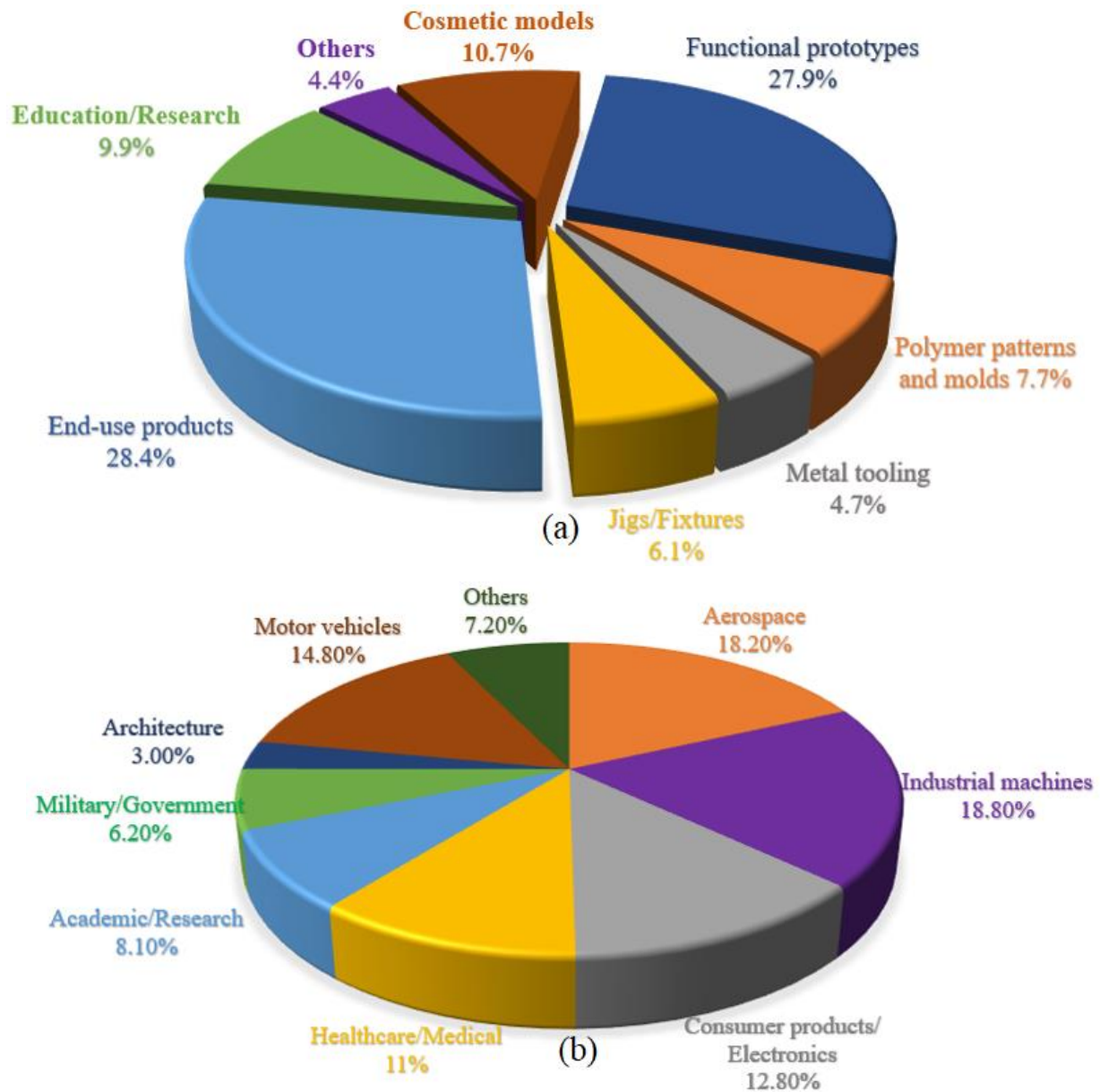


Figure 2. 2 (a) Categories and (b) Industrial sectors of AM applications based on Wohler's Report 2019 [53]

LPBF process also known as Selective Laser Melting (SLM) which uses a high-power laser beam to selectively melt the pre-defined contours in subsequent layers of powder. The molten metal pool rapidly solidifies by cooling [1,54]. Selected regions in each layer are melted by a laser beam, to form a 3D cross-section of the final part [1]. Consequently, the underlying build platform is

lowered followed by the deposition of another layer of powder with the powder coater/wiper mechanism. This cycle is successively repeated until the final three-dimensional solid object is built. The unfused powder is removed and recycled, this entire process is carried out inside a chamber filled with atmospheric gas (Argon, nitrogen), to avoid oxidation (see Figure 2.3).

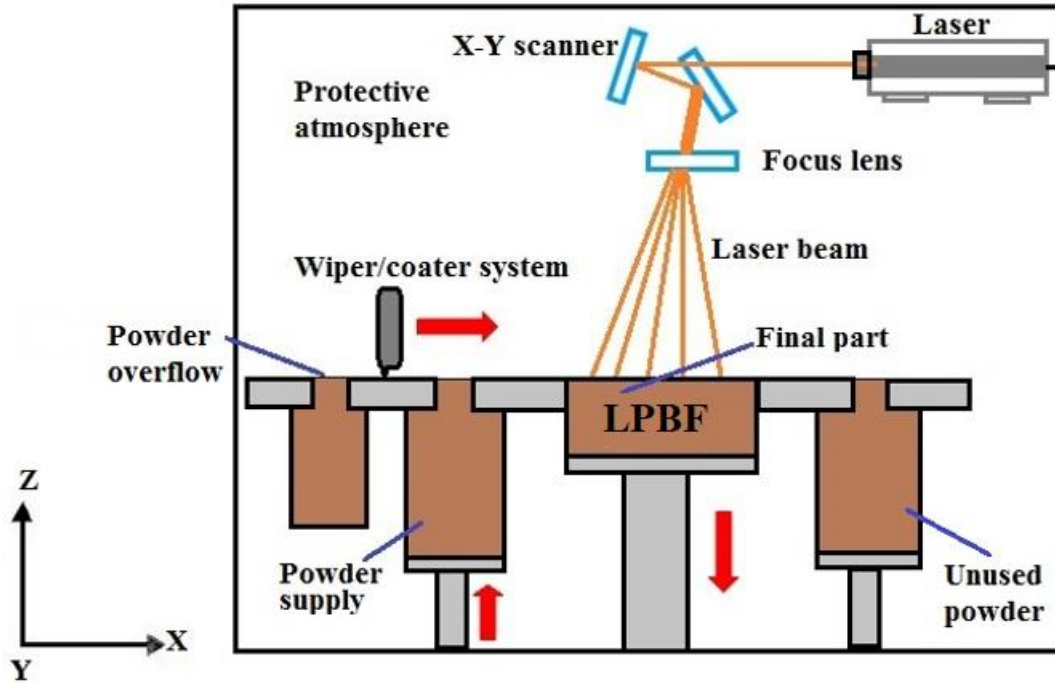


Figure 2. 3 Schematic illustration of the LPBF process

Some applications of the LPBF process are shown in Figure 2.4. LPBF fabricated products possess higher density with refined microstructure, which contributes to excellent mechanical properties, superior surface quality and dimensionally accurate final parts. Such a layer-wise production approach offers the LPBF process an edge over the conventional process in enabling consolidated parts with elaborated internal features for complex assembly, higher production rate, reduced design iterations, and quicker introduction of new products/prototypes to the market which were previously considered unfeasible to manufacture functional end-use products promptly [55-60]. The transition from rapid prototyping to fabricating final products also displays numerous technological barriers such as part variability, and incomplete knowledge related to structure-process-property correlation. Meanwhile, the LPBF process undergoes complicated thermodynamic and heat transfer mechanisms. The surface finish of the scan track is uncontrollable and unpredictable during the printing process which eventually affects the final quality of LPBF products [1,61]. Oxidation of feedstock materials, process induced inevitable

thermal residual stresses generated during complex thermophysical phenomena [62], are the most commonly occurring problems. Dimensional accuracy from a design model to the actual part is another issue faced by LPBF technology [1]. Although as-built LPBF components can be directly used as functional parts, the aforementioned inherent problems need to be addressed before the fabrication of standalone parts, which should be overcome to render a reliable, scalable, and high throughput widely adopted LPBF technique as a viable fabrication process.

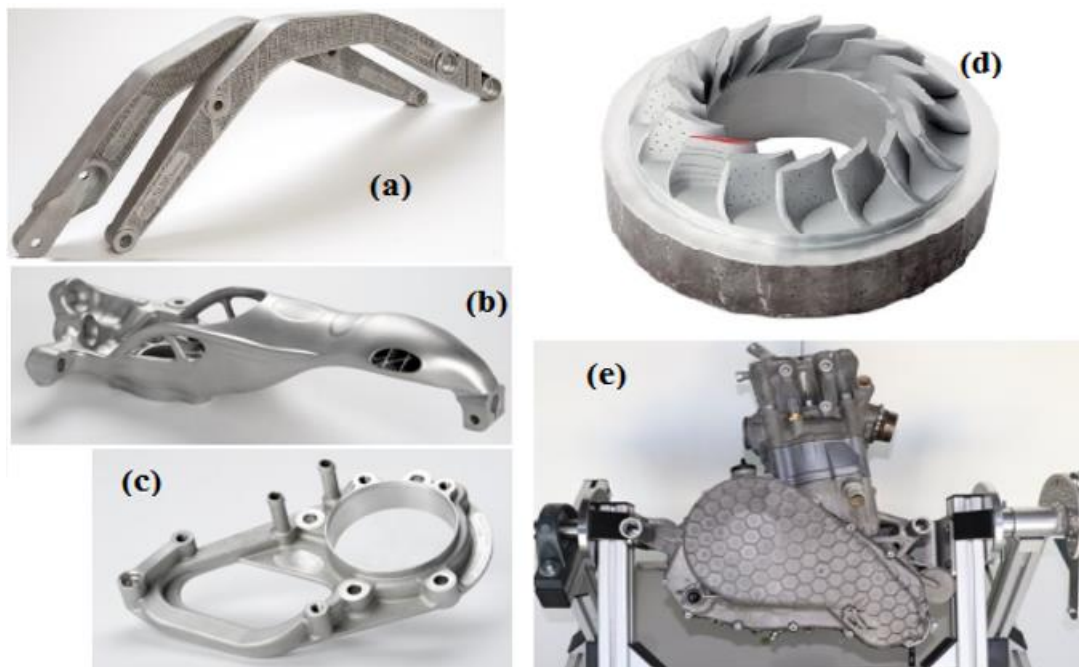


Figure 2. 4 Various LPBF-produced metallic part applications; (a) orthopaedic implant, (b) car steering knuckle, (c) Engine mount cooling channel, (d) aircraft engine blades (e) formula student racing engine [49,50]

2.1.2 Steels in AM/LPBF and their applications

Since their inception, steels and iron-based alloys have been the leading engineering materials for structural and sub-structural applications [63]. The steels have become part of our day-to-day life, and their importance to our society is extensively revealed by their plenitude of applications [1]. These applications include aerospace, automotive, medical, machinery, nuclear reactors, marine/oil and gas, shipbuilding, food and transportation, electronics and consumer applications see (Figures 2.2 a&b) [64,65]. According to the World Steel Association, over 3,500 different grades of steel are produced based on their applications, encompassing unique physical, chemical, and environmental properties [66]. The availability of steels in numerous grades has increased

their properties including higher strength, higher corrosion resistance, good ductility and toughness, low cost and nearly 100 per cent recyclability etc. [67].

Low carbon alloy stainless steels, especially 316L SS, have been one of the most commonly used types of steel among the other varieties due to their low cost, ease of processing, outstanding corrosion resistance, and excellent toughness even under difficult working conditions. The key characteristics of martensitic-type steels include their exceptional combination of superior corrosion resistance, increased strength, and superior mechanical qualities [1]. Martensitic-type steels such as precipitation-hardened (PH) steels (17-4 & 15-5) are used in aerospace, chemical, petrochemical, food processing, general metalworking, oil & gas, power-plant and injection moulding industries [68]. The combination of good corrosion resistance with higher hardness, yield strength and ductility, good weldability and abrasion resistance are necessary for the tools and die-making industry, tool steels fulfil this criterion. The most commonly used tool steels in the metal AM process are carbon-free maraging steels (18Ni-300) [69]. In addition to splendid high-temperature tensile properties, creep resistance and favourable irradiation resistance make oxide dispersion strengthened (ODS) steels perfect candidates for high-temperature turbine blades and heat exchanger applications [70]. The taxonomic classification of steels along with their applications is shown in Figure 2.5 [71]. In addition to the major class of steels (tabulated in Table 2.1), some of the less studied steel types used in the LPBF process are martensitic steels, TRIP/TWIP steels, silicon-based (Fe–Si), nickel-based (Fe–Ni), and cobalt-based (Fe–Co) alloy steels, China low activation martensitic (*CLAM*) steel, etc.

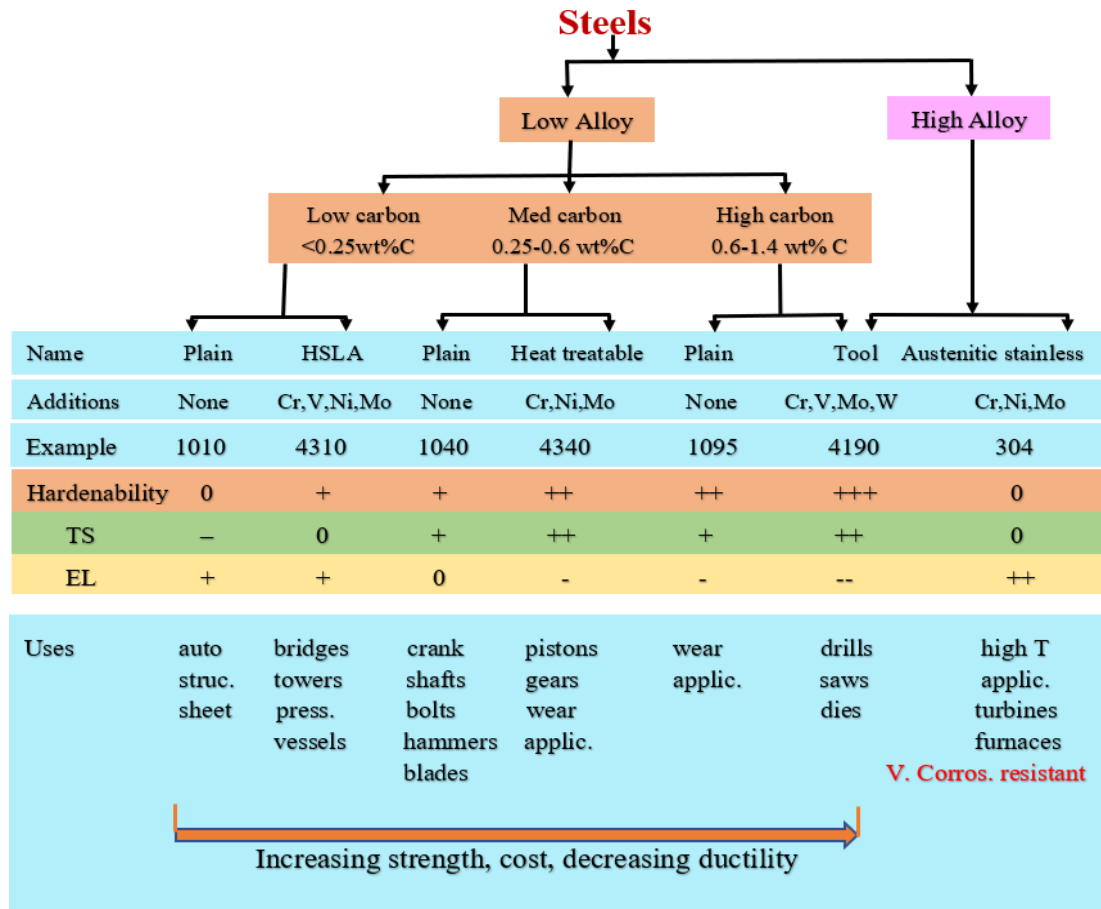


Figure 2. 5 Taxonomy scheme for various Steels. [Based on data provided in Tables 11.1(b), 11.2(b), 11.3, and 11.4, [71].

Table 2. 1 Chemical composition and mechanical properties of a major class of steels fabricated using the LPBF process

Type	Common Name/Grade	C	Cr	Mn	Mo	Ni	Si	Ti	Others	TS (Mpa)	Elongation (%)
Austenitic stainless steel	AISI 316L	<0.08	~17	<2	~2.5	~13	~0.75	-	-	~310	~30
Duplex stainless steel	SAF2705	<0.03	~25	<1.2	~4	~7	<0.8	-	-	~900	~25
PH stainless steel	17-4 PH	<0.07	~17	1	-	~5	1	-	-	~1400	~16
Maraging steel	18-Ni300	<0.03	<0.5	<0.1	~5	~18	<0.1	~0.7	~9 Co	~2050	~8
Carbon bearing steel	AISI H13	~0.4	~5	~0.5	1.15	-	~1	-	-	~1600	~9
ODS steel	PM200	~0.07	19	0.07	0.13	0.03	-	0.5	0.5Y ₂ O ₃	~875	~15

Currently, steels that are used in structural and automobile applications are mostly manufactured by conventional methods like casting, extrusion, and powder metallurgy [[1,72,73] The products produced by these traditional processes have been widely used but many problems persist [1]. The reason pertained to the slow cooling rates of the casting process inducing coarser microstructure,

and the defects related to inherent characteristics (porosity, part shrinkage) can subsist simultaneously, which collectively annihilate the mechanical properties [74-76]. Besides, the fabrication of steels in the standard process is time-consuming due to a series of independent processes (materials preparation, production and assembly) making it less flexible. With extensive development in manufacturing, special attention has to be paid towards the process-structure-performance requirements of steel components. For example, cellular or lattice-type steel structures are primarily used in working at elevated temperatures under extreme environments (missiles, aircraft applications) to thwart oxidation, and corrosion whilst retaining their mechanical integrity [77,78]. Constituent fabrication of complex, functionally graded materials (FGM) for structural components in AM offers the greater advantage of saving time, costs and flexibility (see Figure 2.6). More importantly, AM process reduces the weight and stress concentration factors associated with other conventional welding and joining techniques [79,80]. Despite the fact, some of the traditional manufacturing issues still exist in AM process, the comparative analysis reveals that AM process or LPBF process, has been successful in fabricating defect-free (minimum number of process-related metallurgical defects) good-quality parts exhibiting excellent mechanical properties as compared to conventional processes like casting, extrusion processes [1,81]. The higher strength is attributed to the combined effect of (AM process-induced) refined microstructure (dendritic, cellular type of grains), and potential high dislocation density caused during rapid solidification [81-93]. As technology continues to advance exponentially, the manufacturing process is no longer about just producing physical products. A fundamental shift is imperative to meet the change in consumer demands, the nature of products, and the economics of production and the supply chain. Data-driven models using advanced machine learning algorithms, added sensors and connectivity are capable of revolutionizing conventional manufacturing into smarter manufacturing [1]. Fabrication of smart steel products by utilizing the smart and robust AM technology that possesses designer surface topography and mechanical performance, highly dense and dimensionally accurate, near net shape parts with the reduced requirement of post-processing is going to be a major research and development objective in the future [1,5].

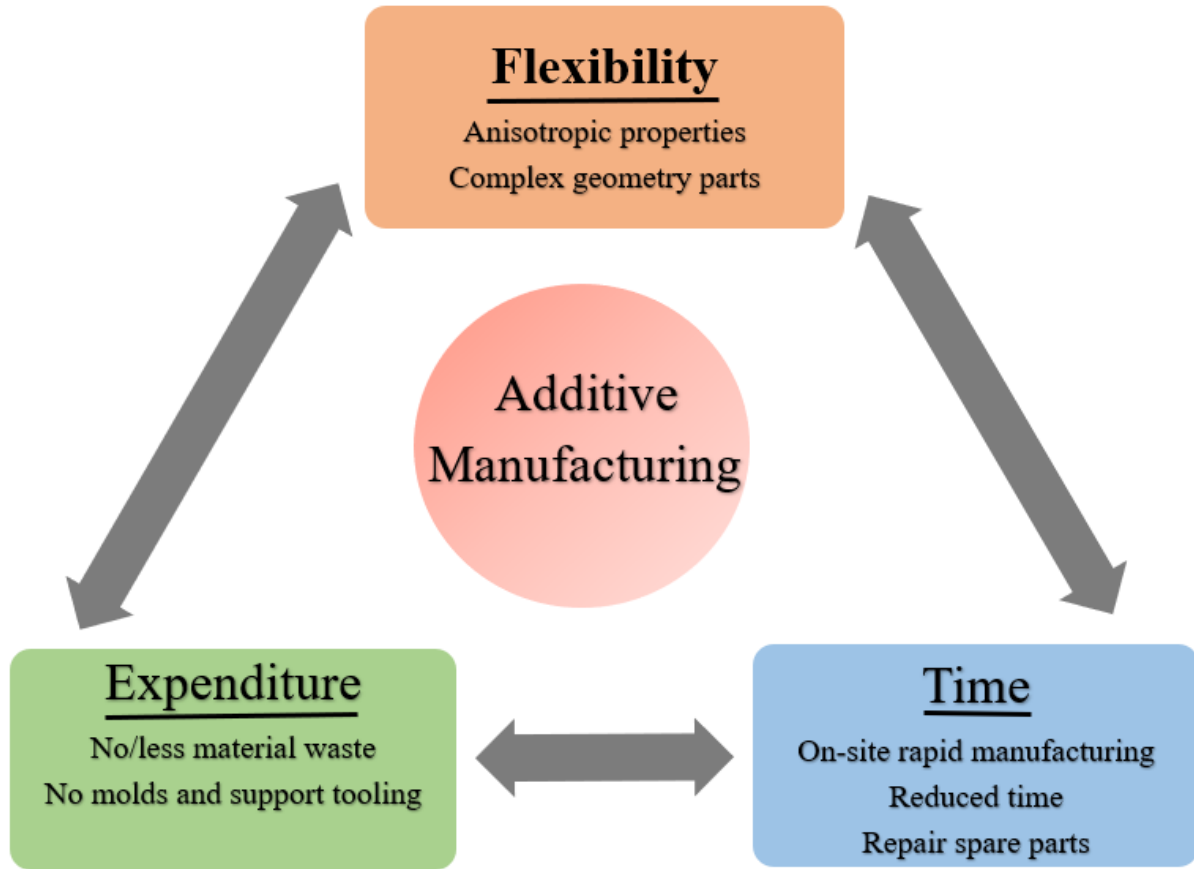


Figure 2. 6 Correlation between Additive manufacturing key features and its advantages.

2.2 Metal AM metallurgical defects and surface asperities

Formation of metallurgical defects such as; balling, porosities, keyholes, cracks, metal inclusions, residual stresses, warping, de-lamination, oxidation, loss of alloying elements, denudation etc., and surface asperities namely; staircase effect, partially-melted/un-melted particles, spatters, re-entrant features [36] etc., are commonly observed during LPBF process (see Figure 2.7.). Incorrect selection of process parameters would likely introduce inevitable metallurgical defects and surface asperities into LPBF fabricated part, which causes adverse effects on the resultant microstructure, surface quality, and mechanical properties [94].

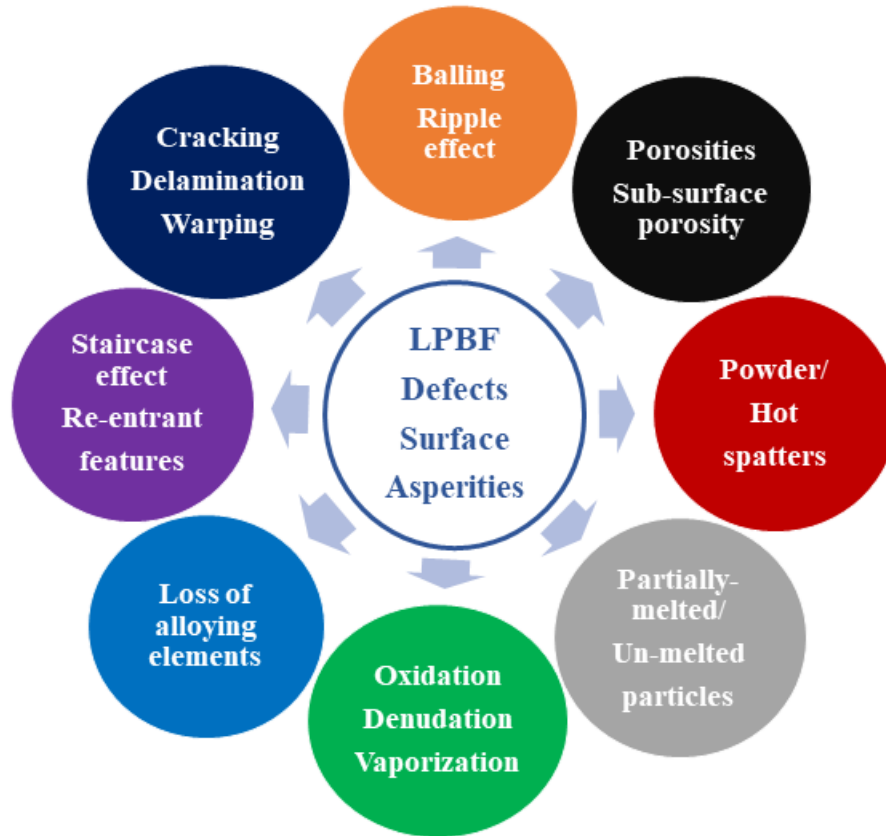


Figure 2. 7 List of various metallurgical defects and surface asperities that emerge during the LPBF process.

2.2.1 Balling

Balling phenomenon is described by the Plateau-Rayleigh capillary instability, which occurs when the deposited melt track sometimes tends to break up into half-cylindrical shapes or into spherical balls [95]. This phenomenon depends on the process variables such as scanning speed, surface tension, viscosity and density of the materials deposited [96]. Balling phenomenon is one of the critical surface defects which is considered the severe processing defect in the LPBF process [97]. Surface tension and wettability have a greater impact on the formation of a molten melt pool. The combination of surface tension and capillary forces drives the molten pool to shrink into its lower surface energy state (a sphere) when the coalescence of individual melt tracks is in poor contact with the underlying substrate resulting in the formation of the balling defect [95]. In other words, the balling defect can also occur when the liquid phase present along the surface and grain boundaries of the molten melt pool fails to completely wet the remaining solid particles and the underlying substrate due to the presence of surface impurity [[1,98]. The balling defect leads to

pores, higher surface roughness, and reduced density causing a lack of fusion between the powder particles/layers, imparts irregular melt tracks, and in some extreme conditions causes obstruction to the deposition process [97]. The severe balling phenomenon on a certain melt track layer inevitably leads to the formation of humping or ripple effects [99]. These ripples can carry forward onto the next layer resulting in a lack of coalescence between the layers causing poor metallurgical bonding and inducing low part density. Ripple defects contribute to the stacking of materials that can have a serious impact on the surface quality of the scan track resulting in poor surface roughness of LPBF-built 316L stainless steels [99].

When the laser beam incident on the powder bed, melting starts instantly at the local positions of the powder particles' surface. The phase transition from solid to liquid molten 'cluster' is formed between the surrounding powder particles, causing a reduction in surface area that gives rise to agglomeration. The selected laser spot size is usually bigger than the (starting) particle size. As the powder particles are melted together, smaller agglomerates gradually grow and are bound to form significantly bigger agglomerates (coarsening) [1]. As this process continues, a further reduction in surface tension of the molten melt pool tends to form a ball-shaped structure (balling). The dimensions of these formed balling structures are several times bigger than the original particle size (see Figure 2.8) [97].

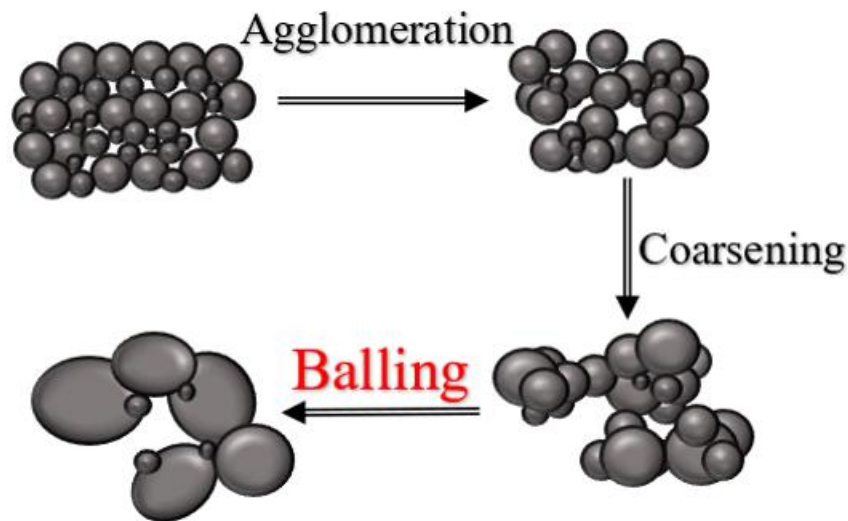


Figure 2. 8 Schematic illustration of balling phenomena [97]

2.2.2 Porosity

The degree of metal powders' compactness is generally low. In addition, existing gas in the powder particles can easily diffuse into the molten melt pool which cannot escape out of the molten melt

pool surface due to rapid cooling and solidification. Thus, porosity is formed in LPBF-fabricated steel parts [100]. Conversely, the gas solubility in liquid metal is commonly high at elevated temperatures which also contributes to the formation of pores. The porosity defects in the LPBF process are classified into incomplete fusion holes, keyhole/or depression defects and voids [100-103].

Incomplete fusion holes are related to insufficient energy input that fails to completely melt the metal powders and inadequate penetration of liquid metal into the previously solidified layer causing poor metallurgical bonding [104]. The lack of fusion defects can range up to a few hundred microns which are irregular in shape and are commonly formed at the melt track layers interface. If the supplied heat input is low, then the formed width of the molten pool becomes too small [1]. The smaller molten melt pool leads to an insufficient overlap between the melt tracks. This insufficient overlap gives rise to the formation of un-melted powders at the melt tracks interface (Figures 2.9 a&b). As a result of incomplete fusion holes, the surface of this location becomes rough which directly obstructs the flow of the molten pool causing interlayer defects. These interlayer defects gradually propagate as the process continues, finally forming a multi-layer defect [100,101].

The keyhole pores are usually spherical (Figures 2.9c&f) in shape caused by the gas bubbles trapped inside the powder particles in the powder mass. The keyhole pores are also attributed to very high laser energy density [93], which leads to the vaporization of low melting point elements within the alloy in the form of gas bubbles. The vapour bubbles can be trapped by a fast-moving laser beam and sometimes be easily dragged to the bottom of the molten melt pool by convective currents. The fast solidification rate does not allow these gas bubbles to arise and escape from the molten melt pool [105,106]. The spherical pores are formed due to trapped gases inside the powders during the powder atomization process or inside the molten pool during the LPBF process. In some cases, the keyhole pore is also referred to as a depression defect that can exist at the end of a melt track with a width almost equal to the laser spot size (Fig. 18e) [102-104]. End-hole is ascribed to very high scan velocities, where laser irradiation time is not sufficient for a deep keyhole formation, instead, an open pore is created at the end of the melt track surface. End hole pore is usually induced by the dominant downward recoil pressure that is exponentially dependent on the temperature of the molten melt pool region which is directly under the laser beam [102, 107].

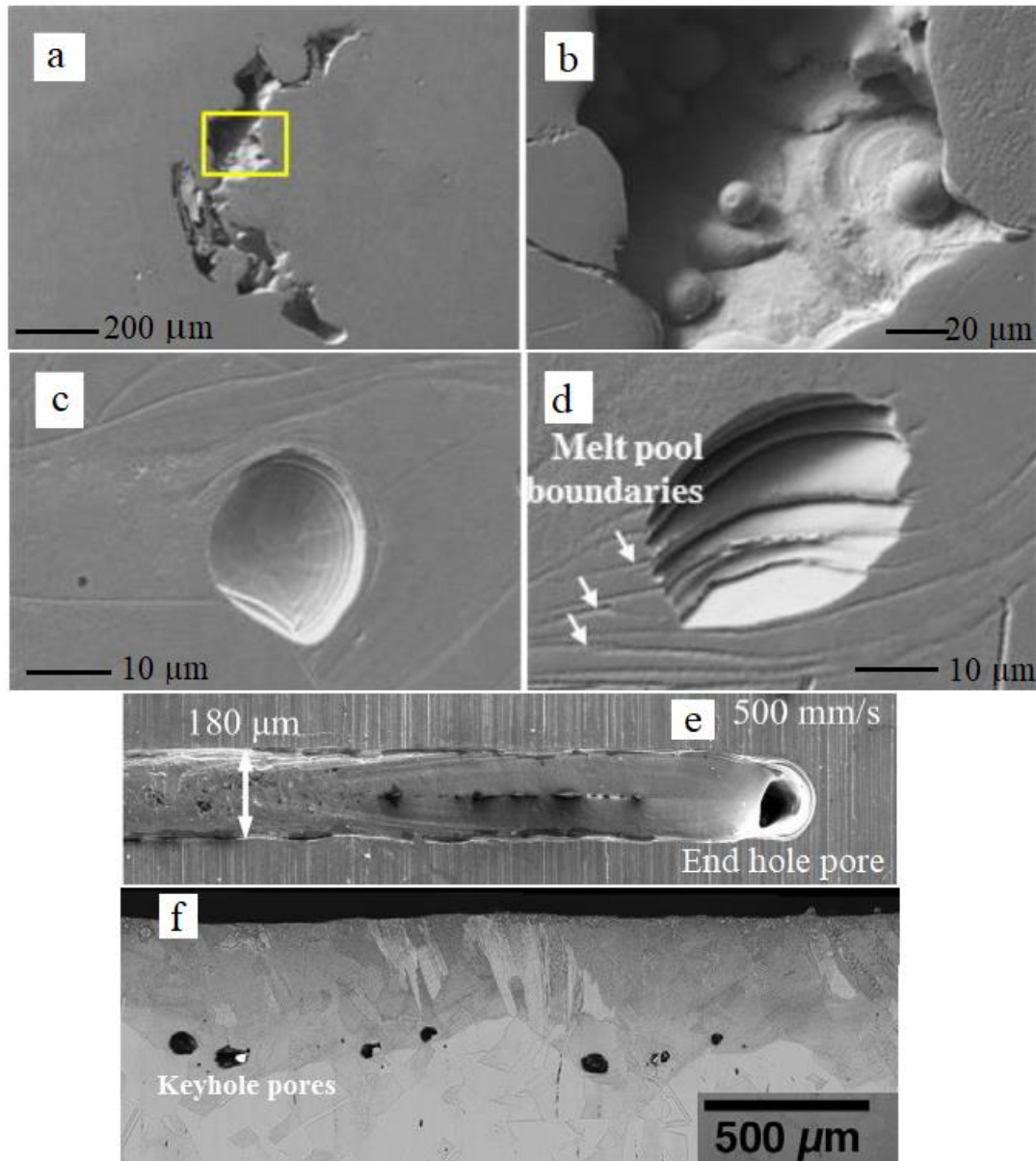


Figure 2. 9 SEM images of porosity defects observed in 316L LPBF samples: (a) low and (b) high magnification of insufficient fusion defect; (c) gas pore; (d) Void/cavity defect; [100], (e) End-of track hole [108], (f) an array of keyhole pores at the bottom of melt tracks [102]

The void formation is not entirely limited to low laser energy input. Perhaps, it also depends on the stability of the melt track. Voids could be either trapped gas pores, lack-of fusion holes or keyhole pore-induced porosities [100]. Voids are generally characterized by inside-layered morphology associated with molten melt pool boundaries (Figure 2.9d). Void defects normally originate from the higher residual stresses generated by the rapid cooling of the molten melt pool,

which also sometimes could nurture the formation of cracks along the melt pool boundaries, leading to final segregation and void formation [100]. There is a strong possibility of voids or open porosity to occur at a higher scanning speed due to the inability of the liquid metal flow to completely fill the surrounding area, where the shielding gas is originally present (see Figure 2.10). Insufficient filling of the neighbouring gaseous region and rapid cooling rates leads to the generation of voids or open porosity of several hundreds of microns at the surface and distributed along the overlapping gaps [106]. Porosities can lead to serious metallurgical defects, yield lower part density, and adversely affect the surface texture and mechanical performance of LPBF fabricated steels.

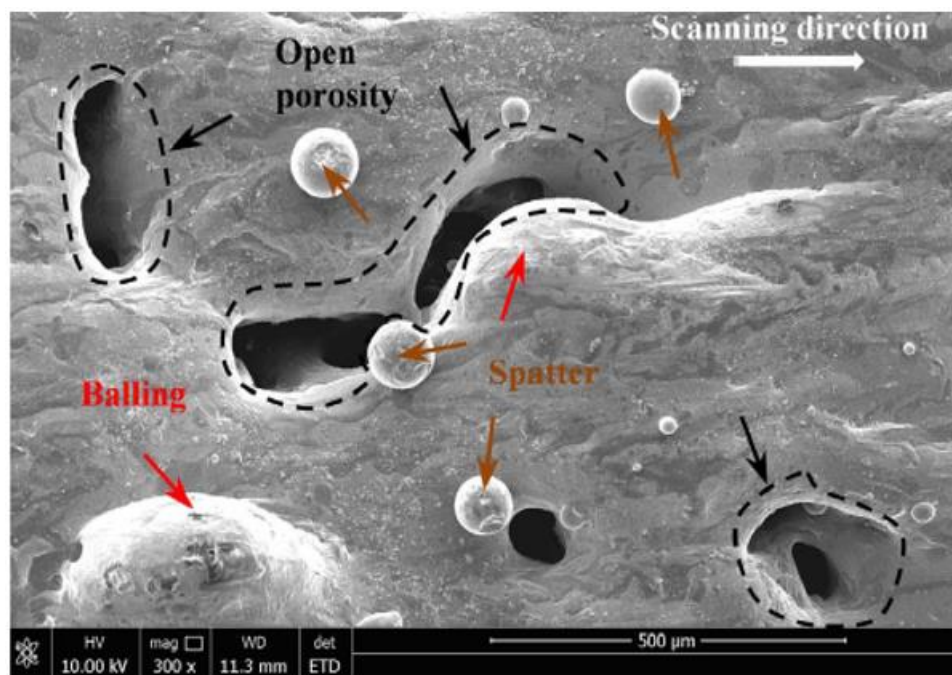


Figure 2. 10 Scanning electron microscope (SEM) image showing open porosity or voids [106]

2.2.3 Residual stress and cracking

Residual stress is a characteristic of the thermal manufacturing processes, and parts produced by the LPBF process are especially vulnerable to residual stresses. Residual stresses can also lead to the formation of various building defects associated with LPBF parts failure [109]. Higher temperature gradients and densification ratios which are attributed to the LPBF process, tend to create higher residual stresses. High thermal stresses cause surface defects and porosity that normally occur around the melt pool. In extreme cases, higher residual stresses result in part distortion, shrinkage, cracking, warping and delamination of LPBF produced part from its support

structures. As a result of this, the resultant mechanical properties, part density, and dimensional accuracy of LPBF parts tend to be substantially compromised [109-111].

Thermal stresses generally occur from the temperature gradient or the solidification-induced shrinkage of adjacent laser-melted zones in solidified material, thereby a decrease in thermal stresses also results in decreased residual stresses. Thermal stresses are mainly responsible for cracking. Based on the expansion behaviour of the material heating or cooling, thermal stresses formed during the LPBF process are classified into (i) temperature gradient mechanism (TGM) in the solid substrate and (ii) the cool-down phase of the melted top layers [112]. In the first case, the top layers of the solid substrate expand thermally when it experiences the high thermal energy gradients induced by the laser beam. The thermal expansion is restricted by the colder underlying solidified layers [1]. This induces elastic compressive stresses in the top layers of the substrate. The thermal expansion may exceed the yield stress of the material and upend the plastic deformation of top layers in the direction of the laser energy source (Figure 2.11a).

The compressive stresses in the material, however, create plastic deformation of the top layers when it reaches the yield stress point. The layer of printed material compresses and bends the opposite way when the plastically distorted layers cool (Figure 2.11b). As a result, the compressive stresses are converted into the residual tensile stresses that cause cracking in the LPBF parts [1,112]. In the second case, the temperature of the upper layer, which has already melted, is initially higher than that of the bottom layer. The upper layer tends to shrink more due to thermal contraction when the molten melt pool cools and solidifies. However, the underlying colder layers again prevent this distortion. As a result, compressive stresses are introduced to the bottom layers and tensile stresses to the top layers [112-114]. Finite element simulation techniques are frequently employed to predict the distribution and evolution of residual stresses due to the complexity of the LPBF process and the challenge of experimental measurement [1,110].

Cracking in the LPBF process can be divided into solidification cracking and liquation cracking (Figures 2.12a&b). Solidification cracking occurs at the terminal stages when dendrites have nearly entirely developed into equiaxed grains and are separated by a thin residual liquid strip in the form of grain-boundary films in a mushy zone. The molten melt pool may be quite weak at this time, making it vulnerable to cracking under tensile stresses. In simple terms, solidification cracking happens when the flowability of the liquid is restricted by increased viscosity at a lower temperature and the inter-dendritic liquid flow is impeded by the solidified dendrite arms [1,115].

Solidification cracking occurs when the localised tensile stresses created across the neighbouring grains are greater than the ultimate tensile strength (UTS) of the fully solidified material at a specific point and temperature [116]. It is discovered that solidification cracking has no discernible impact on the final clad characteristics since it frequently occurs at the top deposit surface. Utilising laser re-melting or machining helps prevent solidification cracking. As soon as it forms, liquid cracking persists in the heat-affected zone and needs to be closely monitored [1,117].

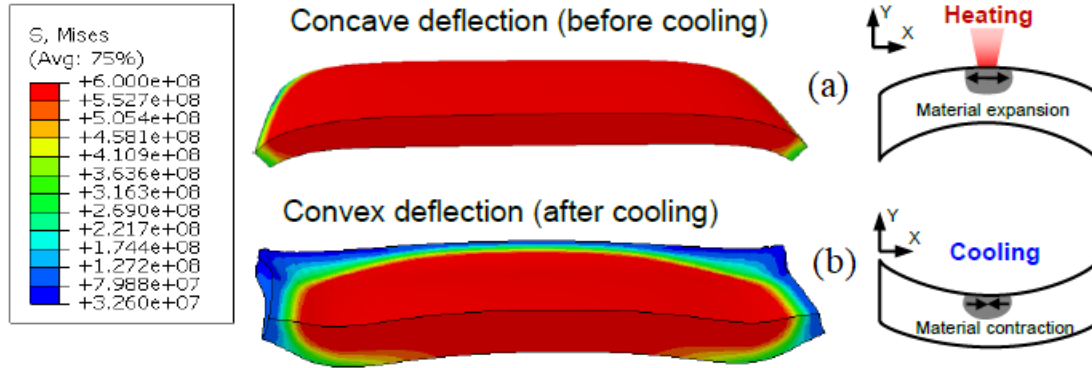


Figure 2. 11 Schematic of thermal gradient mechanism of residual stress in LPBF process (a) heating; (b) cooling [110].

Liquation cracking initiates from the weaker region, i.e. partially melted zone or at the heat affected zone (HAZ) in pre-layers, propagating through the intergranular region with the further deposition proceeding layer by layer [118]. Liquation cracking also known as hot cracking mainly occurs in alloys with high alloying element levels. In HAZ and intersecting zones where layers are re-melted above the eutectic temperature (solidus temperature), these alloys precipitate a number of low-melting eutectics [1,119]. Once a liquation crack is formed, it becomes an initiation site for the crack propagation and cracks gradually expand as the deposition progresses. Liquation cracking tendency depends greatly on grain boundary misorientation, which is influenced by the stability of liquation films and local stress concentration [118].

Ductility-dip-cracking (DDC) is a crucial mechanism for crack initiation/formation when high-angle grain boundaries are present in the LPBF process. It happens at a low temperature where the ductility and tensile strength are low [1,120]. Due to the lack of diffusion in a non-equilibrium rapid solidification process, the solidus and liquidus temperatures decrease, and the temperature range of solidification becomes wider initiating DDC in the LPBF process [120].

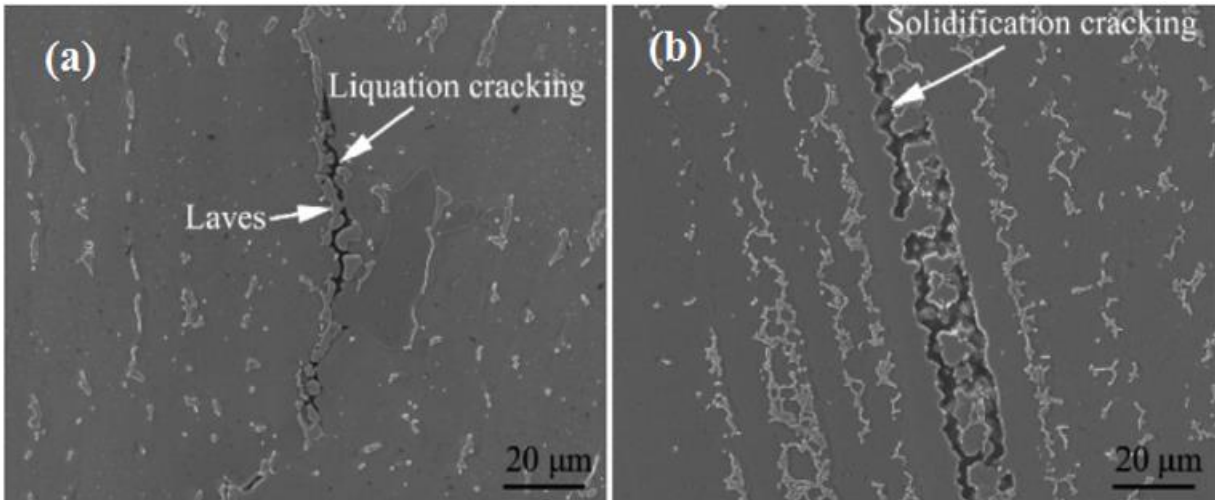


Figure 2. 12 Morphology of cracking (a) Liquation and (b) solidification cracking [117].

The faster melting and solidifying rates in the LPBF process results in tensile residual stresses because of the localized high laser energy input, coupled with the lower thermal conductivity of the powder particles [121]. A higher temperature gradient is developed right next to the laser spot. Due to their lower thermal conduction and higher thermal expansion coefficients, austenitic stainless steel (SS) is more prone to solidification cracking than low-carbon steels [1]. Additionally, certain alloying impurities like silicon (Si), phosphorous (P), and sulphur (S) have a significant effect on cracking in stainless steel alloys. The crack sensitivity can be reduced by decreasing the S+P+Si composition. A significant nitrogen value is harmful to the solidification cracking of stainless steels, which is another intriguing observation [1,122].

The high carbon steels are usually composed of a continuous martensite phase, whereas in SS, a continuous phase is often in the form of retained austenite, which helps in preventing cracking. Preheating in part or totally can prevent excessive cracking in M2 (medium-alloyed tungsten molybdenum steel) and H13 tool steel. Preheating is advantageous in preventing the formation of martensite. Rapid solidification typically produces finer microstructure, although it is insufficient to prevent segregation. However, a low melting phase has enough non-uniformity to prevent segregation and cracking. In general, this kind of cracking is observed in the high copper alloy 17-4 PH SS [1,123]. High silicon steel also showed similar cracking, which was impacted by increased laser energy input [1,121].

2.2.4 Oxidation

To fabricate parts free of oxides, the LPBF processing chamber's atmosphere is crucial. Despite using protective inert environments and a shielding inert gas flow to limit the oxygen content in

the working chamber, there is always a chance of a small percentage of unwanted oxygen content ($\sim 0.1\text{-}0.2\%$) present during the LPBF process [124]. This is because there is undetectable air filling between the powder particles. Similar to the conventional metal casting process, sources of oxides formation in the LPBF process arise from oxygen existing in the surrounding atmosphere entrapped inside the porosity of the powder particles. The entrapped oxygen is unable to be completely vaporized from the surface caused of the extreme intermix of irregular strong laser fluence flow convections of the molten metal pool [124]. Due to a wide area being associated with a powder mass, passive oxide films may also form on the powder's surface prior to melting [1,125]. The presence of oxygen content in the powder might be transferred into an LPBF-fabricated specimen directly [1,126].

Ti_3O_5 , Al_2O_3 , Cr_2O_3 , Fe_2O_3 , NiCr_2O_4 , and NiFe_2O_4 are the common oxide phases formed during LPBF of maraging steels, stainless steels, and Inconel 718 metal powders respectively [125,127,128]. In general, alloying elements like Mn, Si, Ti, and Al present in steels have a higher affinity for oxygen [1]. These elements can be selectively oxidized on the surface of the LPBF-built part [124]. Maraging steel 18Ni (300), Ti and Al have the highest affinity to oxygen. The oxide phase is generally more stable than the nitride in the steels molten melt pool. Small cubic TiN particles are created when nitrogen combines with a fraction of the titanium from the maraging steel [1]. TiN is most likely to be formed by a higher N_2 supply from the atmosphere (see Figure 2.13). In addition, a combined oxide phase containing mainly Ti_3O_5 and Al_2O_3 can also be formed. The development of oxides, nitrides, and carbides follows a similar process to that of other kinds of steel. The formation of oxide layers in the nanoscale range can be quickly evaporated during vigorous mixing and stirring of molten melt pool by a laser beam, resulting in minimal damage to LPBF parts [1]. On the other hand, micrometre range oxides films ($10\text{-}100\mu\text{m}$) of irregular geometry formed cannot be completely vaporized by the stirring action of the laser beam and Marangoni flow. The oxide layer can grow thicker with increasing oxygen content in the atmosphere, at the same time as the layer re-melting. When the re-melting of a new layer begins, the oxide film formed previously breaks down, and part of this oxide hovers on top of the newly formed layer, with the rest trapped inside the LPBF fabricated component. The trapped oxide leads to the formation of oxide inclusion [124,127,128]. Some of the un-melted or partially-melted particles are trapped in these oxide inclusions. The stability of the molten melt pool can be significantly impacted by the oxide residues' and pose adverse effects on the heating, melting, and

fusing of powder particles [1,124]. Thick oxide inclusions increase the surface tension effects, limit the absorption of the laser energy and wetting of substrate, and obstruct molten pool flowability. These oxide inclusions also result in the formation of metallurgical defects such as balling, insufficient melting between powder particles, reduces part densification, induces cracking and consequently lowers mechanical properties [125-127]. It is worth noting that any pickup of moisture from the environment by the feedstock powders paves the way for the introduction of oxygen content into the LPBF system [129].

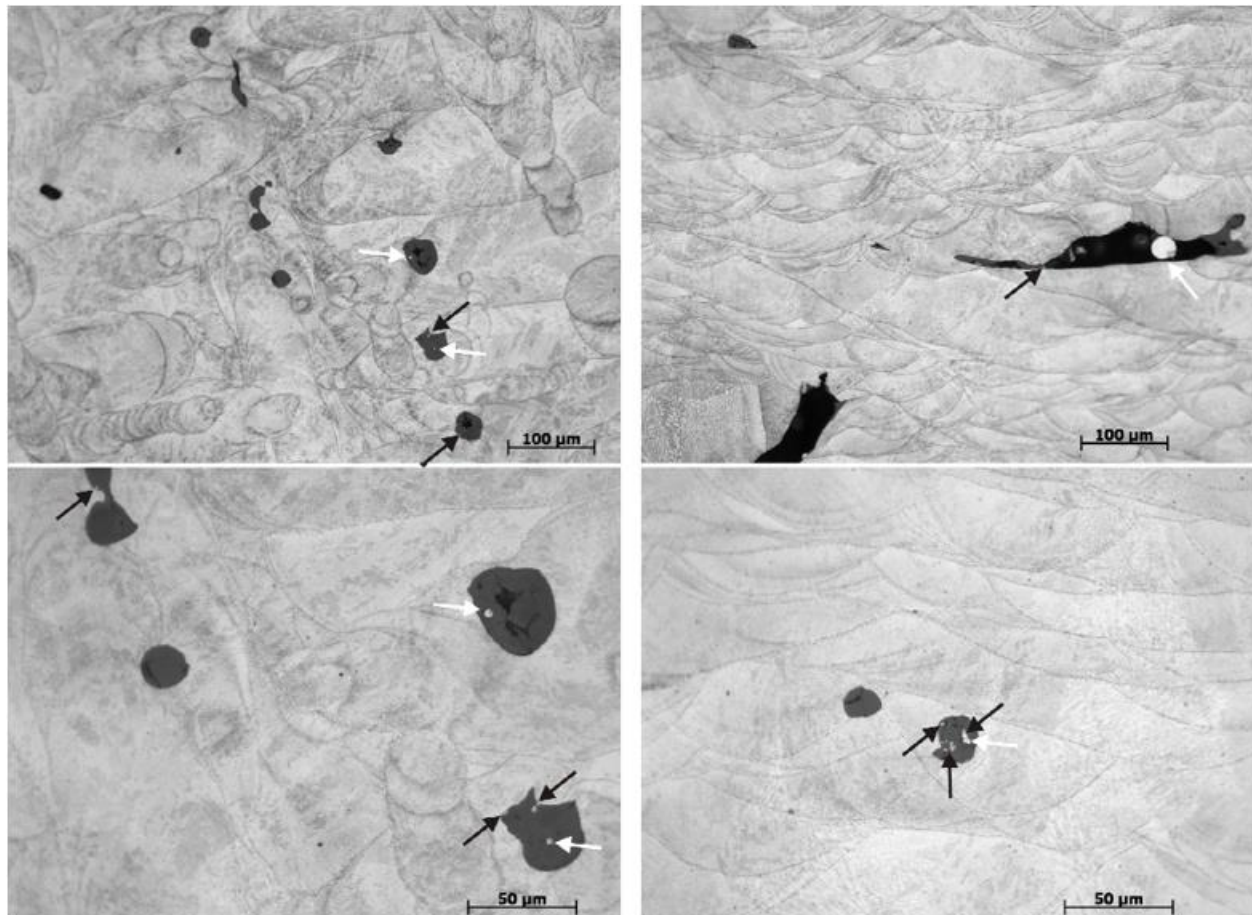


Figure 2.13 Light optical micrographs at different magnifications of the LPBF parts with laser re-melting under pure N₂ atmosphere. Top (left) and side views (right) are showing the melt pool shapes and the dark grey oxides containing white parent powder particles (indicated by the white arrows) and yellow TiN inclusions (indicated by the black arrows) [1,128].

2.2.5 Loss of alloying elements

In the LPBF process and other laser processing technologies, vaporization is intense in a small region right underneath the laser beam where the temperature is high. At a very high laser fluence,

the temperature at the surface of the molten melt pool is higher than the boiling point of steels, which contributes to vaporization. Vaporization leads to the loss of alloying elements, resulting from the concentration and pressure gradients [1]. The concentration of vaporized alloying elements on the molten melt pool surface is higher than that inside the shielding gas [130]. The intensity of vapour pressure at the molten melt pool surface is higher than the surrounding environment pressure, thus the surplus pressure drives vapours containing alloying elements to eject away from the surface [130,131]. The chemical composition of steels produced by LPBF is altered by the vaporisation and segregation of alloying components [1]. For example, nickel, and manganese concentrations were significantly reduced, whilst the increase in silicon and iron alloying elements concentrations was recorded during the LPBF process of Invar 36 steel [96]. Similarly, nickel, manganese and chromium alloy concentrations were decreased with an increase in silicon and molybdenum alloying elements in the LPBF process of 316L stainless steels. This phenomenon was attributed to the concentrations of alloying elements with lower boiling temperatures decreased, while the concentrations of the other alloying elements with higher boiling temperatures increased, except the base alloying element iron [1,96]. Loss of alloying elements reduces part density, causes microstructural defects such as keyholes, pores, spatters, voids, cracks, and un-melted tracks and exhibits poor surface quality and lower mechanical performance of LPBF fabricated parts [82,96].

2.2.6 Denudation

Powder denudation is the apparent depletion of powder particles around the solidified melt track (see Figure 2.14). In a typical LPBF processing environment, the strong evaporation of the metal vapour plumes from the molten melt pool results in denudation [1]. The intense vaporisation causes the pressure to drop inside the vapour plume and produces an ongoing flow of ambient gas towards the centre of the melt track known as Bernoulli's effect. The powder particles along its path, which can be incorporated into the molten melt pool or ejected with the vapour plume, are enough to be swept in by this inward ambient gas flow [1,132]. Increased laser power, faster scan rates, and lower argon gas atmospheric pressure all contribute to greater powder particle depletion. However, if the laser fluence is insufficient to completely melt the powder particles, denudation also occurs because surface tension tends to draw the partially melted powder particles into the molten pool [1,133]. Powder denudation leads to porosity and accumulation of un-melted/partially melted particles between the melt track layers causing a rough surface [134].

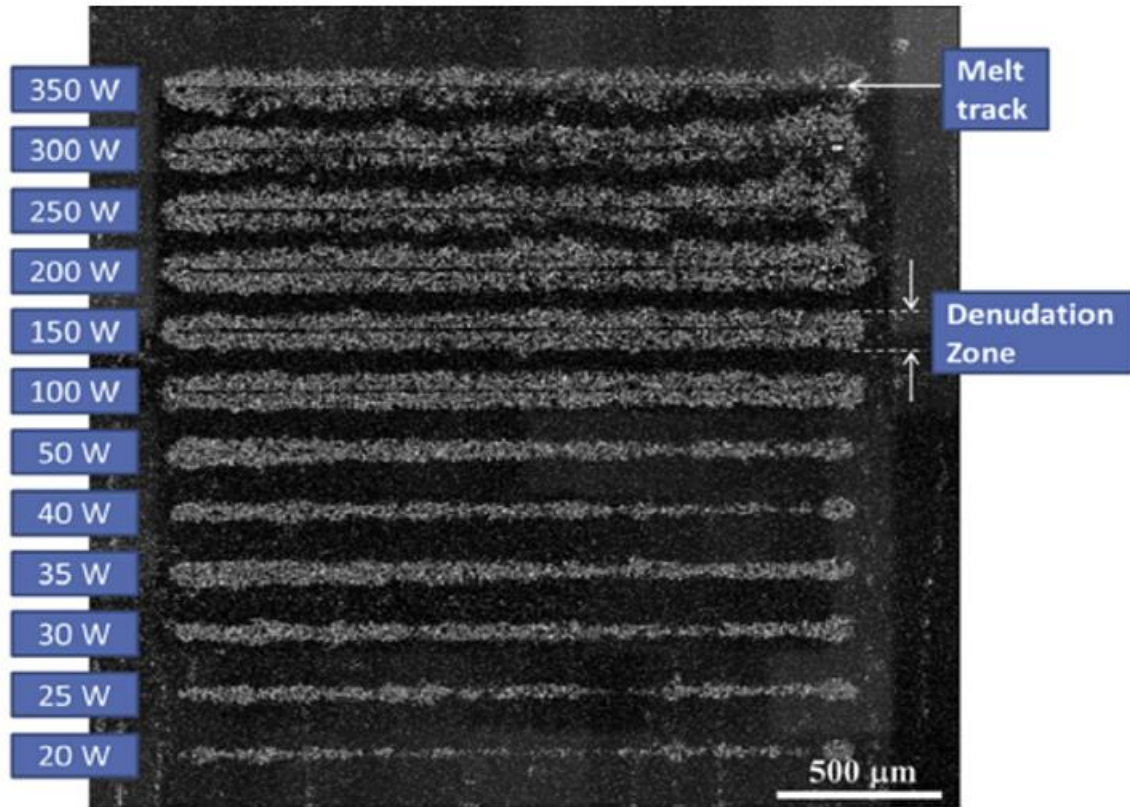


Figure 2. 14 Confocal height microscope image of denuded zones around melt tracks for different laser power and 2 m/s scan speed [132].

2.2.7 Environmental effects

Argon (Ar), Nitrogen (N_2), and Helium (He) are the three most commonly used protective shield inert gases during the LPBF process. In some cases, hydrogen (H_2) is also used as a deoxidizer to provide the required protective environments. LPBF-processed steel components produced under Ar and N_2 environments exhibited near full density values, while the parts produced under the He environment exhibited a density of around 90% using the same processing parameters [1,135]. The reported lower dense part produced under the He environment can be attributed to the shielding gas effect. The higher plasma plumes were generated in the He environment above the molten melt pool restricting the laser interaction. He and H_2 environments could block the laser irradiation, resulting in less dense parts due to the transport of low laser fluence. The lower specific gravity lead to the higher plasma plumes to arise [1]. These plumes can sometimes completely obstruct the laser irradiation causing porosity defects [135]. The lower plasma plumes generated under Ar and N_2 environments maintain good contact between the laser beam and the metal powders, which resulted in near full-density parts with values over 99% [135]. However, it is commonly believed

that the use of N_2 can react with the alloying elements present in the metal powders, forming unwanted nitrides in the solidified microstructure that tend to display a detrimental impact on the final quality of LPBF fabricated parts. The generated plasma plumes impede the laser beam and are often responsible for the variations in final product density [1]. This can be combated by using Ar as the shielding gas and supplying sufficient and continuous energy input, which can overcome the energy losses of metal vaporization and ionization processes [136]. Similarly, employing low atmospheric pressure during the LPBF process of steels offers less resistance to metal vapours which causes a large number of free powder spatters (Figure 2.15a). Therefore, strong environment pressure is recommended. Metal vapours that exist from the surface of the molten pool have to fight against the strong protective environment, which results in fewer powder spatters (Figure 2.15b) [1,131].

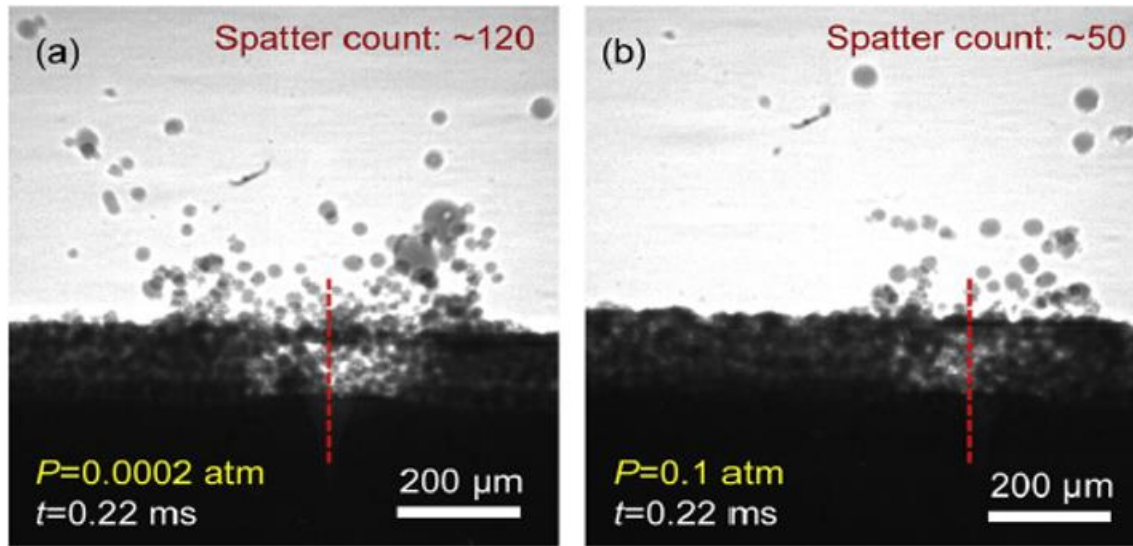


Figure 2. 15 X-ray images showing spatter counts for the same powder bed thickness with different environment pressure (a) weak environment pressure and (b) strong environment pressure [131].

2.2.8 Surface asperities responsible for poor surface quality

Metal AM like LPBF undergoes complex thermophysical phenomena consisting of various heat transfer mechanisms and molten melt flow, resulting in poor surface quality [22]. Some of the major contributors accountable for poor surface quality or rougher surface finish of metal AM parts are: Firstly, LPBF itself induces higher surface roughness as it undergoes a very complex thermophysical mechanism and kinetic phenomena during the layer-by-layer building process. Secondly, the right selection amongst the diverse process parameters plays their part in imparting unique anisotropic fingerprint on surface features generating poor surface quality [19,20], and

finally, miscellaneous factors such as lower process resolution of building part/artefact and layering effects, supporting structures, feedstock materials quality, packing density, morphology, rheology contribute towards the substandard surface quality [22,18,23]. Therefore, the surface quality of metal AM/LPBF parts is perceived to be unpredictable and uncontrollable. The individual or the combination of these three circumstances yields strong surface texture characteristics inherent to the metal AM process, which is usually dominated by the number of already discussed inevitable metallurgical defects and surface asperities or irregularities. The formation of different types of process-related defects and/or surface asperities depends on the type of part/artefact being built, the laser angle of incidence relative to the build platform, and the kind of metal AM processes employed.

The typical surface asperities that appear on LPBF surfaces are the staircase effect, unmelted/partially-melted particles, hot/powder spatters, re-entrant features, cracks, surface and sub-surface porosities, etc. [1,3,36,137,138]. Amongst all, balling, staircase effect, spatters, and unmelted/partially-melted powder particles often originate in surface texture features of the unique fingerprint on curved and/or inclined surfaces of the LPBF components (see Figure 2.16).

The staircase effect is considered one of the major contributing factors promoting substandard surface roughness of metal AM components. Owing to layer-by-layer powder consolidation involved in AM process: the staircase effect also referred to as stair-stepping effect often emerges on both up-skin and down-skin surfaces of curved and inclined AM components (see Figures 2.17 a&b) [6,139,140]. The staircase effect usually corresponds to build inclination angles and layer thickness [141]. As the inclination angles increase the relative surface roughness induced by the staircase effect also increases up to 30°. AM components possessing excellent surface quality with lower surface roughness could be attained by selecting a smaller layer thickness [139].

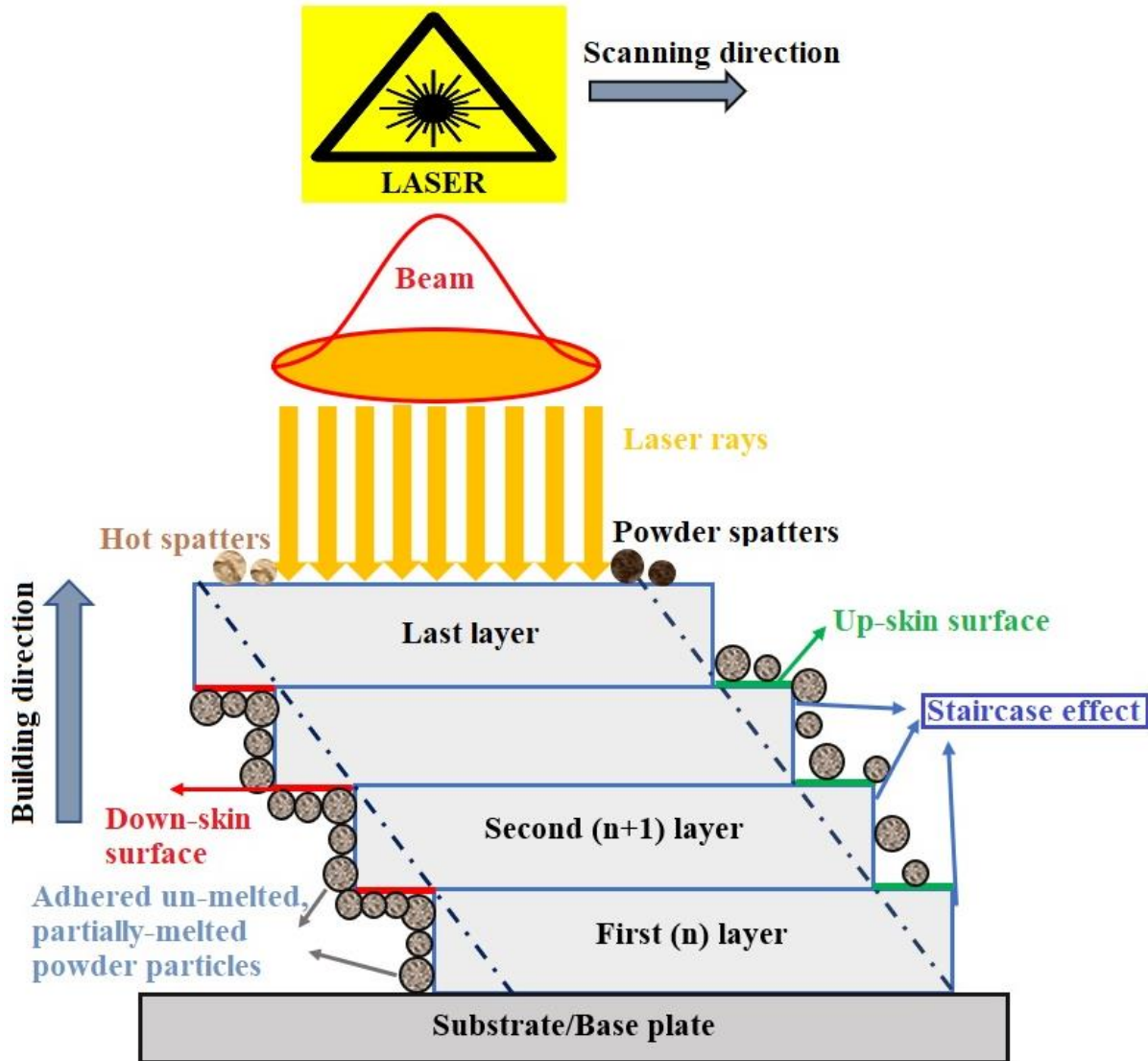


Figure 2. 16 Context diagram of various surface asperities emerge on inclined and curved LPBF surfaces.

Un-melted or partially melted particles emerge on the inclined or curved surfaces (including at edges or corners) due to (i) a lack of sufficient heat energy that fails to completely melt the particles in the molten melt pool, (ii) inadequate re-melting of the melt track, and finally (iii) non-uniform heat dissipation through the support structures as compared to rigid underlying substrate or already solidified melt track layer (see Figure 2.17c) [36]. Balling and spatters are the other inevitable defects that degrade the surface quality of AM components. In saying that, balling is sometimes referred to as the humping effect which is ascribed to tearing or periodic separation and associated shrinkage of molten melt pool into spheroidal balls caused either by lower laser fluence or the

extremely fast movement of the laser beam (scan speed) [133,137,142]. In both situations, there is insufficient heat energy to completely wet the nearby powder particles by the molten melt pool, resulting in balling. An extreme case of balling would lead to a ripple effect [1]. Balling and ripple effect are directly related to surface tension, recoil pressure, and Plateau-Rayleigh capillary instability [1,5,137,24].

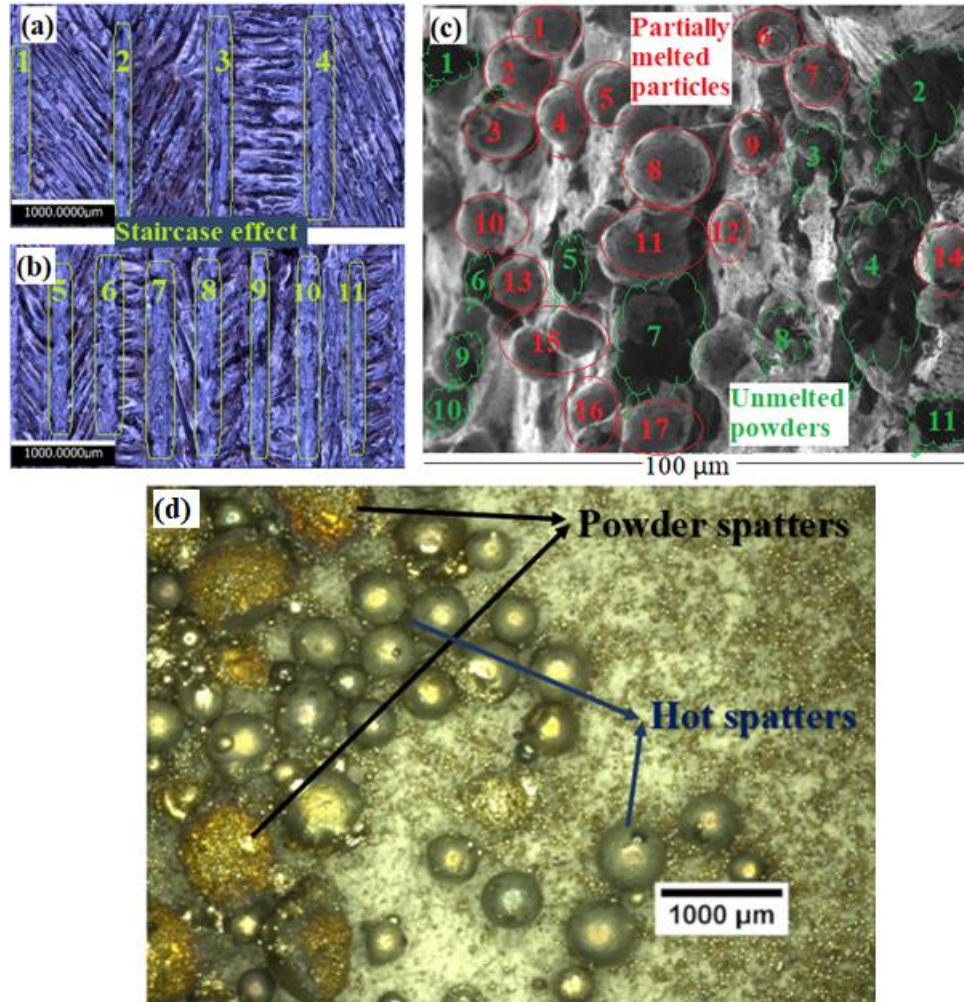


Figure 2. 17 Schematic illustration of surface asperities, (a & b) staircase effect, (c) partially melted particles, un-melted powders and (d), hot spatter and powder spatter that emerge on up-skin and down-skin surfaces of inclined LPBF parts [129].

Powder spatters are generated during the interaction of fast scanning movement of the laser beam with the powder bed: entrained by the low-pressure zone due to the intense vaporization of the jet plume ejecting the powder particles prior to complete melting [133,143,144]. As a result of suddenly unstable laser fluence interaction with part arises when the molten melt pool encounters close contact with a pre-existing large flaw that could lead to the formation of hot spatters see

Figure 2.17d [143,144]. In some cases, down-skin surfaces of metal AM components result in unacceptable rougher surface quality generated by the rigid support remnants which are difficult to detach from the AM part see Figure 2.18.



Figure 2. 18 Schematic showing support remnants attached on the down-skin surface of AM artefact (image captured by placing the AM ball artefact upside down for better visualization)

2.3 Importance of metal AM surface quality

AM perceived as a novel production opened up new opportunities for the complex design of multifunctional lightweight porous lattice structures of wind tunnels, and space applications including rocket engine components from the functional, technical, and economical points of view (see Figure 2.19) [145,146,147]. Cooling (or regenerative cooling) is essential for maintaining the structural integrity of various aerospace applications including high-performing rocket engines which are continuously exposed to higher thermal and environmental conditions [16]. Regenerative cooling (coolant flows through passages around the chamber wall while dissipating heat from the wall) is able to control the wall temperatures and balance the structural margins of the design and material [16]. The standout advantage of AM is that a certain level of desired final part quality (surface roughness in particular) can be achieved or tailored by optimising the process or by carefully introducing intentional porosities, but it is impossible to optimise the surface roughness infinitely [148]. The intentionally induced pores are beneficial in transpiration-cooling components of rocket engines [148, 16]. Also, tailored porosities in air-cooled lattice structures

showed better overall thermal conductance, heat transfer coefficient and fluid mixing without compromising the pumping power [147]. The slope of the engine walls is crucial as the variation in surface roughness can be observed based on the build inclination angles/build orientation [16]. The down-skin surfaces generally attract more particle-features (spatters/ un-melted-partially melted particles) to the sides of the wall potentially increasing the powder becoming trapped in narrow passages of the cooling channels [149]. The surface quality of LPBF also depends on materials, geometry, location of the building part on the substrate, laser incidence angle, post-processing etc. Hence, the parts must be specifically characterised and controlled under the same conditions [12].

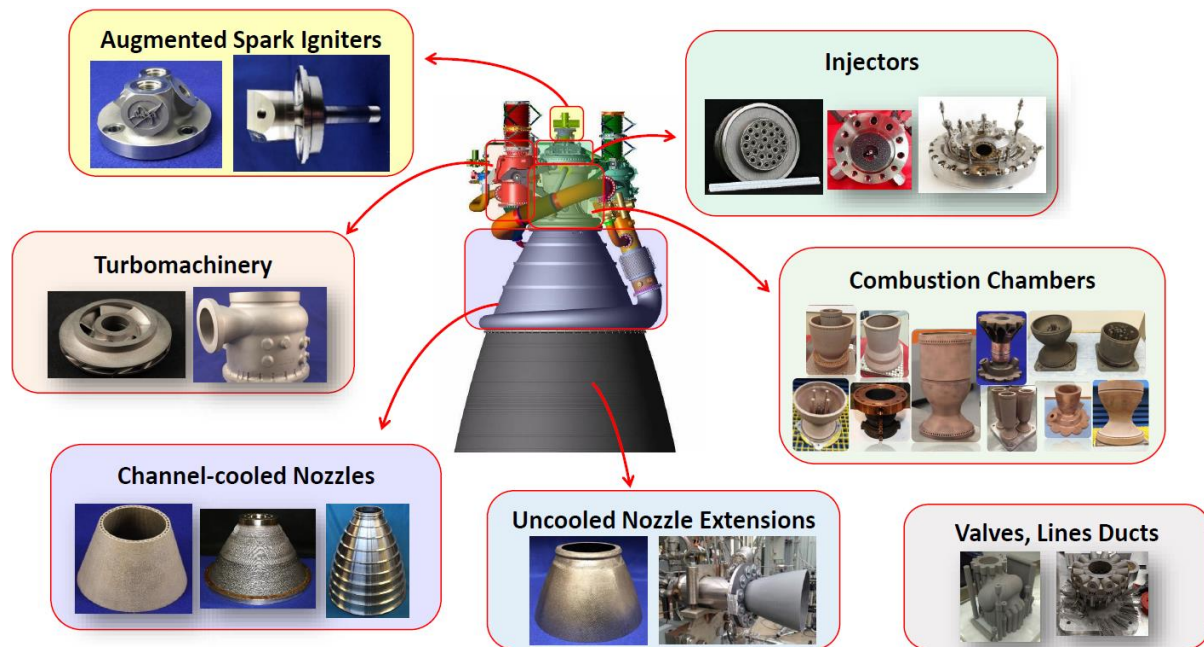


Figure 2. 19 Schematic illustration of advanced AM components of a rocket engine in aerospace applications [145, 146]

AM is showing promise and feasibility in the fabrication of customised patient-specific knee and hip implants and physician-specific complex geometry surgical tools/instruments (see Figure 2.20) [150]. Moreover, the ability of AM for innovative design of lattice-type/hybrid porous structures gives rise to the fabrication of newer types of cardiovascular stents, biodegradable scaffolds, spinal and orthopaedic implants etc, with tailored or optimised surface quality (desired porosities) (see Figure 2.21) [151]. The tailored or optimised surface quality of these AM implants possess interconnected porosities which help in easy fluid flow for nutrient, and waste transportation for in-cell growth, osseointegration-providing better biocompatibility and load-bearing capability,

bone-bonding ability while eliminating the need for autografting [151, 150]. The surface roughness of biomedical implants including dental implants is fundamental to the adhesion and differentiation of osteoblasts at the beginning of the osteointegration [152]. The textured or rougher surface induced by diverse metallurgical defects and surface asperities assists in bone-to-implant contact [152].

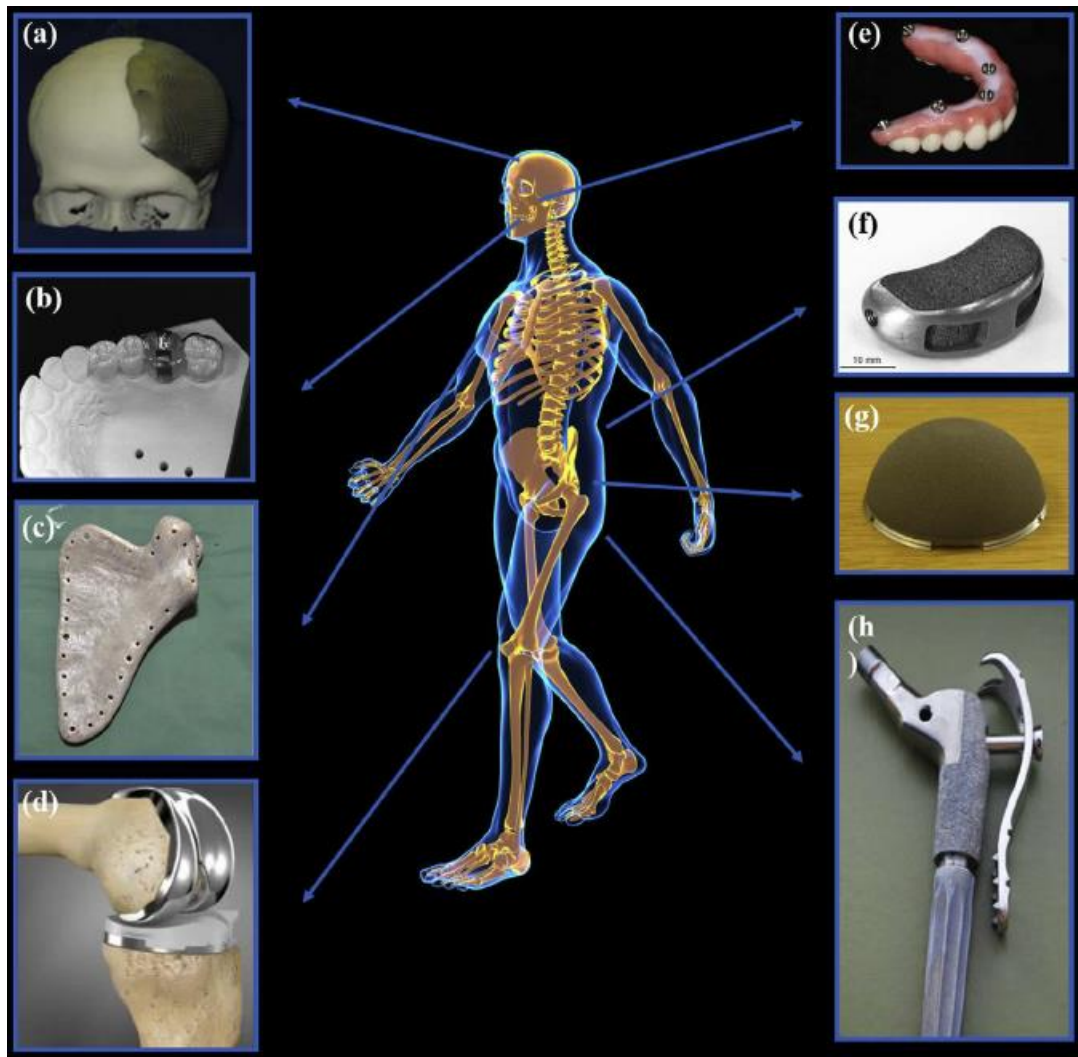


Figure 2.20 schematic illustration of metal AM biomedical applications (a) cranial prosthesis, (b) surgical guide, (c) scapula prosthesis, (d) knee prosthesis (e) dental implants (f) interbody fusion cage, (g) acetabular cup and (h) hip prosthesis [150]

A handful number of researchers attempted to find out the ideal roughness value that maximises the bone cells behaviour to the healing of the tissue around the implant [153, 154]. The widely available dental implant system's bone tissues can adapt for surface roughness within the range of 1–100 μm , and tailoring or modifying the surface topography of these implants could greatly

improve their primary stability and osseointegration [155]. However, the ideal surface texture or roughness for primary stability and osseointegration of biomedical implants still remained a challenge.

Most functional osseointegrated implants and cooling channels require a surface roughness of $0.5\text{ }\mu\text{m}$ - $1.5\text{ }\mu\text{m}$, with the current state-of-the-art of AM, it is non-viable to achieve this extent surface finish. However, early-stage research revealed that these implants' biocompatibility and load-bearing capabilities could be enhanced by designing/modifying and/or tailoring the surface roughness to greater than $4\text{ }\mu\text{m}$ (up to $100\text{ }\mu\text{m}$ in dental implants). Similar certain (higher) surface roughness induced by intentional porosities adds more benefits for extracting heat from cooling and maintaining the structural integrity of rocket engines and other aerospace-related applications. In the case of lubricated fretting and Marines' shoes, the rougher surface helps in more oil retention resulting in smaller wear and friction as compared to a smoother surface. The external surface quality of acetabular bone implants is rougher from the outside and smoother from the inside, whereas the tibial augments possess a rougher internal surface and smoother outside. Therefore, it is crucial to study both external and internal surfaces (quality) built with varying inclination angles. It is important to gain complete insights into various AM surface topography to optimise or tailor the desired surface quality. The available literature completely lacks to characterise, correlate and quantify the diverse metallurgical defects and asperities that emerge on various metal AM surfaces. Also, the existing research is only limited to surface roughness height parameters (R_a/S_a) which gives only decent descriptions of vertical characteristics of the surface deviation. However, it is highly unlikely to describe the surface after two processes (for example, plateau-honed cylinder surface). The basic knowledge of roughness characterisation of R_a/S_a or a finite number of parameters will not provide detailed information to fully understand the variation of the surface roughness/texture and the suitable metrics to represent the complex metal AM surface topographies. R_a/S_a are insensitive to differentiate peaks, valleys and the spacing of the various texture features. Also, R_a/S_a may mislead in many surfaces with grossly different spatial and height symmetry features (for example, milled vs honed) and may have the same R_a/S_a but function quite differently. R_a/S_a fails to provide the general relation between the wavelength and amplitude properties of the surface or any changes occur either in amplitude or spacing. Hence, with mere R_a/S_a information; it is non-viable to optimise or tailor the surface quality to meet the desired requirements for product design benefits and functional performance evaluation.

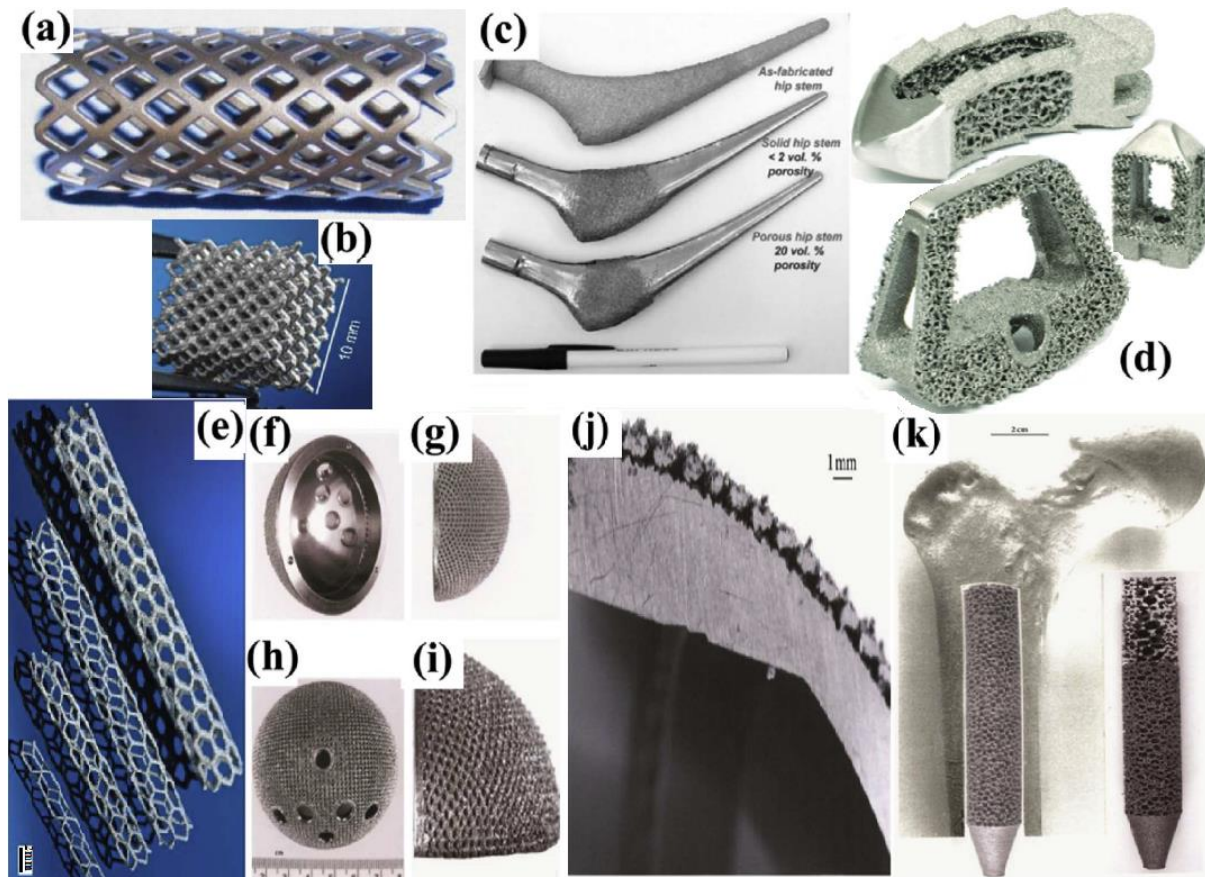


Figure 2. 21 schematic illustration of (a) cylindrical mesh spinal implant [151], (b) biodegradable scaffold with interconnected pores (c) functional hip stems with varying porosity (0% porosity, <2 vol% porosity, and 20 vol% porosity), (d) typical AM porous spinal implant [156] (e) cardiovascular stents (f)–(j) a metal AM fabricated acetabular cup with porous mesh structure (outside) enabling ingrowth, (f), (g) lateral views; (h), (i) higher magnification of the outer porous mesh structure, (j) sectioned view of the acetabular cup; (k) metal AM fabricated intramedullary rod insert [150].

2.3.1 Surface texture metrology

It is widely acknowledged that surface roughness is instrumental in determining the long-term functional performance of fabricated components. The quality of the final part surface is normally adjudged by a number of factors: collectively called by the broader term ‘surface integrity’, which constitutes surface roughness and surface texture or surface quality [160]. Basically, surface roughness and surface texture signify a similar entity, but in practice, they are not exactly the same. For example, surface roughness is referred to the measure of finely spaced microscale asperities

and/or irregularities that exist on the surface texture [161,26,162], whereas, surface texture demonstrates the quality of the final surface by its attributes such as rougher, finer, poor, good etc. [160]. Surface texture or surface finish is the complex nature of a surface, which is generally described by the combination of important features of surface roughness, waviness, lay and form (see Figure 2.22) [125,161]. According to ASME B46.1, surface texture is defined as the features or asperities that display certain local deviations from the intended geometry of a perfectly flat surface [161]. Surface roughness entity can be directly measured and quantified. In contrast, characterisation and quantification of surface texture is not directly possible, instead, it is quantitatively expressed from roughness values [160, 162].

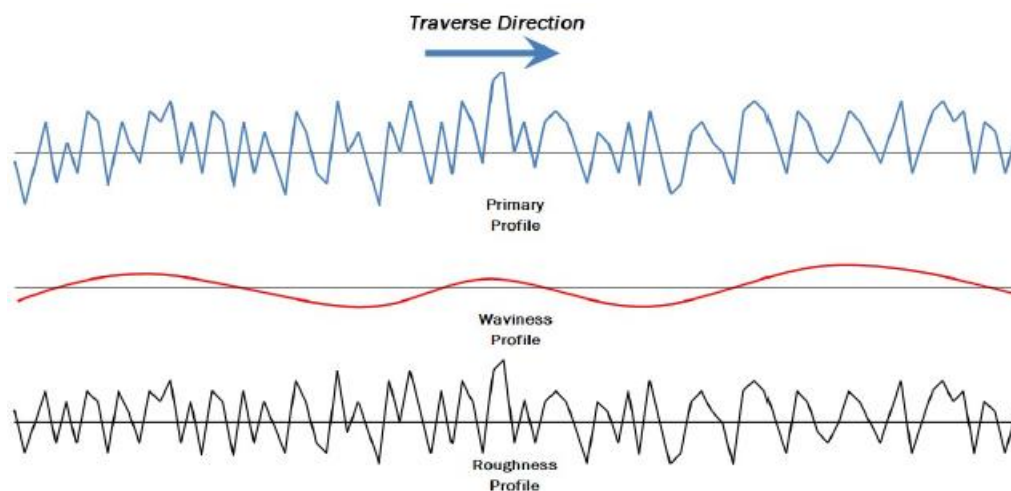


Figure 2. 22 schematic illustration of primary roughness and waviness profiles [161]

The surface is the boundary that differentiates an object from another object, substance or space [161]. Topography typically refers to geometrical present on the surface area. Waviness is a measurement of more widely spaced components of the surface quality or texture and is strictly defined as the irregularities whose spacing is greater than the roughness sampling length [161]. The waviness profile is extracted by filtering out the longer and shorter spatial wavelengths associated with form and roughness, respectively (see Figure 2.23) [161]. The roughness profile is extracted by filtering out the longer spatial wavelengths associated with waviness from the primary surface (see figure below) [161]. The form consists of the widely spaced real surface deviations from the nominal surface that are excluded from surface texture [161]. The lay describes the predominant direction of the surface pattern which is usually governed by the fabrication method being used [161]. Further details about waviness, form and lay are not discussed further as they are out of this research scope. It is important to note that the details of specific surface

topography data acquisition, filtration, segmentation and other surface quality characterising operations adopted in this research are described in relevant chapters 3-6.

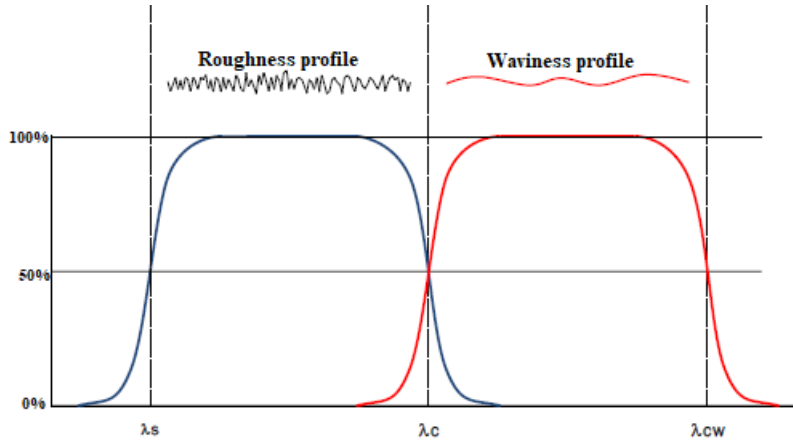


Figure 2. 23 schematic illustration of roughness and waviness profiles extracted from the primary surface [161] (λ_s -shorter wavelength cut-off-roughness, λ_c -longer wavelength cut-off-roughness, and λ_{cw} - longer wavelength cut-off-waviness)

it is paramount to understand the suitable existing metrology techniques and appropriate best practices applied for the precise measurement, characterisation and quantification of surface roughness to ensure compliance with functional hallmarks of industrial standards. Surface texture metrology in here refers to the measurement, characterisation, correlation and quantification of of AM surface topography. Measurement is acquiring surface topographical data, characterisation is extracting valuable quantitative information from the acquired data. Correlation is establishing an interrelationship between the extracted quantified information and the suitable surface texture parameter described on the standard (ISO-25178-2 in this research). Quantification is calculating the defects and asperities including particle features (balling, spatters, un-melted, partially melted particles).

Out of seven surface topography measurement methods that are presently covered is ISO-25178 standard series [3], the two most commonly used surface texture measurement and characterisation methods are contact (profile) and non-contact (areal). The contact method is also known as profile measurement in which the extracted surface topographical data is limited to 2-dimensional (2D), whereas the non-contact (areal surface) measurement consists of extraction of 3D height map of an (x,y) location on a plane with a respective height value (z) [3]. The other areal surface texture characterisation techniques are focus variation measurement (FVM), confocal microscopy (CM) and coherence scanning interferometry (CSI). Although X-ray computed tomography (XCT) has

been a popular method nowadays that is being used to measure the surface quality of a wide range of AM surfaces internal structures such as porosities, sub-surface porosities and re-entrant features etc. The XCT is not standardized yet, hence caution must be exercised before adapting this method. The FV measurement technique has been adopted in this research.

2.3.2 Areal surface texture parameters

2.3.2.1 Height parameters

The unevenness on the surface is mostly analysed by using height parameters.” Sa” arithmetic mean height is an extension of Ra (line roughness) which is the mean of the average difference in height for the average plane evaluated over the completed 3D surface (see Figure 2.24) [32, 157, 158]. Sa represents the arithmetic mean of absolute ordinate Z(x,y) within the evaluation area, the expression for Sa is given in equation (1) [158]. Some of the many advanced functional applications are automotive door handles, switches, copper foils of 5G printed circuit boards and etc.

$$s_a = \frac{1}{A} \int \int |z(x,y)| dx dy \dots \dots \dots (1)$$

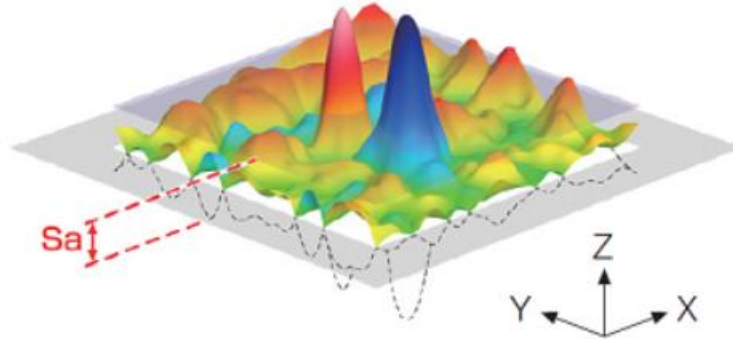


Figure 2. 24 Schematic illustration of Sa [158]

“Sq”-is an easy-to-handle areal surface texture height parameter that is calculated over the complete 3D surface. Sq considers the standard deviation of the height distribution of the entire area and measures the overall roughness of the scanned area under consideration (see Figure 2.25) [158]. Sq represents the root mean square height of Z(x,y) within the evaluation area the expression for Sa is given by equation (2) [32, 158].

$$s_q = \sqrt{\frac{1}{A} \int \int_A Z^2(x,y) dx dy \dots \dots \dots (2)}$$

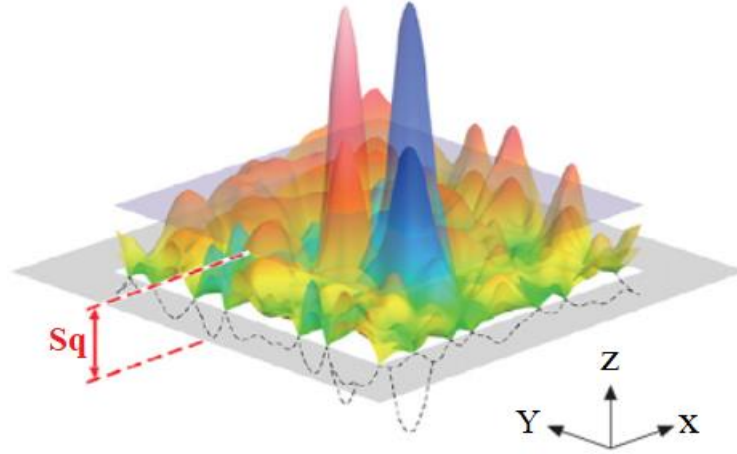


Figure 2. 25 Schematic illustration of Sq [158]

Skewness (Ssk) The Ssk parameter is the extension of the profile (line roughness) parameter Rsk but in three dimensional. Ssk defines the unique distribution of height values above or below the mean plane, which is generally indicated by either a positive or negative value (see Figure 2.26) [32] The Ssk expression is given by the equation (3). If $Ssk < 0$; the distribution deviates above the mean line, $Ssk = 0$; the distribution is symmetrical, $Ssk > 0$; the distribution deviates below the mean line. The Ssk parameter is related to the surface height distribution and hence it is applicable for analysing the abrasion and oil sump of lubricants for slide planes [158].

$$s_{sk} = \frac{1}{s_q^3} \left[\frac{1}{A} \int \int_A z^3(x, y) dx dy \right] \dots \dots \dots (3)$$

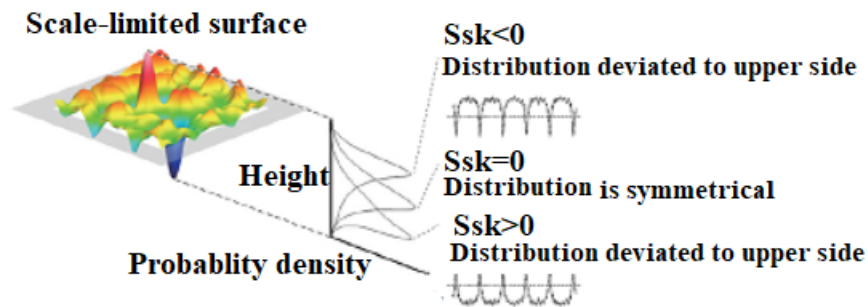


Figure 2. 26 Schematic illustration of Ssk [158]

Kurtosis (Sku) is described by the probability of distribution of height values [32]. The Sku parameter expands the profile (line roughness) parameter Rku but in three dimensional [32,158]. It usually indicates whether the distribution of height values has sharper peaks ($Sku > 3$) or even, smaller and widespread ($Sku < 3$) (see Figure 2.27) [32]. The Sku expression is given by the equation (4). If $Sku < 3$; the height distribution is even, $Sku = 3$; normal distribution, $Sku > 3$; the height distribution comprised of sharper peaks.

The Sku parameter is concerned with the number of peaks and valleys which is generally applied to examine the contact between two objects [158].

$$s_{ku} = \frac{1}{s_q^4} \left[\frac{1}{A} \int \int_A z^4(x, y) dx dy \right] \dots \dots \dots (4)$$

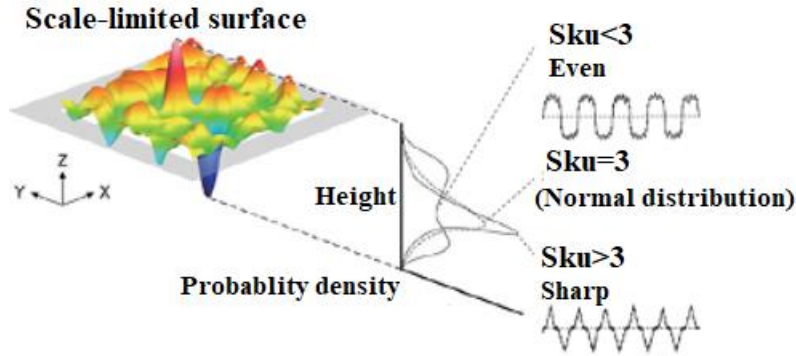


Figure 2. 27 Schematic illustration of Sku [158]

2.3.2.2 Spatial Parameters

Autocorrelation length (Sal) is related to the periodicity of the surface. Sal parameter is defined by the minimum horizontal distance of the autocorrelation function that has the fastest decay to the specified values s ($0 < s < 1$) [158] or the minimum autocorrelation length of the new location with respect to the original location (see Figure 2.28) [32].

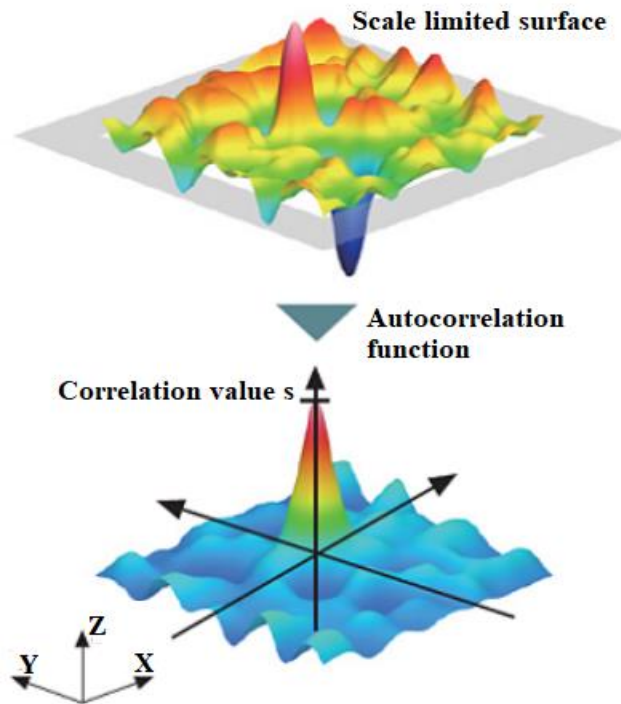


Figure 2. 28 Schematic illustration of autocorrelation length Sal [158]

The texture aspect ratio (Str) is a measure of the uniformity of the surface texture. Str indicates whether the surface is isotropic or anisotropic in nature [32]. The Str value normally varies from 0 to 1; if Str > 0.5 and close to 1 signifies strong isotropy, whereas the Str < 0.3 close to 0 indicates the surface is strongly anisotropic [158]. The spatial parameters are useful to analyse the even size and complexity of parallel grooves and grains in place of height parameters [158].

2.3.2.3 Hybrid parameters

The hybrid parameter(s) is defined by the combination of amplitude and spacing. Any changes in either amplitude or spacing directly influence the final result of the hybrid parameter(s). The hybrid parameters are widely used in tribological analysis, surface slopes, surface curvature and developed interfacial area [159]. “Sdq”- root mean square gradient of the scale-limited surface [32]. “Sdq” is a general measurement of the slopes at all points within the defined area (A) of the scale-limited surface, and also may be used to differentiate the surfaces with similar Sa (see Figure 2.29a) [158]. Sdq is affected by spacing and texture amplitude (For given Sa, wider spaced texture; lower Sdq than the surface with same Sa of finer spaced texture). The Sdq value is Zero (0) for the completely flat or ideal surface (see Figure 2.29b) [157]. Sdq is generally used to distinguish between the surfaces with similar roughness. The Sdq expression is given by the equation 5. Any slope causes a surface's Sdq value to increase. The surface beneath is a plane with 45-degree gradient components and a Sdq value of 1 see figures below c) [32, 157]. Sdq is useful to characterise the sealing systems, and cosmetics appearance and is oftentimes related to the degree of surface wetting by various fluids.

$$s_{dq} = \sqrt{\frac{1}{A} \int \int_A \left[\left(\frac{\partial z(x,y)}{\partial x} \right)^2 + \left(\frac{\partial z(x,y)}{\partial y} \right)^2 \right] dx dy} \dots\dots\dots (5)$$

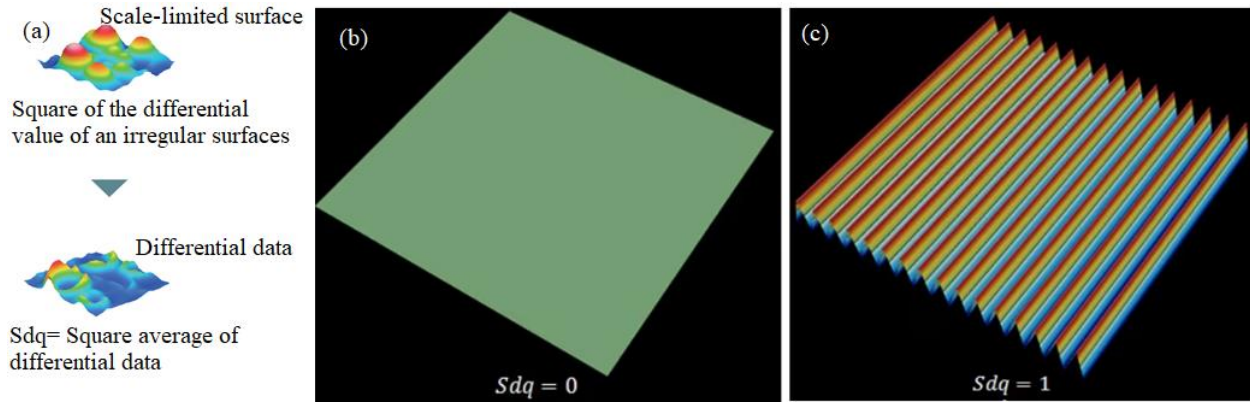


Figure 2. 29 Schematic illustration of (a) Sdq of scale limited surface [158], (b) Sdq=0 for the completely flat/ideal surface, (c) Larger Sdq=1 for the surface containing any slopes [157].

“Sdr” developed interfacial area ratio of the scale-limited surface [32]. The “Sdr” is expressed as the ratio of the additional or incremental surface area of the interfacial area of the scale-limited surface within the defined area (A) (see Figure 2.30a) [32,158]. Sdr is used to differentiate the surfaces of similar amplitudes and average roughness. The expression of Sdr is given by the equation (6). In general, Sdr increases with the spatial intricacy of texture irrespective of changes in Sa value. The Sdr value is Zero (0) for the completely flat or ideal surface (see Figure 2.30b). The presence of any slope on a surface causes its Sdr value to increase. the surface below is a plane with gradient components of 45 degrees, has an Sdr value of of 0.414 (see Figures 2.30c) [32,157]. Sdr is widely applied in surface coatings, adhesion and lubrication applications.

$$s_{dr} = \frac{1}{A} \left[\int \int_A \left(\sqrt{1 + \left(\frac{\partial z(x,y)}{\partial x} \right)^2 + \left(\frac{\partial z(x,y)}{\partial y} \right)^2} - 1 \right) dx dy \right] \dots\dots\dots (6)$$

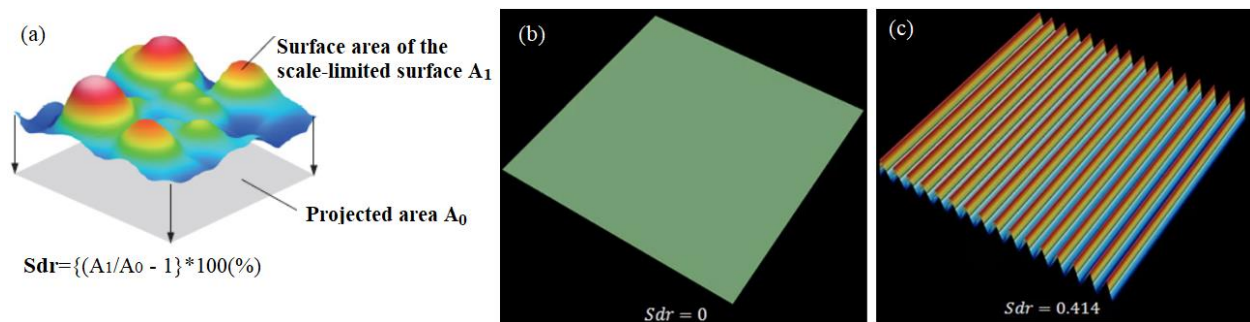


Figure 2. 30 Schematic illustration of (a) Sdr of scale limited surface [158], (b) Sdr=0 for the completely flat/ideal surface, (c) Larger Sdr=0.414 for the surface containing any slopes [157].

2.3.2.4 Functional parameters

Functional parameters are used to examine the functional properties of wear and tribological components. The peak material volume (V_{mp}) parameter is helpful to study the volume density of particle feature characteristics of different surfaces. It is also important to note that volume parameters are obtained by dividing the material ratio curve into three zones by applying two material ratio thresholds $SMr1$ 10% and $SMr2$ 80% with default peak material 0-10% [32]. However, $SMr1$ and $SMr2$ can be adjusted flexibly depending on particular applications (see Figure 2.31). The material ratio thresholds $SMr1$ and $SMr2$ from the Sk parameters are more suited to analyse particle features compared to adopting the default SMr ratio of 10%. The V_{mp} is often used in oil retention and lubrication applications [158].

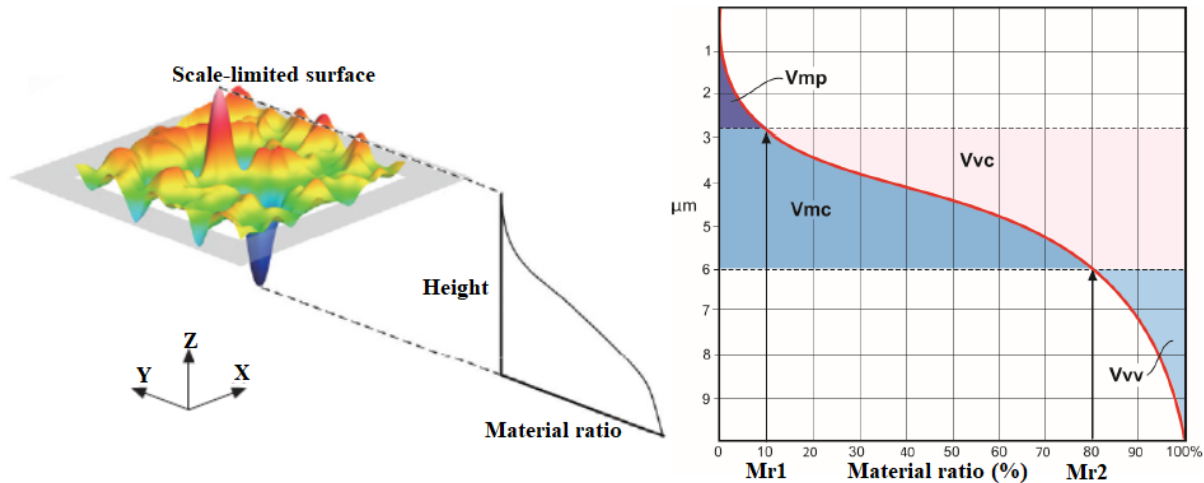


Figure 2. 31 Schematic illustration of peak volume material V_{mp} of scale limited surface [158]

2.3.2.5 Feature parameters

The feature parameter Spd gives the number of peaks per unit area (see Figure 2.32) [158]. Spd is useful to examine the density (smaller or bigger) of the particle features. Spd indicates the density of peaks based on watershed segmentation of surface topography with 5% Wolf pruning [36].

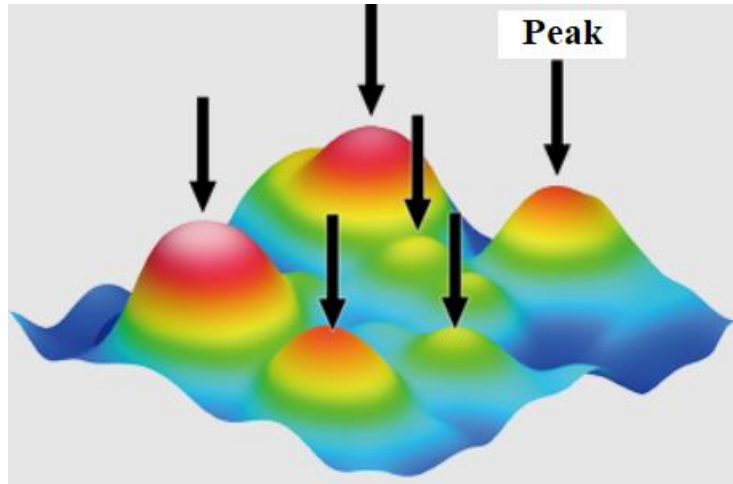


Figure 2. 32 Schematic illustration of peak volume material V_{mp} of scale limited surface [158]

2.3.2.6 Particle analysis

Conventional surface texture metrology is predominantly focused to characterise the overall surface topographical asperities data of the whole measured region by a limited number or set of scalar values. However, these conventional texture parameters are not intending to provide information about the individualities present on the surface. In saying those surface texture parameters are not capable to give details about the number of particles/asperities present on the surface, nor their spatial distribution. Instead, these texture parameters would assist in capturing the overall or entire topographical data (for example, roughness R_a or S_a & S_q , etc.) of the surface of the region being measured. To overcome this limitation, feature-based particle analysis is employed by using a spatially decomposing application of threshold segmentation, according to the S_{mr1} value. The captured surface measurement data consist of digital topographies which have been segmented to isolate partially-melted/un-melted particles and spatters from the surface that provides valuable quantification data, and the perception of the individual surface asperities which form during the LPBF process. Each individual segmented region is referred to as the feature that is then characterized related to its geometrical features.

2.3.3 Influence of process parameters on metal AM surface quality

As aforementioned, surface roughness is a key element and the most common surface texture parameter used to quantify the surface quality, reliability of the surface topographical features, and layering effects. In this perspective, there is a continuous increase in demand to address the impact of critical AM process parameters with reference to the reliability of surface quality linked to the functional performance of metal AM components. Many authors have studied the correlation

between surface roughness and the various AM process parameters [12,13,19,20,142,163-167]. The metal AM processing conditions have a significant influence on the surface roughness of horizontal, vertical and inclined and/or curved surfaces [168]. The summary of AM (including contour) parameters influence on final surface quality is given in Table 2.2.

Fox et al. studied the interrelationship between contour parameters (varying beam power: 25W-195 W, travel velocity: 350mm/s-3000 mm/s), and the angle of overhanging structures (30°, 45°, and 60°) with respect to the surface roughness of LPBF samples [19]. The reported research analysis of surface roughness metrics (R_c , R_{sm} and R_{pc}) demonstrated the shift between surfaces dominated by partially-melted particles and the surfaces predominantly governed by the re-solidified melt track material [19]. However, the correlation between process parameters on R_a was less significant as the authors did not conduct a qualitative analysis of individual features that contribute to the surface roughness [19]. Delgado et al. experimentally investigated the influence of DMLS (direct metal laser sintering) and SLM process parameters (such as scan speed: 300 mm/s-500 mm/s, layer thickness: 0.02 mm -0.06 mm, and building direction: 0°-90°) on the dimensional error, surface roughness, and mechanical properties of iron-based materials [20]. Statistical significance approach analysis of variance (ANOVA) was adopted to analyze the results. The authors revealed the building direction presented a significant impact on the surface roughness and the dimensional error, whereas, the mechanical properties tend to be moderately sensitive to build direction and layer thickness. However, an increase in layer thickness resulted in lower tensile strength and elongation for DMLS samples [20]. Both layer thickness and build direction parameters were influential in SLM samples' part quality, whereas, the build direction showed no impact on the mechanical properties. Overall, scan speed and layer thickness parameters showed a negative effect on both DMLS and SLM-processed parts [20]. Hong et al. studied the impact of various parameters (laser power: 100-200 W, scan speed: 30-270 mm/s, and scan spacing: 20 μ m-200 μ m) on the surface roughness (R_a) during single-layer formation and multi-layer formation tests of SLM of cobalt-chromium (Co-Cr) dental alloys [163]. The authors proposed that excess melting and balling could be avoided by reducing the laser power and increasing the scan speed during the single-layer formation test. In the case of multi-layer formation tests, the reported roughness values (R_a) were 6.1 μ m and 4.2 μ m for the scan spacings of 200 μ m and 150 μ m respectively due to smaller overlap ratios (24 and 43 %) [163]. Similarly, using 60 μ m and 20 μ m scan spacing resulted in R_a values of 3.3 μ m and 3.9 μ m owing to higher

overlap ratios (72 and 92 %). The smoothest surface quality ($R_a=1.8\text{ }\mu\text{m}$) was achieved for 100 μm scan spacing due to the optimal overlap ratio (62%). Overall, it was concluded that laser power, scan speed, and scan spacing were key influencing factors in defining surface quality [163]. A similar kind of research was carried out by Baciú et al. [166], except the authors included an extra parameter in the form of exposure time in their investigation. Tian et al. conducted research to correlate various AM parameters (laser power:100W-400 W, scan speed:1000 mm/s-3000 mm/s, layer thickness:20 μm -40 μm , hatch spacing:0.05 mm-0.13 mm, sloping angles:45°-90°) with surface roughness (R_a) of both up-skin and down-skin surfaces of SLM Hastelloy X alloy [165]. The reported roughness values for up-skin surfaces of the inclined sample were unaffected by different laser powers and scan speeds, but the roughness of the down-skin surface increased with an increase in laser power and decreased with scan speed. A combination of low power (200 W) and a high scan speed (3000 mm/s) resulted in the best roughness of the down-skin surface ($R_a=15\text{ }\mu\text{m}$) [165]. Larger balling appeared for higher scan speeds, while smaller balling was encountered for lower scan speeds and higher power. The heat transfer simulation suggested the optimal melt pool depth comparable to the median powder particle size can also be obtained for this parametric combination (see Figure 2.33) [165]. Surface roughness exhibited a positive correlation between hatch spacing and layer thickness. Overall, the authors found contour scan and skywriting scanning strategies were beneficial to achieve lower surface roughness: the contour scan strategy alleviates surface irregularities and the skywriting scan facilitates uniform energy density [165].

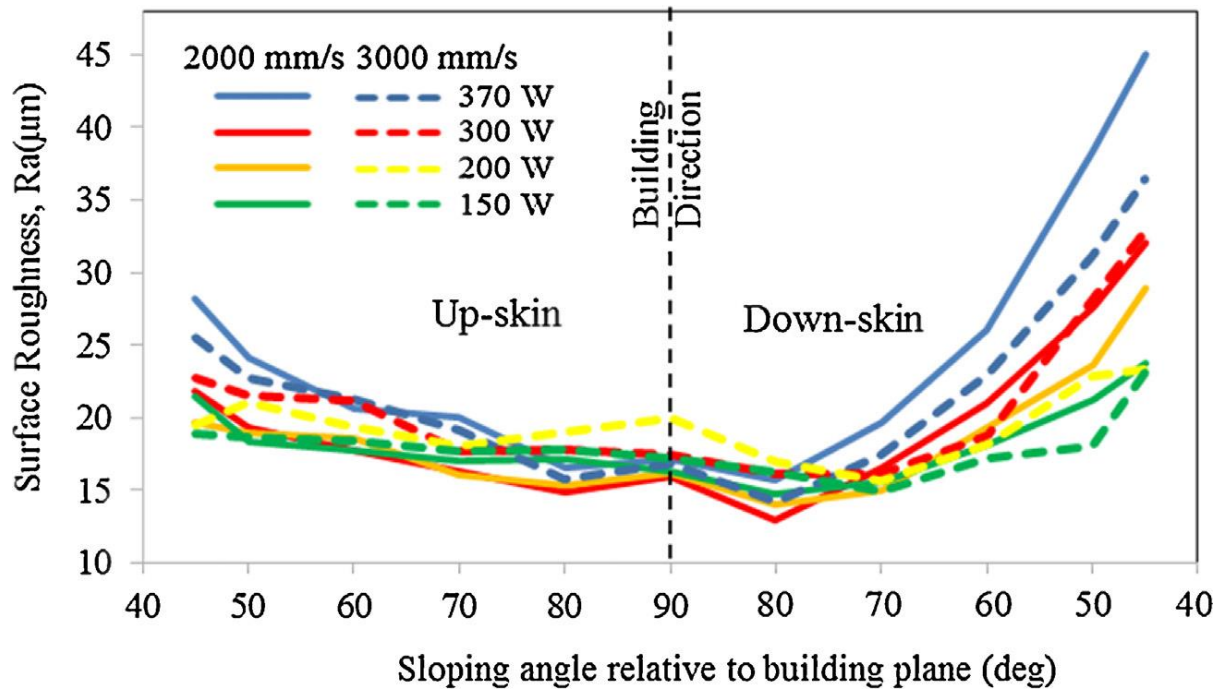


Figure 2.33 Correlation between surface roughness, sloping angles and the process parameters [165].

Gockel et al studied the processing-structure-property-performance (PSPP) using structured light (SL) and computed tomography (CT) techniques for varied contour parameters and the resulting surface quality and the fatigue life characteristics of LPBF 718 alloy [13]. The authors found that surface roughness (S_a from $\sim 17 \mu\text{m}$ to $\sim 7 \mu\text{m}$) decreased with an increase in laser power (from 80W to 120W) for the SL measurement method but this pattern was not clear with the increasing scan speed for the CT technique (see Figure 2.34) [13]. The S_a values for fatigue life did not provide a clear correlation from either of the non-destructive measurement techniques (see Figure 2.35) [13]. This was credited to the increased laser power resulting in keyholing, which would further lead to subsurface porosities. Similarly, increased scan speeds lead to an unstable molten melt pool and balling. Overall, both XCT and SL methods supported S_v trend inversely proportional to the fatigue life, whereas, S_a did not show any correlation to fatigue life from both techniques [13].

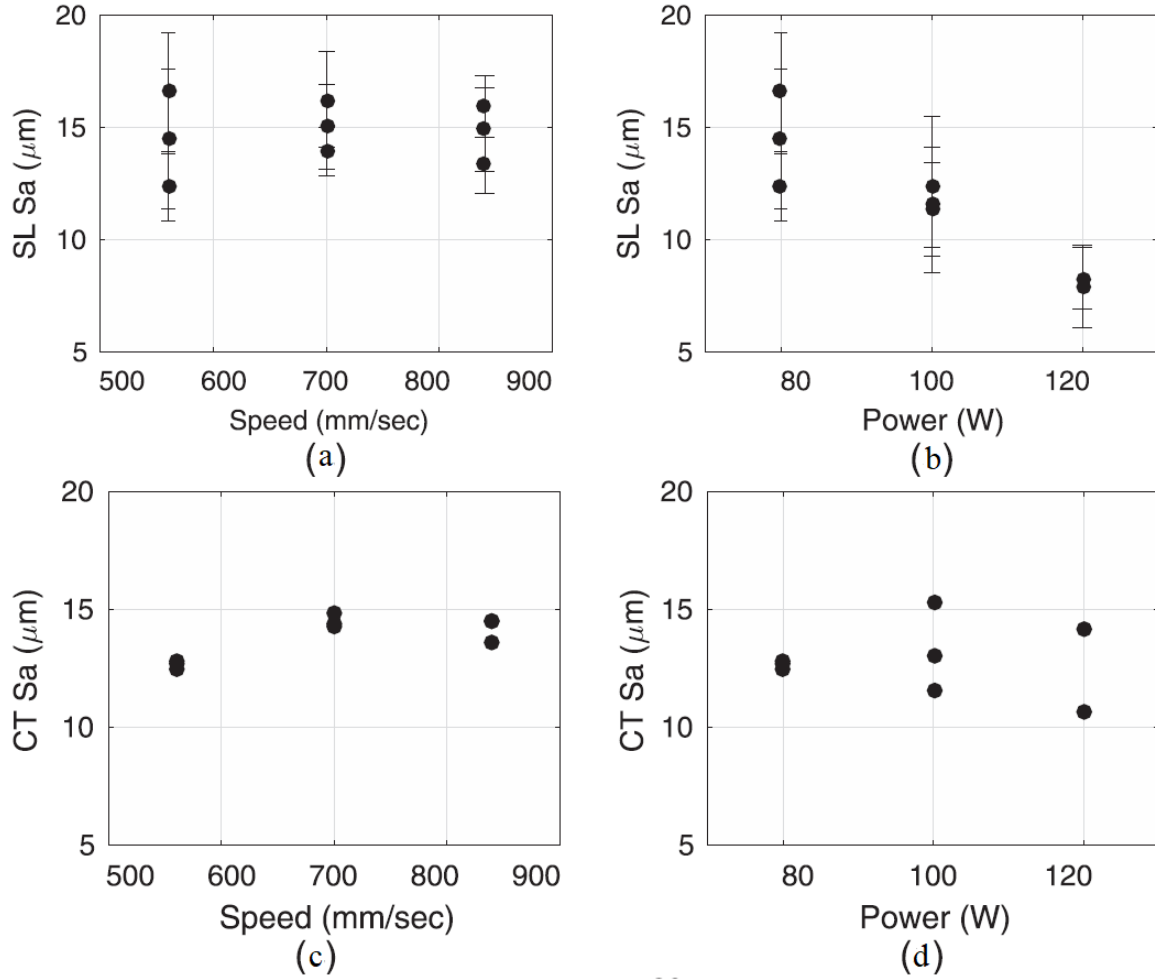


Figure 2. 34 Correlation between contour parameters and the surface quality of two non-destructive techniques (a), (b) structured light, (c), (d) X-ray computed tomography [13]

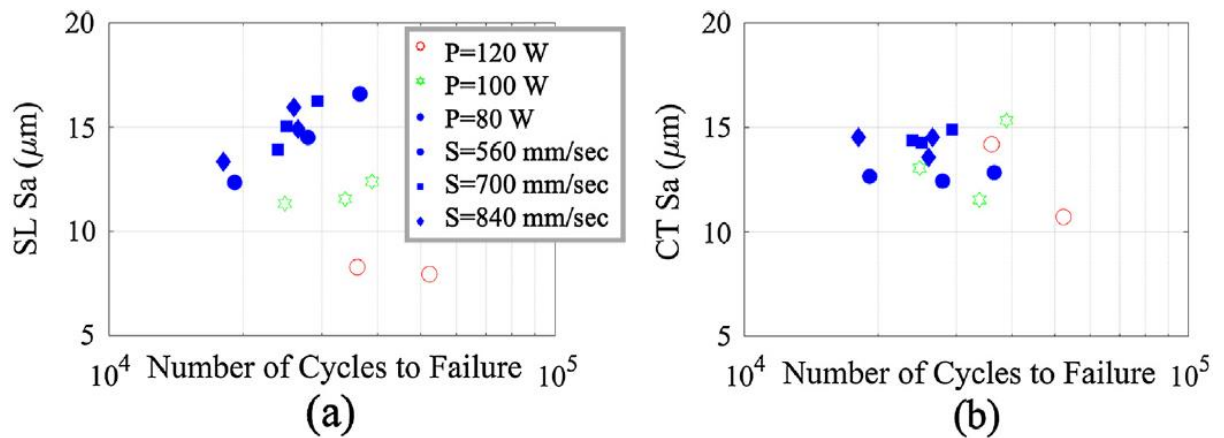


Figure 2. 35 Correlation between contour parameters and the fatigue life (a) structured light, (b) X-ray computed tomography [13]

Attarzadeh et al. studied the changes in the line roughness parameters (Ra) and fractional density with the energy density by varying AM process parameters (laser power:100W-300 W, scan speed:300mm/s-1500 mm/s, hatch spacing:0.06mm-0.24 mm, build height:5mm-50 mm, build direction: parallel(pl) and perpendicular(pr)) [142]. The authors achieved low Ra(pl) ($\sim 3\text{-}8\text{ }\mu\text{m}$) and Ra(pr) ($\sim 4\text{-}12\text{ }\mu\text{m}$) values for energy densities between $\sim 20\text{ J/mm}^3$ and $\sim 60\text{ J/mm}^3$: owing to sufficient energy input for complete melting. A slight increase in energy density resulted in entrapped gas bubbles, balling, and spatters, but the observed line roughness values were insensitive to this marginal change [142]. Fractional density (FD) increased rapidly between $\sim 20\text{ J/mm}^3$ and $\sim 40\text{ J/mm}^3$ energy densities (FD ~ 1 at $\sim 45\text{ J/mm}^3$) and remained constant till $\sim 80\text{ J/mm}^3$, beyond this range FD started to decrease steadily to reach 0.93 for 120 J/mm^3 : which is attributed to lack of fusion holes, internal defects. Overall, FD displayed reversed behavior to line roughness parameters. The low fractional density was ascribed to the balling occurring at higher energy densities [142]. Wang et al investigated the impact of laser energy density on the surface roughness (Ra) of SLM steels [167]. Experimentally measured Ra was found to be in excess of 50% of the theoretical value, which is attributed to inevitable deviations between theoretical assumptions and physical experiments [167]. The authors reported that thin and continuous melt track types are more suitable for the SLM process, and also the surface roughness could be improved by adopting laser surface re-melting without considering the processing and the stress accumulation [167]. Ni et al. studied the impact of balling-induced surface roughness (Ra), microstructure evolution, and corrosion properties of SLM 316L steel with respect to different inclination angles ($0^\circ\text{-}90^\circ$) [24]. It was found that Ra ($2.398\text{ }\mu\text{m}$) for 0° displayed a smoother surface, and 90° tilt angle resulted in poor surface roughness (Ra $\sim 11\text{ }\mu\text{m}$). Polished (3.5% NaCl solution) AM surfaces were characterized by pitting and localized corrosion: mainly originating from pores and balling defects [24]. Similarly, the polished surfaces exhibited lower corrosion resistance as compared to unpolished counterparts (easy to passivate), plus the balling behavior expedited the rate of corrosion in unpolished parts which are attributed to metallurgical porosities and balling. The authors concluded that inclination angles displayed a pronounced effect on surface roughness induced by metallurgical defects [24].

The impact of scan speeds and layer thickness on the side surfaces of a one-pass thin wall component was experimentally studied [169]. A smaller layer thickness and a lower scan speed resulted in a rougher side surface due to excess heat accumulation caused by higher heat input, in

contrast, the surface became extremely porous when a scan speed and a layer thickness exceeded threshold values [170,171]. Although the optimised linear energy density (laser power/scan speed) was adopted for the top surface, the process did not produce acceptable side surface roughness, hence it was preferred to use a relatively lower linear energy density to achieve a lower side surface roughness [170]. The top surfaces produced with too low or too high linear energy densities resulted in poor surface roughness caused by Marangoni flow and recoil pressure due to materials evaporation respectively [171]. The particle size distribution is another notable factor that adversely affects the surface roughness: a predominant coarser feedstock material (with sparse finer particles) leads to larger layer thickness and low powder layer density resulting in a substandard surface finish [170,172].

In addition to the critical metal AM parameters, the scanning strategy plays an important role in determining the final surface quality as it strongly influences the thermal gradient, molten melt pool morphology, and thermophysical behaviour of the AM parts [173,174]. The elevated ridges, commonly known as the “edge effect”, generally affect the final surface quality and sometimes result in poor dimensional accuracy of LPBF parts [173,175]. The edge effect poses a negative impact on AM process itself and implicates adverse effects on the mechanical properties of the part due to contact between these higher edges and re-coater [176]. An appropriate combination of process parameters and the contour scanning strategy certainly improves the surface quality of inclined parts but is a less significant improvement for up-skin surfaces [176]. Matache et al. reported the impact of critical parameters laser power and scanning speed without contour scan on the surface quality (edge and corner effects) of AM IN 625 samples [175]. The authors found that the more stable molten melt pool consisting of reasonably elevated edges and corners was evident for laser power range between 250–300 W and scanning speeds range between 0.7–0.8 m/s [175]. Yonehara et al studied the correlation between surface texture and relative density or internal defects of metal AM components including LPBF process parameters (see Figure 2.36) [177]. The authors found that the width of the molten melt tracks for the higher density (>99%) samples (S15 & S16) remained continuous and relatively constant without any visible grooves and negligible porosities [177]. Conversely, the irregularities in the width of the molten melt tracks were evident in the low-density samples (S10, S12 & S13) surfaces and the obvious presence of several grooves and bumps [177]. This was attributed to the lower laser powers and lower scan speeds which resulted in wider grooves, whereas the higher laser powers with constant scan speed lead to the

unevenness of the molten melt tracks as a result of spattering, lack of fusion holes and larger swelling or beading up phenomena [177]. Surface texture parameters S_{sk} (0.42), S_{ku} (0.32), S_z (0.71), S_v (0.55), S_k (0.78), S_q (0.76), S_{dq} (0.76) and MIC 0.81 reveal a strong correlation between surface texture and relative density/internal defects [177].

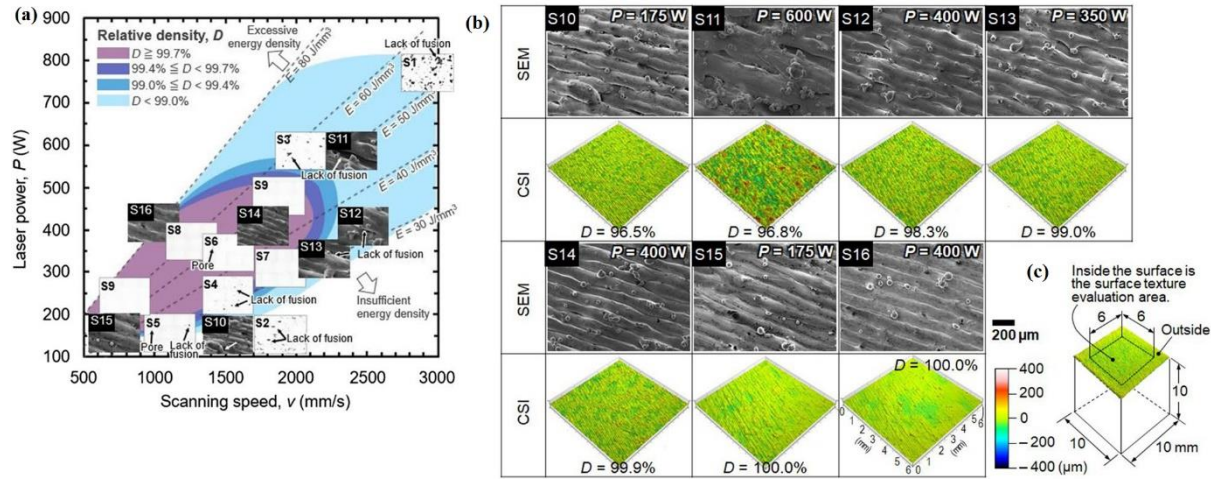


Figure 2.36 Correlation between surface texture and relative density/internal defects—(a) LPBF process map to show a relationship between LPBF parameters and surface texture including internal-defect (S1-S16) samples; (b) SEM and CSI images of LPBF samples (S10-S16) surface; (c) LPBF sample surface texture evaluation region [177].

Chen Z et al studied the correlation between the identical laser scan parameters (including part orientation and shape of the incident laser beam) and surface roughness of LPBF components [168]. The authors revealed that the surface roughness of 40° up-skin surfaces was certainly lower than the down-skin surfaces at 40° with identical laser powers, scan speeds and contour offset parameters (see Figure 2.37). The least surface roughness (R_a) for up-skin $\sim 16.7 \mu\text{m}$ and down-skin $\sim 39.8 \mu\text{m}$ were obtained for scan speed = 1050 mm/s, laser power = 345 W and contour offset = 17 μm [168]. Authors concluded that spatters were distributed across the powder bed by gas flow, and at any given location the surface roughness of the inclined surfaces is affected by the orientation of the surface corresponding to the centre of the LPBF build platform [168]. The AM parameters interrelation with metal AM surface quality is summarised in Table 2.3.

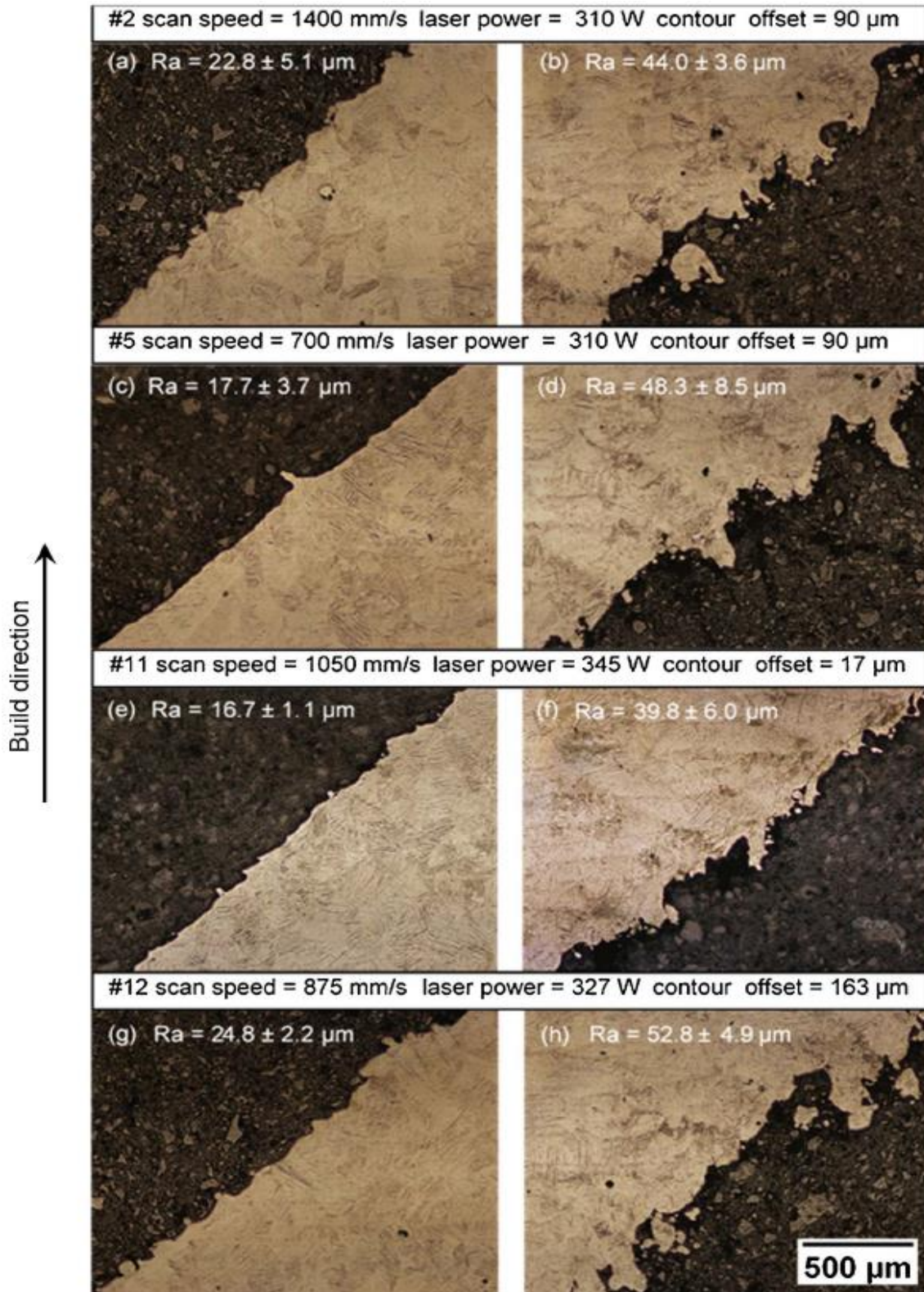


Figure 2. 37Schematic illustration of optical microscope images for 40° up-skin surfaces (left column), and 40° down-skin surfaces (right column) [168].

Table 2. 2 Summary of AM (including contour) parameters influence on final surface quality from the literature

Material	LP (W)	SS (mm/s)	HS (μm)	LT (μm)	Contour/Beam offset (μm)	Ra/Sa (μm)	References
17-4 SS	60	700	-	-	BO=0-20	Ra-90°=10 Ra-150°=18 Ra-180°=4	[178]
17-4 SS	120	700	-	-	BO=80-100	Ra-90°=13 Ra-150°= 16 Ra-180°=4	[178]
17-4 SS	60	350	-	-	BO=80-100	Ra-90°=12 Ra-150°= 17 Ra-180°=4	[178]
17-4 SS	120	1400	-	-	BO=80-100	Ra-90°=11 Ra-150°= 19 Ra-180°=3	[178]
Ti6Al4V	350	770	180	50	-	Ra=20-45	[170]
Ti6Al4V	750	1925	200	50	-	Ra=20-65	[170]
Ti6Al4V	1000	1400	230	100	-	Ra=15-90	[170]
Ti6Al4V	350	770	-	50	CO=180	Ra=10-40	[170]
Ti6Al4V	800	1765	-	100	CO=180	Ra=20-55	[170]
Ti6Al4V	310	1400	100-180	30-60	CO=90	Ra-US=23 Ra-DS=44	[168]
Ti6Al4V	310	700	100-180	30-60	CO=90	Ra-US=18 Ra-DS=48	[168]
Ti6Al4V	345	1050	100-180	30-60	CO=17	Ra-US=17 Ra-DS=40	[168]
Ti6Al4V	327	875	100-180	30-60	CO=163	Ra-US=25 Ra-DS=53	[168]
Hastelloy X	370	1900	50-130	20	-	Ra=20-29	[165]
Hastelloy X	370	1900	50-130	40	-	Ra=13-30	[165]
IN718	80	500-900	-	-	LS	Ra=12-17	[13]
IN718	80-120	560	-	-	LS	Ra=7-17	[13]

IN718	80	500-900	-	-	CT	Ra=12-14	[13]
IN718	80-120	560	-	-	CT	Ra=11-15	[13]
Ti6Al4V	100	600	80	30	-	Ra=8	[179]
	120	800				Ra=6	
	140	1000				Ra=5	
	160	1200				Ra=7	
	180	1400				Ra=6	
	200	1600				Ra=7	
Ti6Al4V	120	400	80	30	-	Ra=5-9	[179]
	140	600				Ra=6-8	
	160	800				Ra=8	
	180	1000				Ra=8-9	
	200	1200				Ra=5-10	
316L SS	180.4-300	700-1178.4	72.2-120	-	-	Ra=8.06-12.18	[180]
316L SS	100	400	80	-	-	Ra=9.5	[181]
	150	700	70			Ra=8.6	
	150	400	90			Ra=7.1	
	150	450	80			Ra=6.3	
	150	500	80			Ra=7.6	
	150	550	80			Ra=8.4	
	150	600	80			Ra=8.2	
	150	600	70			Ra=7.5	
AlSi10Mg	100	1000-2800	150	40	YES	Ra=17-18	[182]
	150	1000-2800				Ra=11-15	
	200	1000-2800				Ra=10-12	
	250	1000-2800				Ra=10-11	
	300	1000-2800				Ra=8-10	
	350	1000-2800				Ra=9-12	
	400	1000-2800				Ra=8-18	
AlSi10Mg	350	1500	150	40	NO	Ra=20	[182]

BO-Beam offset, CO-Contour offset, LS-Light scanning, CT-Computer Tomography

Table 2. 3 Summary of AM parameters interrelation with surface quality from the literature

AM Parameter	Surface quality (Ra/Sa) relation	Reference
Laser power (LP)	LP ↑ Ra/Sa ↑	[183]-[167]
Scan speed (SS)	SS ↑ Ra/Sa ↑	[183], [184]
	SS ↑ Ra/Sa ↓	[185], [186]
Hatch spacing (HS)	HS ↑ Ra/Sa ↓	[187]
	HS ↓ Ra/Sa ↓	[184]
Layer thickness (LT)	LT ↑ Ra/Sa ↑	[36]
Particle size distribution (PSD)	PSD ↓ Ra/Sa ↓	[188]
	PSD ↓ Ra/Sa ↑	[189]
Energy density (ED)	ED ↑ Ra/Sa ↓	[167], [190]
Beam offset (BO)	BO ↓ Ra/Sa ↑	[191]
Laser re-melting (LSR)	LSR ↑ Ra/Sa ↓	[167] [192]
Substrate position (SP)	Centre to the corner; Ra/Sa ↑ for flat surfaces Ra/Sa ↓ for inclined surfaces	[193]
Shielding gas flow (SGF)	Away from the gas flow Ra/Sa ↑	[191]

2.3.4 Influence of scan strategies on metal AM surface quality

The various scanning strategies, such as meander, stripe, island, cheeseboard, hexagonal, line and rotate scanning at different angles, zig-zag, and in-out and out-in scanning strategies are often adopted in an LPBF process [173,194-196]. Cheng et al. investigated the impact of eight different scanning strategies by both simulation-experimental approaches on the stress and deformation evaluations of AM components [173]. The authors found that the 45° and 67 ° line-scanning strategies displayed the minimum stress and deformations. The in-out scanning strategy resulted in the highest deformation [173]. However, the authors reported no significant difference in deformation between line scanning, 45° line scanning, and 45°, 90° and 67° rotation scanning cases [173]. Yasa et al. [197] reported that the use of a contour scan amplifies the edge effect, but that the use of raster scanning rather than unidirectional scanning can further enhance the top surface's flatness [197]. Paraschiv et al investigated top surface deformations (edge and corner effects) by

varying hatch angle rotations (45° , 67° , 90° , (see Figure 2.38)) and laser re-melting technique. The authors found that samples built without a contour and with hatch angles of 45° and 67° displayed more noticeable edge and corner effects, while the hatch rotation angle of 90° produced the fewest deformations [174]. The samples built with contour and hatching angles displayed lower corner heights (45° :17%, 67° :31%, and 90° :19%) respectively [174]. The ridge height of both edge and corner effects increased with an increased number of laser re-melting passing of the top layer. However, this ridge height was reduced by using a lower VED for melting the top layers [174].

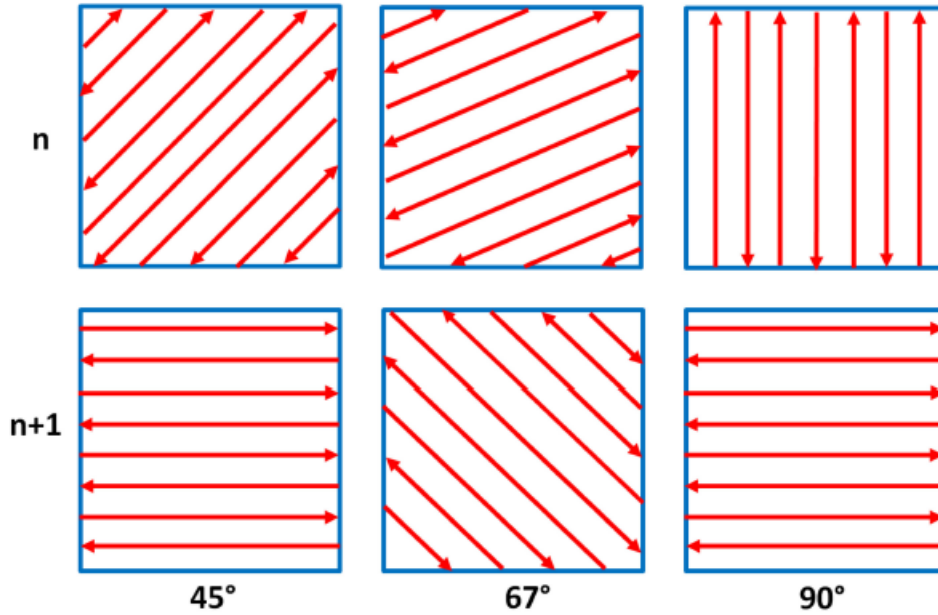


Figure 2. 38 Schematic illustration of different Hatching angles used for metal AM of IN 625 samples [174].

Jiang et al studied the impact of LPBF process parameters and scan strategy on the lower surface (see Figure 2.39) quality (overhanging structure) of LPBF metal components [198]. The authors found that laser energy density (E_F) had a significant influence on the lower surface quality; Higher E_F led to the sinking of the molten melt pool and slag hanging on overhanging structure's lower surface, and too low E_F resulted in insufficient melting, melt pool agglomeration, pores and powder spiraling [198]. However, the cross-melting (I) and non-melting (II) strategies yielded better lower surface quality at low and high E_F (see Figure 2.39bcd) [198]. The combination of lower E_F and scan strategy I presented the best surface quality ($S_a \sim 25 \mu\text{m}$), similarly higher E_F combined with scan strategy II displayed a reasonable $S_a \sim 30 \mu\text{m}$ for the lower surface of the overhang structure (see Figure 2.39d) [198]. The authors concluded that the surface quality of the lower surface could

be accurately evaluated instantly by the cooling time of the molten melt pool during the fabrication of the lower surface overhang structure [198].

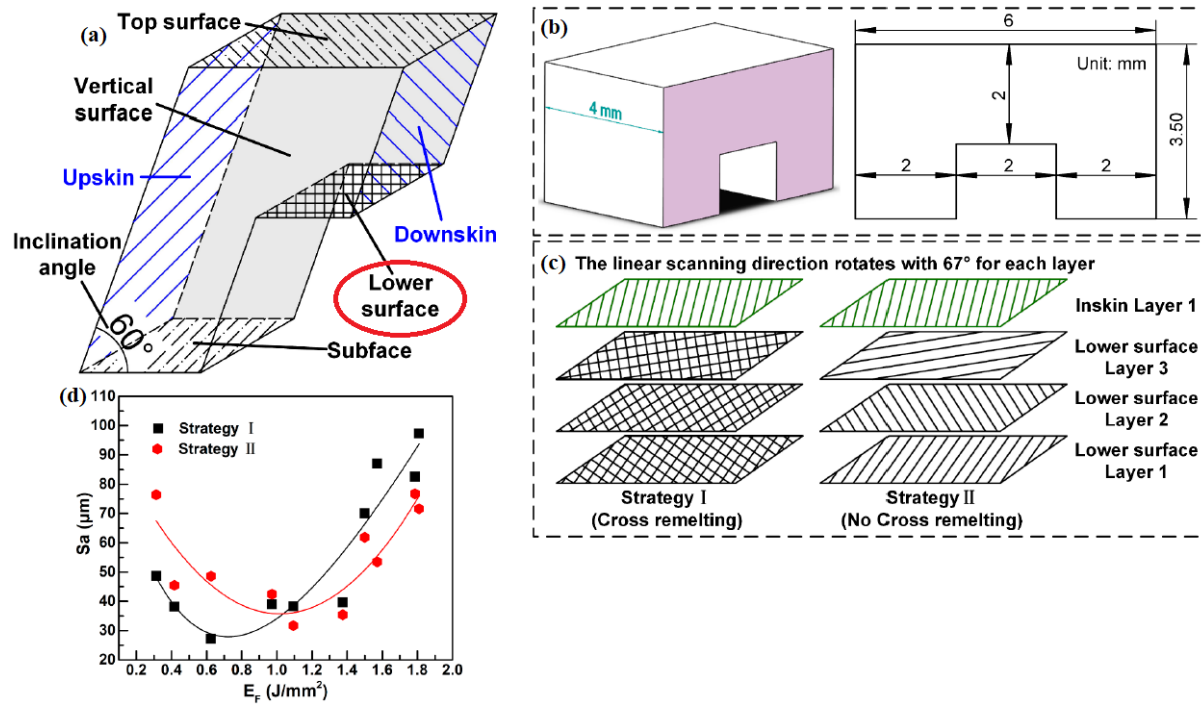


Figure 2.39 Schematic illustration of (a) depicting lower surface, (b) overhanging structure part dimensions (c) different scan strategies, and (d) Sa results [198]

Giganto et al studied the impact of different scan strategies (normal, concentric and hexagonal) on the final surface quality and mechanical properties of LPBF 17-4 PH steels (see Figure 2.40) [199]. For the top surface; the authors considered the hexagonal scan strategy as most appropriate for lower roughness (Ra) of 9.38 μm and porosities, whereas, the concentric strategy(C) presented the lowest porosities despite larger and irregular pores, ductile fracture (~1180 MPa), higher geometrical errors with lower Ra of 5.12 μm for lateral surfaces with large scanning vectors (see Figure 2.41) [199]. The normal(N) and hexagonal(H) scan strategies for the top surface achieved good (identical) mechanical properties (1103 MPa, 1104 MPa respectively) as well as dimensional and geometrical qualities (see Figure 2.42) [199]. N&H strategies present lower dimensional and geometrical errors, C strategy presents higher geometrical and dimensional errors [199].

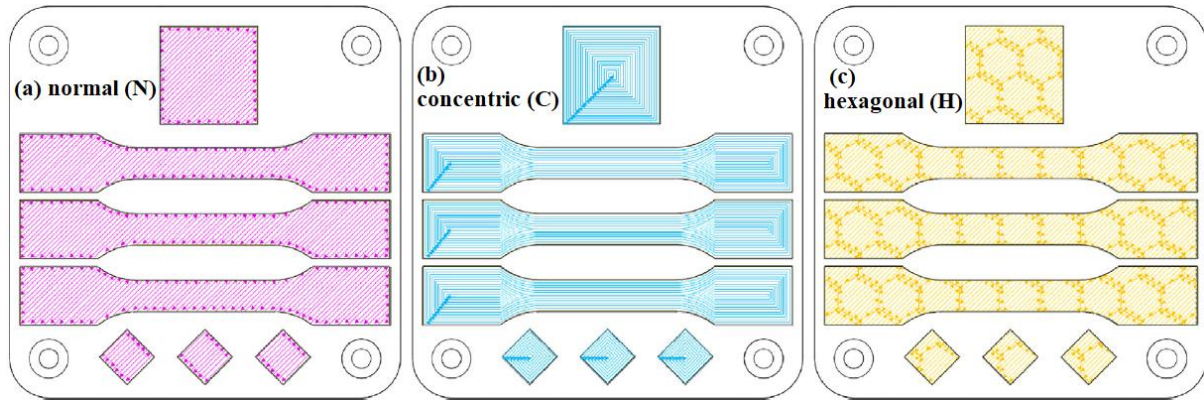


Figure 2. 40 Schematic illustration of various scan strategies adopted (a) normal, (b) concentric and (c) hexagonal [199].

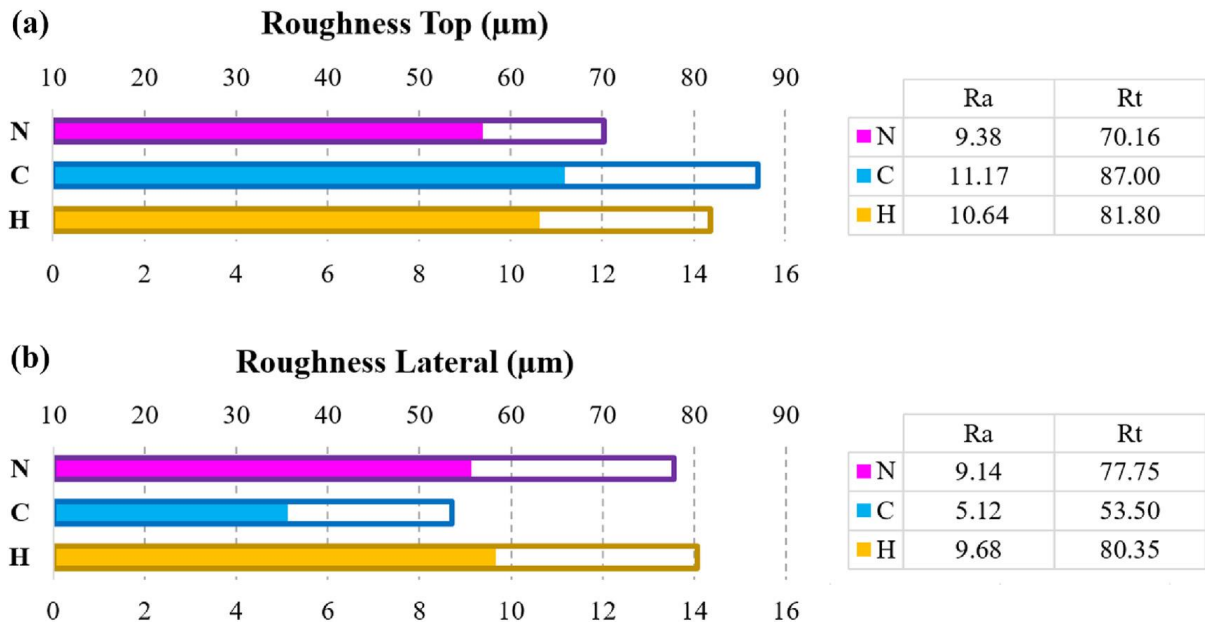


Figure 2. 41 Roughness values for (a) top and (b) lateral surfaces for various scan strategies [199].

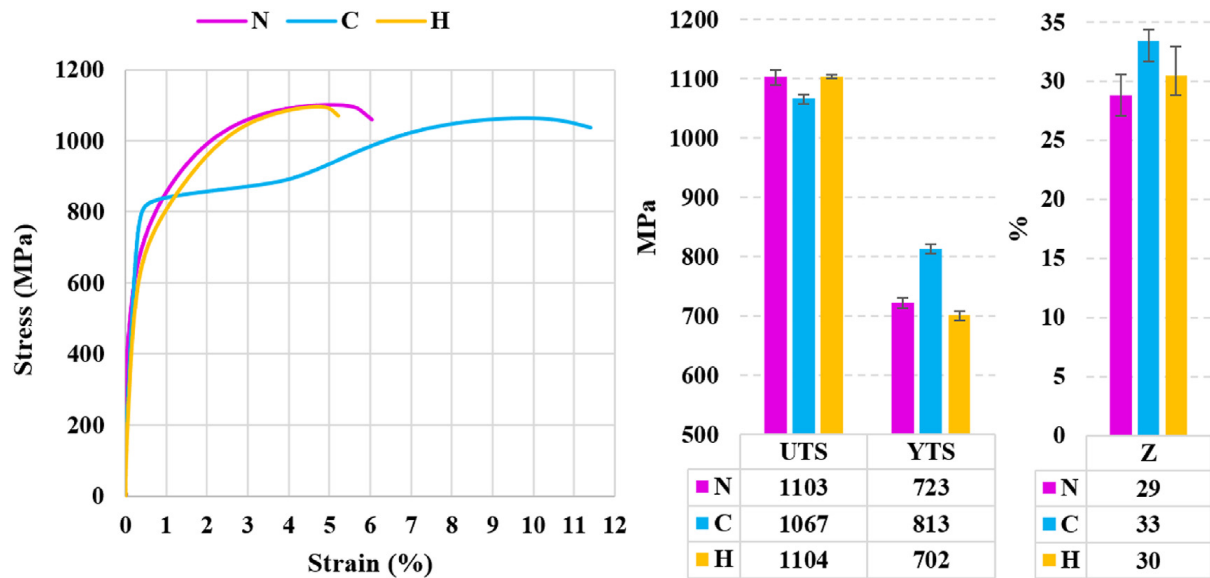


Figure 2.42 Stress-strain curve, UTS values for top and lateral surfaces for various scan strategies [199].

Miao et al utilized four different scanning strategies to study the effects of thermal gradient concentration linking to micro-voids, surface roughness (horizontal and vertical), porosity, tribological properties and microhardness of LPBF processed GO/TC4 nanocomposites (see Figure 2.43a-d) [200]. The authors found that L-scanning or S-scanning strategies adopted samples were seriously affected by a large number of micro-voids and defects due to higher thermal concentration, but the C-scanning strategy presented the optimal performance with the least surface roughness (Ra) of $\sim 2.80 \mu\text{m}$ (horizontal surface) and $\sim 1.02 \mu\text{m}$ (vertical surface) out of all scan strategies; credited to the lower temperature gradients (see figure be) [200]. The L-scanning strategy performed poorly for both horizontal and vertical surfaces with Ra of $\sim 9.20 \mu\text{m}$ and $\sim 6.60 \mu\text{m}$ respectively. L-scanning showed a larger COF (0.5117), i.e., 20.54% higher than C-scanning displayed a superior friction coefficient and wear volume. H-scanning exhibited better wear resistance than L and S scanning strategies (see Figure 2.44a-c) [200].

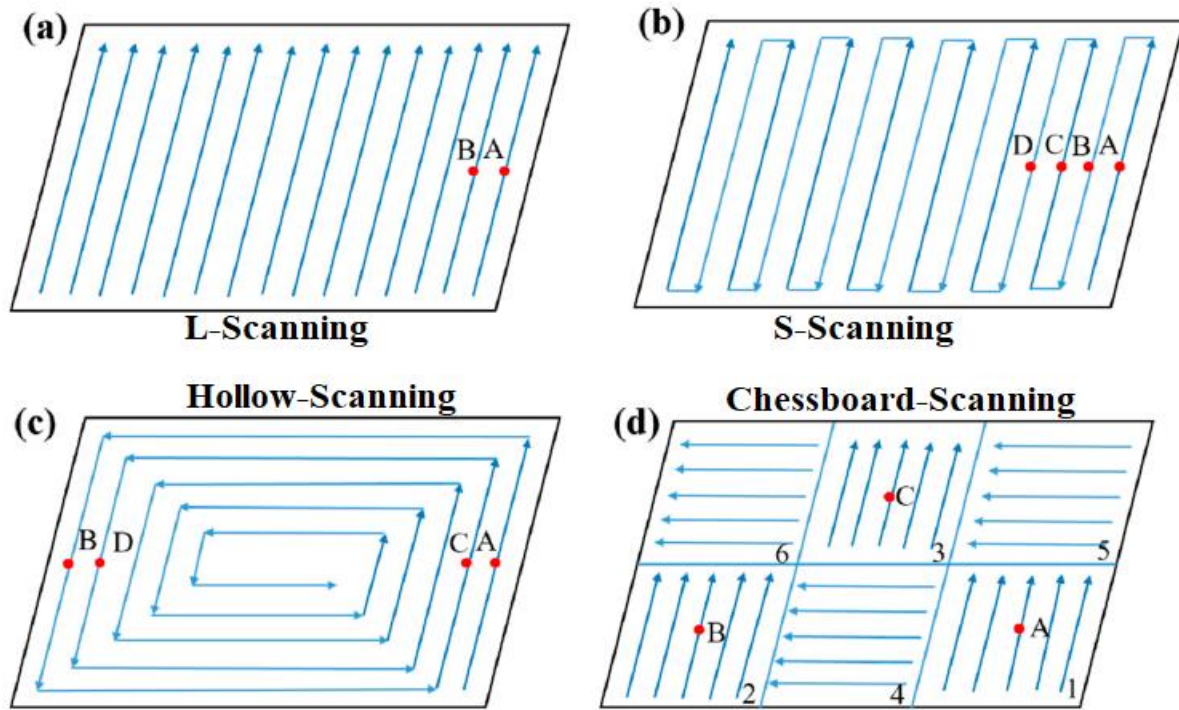


Figure 2. 43 Schematic illustration of four different scan strategies used in LPBF process [200]

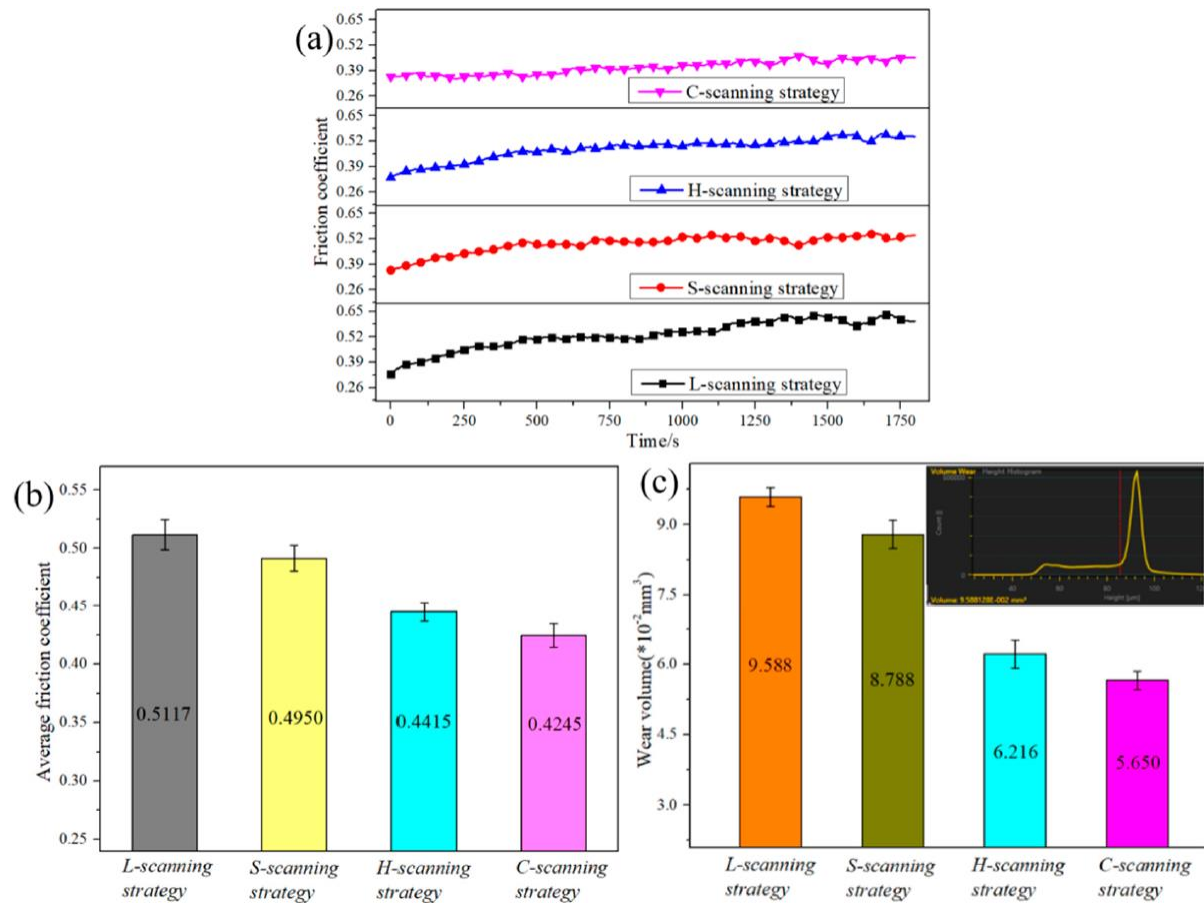


Figure 2. 44 Tribological properties of LPBF under different scan strategies: (a) real-time friction coefficient; (b) average coefficient of friction and (c) wear [200].

2.3.5 Tribological and corrosion properties of metal AM components

A thorough investigation of currently available literature on the tribological and corrosion behavior of metal AM parts reveals that the research is still in the early stages. Presently, lubricated fretting components like cylinder liners and Marines' shoes prefer a rougher surface that helps retain more oil, resulting in smaller wear and friction compared to a smoother surface. However, to expand LPBF applications into frictional pairs, it is paramount to study the metal AM's friction, wear and corrosion performance under various conditions [201]. Wear is defined as the loss or displacement of material from a contacting surface [1]. The wear rate of metal AM steels linearly depends on the volume percentage of the porosity [201]. The reported wear rate was 6-17% higher than bulk steels for less dense LPBF process of steels with the presence of porosities. The wear track on bulk 316L SS was covered with oxide film with a dark grey cracked surface appearance ("O" marked) (see Figure 2.45a), these oxide films were removed to form a smooth wear debris leaving a rougher dark surface: typical mild oxidative wear [202]. In contrast, the SLM surface displayed a wider, rougher and metallic appearance wear track: the primary wear mechanism is due to easy crack initiation and propagation originating from pre-existing process-induced surface porosities, cracks and craters defects that subsequently lead to the premature failure of the component at lower applied loads [203,202] (see Figure 2.45b). It is possible to achieve equivalent or superior wear resistance than conventional steels if LPBF-built steel components are fully dense with minimum surface defects [202, 203].

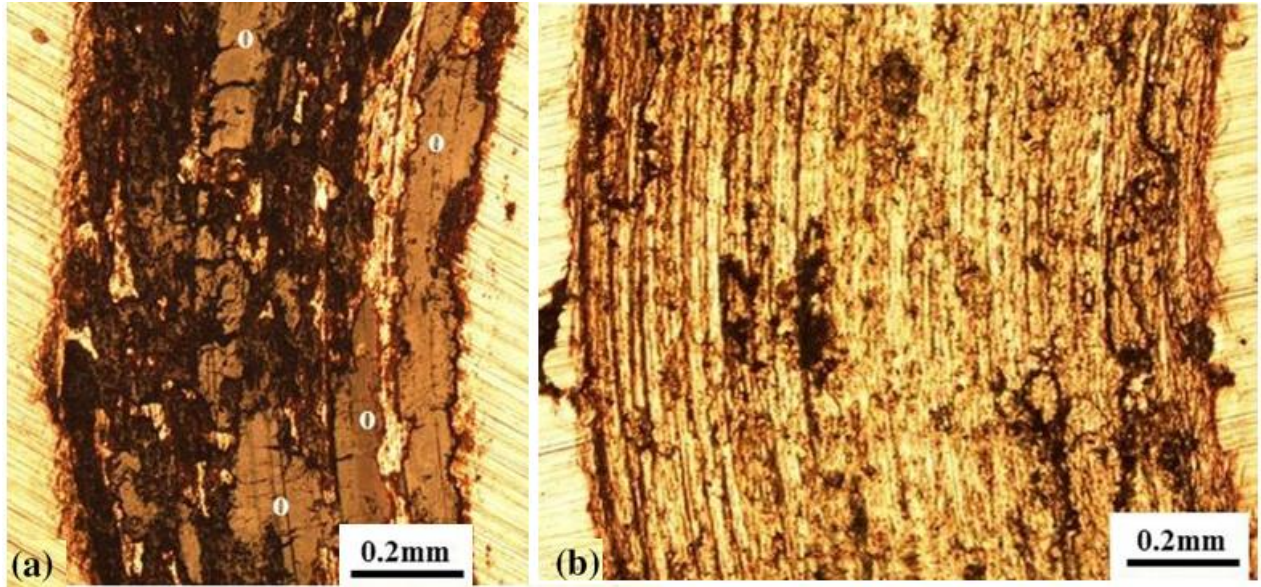


Figure 2.45 Comparison of wear rate in dry wear test condition at 120rpm, 10N (a) bulk 316L and (b) LPBF 316L (175 mm/s, 150 W) samples. “O” marks in (a) indicate tribo-oxide film. [202]

The cyclic polarisation curves measured in 0.9% NaCl soln for bulk and SLM showed similar electrochemical corrosion behaviour, but the forward scan curves of SLM contained many current spikes as a result of metastable pitting formation: signifying the porosities in SLM promote corrosion instability at high anodic potential (see Figure 2.46a) [202]. The authors found that if the full density is achieved for the SLM steel sample then the corrosion behaviour will be the same as the bulk 316L steel samples (see Figure 2.46b) [202].

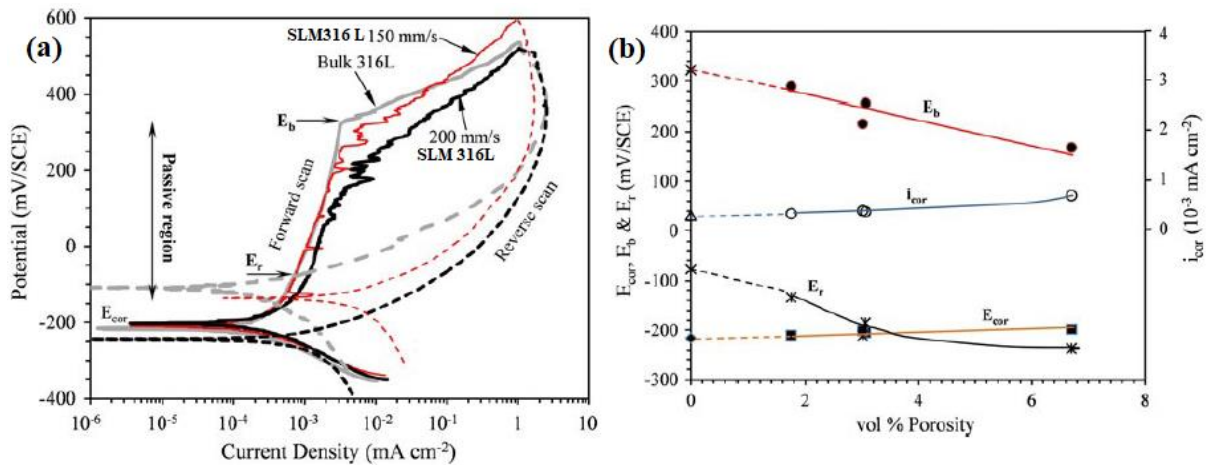


Figure 2.46 Schematic illustration of cyclic polarisation curves in 0.9% NaCl soln at a scan rate of 1mV/s for (a) bulk 316L SS and selected SLM (150mm/s and 200mm/s) samples, (b) E_{cor}, E_b,

Er and icor as a function of volume porosity. (Ecor-corrosion potential, Eb-breakdown potential, icor-corrosion current density, Er-repassivation potential) [202].

Lia et al investigated the impact of building directions and different loads, temperatures and frequencies on the tribological properties of SLM 316L steels (see Figure 2.47a) [203]. The authors showed that build directions have the least impact on COF and wear (see Figure 2.47b), while the COF decreased significantly at the higher temperatures, and wear was at its peak at 200°C (see Figures 2.47cd) [203]. The wear rate gradually decreased due to the fact that oxide films acted as lubricants and protected them from further wearing [203]. The COF was not affected remarkably at higher contact pressure but the wear tends to be higher at higher contact pressure [203]

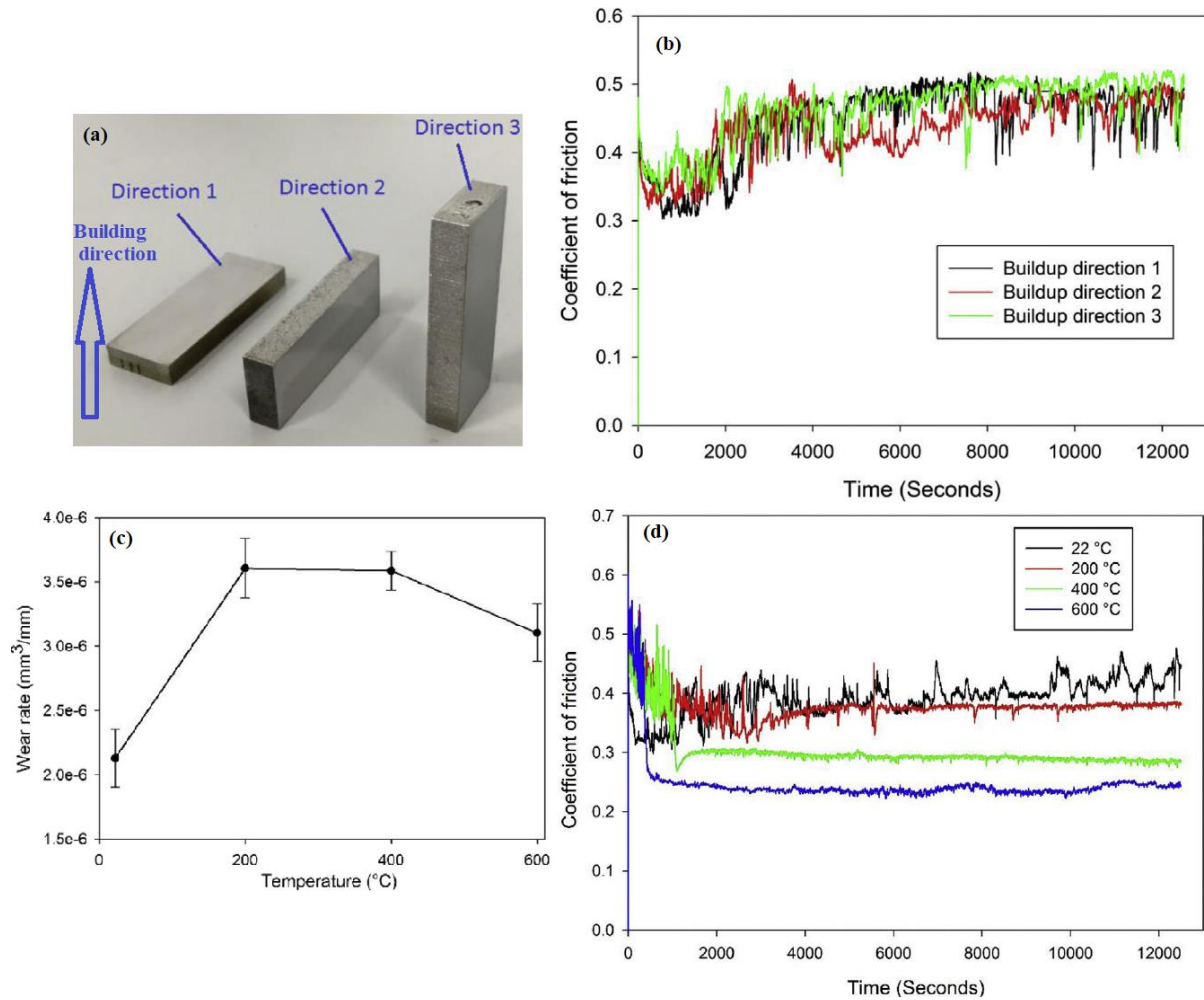


Figure 2. 47 Schematic illustration of (a) different building directions, (b) Coefficient of friction for respective building directions, (c) wear rate and (d) COF at different temperatures [203].

Kazempour et al investigated the microstructure and corrosion susceptibility of SLM 316L SS in aqueous 3.5 wt.% NaCl solution. The cyclic potentiodynamic polarization results for SLM samples

showed better pitting resistance and a lower rate of metastable pitting as compared to wrought alloy irrespective of the build orientation (see Figure 2.48a) [204]. The shorter immersion time posed a negligible effect on both corrosion and pitting potentials. However, the longer immersion time and the electrochemical impedance spectroscopy results confirmed that process-induced bigger size highly dense porosities and surface asperities posed significant adverse effects in lowering the electrochemical potential stability of SLM samples aligned perpendicular to the building direction [204]. The pits, grain, and sub-grain boundaries and melt pool of wrought and SLM samples are evident in (see Figure 2.48bcd) [204].

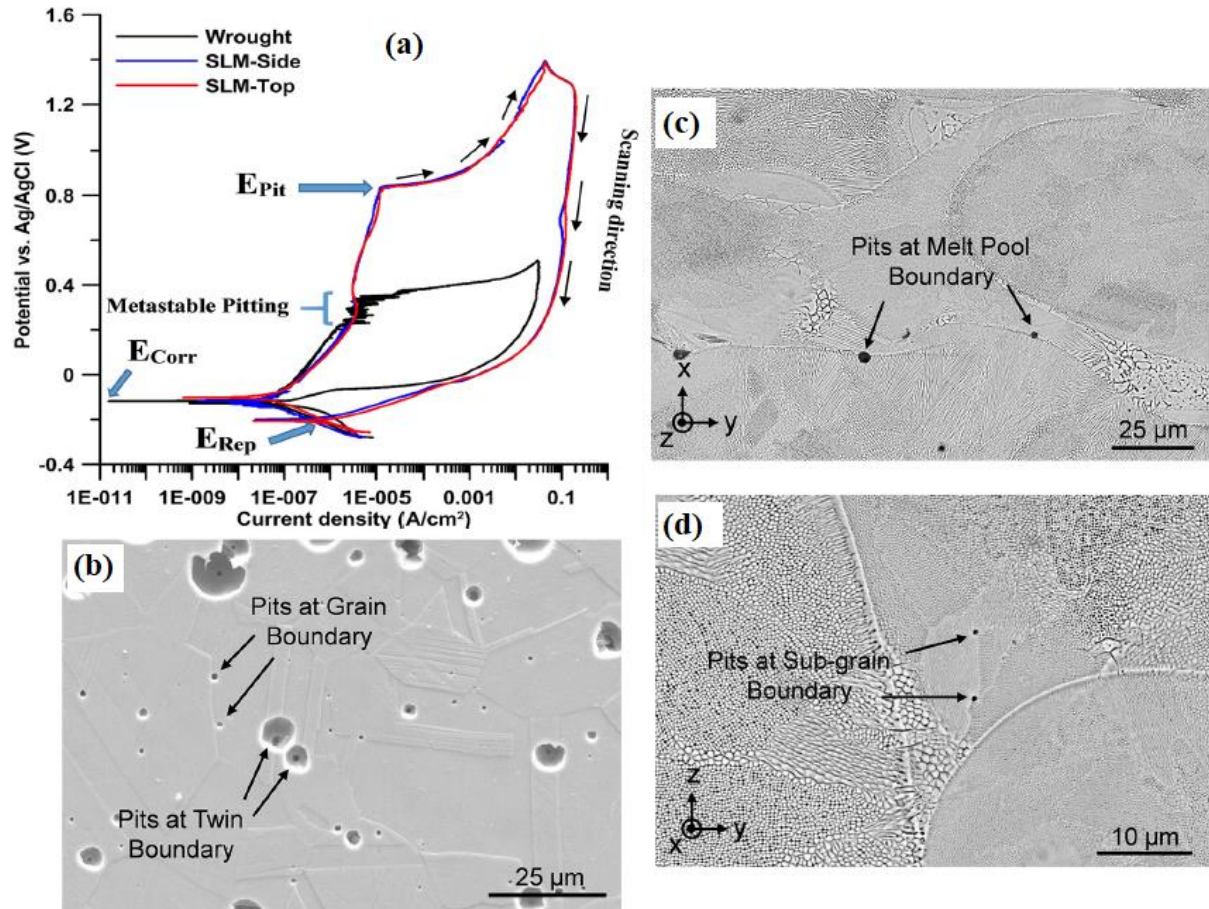


Figure 2. 48 Schematic illustration of (a) Cyclic potentiodynamic polarization curves of wrought and SLM samples. (b) SEM images of the wrought, (c and d) SLM-316L-SS sample after corrosion-testing [204]

2.3.6. Surface quality prediction of metal AM surfaces built with varying inclination angles

The majority of the existing literature on surface roughness prediction models often use theoretical calculation pertaining to the staircase effect and cusp height/geometry of inclined and/or curved AM surfaces (see Figure 2.49) [164,205,206]. The surface roughness prediction model for down-skin surfaces was examined by Charles et al. in addition to carrying out the experiments to correlate AM process parameters with roughness Sa [164]. Their prediction model for optimisation of process parameters revealed that minimising the obtained Sa value at 45° and 35° down-skin surfaces were achieved individually with an average error percentage of 5% and 6.3% respectively [164]. In order to determine the importance of powder size distribution, Rausch et al. looked at a predictive simulation of LPBF process windows [205]. Their research's main goal was to identify the single- or multi-layer binding defects that result in porous structures between melt tracks [205]. They also attempted to achieve the minimum possible surface roughness of the final part and thus lower the efforts required for the surface post-processing [205]. From their combination of porosity and surface roughness prediction simulation model, the authors discovered that a greater number of porosities and higher surface roughness are interrelated. As a result of balling and wetting-related effects increased porosities were formed which led to uneven surface asperities on the subsequent layers, [205].

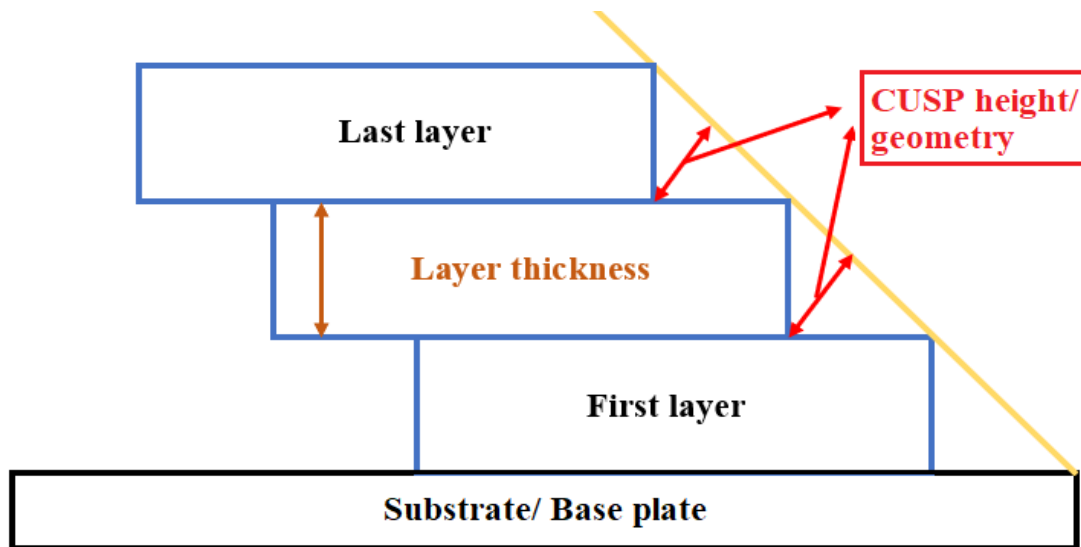


Figure 2. 49 schematic illustration of cusp geometry

In addition to the physical experiments, Wang et al. examined a theoretical model of upper surface roughness of single-track and multi-track fabrication of LPBF steels to improve the part quality [167]. The authors' theoretical analysis revealed that surface roughness was mainly affected by

the melt track width, hatch spacing and layer thickness. The maximum recorded theoretical Ra was $\sim 15 \mu\text{m}$, likewise maximum measured Ra was $\sim 25 \mu\text{m}$: 50% more than the theoretical value [167]. The huge difference in observed Ra values was credited to deviations in theoretical assumptions and the complex nature of AM process, which is extremely difficult to control and is unpredictable [167]. Barari et al. inspired to develop a full imperial model of surface roughness as a function of layer thickness and part orientation using a polynomial interpolation to predict the cusp height [140]. The developed model was implemented and applied with the aim of accurate representation of cusp geometries with non-uniform rational B-spline (NURBS) curves to predict and control the surface quality of Fused deposition modelling (FDM) processed parts [140]. It was interesting to note that the measured Ra close to 90° was more than the theoretical value due to corner curves of cusps being neglected in practice, in addition, the width of the staircase ought to be small or close to 0 at 90° [140]. Authors promoted that their developed model could be applicable to all layer-based AM processes to optimize the two most important AM parameters namely layer thickness, and part orientation to attain the desired surface roughness for the critical features of AM parts [140]. RK Ek et al. constructed two levels full factor (2^4) design of experiments (DOE), mathematical model, to elucidate the impact of EBM parameters on the average surface roughness (Ra) of vertical surfaces [30]. Selected design factors such as the number of contours (NC), contour offset (CO), a combination of speed and current in contour (SC) and line offset (LO) because they were compatible to work simultaneously and anticipated to influence surface roughness [30]. Ra of vertical surfaces (03 builds: I, II, III) was found to be $24 \mu\text{m}$, $29.5 \mu\text{m}$ and $28.5 \mu\text{m}$ with their standard deviation $0.39 \mu\text{m}$, $0.57 \mu\text{m}$ and $0.53 \mu\text{m}$ respectively. Ra was evaluated using profiler software and calculated using MATLAB including the results from DOE. Authors found that CO and SC were notable influencing factors of Ra, followed by a combination of NC and CO had some influence but rather lesser tolerance level than CO and SC [30]. Taufik et al. adopted an innovative approach based on the combination of theoretical and empirical models to study and predict the randomness in the geometry of build edge profiles, composed of the perimeter, raster and combination of both layer deposition patterns that are deemed to reduce the predictive error of roughness models in FDM process (see Figure 2.50 abc) [207]. The authors tested the robustness of these proposed models with respect to various inclination angles, and with the existing semi-empirical and theoretical models in the literature. It is interesting to note that build edge profiles are different at 0° , and in the range of 0° - 30° , and

30°-90° build inclinations: variations in height and base length deviations impart sudden changes in surface profile and thereby surface roughness of FDM parts (see Figure 2.50def). The obtained results clearly indicated that these advanced models were beneficial in reducing prediction errors [207].

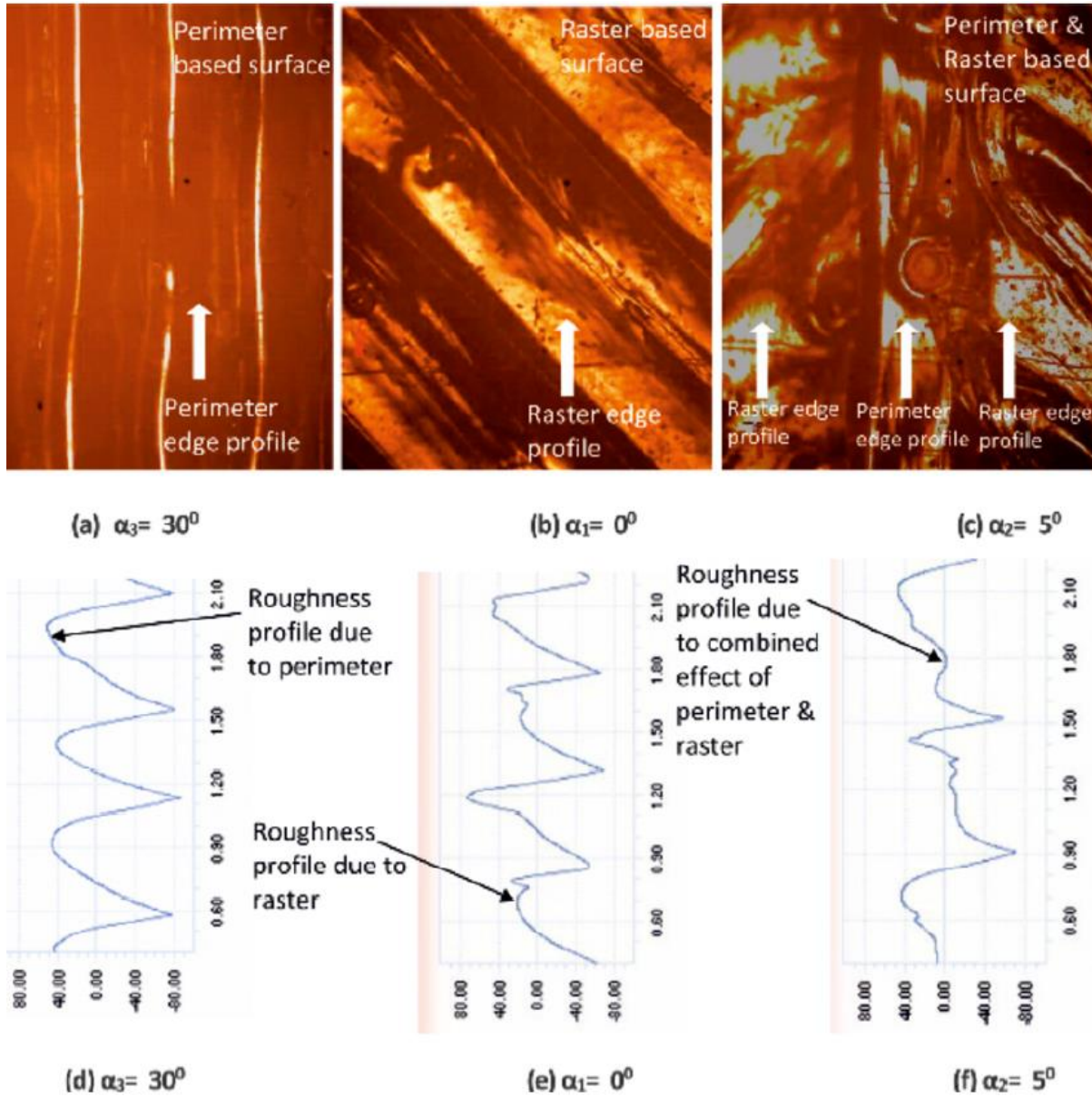


Figure 2. 50 Schematic illustration of layer deposition patterns (a) the perimeter, (b) raster and (c) combination of both, (d) roughness profile of perimeter, (e) roughness profile of raster, (f) roughness profile of combined effect [207].

Ozel et al. used a genetic algorithm and artificial neural network (ANN) to generate predictive model capability for ascertaining the link between LPBF process parameters (energy

densities: 113.75 J/mm³, 12.88 J/mm³ and 134.48 J/mm³, scan stripe pattern: 67° and 90°) and resultant surface texture parameters (Sa, Sq, Ssk, and Sku) (see Figure 2.51abc) [208]. The reported Sa values were in the range of 3.15µm-4.80 µm, and Sq values: 3.90µm-6.12 µm for the top surfaces (XY). Similarly, Sa values were in the range of 2.70µm-8.40 µm, and Sq values: 3.75µm-10.61 µm for side surfaces (YZ) [208]. Ssk values turned out to be negative for all the samples, while all the surface samples displayed positive kurtosis. Overall, the predicted values were in good agreement with the measured results showing that predictive tools could become handy to implement during the process planning stage of the production. However, the downside of this proposed predictive method was found to be less effective or difficult to predict the surface texture parameters of side surfaces (YZ) and restricted sample size for training ANN [208].

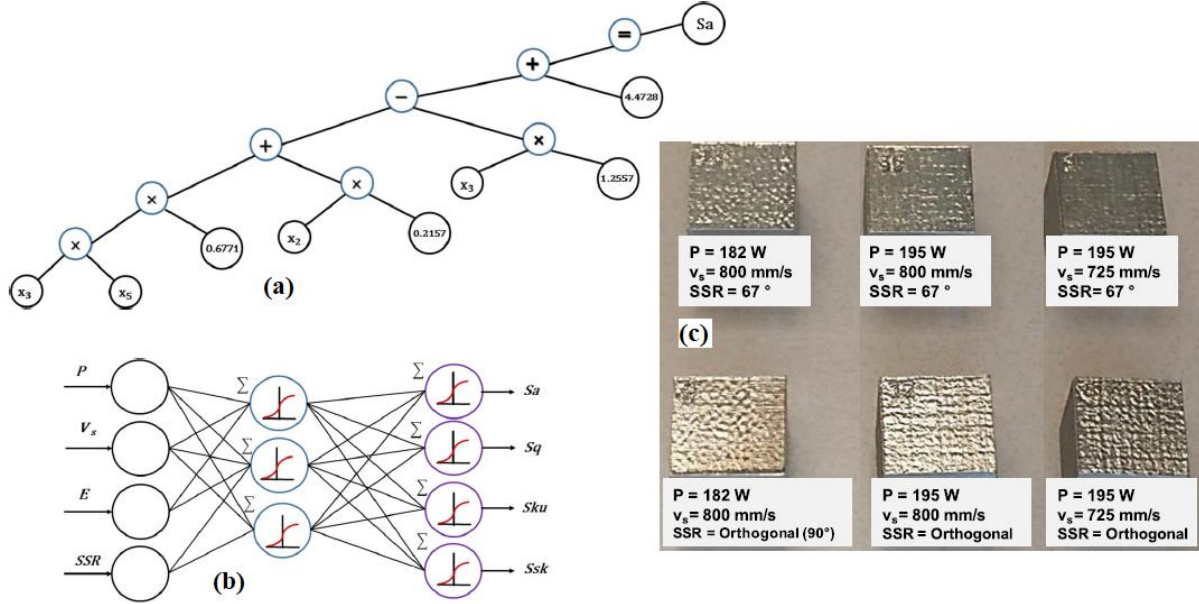


Figure 2. 51 Schematic illustration of (a) genetic programming tree optimal structure, (b) multi-layer feed forward neural network (c) fabricated test cubes [208]

A similar neural network model was applied to predict the distribution of roughness within the build volume, considering the interactive effects of powder recoating, spattering, gas flow and heat transfer which the responsible for intra-build inconsistency in the LPBF process [209]. Delfs et al. studied the prediction model to optimize the build orientation to improve the surface quality and build time of AM parts [210]. Adhered particles and staircase effect formed on up-skin (0°-90°) and down-skin (90°-180°) surfaces were considered for the simulation of the surface quality prediction model [210]. Experimental Ra and Rz values were found to be in the range of 20µm-149 µm, and 27µm-177 µm for 05 tilt angles between 15°-75°. Likewise, Simulation Ra and Rz

values were in the range of 21 μ m-148 μ m, 25 μ m-190 μ m respectively. It was worth noting that measured roughness results were in accordance with the predicted roughness values of the simulation [210]. Rott et al. proposed a novel parameter surface relation angle (ζ) to predict surface roughness (R_a), and to quantify the interdependency of laser interaction vs surface orientation [211]. It was important to note that by using the constant ζ , the range of R_a on surfaces across the entire build platform was reduced from 19 μ m to 11 μ m as compared to its counterpart constant surface normal polar angle (α) [211]. Authors reported the decrease in standard deviation from 5 μ m to 2 μ m by adopting this novel prediction method, plus ζ could also be handy to predict the position-dependent surface roughness of down-skin surfaces prior to the AM process for a given parameter set [211]. F.Kaji et al proposed an empirical model to predict the surface roughness distribution of fused deposition modelling (FDM) part based on actual observation and modelling of cusp geometry (edge profiles could critically affect the surface quality) using local surface slope and layer thickness [206]. The developed methodology was implemented on the three-piece geometric pattern assumed to describe the cusp profiles and calculate the surface roughness based on a centre-line standard. The results were validated with a variety of experimental case data by comparing the actual surface roughness vs predicted roughness values [206]. The authors concluded that this new approach could be efficiently adapted to predict and to optimize FDM parameters to achieve the desired level of surface roughness [206].

Galati et al. analytically investigated the surface roughness prediction model for various inclinations angles including up-skin and down-skin surfaces and cavities, model was validated by carrying out physical experiments [212]. Full factorial DOE was tailored, in addition to profile (R_a , R_q , R_z) and areal surface texture parameters (S_a , S_q , S_z) were adapted to relate the interdependency of sloping angles (30°-55° with 5° increments) and surface roughness of ad-hoc artefact [212]. see Figure 2.52abc) The role of waviness was less significant; surface roughness and texture followed the same trend while distinguishing overall AM surface morphology with respect to various sloping angles. The surface orientation and sloping angles displayed a significant impact on surface roughness, the predictive model was found to be robust and consistent with the experimental observations [212].

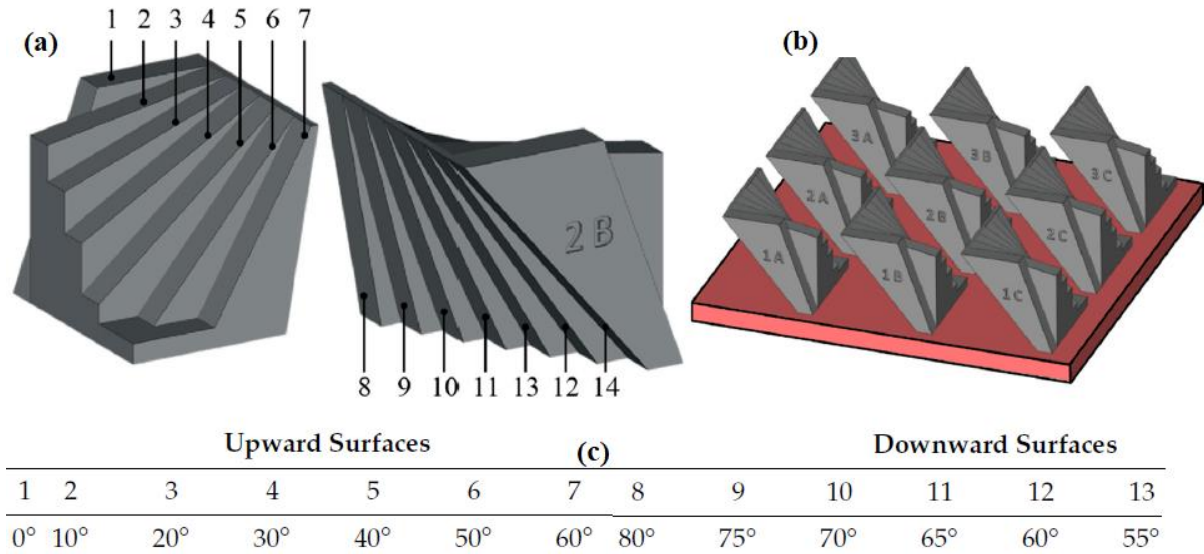


Figure 2. 52 Schematic illustration of (a) artefact; and (b) single job positions of the replicas on substrate, and (c) surfaces identification [212].

Bacchewar et al. studied the impact of laser power, layer thickness, build orientation, and hatch spacing parameters on the surface roughness of selective laser-sintered (SLS) parts. Central rotatable composite design (CCD) of experiments for planning and analysis of variance (ANOVA) was used to establish process variables adequacy of the developed model on surface roughness [213]. Authors reported that layer thickness and build orientation are significant factors affecting the up-skin surfaces, while laser power, build orientation and layer thickness have been found to be significant parameters for down-skin surface roughness. [213]. Furthermore, the authors developed the empirical models to estimate the surface roughness, in addition to employing the trust-region-based optimization method (MATLAB module) to obtain a set of process parameters to achieve the best surface finish. The authors concluded that the predicted results were in good agreement with the confirmed experimental findings (truncheon case study) in the range of 10° to 70° [213]. Campbell et al demonstrated an empirical model with the least range of inclination angles where the surface roughness can be considerably predicted for several rapid prototyping processes (SLA, Jetting, LOM and FDM) [214]. SLA measured part confirmed the reputation for predictable surface quality with $R_a < 10 \mu\text{m}$ for down-skin surface inclination angles between 90°-150°, whereas the reported $R_a \sim 10 \mu\text{m}$ or higher for up-skin surfaces. Similar $R_a \sim 10 \mu\text{m}$ values with a general shape of the plot following theoretical values very closely were observed in the LOM process signifying that surface roughness can be reasonably predicted [214]. FDM results showed that between 45°-80° surface roughness was predictable, while the measured roughness

values within 45° being horizontal displayed variations. Up-skin surface roughness of Jetting process was reasonably predicted, whereas the measured results for the down-skin surface oscillated wildly see Figure 2.53) [213]. The authors also drew a conclusion that the stair-case effect does not appear to be the main factor in determining surface roughness [214].

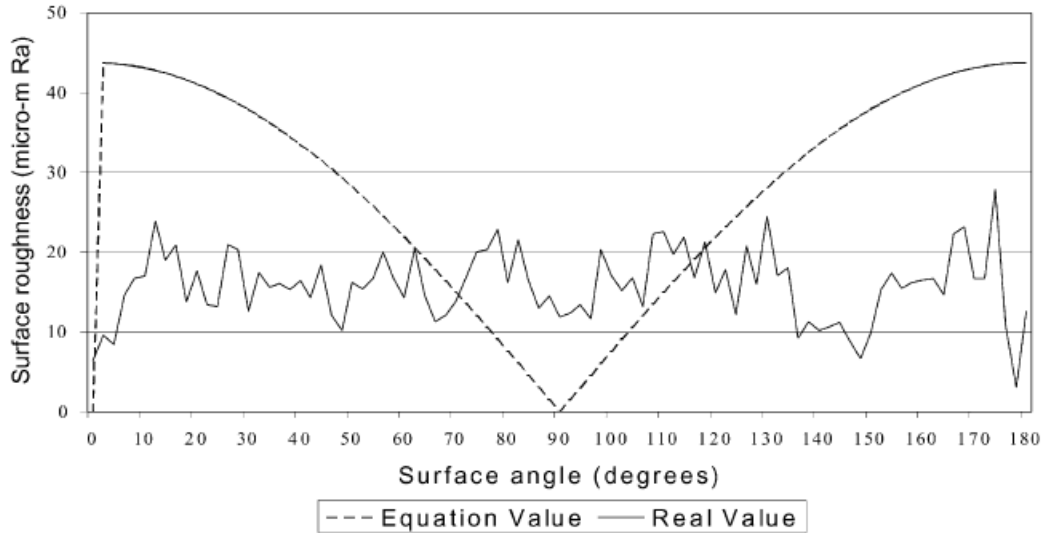


Figure 2. 53 Schematic illustration of equation and real surface roughness values for various inclination angles [213]

Strano et al. developed a mathematical model comprised of particles on top surfaces in addition to the stair step effect to accurately predict the surface roughness of SLM parts [215]. Also, they carried out experiments to investigate the key contributing factors influencing the surface roughness morphology at different sloping angles. Their surface analysis revealed in the range of 5° – 15° , the width of each step ($228\text{ }\mu\text{m}$ – $74\text{ }\mu\text{m}$) was bigger than the average particle diameter ($20\text{ }\mu\text{m}$) therefore, the observed surface displayed a characteristic stepped profile. The presence of partially bonded particles resulted in higher surface roughness at 90° even though the stair-case effect was not evident [215]. The authors concluded that the theoretically predicted roughness values were in good agreement with the experimentally observed results, which is useful to improve the surface quality and thus reduce the requirement of post-processing [215].

2.3.7 Surface texture characterisation of metal AM surfaces with varying inclination angles

As previously stated the surface texture of metal AM components are usually influenced by numerous factors such as powder particle density, layer thickness, build inclination angles, build orientations, heat input, and post-processing operations [36,138]. Many authors have invested their efforts to determine the exact role of various build orientations and sloping angles relative to the

emergence of surface asperities, plus they adapted measurement and characterisation methods using both profile (ISO 4288 [216]) and areal texture parameters (ISO 25178-3[217]). A summary of profile/areal surface texture measurement and characterisation available from the existing literature is given in Table 2.4 It is interesting to note that different measurement lengths/areas and cut-off wavelengths (λ_c – the cutoff wavelength to separate the waviness from the roughness, λ_s – the cutoff wavelength to separate the roughness from the shorter wavelength components) were adopted and various surface texture parameters were studied. For example, Triantaphyllou et al. adopted a cut-off wavelength (λ_c) of 8 mm and a noise cut-off wavelength (λ_s) of 8 μm [138]. Cabanettes et al. used λ_c 250 μm to isolate the welding tracks at 0° inclination [218]. Newton et al. used λ_c 70 μm to remove larger-scale topographic formations (i.e. long spatial wavelengths), i.e. any feature potentially larger than a particle or spatter formation [219]. In general, the measurement area/length and cutoff wavelengths should be selected upon the surface roughness scale [31,220,221]. ISO 4288 recommended suitable sampling lengths and cutoff wavelengths corresponding to each roughness range [222]. However, the metal AM or LPBF surface topography displays a different nature from the conventionally machined surfaces. It is unsure whether the current ISO standards are applicable to metal AM surfaces. This leads to the attempts on choosing various measurement areas/lengths and cutoff wavelengths as evidenced in Table 2.4. Whip et al. explored both destructive and non-destructive measurement techniques to examine the AM component surface roughness built with varying contour parameters [33]. In addition, the statistical relationship between contour parameters, profile/areal surface roughness height metrics (S_a/R_a , S_q/R_q , R_{sk}/SSk , R_{ku}/Sku , R_p/Sp , R_v/Sv , R_z/Sz), and additional non-standard metrics (S_{vk}/R_{vk} , S_{mR2}/R_{mr2} to quantify reduced valley depth, and dale height) plus general trends were presented [33]. The observed results showed that the destructive techniques are required to disclose notch-like features adhered to the surface, while the non-destructive measurement techniques are more beneficial to provide a statistically significant sample size [33]. This was attributed to areal measurements failing to accurately capture the maximum valleys on the surface, likely due to the presence of other surface features concealing the true depth, but, profile measurements are able to provide the true profile of the surfaces containing valleys and peaks [33]. Tato et al. adopted qualitative and quantitative comparisons of surface texture measurement and characterisation (S_a , S_q , S_{sk} , S_{ku} , S_{al} , V_{mp} , V_{vv} , S_{dq} , and S_{dr}) of metal AM parts using vertical scanning interferometry (CSI), imaging confocal microscopy (CONF), focus variation microscopy (FVM),

and advanced continuous confocal technology (C-CONF) to compare and verify data sets of each method resolution and acquisition time in order to investigate their ability and suitability to demonstrate metal AM surface topographical features (see Figure 2.54ab) [223]. It is worth noting that the FVM surface lacked to identify ripples as it presented lower lateral resolution capability but other methods were successful. Overall, the wall surface presented more challenges to measurement compared to the base surface for all the surfaces, which is attributed to a bigger amount of non-measured points due to a bigger amount of complex high aspect ratio features. [223]. CSI took 13 times more acquisition time than FVM for measurement, and 05 more times compared to CONF, whereas, C-CONF displayed a midway performance between the FVM and CONF [223].

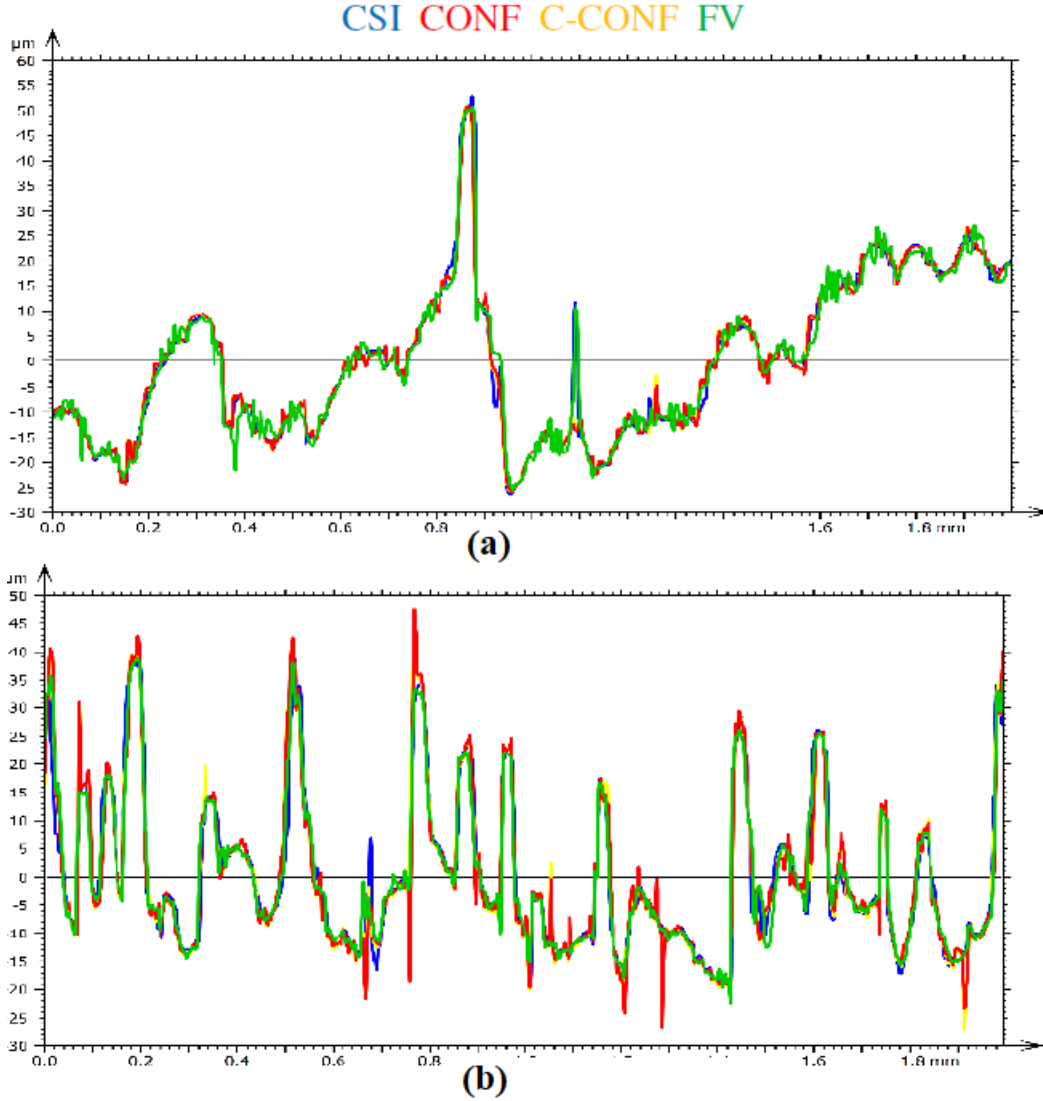


Figure 2. 54 Schematic illustration of roughness profiles obtained by four measurement methods (CSI, CONF, C-CONF and FV) acquired at the same location for (a) B surfaces and (b) W surfaces [223].

Zhou et al. investigated the surface texture attributes (S_a , S_k , S_{pc} , and V_{mc}) and surface profile (R_a) with five representative curvature samples (C_1 -to- C_5) at up-skin and surfaces of AM parts [224]. C_1 and C_5 displayed higher R_a values ($14 \pm 2 \mu m$) approximately 1.3 times than C_2 , and C_4 curvatures R_a values $10 \pm 1 \mu m$ and $11 \pm 2 \mu m$ [224]. Authors attributed the poor roughness of C_1 and C_5 to the presence of surface abnormalities: microcracks, and un-melted particles agglomeration on up-skin surfaces, whereas, C_2 and C_4 exhibited better melting and solidification. Overall, the C_5 curvature sample attained the worst surface texture parameters with $S_a: 13 \pm 1 \mu m$, $S_k: 37.33 \pm 2.08 \mu m$, $S_{pc}: 3.66 \pm 0.29 \text{ mm}^{-1}$ $V_{mc}: 12.61 \pm 0.33 (1/m)$ [224]. Kozior et al.

analyzed the greater impact of sample build orientations (0° , 45° & 90°) on roughness profile parameters (R_p , R_v , R_z , R_c , R_t , R_a , R_q , R_{sk} , R_{ku} , R_{Sm} , R_{dq} , R_{mr} , R_{dc}) and surface texture parameters (S_a , S_z , S_q , S_{sk} , S_{ku} , S_p , S_v , S_{al} , S_{tr} , and S_{td} , S_{dq} and S_{dr} , S_{mr} , S_{mc} , and S_{xp}) of metal AM 316L parts [225]. 10 out of 13 profile parameters displayed less than mean values (30 measured samples) from 2.6% to 11.7%. The areal orientation texture parameter S_{td} expressed in degrees recorded less than average values, i.e. at 0° : 13.3 deg, at 45° : 93.1 degrees, and at 90° : 87.8 degrees [225]. Similarly, the functional surface material ratio parameter S_{mr} expressed in percentage (%), showed the greatest deviations for the inclined angle 45° and 90° at 136.7% and 210.6% respectively which are useful to depict the impact of sample build orientation on surface roughness. The authors concluded that the best build orientation 0° inclination demonstrated higher surface quality with the least surface roughness values during both profile and surface texture parameters measurement and characterisation [225]. Triantaphyllou et al characterized surface texture (R_a , R_z , and S_a , S_q , S_{sk}) of metal SLM and EBM up-skin and down-skin surfaces relative to different sloping angles (0° , 30° , 60° , and 90°) and post-processing (grit blasting) [138]. Additionally, the emergence of re-entrant features and the impact of lay (underlying directionality) due to the layer-build approach were also investigated.

The difference between the minimum and maximum across the lay R_a was found to be $2.9 \mu\text{m}$ for the 0° up-skin EBM surface but lacked clear distinction for the down-skin surface. On contrary, the SLM surface exhibited R_a $4.8 \mu\text{m}$ along and across lay for the down-skin surface at 0° [138]. Authors found the tactile method not suitable to characterize re-entrant features, S_a and S_q were suited to metal AM areal measurements, whereas, S_{sk} was used to differentiate up-skin and down-skin surfaces of both as-built as well as post-processed SLM samples see Figure 2.55) [138].

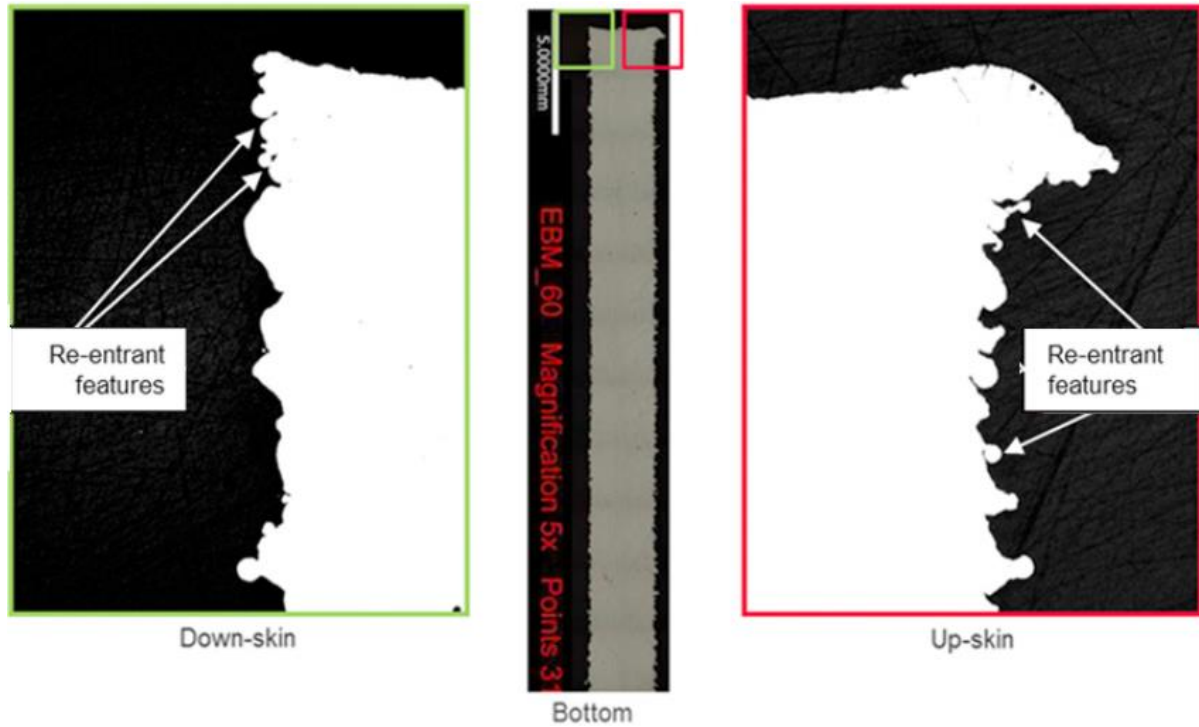


Figure 2.55 Schematic illustration of re-entrant features on up-skin and down-skin surfaces [138]

T. Grim et al laid their focus on the classification of different surface orientations plus a special issue in laser sintering: orange peel severity by a new measurement approach using a confocal microscope and 3D surface parameters [29]. The authors reported that hybrid parameters (S_{dr} and S_{dq}) along with spatial parameters (S_{al}) based on ACF were suitable for classification (see Figure 2.56a&b). However, they found that laser-sintered surfaces are more difficult to classify due to the lower level of detail of the surface's typical surface effects [29]. Overall, it was concluded that laser-melted AM parts displayed a strong correlation between the surface inclinations and areal parameters, in addition, the quantification of orange peel severity by surface parameters, was possible [29].

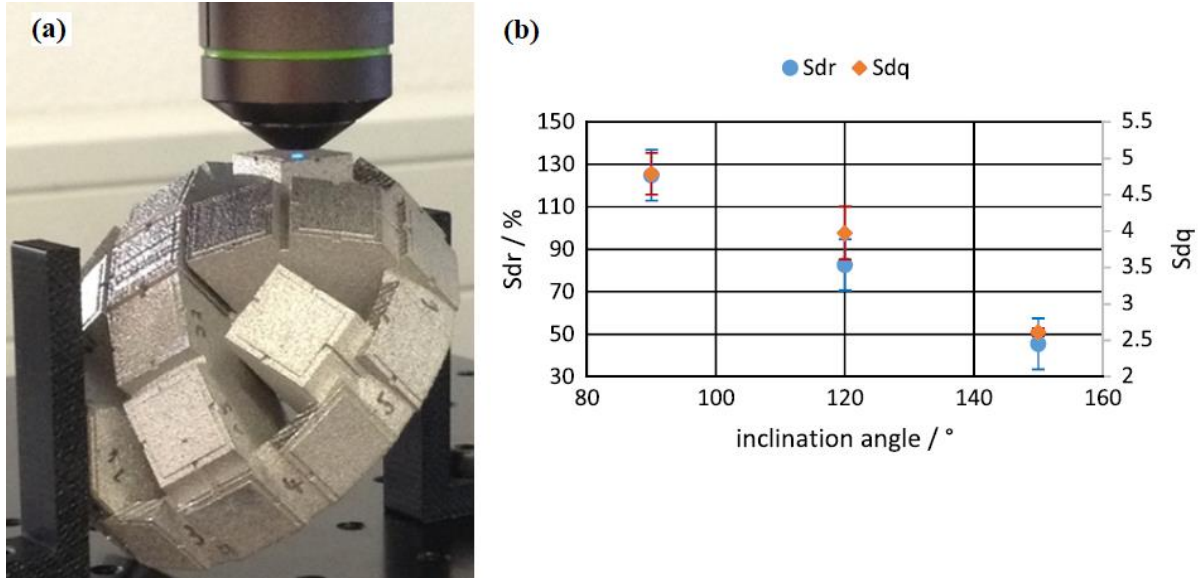


Figure 2. 56 schematic illustration of (a) artefact, (b) Sdr and Sdq for varying inclination angles [29]

Newton et al investigated surface topography (staircase effect, spatters, and particles) of EBM surfaces as a function of orientation (0° - 180° ; 0° - 90° : up-skin, 90° - 180° : down-skin) with respect to building direction using the combined approach consisting of texture parameters (S_a , S_q , S_{sk} , S_{ku} , S_z), and feature-based characterisation [219]. It was reported that feature-based characterisation could be useful to describe additional perspective on the surface quality, and possibly support for better research understanding of the interrelationship between metal AM parameters and resultant surface roughness, plus feature-based characterisation also become handy to produce texture parameters values without the presence of unwanted features [219]. Authors concluded that adapting the combined approach of texture parameters and feature-based characterisation does not solve the AM process problem explicitly instead this approach provides a novel viewpoint to help solve this kind of AM process-related issue [219]. More recently researchers from EPSRC Future Metrology Hub at the University of Huddersfield investigated the interrelationship between various up-skin and down-skin surface inclinations (0° - 180°) vs areal surface texture parameters (S_a , S_q , S_{sk} , S_{ku} , S_{al} , S_{tr} , S_{dq} , S_{dr} , V_{mp} , S_{mr1} , S_{pd}) and feature-based particles analysis of SLM Truncheon artifact [36]. The authors found a strong correlation between the various surface inclinations and the resultant surface texture of the SLM artifact. In addition, the authors concluded that staircase effect, and particle features (spatters and un-melted/

partially-melted particles) influence the surface texture characteristics fingerprint on inclined metal AM surfaces (see Figure 2.57) [36].

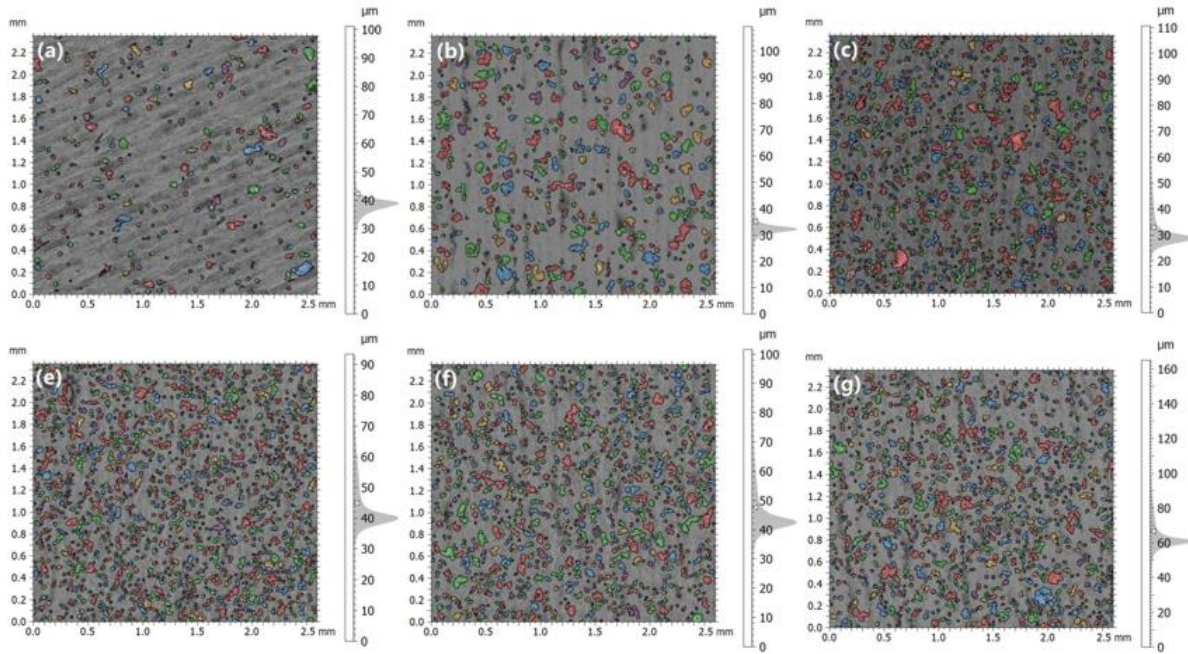


Figure 2. 57 Schematic illustration of quantification of particle features on various build inclination angles [36]

Snyder et al. examined the impact of three (vertical, horizontal, and diagonal) build directions on micro-sized internal channel tolerances and roughness levels of SLM 718 alloy test coupons [226]. Non-destructive XCT technique was employed to scrutinize interior surface roughness, dimensional tolerances, and deviations from the actual computer-aided design (CAD) model. The authors found that vertical build direction produced the highest quality test coupons with the lowest internal surface roughness ($R_a = 8.4 \mu\text{m}$), and inscribed channel diameter of only 3% smaller than the design intent, but the tolerance values of concentricity, total runout, and circularity were lowest [226]. Horizontal and diagonal built test coupons recorded R_a values of $16.1 \mu\text{m}$ and $16.3 \mu\text{m}$ respectively, with the corresponding maximum inscribed diameters 18% and 16% smaller than the actual design intent. The differences in obtained results were ascribed to the inconsistency in heat conduction owing to the different build directions [226]. Furthermore, to the roughness levels and tolerances, the impact of build direction and channel shape were investigated on the pressure and heat transfer measurements of small-scale internal channels [12]. It was revealed that heat transfer performance showed marginal change, whereas, the difference in pressure loss occurred with different channel shapes and build directions [12]. Gui et al studied the generation of internal

defects during the EBM process using the quantitative criterion hybrid parameter S_{dr} to determine the surface quality (even, uneven, and porous) based on the surface flatness [127]. The authors reported that even surfaces are free of internal defects, hence resulting in higher density (7.769 gm/cm^3) [127]. Parts with uneven surfaces contained a large number of spherical pores due to excess heat input, while parts with porous surfaces exhibited irregularly shaped defects and unmelted powders owing to insufficient energy input [127]. The summary of surface roughness with respect to different fabricating conditions is given in Table 2.5

Table 2. 4 Summary of areal/profile surface texture measurement and characterisation from the literature

Layer thickness (μm)	Measurement size (mm)	Form removal	λ_c (μm)	λ_s (μm)	Studied parameter	Sa/Ra (0°, \approx 40°, 90°) (μm)	References
30	FVM: 3.22×1.9	2 nd polynomial fitting	250	-	Sa, Spk, Svk, Sdq, Sfd, Ssk, Rsm	10.69, 16.71, 22.6	[218]
20	Profilometer 10×1	-	-	-	Ra, Rsm	9.2, 15.9, 13.2	[215]
-	FVM: 3×3	Levelling	70	5	Sa, Sq, Ssk, Sku, Sz, Feature parameter	8.26, 14.54, 20.12	[219]
-	Contour GT: 1.26×0.94	-	-	-	Sa, Sq, Sku, Ssk, Sp, Sv, Sz	15.8, 36.8, 54.3	[228]
120-200	FVM: 5.4×5.4 Profilometer: 12.5	λ_f 5 mm	1mm 2.5mm	-	Sdq, Sdr, AFC, Sa	-	[29]
-	FVM: 2.85×2.16 PGI: 0.04	-	2.5/8 mm 2.5/8 mm	8 8	Sa, Sq, Ra, Ssk	14, 13.75, 35	[138]
-	Profilometer	-	2.5 mm	-	Ra	7.5, 29, 14	[229]

Table 2. 5 Summary of surface quality with different fabricating conditions from the literature

Materials Build orientation	Measuring direction	Surface roughness (Ra/Sa) μm	References
316L SS flat-built	Longitudinal Traverse crossed	Ra-6.06 Ra-6.87 Ra-7.44	[230]
316L SS 45-built	Longitudinal Traverse crossed	Ra-14.40 Ra-15.07 Ra-14.83	[230]
316L SS upright-built	Longitudinal Traverse crossed	Ra-16.20 Ra-15.83 Ra-16.50	[230]
IN718 alloy horizontal	As-built	Ra-14	[231]
IN718 alloy vertical	SL CT	Sa-8-17 Sa-10-15	[13]
17-4PH SS scan strategy	Normal Concentric Hexagonal	Ra-9.38 Ra-11.17 Ra-10.64	[199]
TiAl4V (contour)	Upskin-40° Upskin-50° Upskin-60° Upskin-70° Upskin-80° Upskin-90°	Ra-12 Ra-13 Ra-13 Ra-13 Ra-13 Ra-12	[170]
TiAl4V (contour)	Downskin-40° Downskin-50° Downskin-60° Downskin-70° Downskin-80° Downskin-90°	Ra-20 Ra-19 Ra-18 Ra-15 Ra-13 Ra-12	[170]
IN625 alloy (flat)	At 0°	Ra=5.70	[232]
IN625 alloy (inclined)	At 45°	Ra=13.04	[232]
IN625 alloy (vertical)	At 90°	Ra=31.39	[232]

2.4 Metal AM critical process parameters optimisation

The surface quality of an AM part is vital in determining the dimensional accuracy, and post-process treatments, also enhance the functional performance of the final products [233]. The surface quality of a load-bearing engineering part is crucial in industrial applications, with certain applications requiring surface roughness of 0.8 μm or more to avoid premature failure from the surface-initiated cracking [234]. However, it is highly unlikely to improve the surface quality infinitely as it is exceedingly difficult to reduce the surface roughness value to $<1 \mu\text{m}$ by optimizing the LPBF process alone [235, 165]. Despite having huge advantages of indefinite geometrical freedom and minimal material waste, LPBF still suffers from poor surface quality.

It is necessary to have a strong understanding of AM parameters' influence on the resultant surface quality [236]. Having a comprehensive knowledge of AM enables the fabrication of load-critical parts with enhanced surface integrity [236]. For example, the complex thermo physical phenomena that occur rapidly in microscopic scales during laser powder-bed interplay are very crucial as they define the final surface quality of the LPBF parts [35]. The primary factors responsible for the poor surface quality of the LPBF parts are metallurgical defects and surface anomalies such as balling, porosities, spatters, delamination, cracks, staircase effect, and un-melted, partially-melted particles [1,36]. Other secondary factors that result in the inappropriate surface finish are layer-by-layer powder consolidation, powder morphology, rheology, flow characteristics, laser incidence angles, part location, build orientation, poor process resolution, and support remnants [1,35]. The emergence of defects and surface anomalies along with the secondary factors results in poor surface quality, limiting the rapid advancement of LPBF parts applications.

The existing research found that satisfactory surface quality can be achieved by controlling the critical AM process parameters [138,236-238]. Amongst all, the critical LPBF process parameters deemed mainly responsible for surface quality are laser power (LP), hatch spacing (HS), layer thickness (LT), point distance (PD), and exposure time (ET) [235,236, 238]. These five parameters deliver the required energy by a pulsed laser beam to a volumetric unit of powder material (see Figure 2.58a & b). Laser power (LP) is responsible for imparting the required heat input or thermal energy to melt the powder particles which would result in the formation of a minuscule molten melt pool. The duration at which the laser beam is exposed to the surface of the powder bed describes the scan speed (SS). The scan speed of the laser in LPBF systems is controlled by the actuator system, consists of a series of lenses and is reflected by a mirror onto the powder bed

surface or onto the substrate surface. The solidified molten melt pool becomes a melt track layer. LPBF fabricated component comprises thousands of melt track layers which determines the final part quality. It is, therefore, recommended to take immense precaution while selecting the laser power. Lower laser power or higher layer thickness causes insufficient energy input penetration to achieve effective overlap between the melt track layers leading to the formation of a lack of fusion (LOF) hole porosities [1,239,240]. An extremely higher laser power leads to a melt pool evaporation that ultimately increases the surface roughness [1,241]. Similarly, at a relatively lower scan speed, and a fixed or higher laser power, the supplied energy becomes higher, resulting in higher thermal stresses and keyhole porosities [240,242]. The higher energy input results in a greater temperature gradient, this in conjunction with higher thermal residual stresses often lead to thermal cracks [243,244]. Conversely, at a relatively lower laser power and a higher scan speed, the supplied low-energy input is not sufficient to completely melt the surrounding powder particles (by wetting), leading to the formation of the balling [245]. Darsun et al studied the effect of scan speed on the surface quality of SLM 316L steels [246]. The authors found that using higher scanning speeds resulted in detrimental defects, discontinuity, pores and cracks on the surface. This adverse effect can be attributed to the insufficient melting of powder particles caused by a very fast-moving laser beam [246]

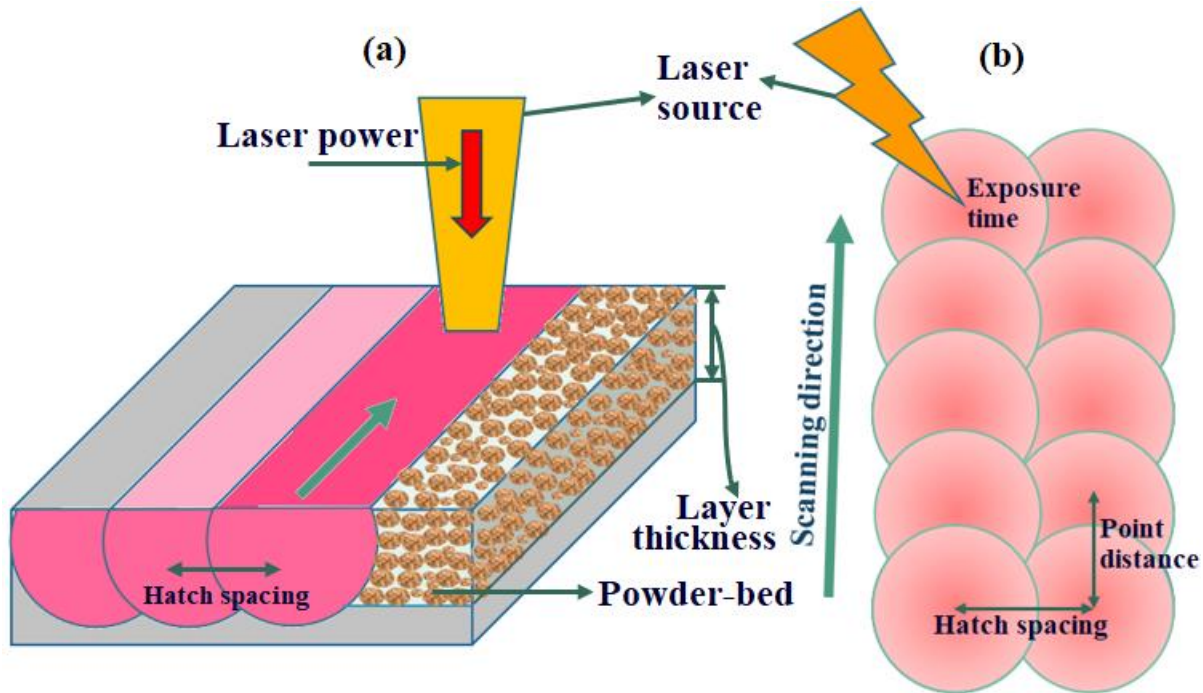


Figure 2. 58 Schematic illustration of LPBF process critical parameters (a) laser power, layer thickness and (b) hatch spacing, point distance and exposure time

The length between the centre points of two successive molten melt tracks is defined as hatch spacing. Overlapping between the two molten melt tracks is determined by the hatch spacing.

The height or the vertical distance between the two successive molten melt track layers along the build direction of an LPBF fabricated component is denoted by layer thickness (LT). Smaller hatch spacing gives rise to a higher degree of overlapping which will be helpful in supplying sufficient distribution of heat energy to melt the powder particles completely. In the meantime, opting for bigger hatch spacing results in lower overlapping (see Figure 2.59).

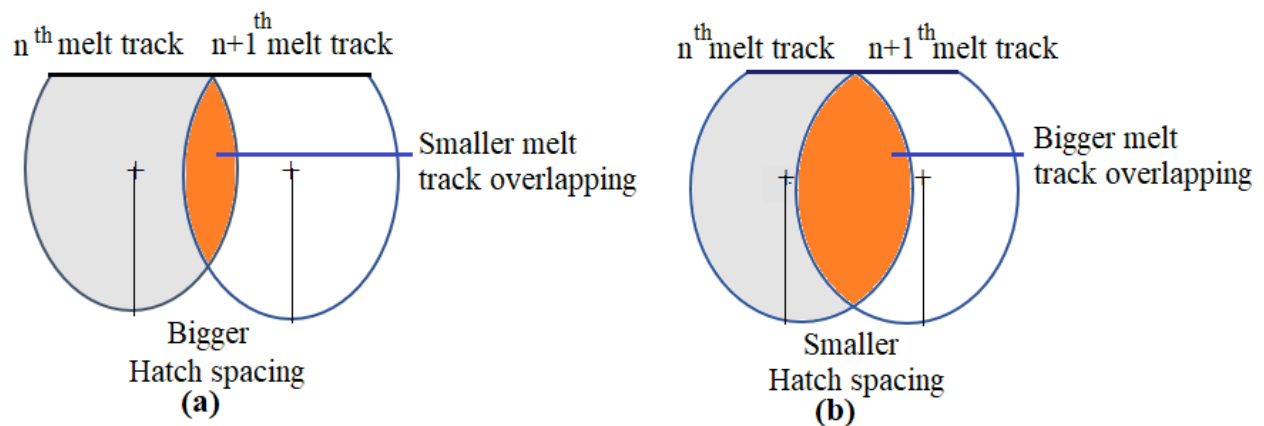


Figure 2. 59 Illustration of hatch spacing with respect to melt track overlapping in LPBF process.

The smaller hatch spacing leads to the formation of thermal cracking caused by the bigger overlapping of melt-track layers, while the selection of higher hatch spacing gives rise to less supply energy input with smaller melt-track overlapping [1]. The combination of a higher temperature gradient along with the larger residual stress often results in cracks in/on the AM part, which finally leads to poor surface finish [1]. Likewise, choosing a lower point distance leads to excessive heating of the melt track layer, while opting for a higher point distance fails to form the melt pool properly, again leading to porosities. In contrast, higher exposure time induces excessive heating, higher residual stresses, and evaporation, whereas lower exposure time lacks the complete melting of the melt pool, causing various porosities [246].

The surface quality of metal AM processes (LPBF, EBM and DED) is significantly affected by the feedstock materials, artefact design, adopted process parameters and post-processing operation [5]. The resultant surface roughness differed between each of these metal AM processes, and layer thickness turned out to have a substantial impact on the resultant surface roughness [5,247]. It is unfair to compare the surface quality of DED with EBM and LPBF irrespective of the parameters used because the higher deposition rate induces a larger molten melt pool size in DED leading to higher surface roughness [5, 247]. Casalino et al. studied experimental and statistical optimization concerning the microstructure, mechanical properties and surface quality of LPBF maraging steels [37]. Authors reported parts with a higher relative density of 99% resulted in low porosities, and the statistical optimization found the best properties are achieved when the parts are built with laser power higher than 90W and 220 mm/s scan speed [37]. Sinico et al. optimized DOE parameters for layer thickness (LT) 120 μm fabrication of M789 maraging steel using high-speed LPBF to study the surface quality and enabling productivity $>30 \text{ cm}^3/\text{h}$ [248]. Although the authors achieved a higher theoretical productivity rate of $>35 \text{ cm}^3/\text{h}$ at 99.5% relative density the obtained roughness value of 38 μm is well above the usual LPBF average Ra value range of 5-18 μm [248]. Qiu et al. studied the surface structure and porosities of LPBF concerning different scanning speeds and layer thicknesses [248]. A fixed layer thickness of 20 μm and scan speeds below 2700 mm/s resulted in lower porosities and acceptable surface quality with Ra values of 5-13 μm while increasing the layer thickness to 40 μm and above (60 μm) resulted in poor surface structure caused by significant porosities and unacceptable Ra values of $\sim 22 \mu\text{m}$ and 60 μm respectively [249]. Aqilah et al. studied the effect of process parameters on 316L SS surface roughness and statistical analysis using signal-to-noise (S/N) ratios and analysis of variance (ANOVA) to obtain an optimal

set of LPBF parameters [235]. The authors found laser power was the most significant parameter that affected the surface roughness, and based on statistical regression analysis the optimum obtained values for predicted Ra was 5.03 μm and S/N ratio -18.01 respectively [235]. Tian et al. presented a parametric optimization and statistical ANOVA of LPBF parameters laser power, scan speed, layer thickness, and inclination angle on surface roughness [236]. Based on their experimental and statistical analysis, the Ra 20-28 μm of up-skin was influenced by laser power, inclination angle and layer thickness while down-skin Ra 23-45 μm was mostly affected by laser power and inclination angles. Furthermore, the shape of the molten melt pool and staircase effect was found to define the up-skin surface, whereas adhered un-melted, partially-melted particles determine the down-skin surface roughness [165,236]. Bacchewar et al. examined the statistical modelling, central rotatable composite design (CCD) DOE optimization, and ANOVA to correlate the impact of SLS process parameters on surface roughness [213]. The predicted and experimental Ra values of the up-skin surface are found to be 8.02 \pm 5.20 μm and 8.16 μm respectively. Similarly, predicted and experimental Ra values for down-skin surfaces are 3.76 \pm 2.93 μm and 5.65 μm respectively [213]. ANOVA revealed build orientation displayed a significant impact on surface roughness. Also, layer thickness and laser power played a major role in achieving higher roughness of down-skin surfaces. It was found that the predicted results were in good agreement with experimental findings, especially in the range of 10°–70° [213]. Galati et al. conducted physical experiments to verify the statistical full-factorial DOE surface roughness prediction model corresponding to various inclinations angles including up-skin and down-skin surfaces and anomalies of the EBM ad-hoc artefact [212]. The authors adopted profile (Ra, Rq, Rz), and areal surface texture parameters (Sa, Sq, Sz) to interpret the inter-dependency of sloping angles (30°–55°) and surface roughness [212]. The Ra ranged between 14.9 μm –23 μm , and the Sa ranged between 18 μm –55 μm , while both profile roughness and texture followed a similar trend while distinguishing the overall EBM surface morphology. Surface orientation and sloping angles displayed a significant impact on surface roughness, and the statistical model turned out to be robust and consistent with the experimental observations [212]. Gui et al. adopted 5 different machine-learning techniques to examine the parametric optimization of internal defects concerning the surface morphology of EBM carbon steel S30C alloy [227]. The authors classified the surface quality based on the flatness of the surface by determining a quantitative criterion, Sdr < 0.015 for an even surface; Sa \geq 80 μm for an uneven surface; Sdr \geq 0.015 and Sa < 80 μm for a

porous surface respectively [227]. From their support vector machine with the highest model performance they predicted the optimal set of EBM parameters concerning internal defects are current = 2.5–10 mA, scan speed = 200–1000 mm/s, line offset = 0.11–0.25 mm, or current = 2.5–10 mA, scan speed = 200–750 mm/s, line offset = 0.27–0.33 mm [227].

Based on the critical analysis of existing literature on LPBF of different types of steels, three LPBF processing windows have been proposed such as lower processing window, higher processing window and finally optimum processing window (see Figure 2.60). for a brief overview of LPBF processing windows, and their impact on final part quality. This proposed LPBF processing window gives an overall idea of the role of the most important parameters namely laser power, scan speed, layer thickness (LT), hatch spacing (HS), and significance of atmospheric (ATM) pressure on the final part quality. Also, it is believed that this processing window label would be helpful in the selection of the optimum or right/appropriate combination or set of process parameters to achieve superior final part quality.

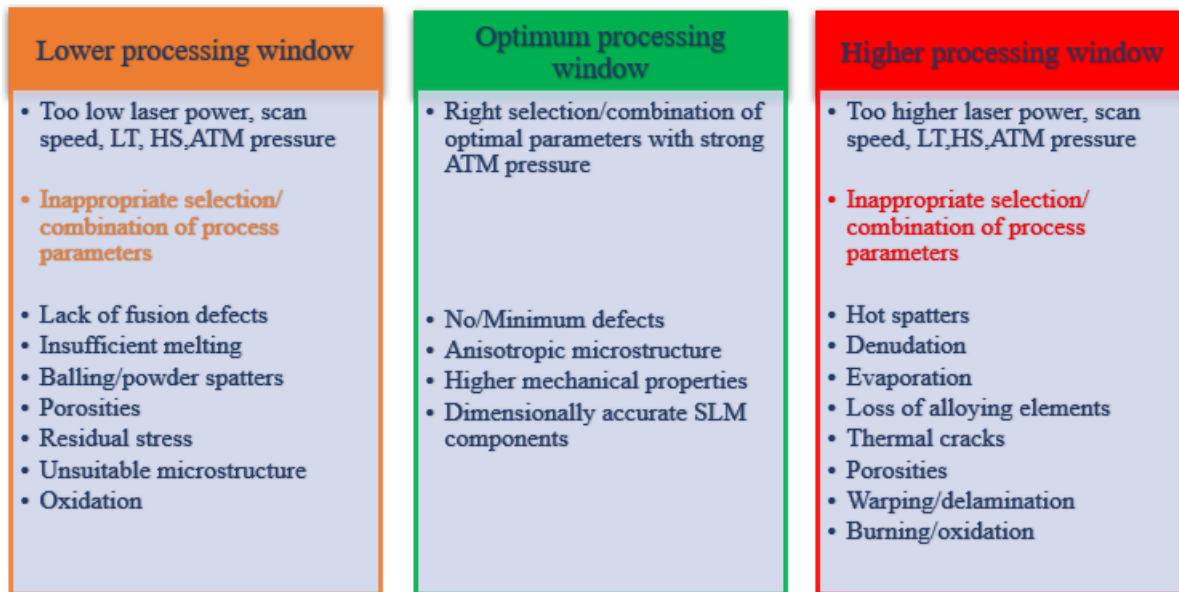


Figure 2. 60 Label of LPBF processing windows and their impact on final part quality

2.4.1 Taguchi design of experiments

Taguchi method is generally referred to as a robust powerful statistical design tool in which the modified or standard design of experiments is employed to enhance the quality of manufactured products by identifying the best or right parametric combination of the control factors [250,251]. The results obtained from the Taguchi method may not be optimal, but the process is undoubtedly improved when these results are implemented [250,251,213]. Additionally, Taguchi's robust

design increases the quality of final products by minimizing the impact of noise factors on the performance of the product. This approach tends to help save money and time by reducing a vast number of iterations, the response variation, and limiting the time-consuming trial-and-error method of conducting experiments within the permissible limit of control factors and levels [250]. Finally, Taguchi's robust design mainly depends on the two most powerful tools, such as orthogonal arrays to define the DOE, and the S/N ratios to measure the quality [251].

Taguchi method generates special orthogonal arrays, which are used to analyse the results utilizing signal-to-noise (S/N ratios) and to ensure a design is unaffected by the influence of uncontrollable factors. These created orthogonal arrays give an idea about what factor levels should be chosen every time to conduct the fewest experimental runs. It is imperative to focus only on those fewer runs essential for the analysis. The S/N ratio combines a performance characteristic with its sensitivity to noise factors to measure the quality of a design. In addition, S/N plots are used to determine the levels that keep the process at its target value, in a visual way [213,251]. The signal-to-noise (S/N) ratios are the logarithmic functions used to identify the dominant control factor or optimal parameter settings, which help to analyse the data and predict the optimal responses. The Delta value represents the difference between the maximum and minimum S/N ratio for the levels of each factor, and the significance of a controlling factor, with a higher Delta value indicating a greater significance of that specific control factor. The S/N ratios in this research are calculated with the primary objective using the "smaller the better" given by the logarithmic relation shown in Equation 7 [213,250,251].

$$n_s = -10 \log_{10} \left[\left(\frac{1}{n} \right) \sum y_i^2 \right] [dB] \dots\dots\dots (7)$$

where 'n_s' - (S/N) ratio-calculated using the experimentally obtained results (surface roughness Sa, in this research), 'y_i' - an experimentally observed value of 'ith' experiment, and 'n' - the number of times each experiment is repeated [250].

2.4.2 Statistical analysis of variance (ANOVA)

The ANOVA is the primary step in analysing factors that impact the given data set. ANOVA is one of the statistical analysis tests used to identify whether there is any statistically significant difference between two or more categorical groups at the same time to determine whether an interrelationship exists between them. [252,253]. The result of ANOVA (F-statistic or F-ratio) allows analysing the multiple groups of data to identify the variability between samples and within the samples [253]. A one-way ANOVA evaluates the impact of a single factor on a single response

variable, whereas a two-way ANOVA examines the impact of two independent variables [252]. The main purpose of employing statistical ANOVA in chapter 4 is to analyse the statistical significance of the impact of different control factors and their interactions on the experimentally obtained surface roughness values [212]. A comprehensive statistical ANOVA is carried out to evaluate the impact of inclinations angles, build orientations, and the type of surfaces on the resultant surface roughness [211,212]. The significance threshold or risk level is usually set at $\alpha=0.05$.

2.5 Microstructure, mechanical properties and post-processing treatments

2.5.1 Microstructure characteristics of metal AM components

Microstructure evolution during LPBF is not trivial. It is impossible to attribute the microstructure characteristics of a specific type of steel to all other types of steel. However, it is necessary to understand the general aspects of microstructure evolution in the LPBF process of steels for further research. The microstructure evolution of the metal AM processed steels was simulated, and experimentally studied in both horizontal and vertical planes [254-256]. Tan et al. studied the microstructure evolution of the LPBF process of maraging steels in both horizontal and vertical planes [256]. The authors noticed massive submicron-sized hexagonal cellular grains uniformly distributed at the centre, and needle-shaped elongated grains prevalent at the boundaries of the melting tracks (perpendicular to the scanning direction) [254]. These microstructure characteristics would form in response to the instant melting and rapid solidification at higher cooling rates during LPBF processing of maraging steels (see Figure 2.61a). Heat input drops exponentially in a horizontal plane as the solidification rate (R) rises. This is because the temperature-dependent thermal flux generated by laser fluence would be substantially higher at the melt tracks centre, in contrast with the thermal flux at the boundaries due to heat dissipation [256]. Owing to the simultaneous action of higher heat dissipation and faster cooling rate, the temperature of liquid metal (T_L) at this point reaches well below the melting point (T_M) at the centre, and the degree of undercooling ($\Delta T = T_M - T_L$) is sufficiently high enough for the new grains to nucleate in random orientations [256]. Furthermore, the growth rate of the crystal nucleus is consistent in all directions resulting in the easy formation of equiaxial crystal grains. The equiaxial crystals exhibit hexagonal cellular structures as seen in Figure 2.61b. The formation mechanism of various crystals morphologies in a vertical plane is shown in Figure 2.61c. Planar solidification structure could be observed at the bottom of the molten melt pool (G is the maximum & $R \sim 0$). As G/R ratio decreases

with the gradual increase in R , ascending from the bottom of the melt pool in layer stacking/or building direction cellular dendritic structure is visible. A further decrease in G/R value to reach the middle of the molten melt pool, the cellular structure is prevalent followed by a finer/coarser equiaxed crystal that is predominantly evident at the boundaries of the molten metal pool [37,254-257].

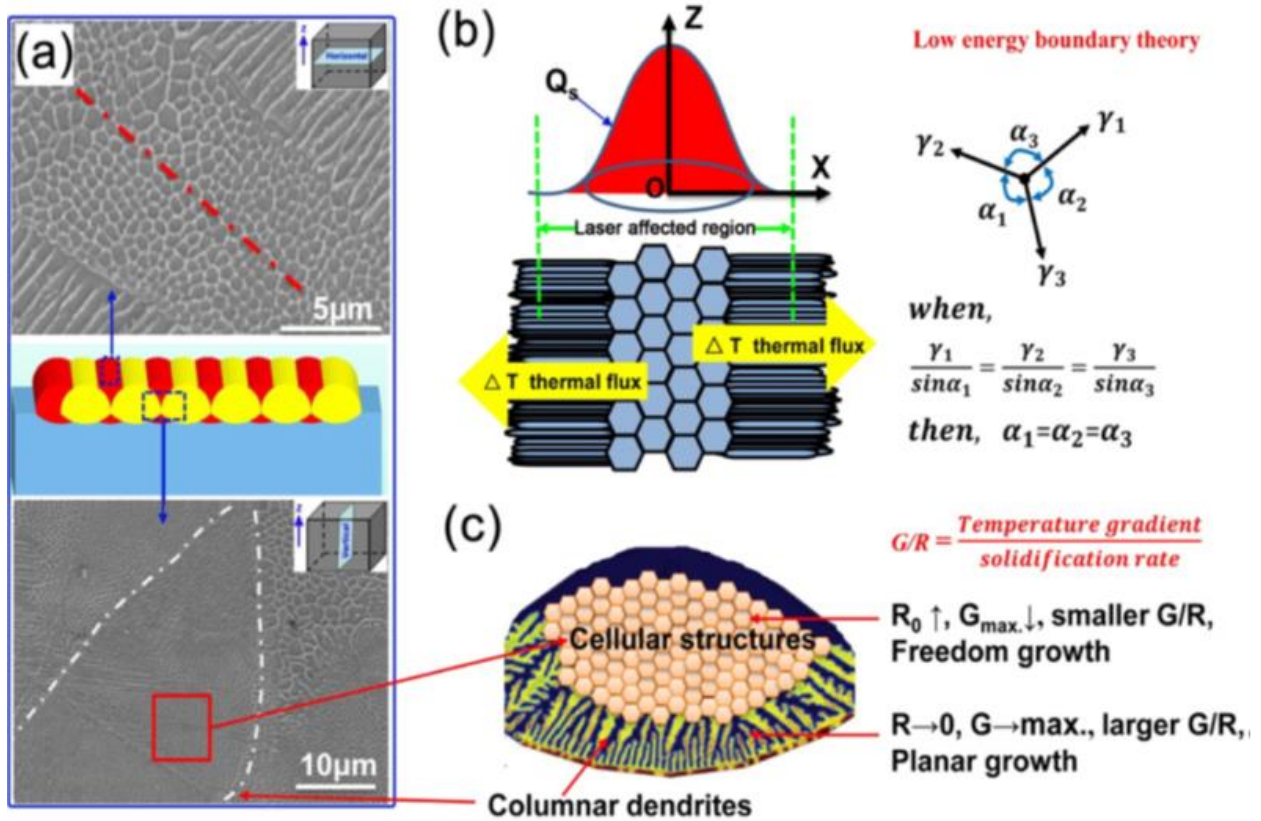


Figure 2. 61 Microstructural evolutions of LPBF fabricated specimens: (a) the characteristic morphologies of the horizontal and vertical cross-sections; (b) the schematics and formation mechanism of the cellular crystals and elongated acicular crystals; (c) schematics and formation mechanism of the microstructures in the molten pool and overlapped area [256].

Boes et al. reported the heterogeneous dendritic microstructure consisting of low thermal gradients induced fine equiaxed grains, and the elongated dendrites were influenced by higher thermal gradients at lower solidification rates [258]. Microstructures of LPBF-built 316L steel parts characterized by the columnar grains of austenite with intercellular segregation of Mo, Cr and Si alloying elements, resulting in the formation of non-equilibrium ferrite [259,260]. The occurrence of sub-grain cellular structure (less than 1 μm) can be mainly related to the micro-segregation of primary elements such as Mo, V and C, due to the Marangoni convection and the difference in

temperature between the inside and outside of the molten metal pool [126]. Columnar grains with ferrite content ~68.8%, and grain orientation predominantly in $\langle 001 \rangle$ direction with an average grain length-to-width ratio of 11.5:1 has been reported during the LPBF process of duplex stainless steels [261]. The microstructure of the LPBF process of duplex steels was largely composed of ferritic with small traces of austenite and nitrides (presumably Cr₂N) nucleating at grain boundaries. It is worth noting that the growth morphology of austenite is along the grain boundaries or of the Widmanstätten type [261].

A needle-shaped nano precipitate martensite with a width of ~200 nm and 15–50 nm in length was observed at 450–510°C in LPBF processing of maraging steels [256,262]. A very fine microstructure ($< 2\mu\text{m}$ or less) mainly consisting of $\alpha\text{-Fe(M)}$ phase (M, Cr, Ni, Mo) formed during the LPBF process of nickel-molybdenum alloy steels [263]. The microstructure of the LPBF-built hot work steel is characterized by $\alpha\text{-Fe}$ dendritic cells decorated at the grain boundaries by the carbon-rich $\gamma\text{-Fe}$ regions [264]. The finer microstructure with evenly distributed grains of the 316L stainless steels produced by LPBF allowed for better mechanical properties without sacrificing its ductility [260]. A schematic illustrating typical microstructure at various length scales formed during the LPBF process of 316L SS is shown in Figure 2.62a. Wang et al. accredited this combined property to the superior nature of the microstructure composed of solidification cells, low & high angle grain boundaries, dislocations, and oxide inclusions [260] (Figure 2.62b-h).

LPBF process of austenitic SS is almost extensively restricted to 316L SS and 304L SS. 316L and 304L SS are in a composition range where the solidification front is dominated either with a primary (δ) ferritic phase or with a primary austenitic (γ) phase. LPBF processing of stainless steels exhibits fully refined austenitic microstructure, with the columnar solidification grains $\sim 1\mu\text{m}$ diameters or less [67,265,266–268]. The number of solidified columnar grains may vary from tens and/or hundreds that are very similar to the crystal orientation, collectively forming a single austenite grain i.e. a material volume responsible for high-angle grain boundaries (Figure 2.62b&c.) The grains formed in as-built LPBF SS samples are finer than those of conventional processes [114,110,266–268]. LPBF process of this type of steel is fully austenitic and there is no conclusive evidence of any solid-state phase transformations [114,266,269–271]. The intercellular regions show an enrichment with Cr and Mo, which are, however, not sufficient to stabilize the ferrite [268,260] (Figure 2.62i). A strong fibre texture with $\langle 001 \rangle$ crystallographic direction aligned along the build direction (i.e. against fast heat dissipation direction) was revealed during

LPBF process of steels [114,271]. The strong texture is caused by the $\langle 001 \rangle$ crystallographic direction, as it is the fastest-growing direction in the solidification of cubic metals, and hence dendrites or cells grow aligned with the temperature gradient [272].

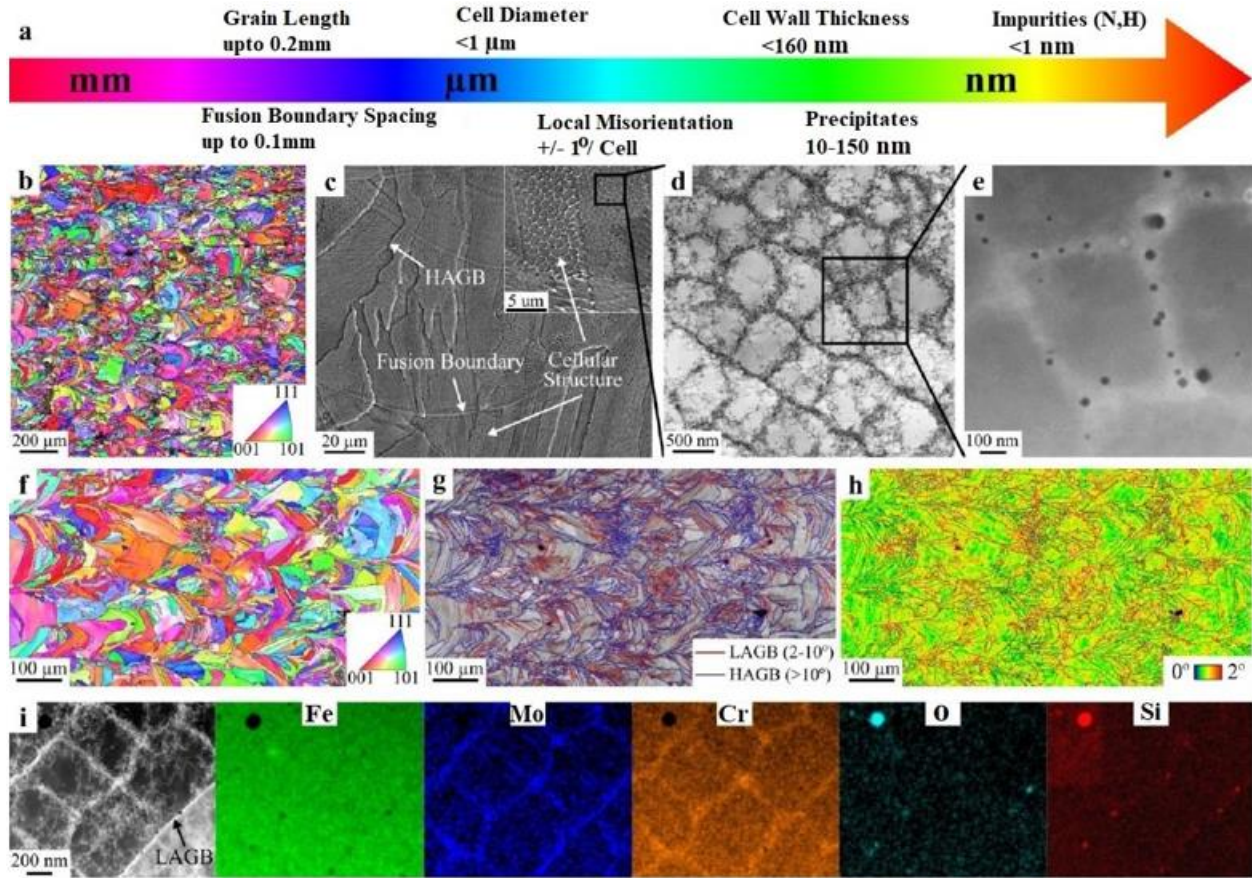


Figure 2. 62 Schematic illustration of the typical LPBF microstructure of 316L SS. (a) label of microstructure at various length scales, (b) A electron backscatter diffraction (EBSD) inverse pole figure (IPF) showing grain orientations, (c) SEM images of fusion boundaries, high-angle grain boundaries (HAGBs), solidification cellular structures, (d) TEM images of solidification cells, (e) High-angle annular dark-field (HAADF) scanning TEM image (STEM) of the solidification cells of d, (f) EBSD with a 1- μm size, (g) EBSD image of superimposed HAGBs and low-angle grain boundaries (LAGBs). Legend representation, HAGBs ($>10^\circ$) coloured in blue and LAGBs ($2-10^\circ$) coloured in red. Fraction of HAGBs and LAGBs is $\sim 59\%$ and $\sim 41\%$, (h) Kernel average misorientation (KAM) map of local misorientation across the individual grain, (i) HAADF STEM image of segregated Mo and Cr alloying elements into the solidified cellular structure and LAGBs, while EDS confirms the corresponding Fe, Mo, and Cr. Also, EDS confirms that these particles are predominantly rich in Si, O, and Mn [260].

Z. Sun et al. employed a modified laser scan strategy by adopting relatively high laser power with smaller hatch spacing to improve the mechanical properties of LPBF-processed 316L SS [273]. This modified approach leads to the formation of a new $\langle 110 \rangle$ crystallographic texture along the build direction instead of a regular $\langle 001 \rangle$ texture. The modified $\langle 110 \rangle$ crystallographic grain orientation favours the twinning effect under deformation, as a result of this the material experiences higher strain hardening rates which profits in achieving superior mechanical properties (ductility and UTS) [273]. H. Sun et al. moved a step forward to show that it is possible to regulate crystallographic texture by carefully controlling the process parameters during the LPBF processing of 316L steel. They reported crystallographic lamellar microstructure $\langle 100 \rangle$ and $\langle 110 \rangle$ oriented grains along the build direction [274]. As already mentioned texture control could be a reliable tool to control anisotropic microstructure in yield and tensile strength [275]. However, the strain hardening behaviour is predominantly dependent on grain morphology, resulting in anisotropy in ductility despite the reduced crystallographic texture [275]. LPBF process of maraging steels displayed different solidification microstructure with cellular/dendritic sizes $\sim 0.3\text{--}2\text{ }\mu\text{m}$ as compared to conventional built maraging steels [276,277]. The cellular structure in LPBF processing of maraging steels is a result of microsegregation during solidification which enriches some of the alloying elements in the inter-dendritic regions. The LPBF built H13 tool steel revealed the solidification cells or dendrites in the microstructure with retained austenite evident in the inter-dendritic regions. The observed size of the cells/dendrites was in the range of $0.5\text{ }\mu\text{m}$ - $2\text{ }\mu\text{m}$. It is worth noting that there is only limited information available in the literature regarding the crystallographic texture of H13 tool steels and maraging steels, which is most likely related to the very weak crystallographic texture [1,278].

As-built LPBF processed 17-4 PH steel displayed a high fraction of austenite phase or even fully austenitic microstructure. Facchini et al. reported LPBF of 17-4 PH stainless steel contained 72% austenite and 28% martensite [279]. In addition, the presence of little traces of Nb-rich carbides was unsure [123]. TEM confirms the presence of retained austenite between martensite slabs. LPBF process of 17-4 PH steels (including austenitic, martensitic and ferritic steels) usually display strong crystallographic grain orientation in $\langle 001 \rangle$ direction aligned along the building direction (z-axis) [280,281].

LPBF process of twinning/transformation-induced plasticity (TWIP/TRIP) steels: high manganese steel was investigated by [282], the microstructure consisted of mainly austenite, together with α -

and ϵ -martensite, along the small quantity of Mn segregation was evident in comparison with cast ($X_{30}Mn_{22}$) steels [1,282].

LPBF synthesized mechanically-alloyed oxide dispersion-strengthened (ODS steels) PM2000 steels revealed a homogeneous distribution of retained oxides. However, the average sizes of these retained oxides were in the range of 48nm –61 nm, which are significantly coarser than the conventionally-produced PM2000 steels (30 nm) [283]. A similar microstructure wholly ferritic in nature was reported during LPBF built mechanically alloyed PM2000 or MA956 steels [284-286]. The fully ferritic microstructure exhibited strong fibre texture with the $\langle 001 \rangle$ direction parallel to the build direction. A uniform distribution of both finer and coarser oxides was seen in the ferritic microstructure [284]. The presence of both finer and coarser oxides could be attributed to the agglomeration of nanometre-sized oxides [286]. The strong crystallographic texture results in the anisotropic mechanical performance of LPBF-processed ODS steels [286]. The crystal structure of the oxides is sometimes represented by $Y_2Ti_2O_7$ or $Y_4Al_2O_9$ [269]. LPBF fabrication of Fe–14Cr–1W powder mechanically alloyed with Y_2O_3 , and TiH_2 reported a similar microstructure to the one described above for the LPBF process of PM2000 [287].

2.5.2 Tensile properties of metal AM components

The present studies on the mechanical properties of the LPBF process of steels are mostly concentrated on evaluating hardness, tensile performance and fatigue properties. Tensile and hardness properties are summarized in Table 2.6 A schematic overview of the basic mechanical properties of most common steels used in LPBF processes and conventional processes is shown in Figure 2.63. This figure intends to provide a broad overview of the results reported in the literature, however it is not applicable for all classes of steels, and often depend on the material properties and LPBF processing conditions [1].

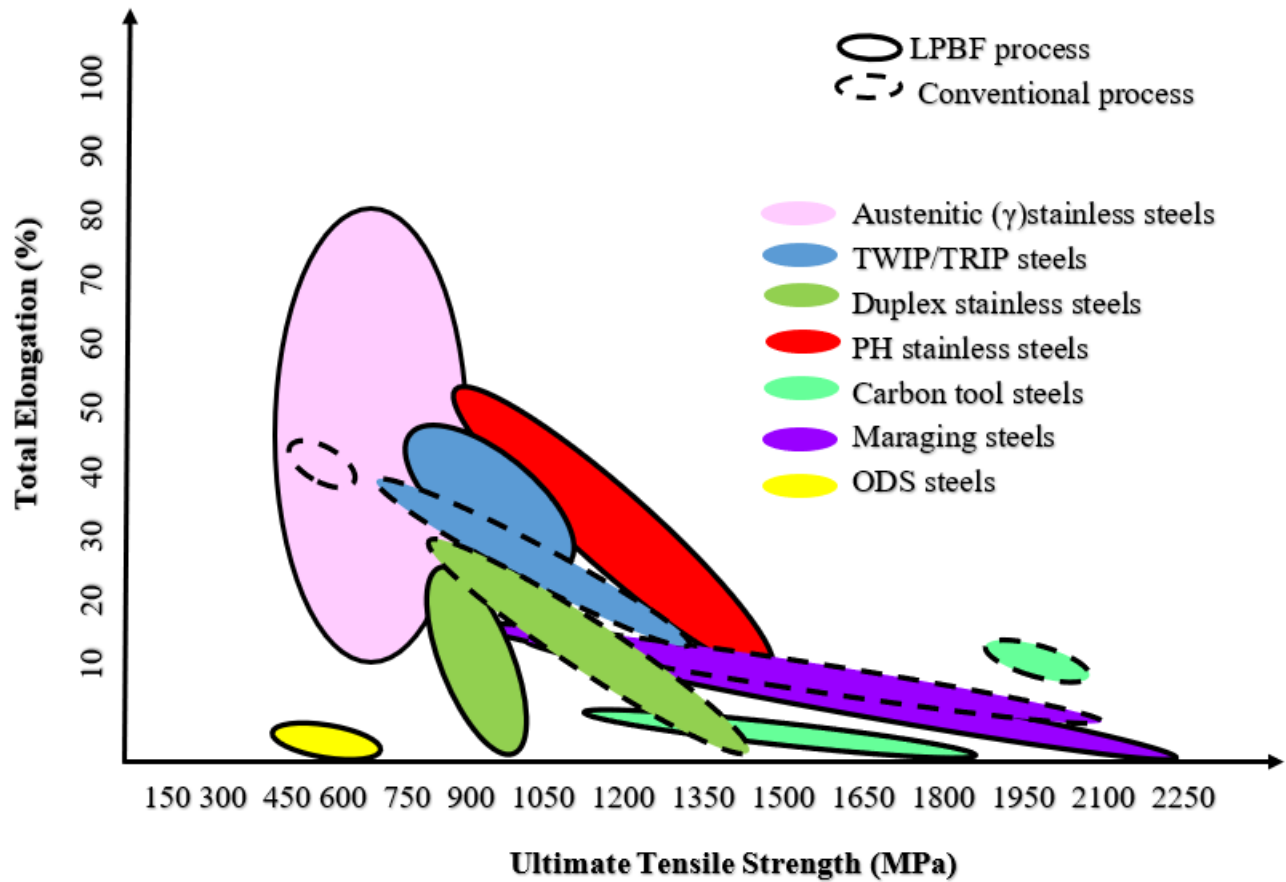


Figure 2. 63 Schematic illustration of overview of mechanical properties of LPBF processed and conventional processed steels. Steel type is indicated by the field colour, whereas the field border represents the process type [1].

From the existing literature, average Vickers hardness values for LPBF processed steels range from 408-900 HV, which is certainly higher than wrought materials [88,261]. LPBF produced tool steel presented the refined microstructure comprised of low martensite phase and a high quantity of fine carbides and the alloying elements (V, Mo, C) that are much more uniformly scattered in the material as compared to the as-cast state which resulted in higher hardness values [1,88]. The microstructure of LPBF-built samples determines the mechanical properties and the difference in tensile properties along various directions is mainly due to the easy introduction of metallurgical defects into the bonding area between two adjacent melt track layers [1]. The tensile properties of the LPBF fabricated samples along the vertical direction are inferior, as compared to those samples built in the horizontal direction [288]. To obtain the higher tensile properties, besides the position of the sample in the horizontal direction, laser fluence also plays an equally important role.

A low laser fluence (104.17 J/mm^3), unsurprisingly, resulted in higher porosities (lack of fusion holes or crater-like voids). The porosities act as the main sites for crack initiation triggering brittle fracture with limited plastic deformation, causing cracks propagation under tensile loading conditions (see Figure 2.64a). It was reported that using optimized energy density (125 J/mm^3 , 156.25 J/mm^3), the part density reached to its maximum, and the obtained microstructure displayed decently refined dimples with numerous grain boundaries that would block dislocations movements causing the material to resist deformation resulting in higher yield strength and tensile strength (see Figures 2.64b&c) [103]. It is worth noting that LPBF fabricated steels are strengthened without losing their ductility, unlike work hardening which improves tensile strength by sacrificing ductility. Adapting excess energy density (178.57 J/mm^3) resulted in decreased toughness due to the high degree of overheating of the molten melt pool, causing larger and shallow dimples with lower resistance to dislocations (see Figure 2.64d) [103,289].

As a result of the finer microstructural texture, the mechanical properties of LPBF-manufactured steels have been improved. Additionally, a refined microstructure offers greater resistance to sliding and other plastic deformation mechanisms, such as dislocation motions [1,100]. Owing to the high density of low-angle grain boundaries, and the fine cellular microstructures associated with LPBF processing, the yield strength (YS) of 316L stainless steel is greatly improved [81]. The unique development of crystallographic lamellar microstructure (CLM) via the strengthening LPBF-built 316L steel resulted in higher YS, ultimate tensile strength (UTS), and significantly higher ductility [84]. The grain refinement of the nano-cellular structures, the presence of nano-size carbides along with the negative residual stress resulted in superior YS, UTS and higher ductility [82], in LPBF steels as compared to traditional processes such as casting, extrusion and laser engineered net shape [1,85,86]. Similar higher yield strength and/or better ultimate tensile strength and compressive strength values (CS) [YS=455-640 MPa, UTS=579-2100 MPa, CS=3796 MPa] have been achieved in LPBF fabricated steels [88,89,289]. In some cases, higher elongation [86,87], and higher toughness are reported, the reason for this is attributed to the stress-induced austenite-to-martensite transformation [1,90].

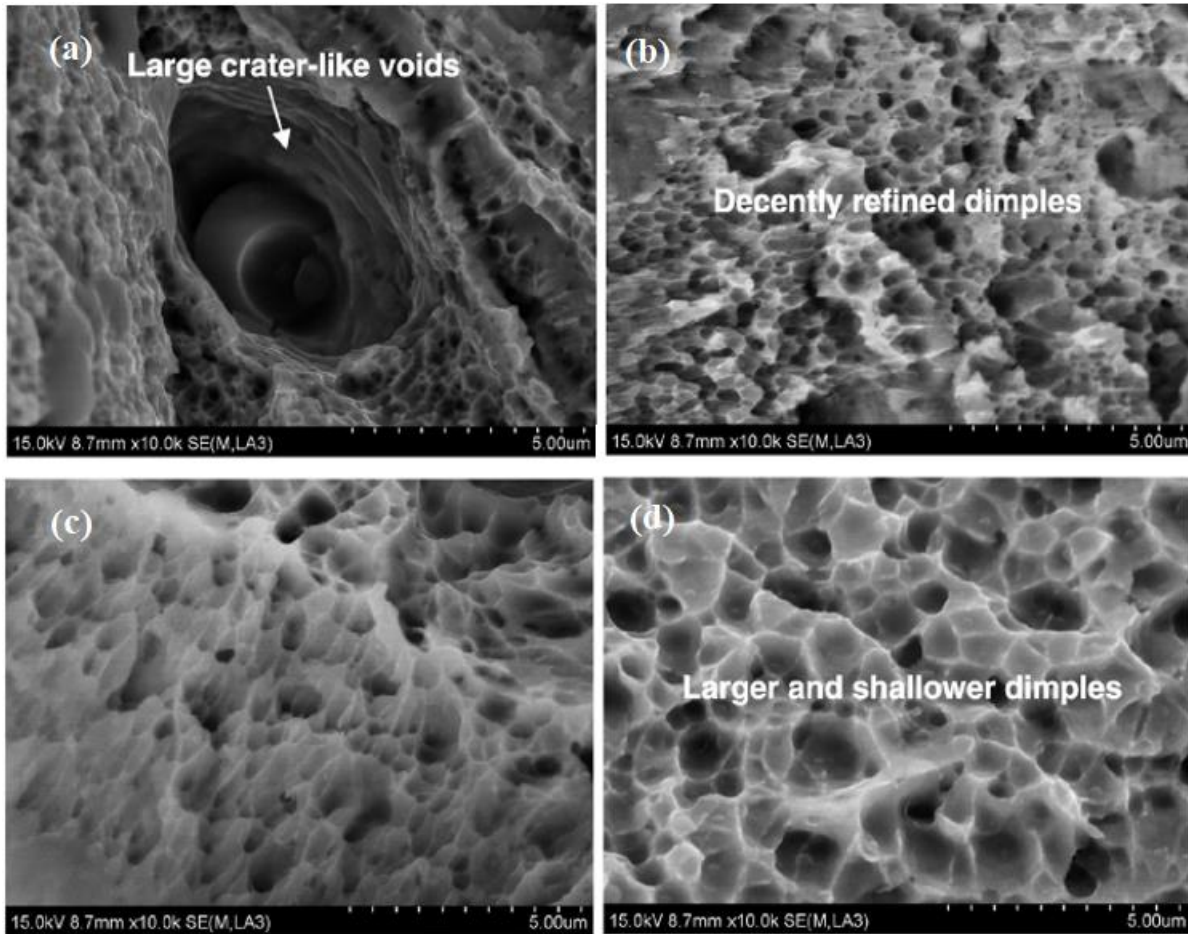


Figure 2. 64 Typical SEM images taken from the tensile fracture surfaces of LPBF -processed 316L specimens at different laser energy densities of (a) 104.17 J/mm^3 ; (b) 125.00 J/mm^3 , (c) 156.25 J/mm^3 and (d) 178.57 J/mm^3 [103].

It is well acknowledged that LPBF-processed stainless steels often display superior YS and UTS [114,260,267,268,275, 290-292] as compared to conventionally manufactured steels. The reported YS values and UTS values from the literature show high variability and are in the range between 350–600 MPa, and 480–800 MPa respectively. Typical YS and UTS values for conventionally processed stainless steels lie in the range of 230–290 MPa and 580–590 MPa [293]. Additionally, LLPBF-processed steels display a higher yield-to-tensile strength ratio [114,267,290,292]. However, some of the researchers reported lower fracture toughness and elongation to fracture; as low as 12% for LPBF-built stainless steels as compared to the wrought material typically; 40–50% [267,294]. The majority of the studies reported a higher elongation to failure and fracture toughness up to 67% [114,260,268,275,292,295]. The higher yield strength and tensile strength have been related to the finer microstructure and dislocation substructure as per the Hall-Petch

relation [260,268,275,291]. Also, in LPBF-built steel components, the defects in the microstructure (brittle phases/inclusions, porosity) have a strong negative impact on the elongation to fracture. LPBF fabricated duplex SS 2507 resulted in much higher YS and UTS, along with a moderate elongation at fracture (~8%), and a ductile fracture mode compared to conventionally produced ones. The higher mechanical strength and average ductility of the LPBF-built sample were the results of exclusive ferritic microstructure [296]. Unlike austenitic stainless steels, TRIP/TWIP steels are regarded as fully austenitic metastable steels which exhibit transformation-induced plasticity or twinning-induced plastic deformation [1]. Haase et al. studied the LPBF process of high-manganese steel (X30Mn22) [282]. From their study it was revealed that the TRIP/TWIP effect was certainly functional when subjected to tensile deformation of the material, and also described its anisotropy arising from the strong (LPBF-typical) fibre texture. The reported YS and UTS were better in all the directions as compared to conventionally processed standard steels (302–416 MPa vs. 275 MPa and 906–1065 MPa vs. 894 MPa, respectively), but the elongation at fracture was lower (24–31% vs. 52%). These types of steels offer high work hardening ability which makes them attractive for applications where high energy absorption, high strain hardening rates, and high ductility are required [282].

Owing to the presence of martensite and austenite in different proportions in 17–4 PH steel microstructure, hardness and mechanical properties of LPBF processed 17-4 PH steel dispersed over a wide range of values. It is worth noting that lower mechanical properties were not only due to the presence of a softer austenite phase but also due to the precipitation reaction that takes place in martensite during ageing [39,297,298]. Overall LPBF process of 17-PH steels is typically softer and less strong than wrought and age-hardened materials [299]. In general, the mechanical properties of LPBF maraging steel are comparable to conventionally produced steel materials, but not entirely identical. LPBF-produced maraging steels display equal or slightly better YS and UTS as compared to conventional ones despite the finer microstructure resulting from the LPBF process [1,300,256,301].

Hardness values recorded for LPBF-produced H-13 tool steels range from 570HV-680HV, (and marginally higher 745HV when measured in the skin area [302]) [126, 303,304]. These values are close to or even superior to as-quenched wrought H13 steels, contemplating the fully-martensitic state. Most of the LPBF maraging steels reported much lower YS and UTS values because of

severe brittleness, this state easily gives away without any resistance to the applied loads resulting in the premature failure of the tensile samples [1,302-307].

The strong crystallographic texture $\langle 001 \rangle$ of LPBF processed ODS steels lead to an anisotropic mechanical behaviour, i.e, ductile fracture when strained in the build direction, but brittle trans-granular fracture when strained perpendicular to the build direction [284]. Employing additional post-process heat treatments, the tensile strength numbers reached somewhat closer/equal to the conventionally produced ODS steels [284]. Due to the wide range of technological parameters involved in LPBF process, which result in the formation of an anisotropic microstructure, variation in the part densities, and the mechanical properties of steel samples, which are available in a variety of grades depending on specific applications, differ from one another [1,277].

Table 2. 6 Tensile and hardness properties of metal AM from different literature

Materials	Condition	Hardness (HV)	Yield Strength (YS)	Ultimate tensile Strength (UTS)	Elongation (%)	Reference
Maraging Steel (MS)	LPBF	—	~915	~1165	~12.44	[256]
	LPBF aged	—	~1967	~2014	~3.28	[256]
	LPBF solution	—	~962	~1025	~14.40	[256]
	LPBF solution aged	—	~1882	~1943	~5.60	[256]
316L stainless steel (SS)	LPBF	—	455	579	~50	[256]
FeCrMoVC tool steel	LPBF	~900	—	—	—	[88]
316L SS	LPBF $\Psi = 0$	—	~494	~640	~56.7	[89]
	LPBF $\Psi = 45$	—	~498	~606	~59.9	[89]
	LPBF $\Psi = 60$	—	~536	~601	~62.7	[89]
	LPBF $\Psi = 90$	—	~489	~548	~43.7	[89]
316L SS	LPBF	~281	—	~590	~21.1	[103]
Austenitic SS	LPBF single	—	~346	~921	~69.9	[84]
	LPBF CLM	—	~387	~924	~67.5	[84]
316L SS	LPBF low power	~241	~500	~625	~47	[308]
ASTM A131 steel	LPBF 250mm/s	—	~938	~1037	~4.5	[104]
	LPBF 300mm/s	~241	~850	~1050	~4.75	[104]
316L SS	LPBF	—	~1100	~1200	~20	[83]
316L SS	LPBF	—	~517	~633	~74	[85]
304L SS	LPBF	—	~485	~712	~61	[86]
Invar 36	LPBF	—	~350	~400	~64	[82]
316L SS	LPBF heat treated(HT)	—	~550	~620	~90	[82]
17-4 PH SS	LPBF opt parameters	~355	~650	~940	~4	[309]
17-4 PH SS	LPBF	~395	~750	~950	~3.6	[309]
17-4 PH SS	LPBF	~475	~940	~1150	~2.8	[309]
Maraging Steel	LPBF	—	~750	~1200	~17	[310]
MS-10%WC	LPBF	—	~650	~1000	~7.5	[310]
17-4 PH GA	LPBF 60 μ s time	—	~1116	~1358	~5.1	[311]
17-4 PH WA	LPBF 80 μ s time	—	~500	~990	~3.3	[311]
316L SS	LPBF	~202	—	~750	—	[312]
	LPBF HT@ 650C 2hrs	~210	—	~700	—	[312]
316L SS	LPBF	~209	—	—	—	[313]
	LPBF HT	~215	—	—	—	[313]
CLAM steel	LPBF HT HIP	—	—	~966	~5	[313]
	LPBF	—	—	~757	~9	[314]
	LPBF 573K	—	—	~694	~18	[314]
316L SS	LPBF 873K	—	~550	~1016	—	[315]
	LPBF 1273K	—	~459	~969	—	[315]
	LPBF 1673K	—	~440	~941	—	[315]
	LPBF/plain carbon steel substrate	—	~347	~836	—	[315]
Maraging steel	LPBF/MS substrate	~450	~174	~712	—	[315]
	LPBF/H13 substrate	—	—	~2100	~15	[316]
		~286	—	~1200	~13	[316]
		~608	—	~1180	~11	[316]

2.5.3 Fatigue properties of metal AM components

LPBF-processed steels are exposed to dynamic loading conditions in many functional industrial applications; Hence, a thorough understanding of fatigue behaviour characteristics is prerequisite to evaluate their fatigue life. However, the studies pertaining to the fatigue studies of LPBF steels are limited in the available public literature. Surface polish and building directions are the two most crucial factors that influence the fatigue lives of LPBF processing of steels [1,100,289,317]. Furthermore, process parameters along with fatigue testing conditions also influence the fatigue life of LPBF-built steels [318,319]. The fatigue limit of the LPBF fabricated part mainly depends on its surface finish. It is well acknowledged that fatigue crack initiates from the surface of metallic materials. Similar to conventionally manufactured steels, LPBF-manufactured steels are greatly affected by the rough surface quality, induced by various surface asperities such as micropores, surface cracks, staircase effects, spatters, un-melted and partially-melted particles emerge on various LPBF surfaces. Additionally, additive layer building strategy and the complex thermophysical phenomena of LPBF process impart unstable molten melt pool which further aggravates the surface quality or surface roughness [1,36,320,321]. The higher surface roughness (R_a) paves the way for the higher local stresses under the dynamic loading conditions, which result in lower fatigue limits and consequently reduces the fatigue life of LPBF processed steels [322]. The high cycle fatigue (HCF) limit is strongly dependent on surface roughness-related defects compared to low cycle fatigue (LCF). Hence, the HCF performance of LPBF steels can be improved by decreasing the surface roughness and the defects that occur on the part surface [322-324].

The build direction is another important factor that significantly influence the fatigue property [1]. The direction in which the load is applied to the built layers during the LPBF process defines the fatigue strength [289,325]. The building direction governs the size, shape and distribution of the LPBF processed defects, such as insufficient fusion holes and porosities that are elongated perpendicular to the building direction [326,327] (See Figure 2.65a-d). The horizontally built components (build direction parallel to the loading axis) are exposed to longer inter-time intervals which experience higher cooling rates and faster solidification (See Figure 2.65 b&d). Thus, a formation of finer microstructure and higher distribution of smaller scale porosities causes less stress flow and concentrations around the defect that results in better fatigue limits as compared to vertical built component (build direction perpendicular to loading axis). The stress concentrations

are maximum in vertical components due to comparatively weak interfacial bonding between successive layers and the axis of linear and planar bigger-size defects (Figure 2.65a&c). The arrangement of these defects normal to the loading direction provides easy access paths for voids to grow bigger and coalesce, causing failure at lower fatigue limits. Irrespective of the building direction, LPBF-built parts are generally more susceptible to fatigue characteristics [100,318,328,329].

LPBF induces distinct (elongated grain structure along the build direction) microstructure as compared to the conventional process of steels. Also, the LPBF process stimulates higher surface roughness, which is particularly detrimental to their fatigue performance [330,332]. Nehzadfar et al. studied the fatigue behaviour of the LPBF process of steels under the influence of process-induced defects such as voids, oxides, un-melted powder particles, and other surface defects causing higher roughness. The fatigue life of LPBF fabricated 17-4 PH was studied by [289,332], the authors reported that in addition to anisotropic distribution of process induced defects, the fatigue life was highly dependent on build orientation under both low-cycle and high-cycle fatigue properties [1]. The fatigue limit of LPBF-built components depends on the directions of the load applied. For parallel loading to the direction of grain growth, the crack path was highly tortuous, resulting in slow crack propagation and yielding high fatigue limit [331]. In the other case loading perpendicular to the grain long axis, the crack propagation along grain boundaries was straight and easy without any resistance to the applied load [114,267]. Croccolo et al. found that the fatigue properties of LPBF processed maraging steels were isotropic, and with a fatigue limit of 600 MPa [333], which is approximately equal to $1/3^{\text{rd}}$ of the static yield strength; which is in line with the fatigue limit obtained for conventionally-produced maraging steels [334,335]. Isotropy is caused because of the weak texture in this type of steel as a consequence of the martensitic phase transformation. The LPBF H13 tool steel displayed a substantially shorter fatigue life than that of traditionally fabricated steel [1,306], which is ascribed to the process-induced residual stress and the higher surface roughness [304]. The higher surface roughness of LPBF-processed steels is particularly detrimental to fatigue performance. It is found that by employing post-process surface finishing treatment, the fatigue limit can be doubled [114,323]. Hot-isostatic-pressing (HIP) and stress relief heat treatments both have a negligible impact on fatigue performance, however following surface finishing post-process treatment, the fatigue limit is predominantly found in the range of conventionally processed steels [1,114,267,323]. The biggest challenge the LPBF process

pose is the selection of the optimum set of processing parameters from a wide array of parameters. Each individual metal AM parameter presents its unique impact on the final part quality, hence, controlling and estimating the final product quality is considered very challenging task [1]. Inappropriate energy densities result in the formation of unfavourable defects, which impart local stress concentrations during cyclic loading and lead to premature fatigue failure. Even by selecting optimum laser fluence, a few small entrapped spherical gas pores inevitably occur in the LPBF processed parts. However, the effect of these pores on the fatigue life of LPBF-processed 316L steels is unaccountable, as they are less sensitive to notch due to their higher ductility and more resistance toward defects and residual stresses [336]. LPBF process-induced defects formed due to lower or extremely higher energy densities are more detrimental to HCF because of their higher level of stress concentrations [337].

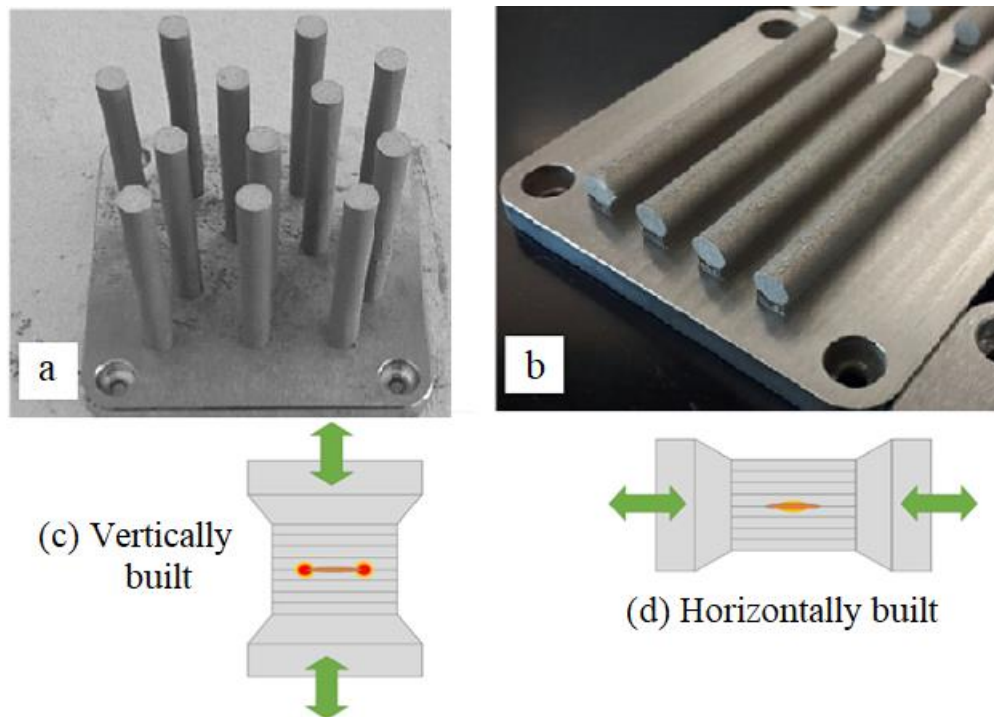


Figure 2. 65 Schematic illustration of LPBF build directions and stress concentrations associated with it, (a) vertically built, (b) horizontally built LPBF specimens, (c) higher stress concentrations around the defect in the vertical sample, (d) fewer stress concentrations in the horizontal sample [289]

2.5.4 Impact of build orientations on metal AM surface quality and Fatigue life

The impact of different build orientations on the surface quality and fatigue properties has been summarized in Table 2.7. The general discussion about the surface quality concerning various build orientations and the fatigue properties has already been discussed in the previous **section 2.5.3**. Yadollahi et al studied the impact of build orientations (horizontal and vertical) on fully-reversed strain-controlled fatigue behaviour of LPBF 17-4 PH stainless steels [289]. The authors found that the vertically oriented sample showed larger and irregular voids, cavities, pores and lack of fusion holes due to lower laser fluence which aligned perpendicular to the fatigue loading conditions and acted as higher stress concentration areas resulting in lower fatigue strength (236820 cycles at a strain amplitude of 0.15% (see Figure 2.66ab), and 6422 cycles at a strain amplitude of 0.3% (see Figure 2.66cd)) as compared to horizontally oriented sample [289]. The higher fatigue strength of horizontally oriented samples was credited to the finer microstructure and the various process-induced defects aligned parallel to the loading conditions giving rise to higher resistance to fatigue loads and hence displaying higher fatigue strength (93470 cycles at a strain amplitude of 0.2%, and $\sigma_m = -62$ MPa, 551649 cycles at a strain amplitude of 0.2%, and $\sigma_m = +60$ MPa) (see Figure 2.66ef) [289]. The tensile testing results followed the same trend as fatigue life, with the vertically oriented sample showing a UTS of 940 MPa and the horizontally oriented sample a UTS of 1060 MPa [289].

Tullis et al reported the significant influence of bulk parameter-surface roughness on the fatigue failure mechanism of vertically oriented samples, and the least impact of microstructure on the fatigue growth life [338]. The authors found that the vertically oriented sample displayed varying surface roughness values between 10-25 μm and fatigue lives in the range of 15000-25000 number of cycles [338]. The lower fatigue lives were attributed to the multiple surface cracks, porosities, and sub-surface porosities acting as high-stress concentration regions for crack initiation, easy crack propagation and eventually leading to failure at lower fatigue loads [338].

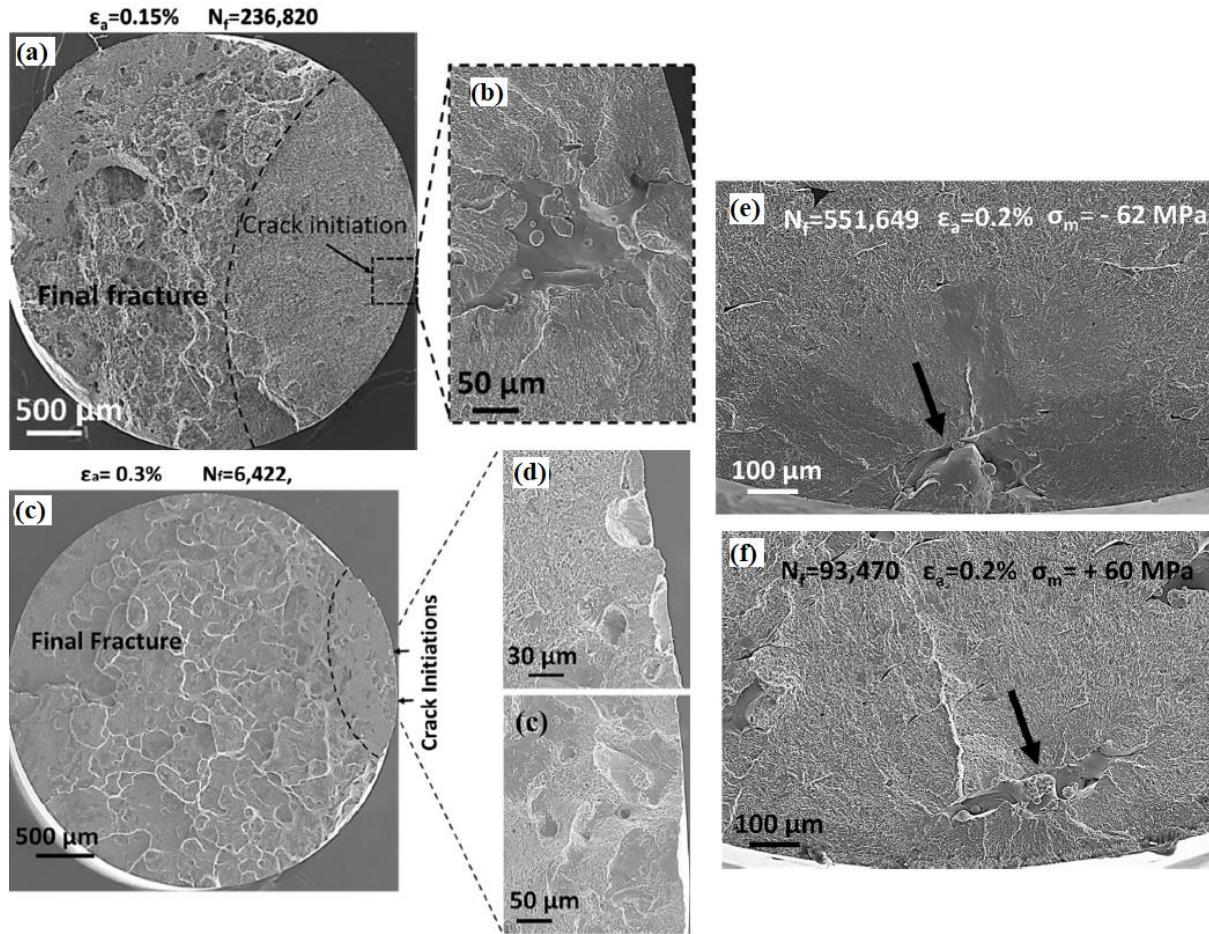


Figure 2. 66 Schematic illustration of vertically oriented fracture surfaces (a) 236820 cycles at 0.15% strain amplitude, (b) higher magnification image of (a) (c) 6422 cycles at 0.3% strain amplitude, (d) higher magnification image of (c), (e) horizontally oriented fractured surface 551649 cycles at 0.2% strain amplitude at σ_m -62 MPa, and (f) horizontally oriented fractured surface 93470 cycles at 0.2% strain amplitude at σ_m =+60 MPa [289].

Shrestha et al studied the effect of three build orientations (horizontal, vertical and diagonal) on the fatigue life of wrought and LPBF 316L steels [339]. The longer fatigue lives (10^3 - 10^6) were recorded for the horizontally oriented samples, while the diagonally oriented sample displayed shorter fatigue lives (10^3 - 10^5) [339]. The H and D samples' average fatigue lives are comparable at a strain amplitude of 0.4% which could be ascribed to fewer effects of the crack initiation stage and sensitivity to defects under low cycle fatigue [339]. The lack of fusion hole defects (oriented perpendicular to applied stress) was responsible for the shorter fatigue life of the vertically oriented sample (10^3 - 10^5) (see Figure 2.67ab). The crack initiated from the larger partially melted defect for the diagonally oriented sample (see Figure 2.67cd). For the horizontal sample, the crack was

initiated from the unmelted powder particles (see Figure 2.67ef) [339]. Overall the build orientations have less impact on build orientations.

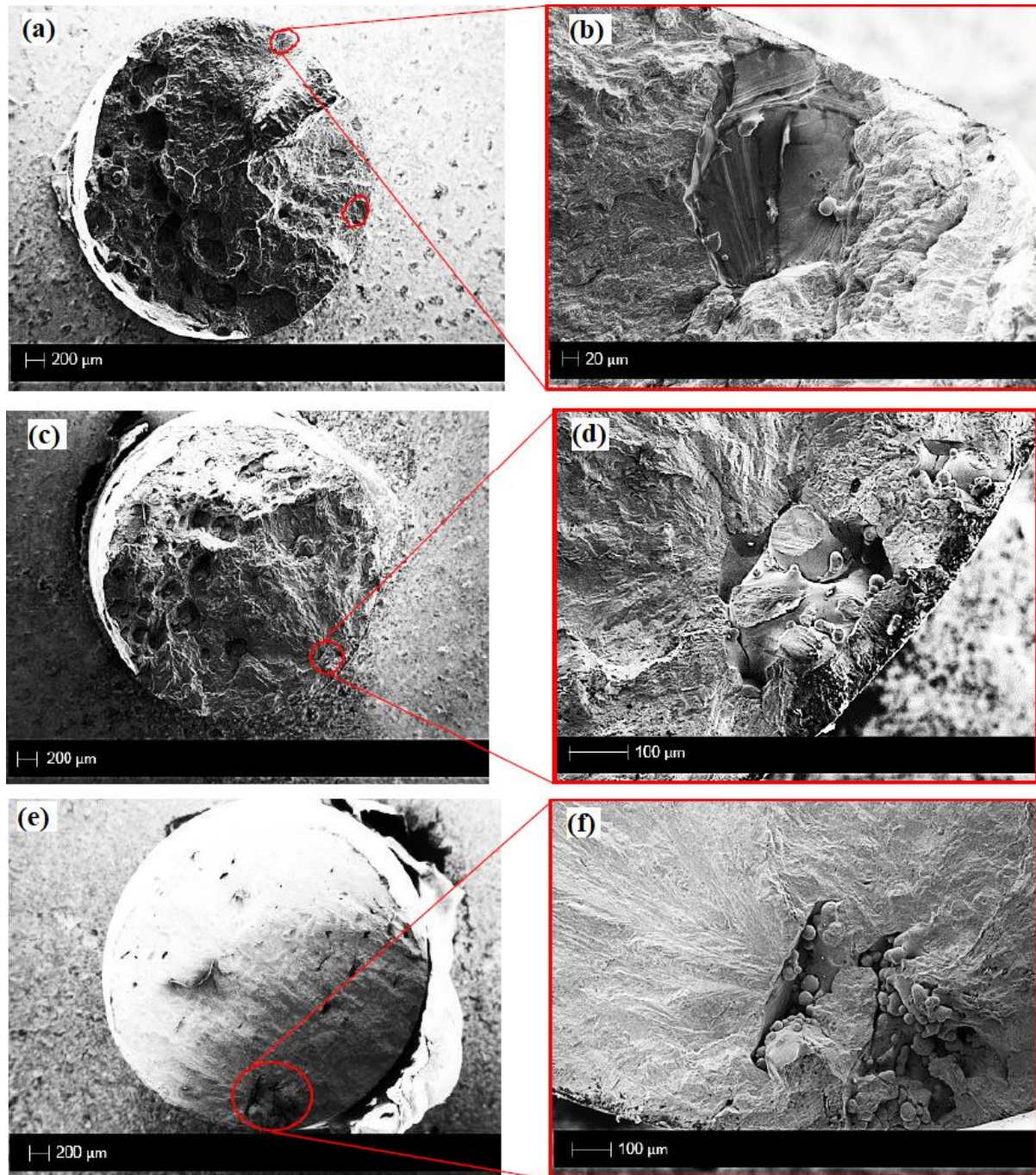


Figure 2. 67 Schematic illustration of (a) vertically oriented fractured surface (b) lack of fusion hole (void), (c) diagonally oriented fractured surface, (d) partially melted particle, (e) horizontally oriented fractured sample and (d) un-melted powder particle [339]

Table 2. 7 Summary of surface quality, tensile and fatigue properties of metal AM components with different build orientations

Material	Building orientation	Surface roughness (Ra/Sa) μm	Ultimate tensile strength (MPa)	Fatigue life (Nf-number of cycles to failure)	References
IN718 alloy	Vertical	Ra-14	1137	5000	[231]
IN718 alloy	Vertical-SL	Sa-8-17	-	10^4 - 10^5	[13]
	Vertical-XCT	Sa-10-15		10^4 - 10^5	
316L SS	Horizontal	-	700	10^3 - 10^6	[339]
	Vertical	-	675	10^3 - 10^5	
	Diagonal	-	550	10^3 - 10^5	
TiAl4V alloy	Normal	Ra=11 Sa=7.84	959 (std)	-	[340]
IN718 alloy	Vertical	Sa=10-25	-	15000-25000	[338]
17-4 PH SS	Horizontal	-	1060	93470-551649	[289]
	Vertical	-	940	6422-236820	
316L SS	Torsion	Sa=11-13.5	-	$2 \cdot 10^6$ cycles at 92.5 MPa	[341]
	Bending	Sa=11-14	-	$2 \cdot 10^6$ cycles at 90 MPa	
	Tension	-	-	$2 \cdot 10^6$ cycles at 127 MPa	

2.5.5 Effect of post-process treatments on metal AM surface quality

The use of optimised AM process parameters and contour strategies is merely not sufficient to achieve the standard surface quality required to meet the functional performance of end-use products [174]. There are other influencing factors influencing the poor surface quality such as build direction and designed CAD model preliminary slicing into layers; the resulting contour of a real part is a stepped approximation of a nominal surface that depends on the theoretical curvature and the sloping angle with respect to building direction [230]. Both up-skin and down-skin surfaces

of inclined or curved LPBF components are affected by the stair-steeping effect or staircase effect [1,12,36]; caused by the discrepancy between the stacking of the 2D layer-by-layer building approach of AM process and the original 3D design model [170]. To overcome these shortcomings; one or other form of post-process surface finishing treatment is necessary to achieve an adequate surface finish and enhance the fatigue life and eventually meet the mechanical and aesthetic requirements [1,12,36].

The impact of post-process treatments on microstructure, surface texture and mechanical properties of LPBF-built steels have been studied by many researchers [256,313-315,328-337,342-349]. Unlike hot-working processes, cold-working post-processing methods like shot peening can be employed. Shot peening improves surface roughness, microhardness, compressive yield strength, and wear resistance by inducing compressive residual stresses, grain refinement, and macro strain [1,330]. Finish machining (FM), vibratory surface finishing (VSF), drag finishing (DF), laser polishing, magnetic field-assisted finishing, grinding, sandblasting, and electro-polishing are other post-processing techniques that are primarily focused on improving the surface integrity characteristics of LPBF steels [1]. The surface roughness of LPBF-built steels can be reduced (from 8.2 μm to 0.05 μm) by grinding [336]. Lower surface roughness (by 48.72%) was reported after sandblasting in two phases [166,350].

Alfieri et al studied the post-processing treatment via laser surface modification to improve the surface roughness (R_a) by controlling the scanning optics and beam wobbling of the LPBF process of stainless steel [230]. As-built vs post-processed samples in three building modes (flat-built, 45°-built and upright-built) and in three measuring directions namely Longitudinal (L), Traverse (T) and crossed (C) were studied (see Figure 2.68) [230]. The authors found higher average R_a for 45°-built (14.40-15.07 μm) and upright-built (15.83-16.50 μm) samples, while no significant difference in standard deviation was reported among longitudinal, traverse and crossed roughness which is ascribed to thin layering led to uniform surfaces [230]. Similarly, the authors reported the improved R_a values (by 79-92%) less than 2 μm for (most of) both 45°-built and upright-built post-processed (LSR) samples; which is credited to the higher starting roughness and the lower reflectivity and also melting of the higher surface peaks results in better the response [230].

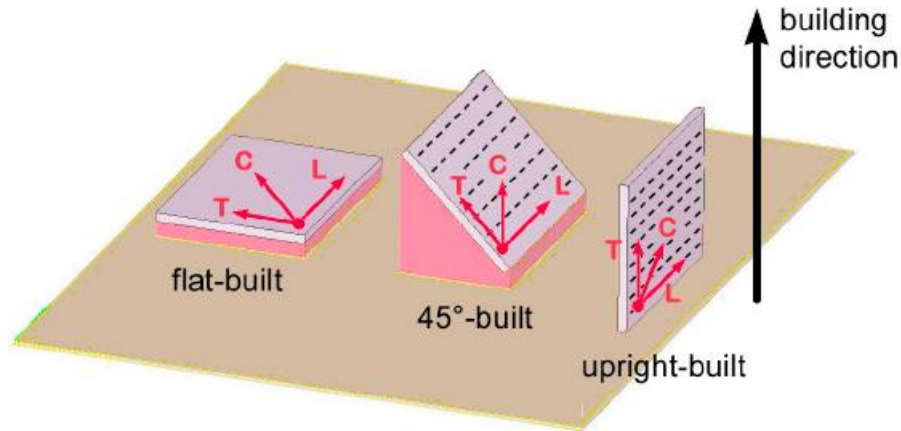


Figure 2.68 Schematic illustration of three building directions used in the metal AM process [230] Yan et al studied the impact of building directions (0° , 45° , 90°) on the surface roughness, tribological properties, and microstructure of LPBF components [232]. The reported surface roughness of the 0° surface was the lowest ($R_a=5.706 \mu\text{m}$), while the roughness value of the 45° surface was the highest ($R_a=31.397 \mu\text{m}$, @ $90^\circ R_a=13.04$). The wear rate of $57.2 \times 10^{-6} \text{mm}^3/(\text{Nm})$ and coefficient of friction (COF) 0.31 was recorded for the 0° sample, and the wear rate and COF for both 45° and 90° surfaces were higher [232]. The authors concluded that building directions had a significant impact on the surface roughness and tribological properties [232].

Denti et al studied the impact of various surface finishing methods on the surface texture parameters and the fatigue life of LPBF components [351]. The authors reported that the plastic media blasting surface roughness (S_a) improved by 77%, reduced peak S_{pk} by 86%, and reduced valley depth S_{vk} by 83%. Sandblasting and laser shock and metal shot peened samples displayed negative skewness (S_{sk} of -0.137, -0.130 and -0.203, respectively) [351]. The main texture ratio (Str ; 0.629) and texture direction (Std ; 82°) coincided with the orientation of the layers (Figure 2.69a). The observed texture ratio (Str) values (ranging between 0.518-0.789) for the various surface treatment samples (Figure 2.69b-g) were evidently similar to the as-built material reference datum; implying that, surface texture persisted even after undergoing various surface treatments except sandblasting [351]. The surface finishing treatments presented significant improvements in fatigue life with the maximum stress level (σ_{max}) corresponding to the endurance limits set at 2×10^6 cycles for as-built samples was 50 MPa. Similarly, the σ_{max} corresponding to the endurance limit was increased by 80% for plastic media blasting, sandblasting, ceramic, and metal shot peening surface finished AM parts [351].

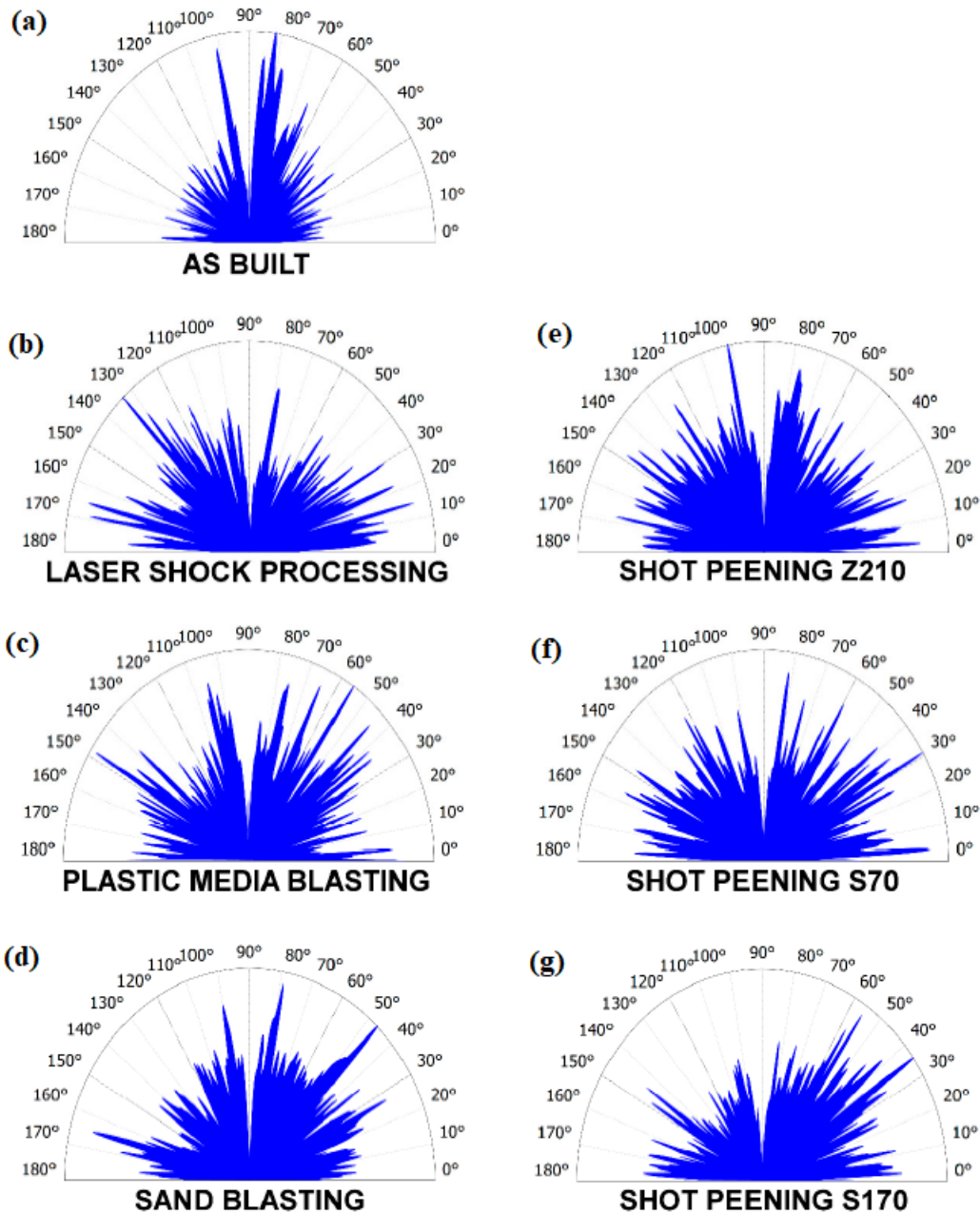


Figure 2. 69 Schematic illustration of polar spectrum graphs of (a) as-built samples (b) shock processing; (c) plastic media blasting; (d) sandblasting; (e) ceramic shot peening; (f) S70 metal shot peening; (g) S170 metal shot peening [351].

Cren et al examined four different samples (as-built, CNC-built, LPBF+mechanically polished CNC+mechanically polished) surfaces to assess and characterize the surface quality (including biological properties) of LPBF implant-supported prostheses and particularly trans-gingival components [340]. The LPBF+mechanically polished sample displayed the least surface

roughness (Ra) of $\sim 0.07 \mu\text{m}$. The reported 3D surface roughness (Sa) for CNC+mechanically polished was $0.05 \mu\text{m}$ which is almost close to the Sa of LPBF+mechanically polished ($0.06 \mu\text{m}$) [340]. The authors concluded that the surfaces obtained by the recommended surface finishing methods appeared to be compatible with a prosthetic application type 4 according to ISO 22674 [340]. Melia et al experimentally examined how build angle affects the average surface roughness and breakdown potential (corrosion: Eb) for PBF 316L parts of 6 different surface finished states: as-printed, ground with SiC paper, tumble polished in abrasive media, electro-polished, chemically passivated, and the application of a contour/re-melt scan strategy [352]. The smoothest surface finished conditions ground and electro-polished states led to Eb near the material's limit ($\sim +1.0 \text{V}_{\text{Ag/AgCl}}$), whereas the other surface finished samples exhibited the lower Eb [352]. The build angle also presented a significant impact on surface roughness, additionally surfaces with high angles from the build direction also led to higher surface roughness values [352]. Wang et al attempted to improve the surface quality by studying the effect of surface re-melting and multi-layer profile scanning strategies based on systematic studies of the impact of laser power, scanning speed and inclination angle on different surface morphologies and roughness of LPBF parts [179]. The minimum roughness (Ra) of $4.41 \mu\text{m}$ was reported for the upper surface with the corresponding line energy density of 0.22 J/mm . With the increase in scan speed, the roughness of both upper and lower surfaces increased significantly [179]. The authors reported the decrease in surface roughness values with the increase in inclination angles, which was ascribed to the combined effect of the step effect and powders adherence. The surface re-melting improved the surface roughness by 35.68% ($2.65 \mu\text{m}$), and the multi-layer profile scanning process strategy could reduce both upper and lower surface roughness by more than 50% [179]. Chen et al studied the impact of core LPBF parameters including contour scan parameters (performance and intermediate, speed), and surface finishing treatments on the final surface roughness and the fatigue life of metal AM components built with varying inclination angles [170]. The reported roughness (Ra) for performance and intermediate ($35 \mu\text{m}$ - $65 \mu\text{m}$), and speed ($35 \mu\text{m}$ - $90 \mu\text{m}$) samples was higher for down-skin surfaces irrespective of contour scan, whereas a lower Ra trend ($12 \mu\text{m}$ - $45 \mu\text{m}$) for up-skin surfaces was evident for all these samples (see Figure 2.70ab) [170]. Similarly, none of the intermediate samples reached a fatigue life of 10^5 cycles under maximum stress of 200 MPa, performance samples reached 250-350 MPa under the same stress; due to crack initiation from the rough surfaces (see Figure 2.71) [170]. The authors concluded that surface

roughness is a primary fatigue-life limiting factor for LPBF components, contour scan with optimised parameters could improve surface finish and also roughness strongly depends on the build orientation [170].

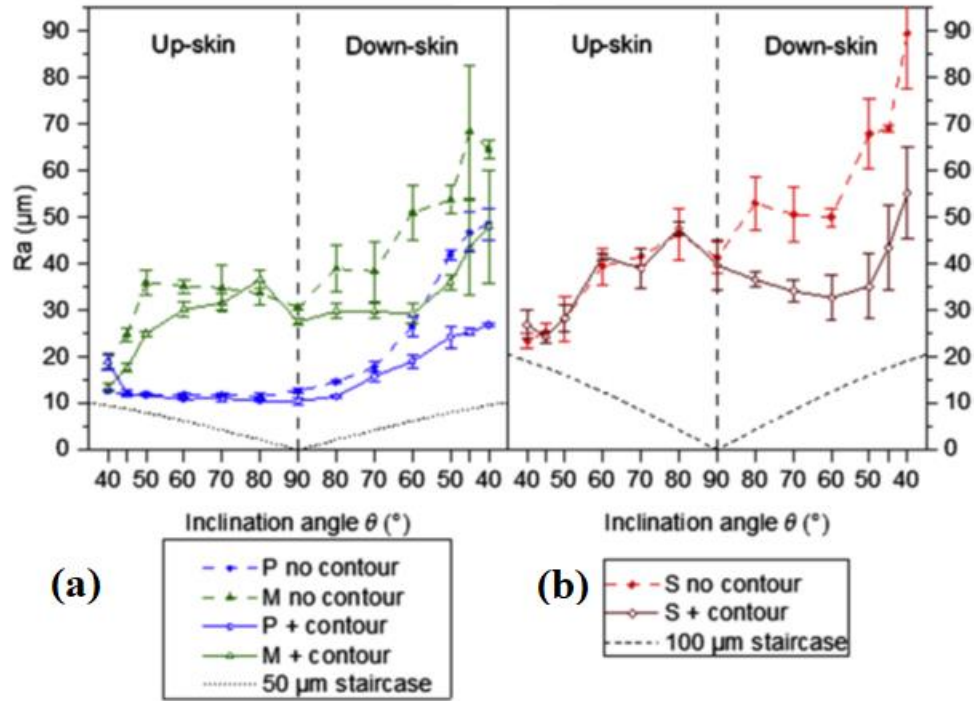


Figure 2. 70 Ra values of different surfaces built with varying inclination angles and with different processing parameters. (a) “Performance” and “Intermediate” samples results, and (b) “Speed” samples result [170].

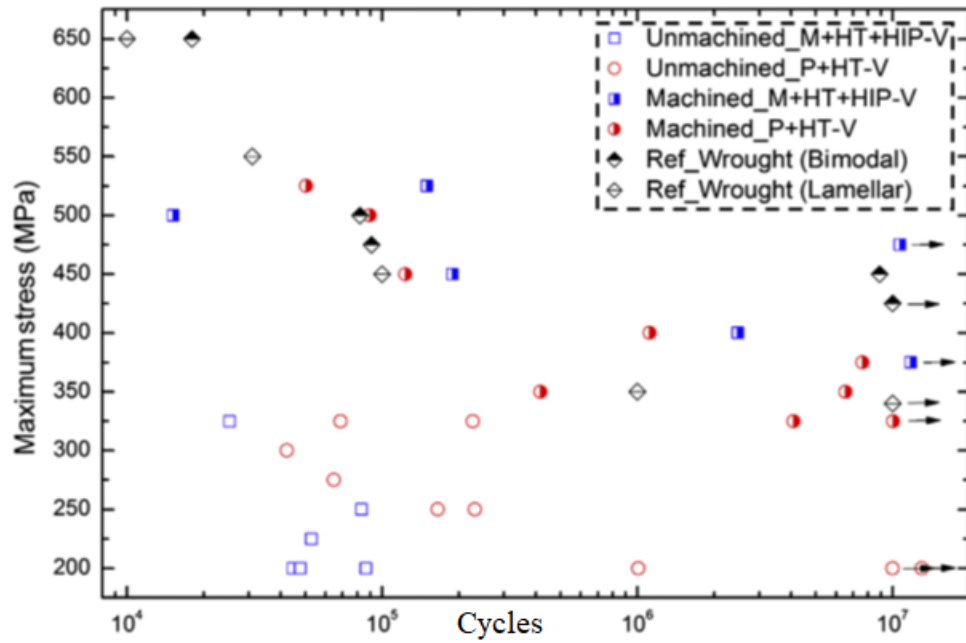


Figure 2. 71 Fatigue properties of LPBF Ti6Al4V samples. The black arrows data points indicate the fatigue tests were stopped at 10^7 cycle fatigue life has been reached. [170]

Wan et al studied the impact of layer thickness and surface machining on surface roughness, tensile and fatigue properties of LPBF IN718 parts at 650°C [231]. The recorded yield strength (σ_{yield}), ultimate tensile strength (σ_{UTS}), and fracture strain (ϵ_f) of the machined sample at 650°C were found to be 978.2 MPa, 1137.4 MPa and 13.9% respectively; which are superior than wrought counterparts (see Figure 2.72a) [231]. The authors reported that the thinner un-machined samples (G1) displayed longer fatigue life ($\sigma_a = 265.5$ MPa: ~ 5000 cycles) than the thicker parts, the opposite was revealed for the thicker machined samples (G2) ($\sigma_a = 405$ MPa: ~ 8000 cycles) [231] (see Figure 2.72bc). The researchers revealed an increase in fatigue strength by $\sim 50\%$ by adopting surface machining and polishing, and the surface roughness (R_a) was reduced from $14\text{ }\mu\text{m}$ to ~ 100 nm. Finally, defect shape has more impact on fatigue properties as compared to defect depth [231].

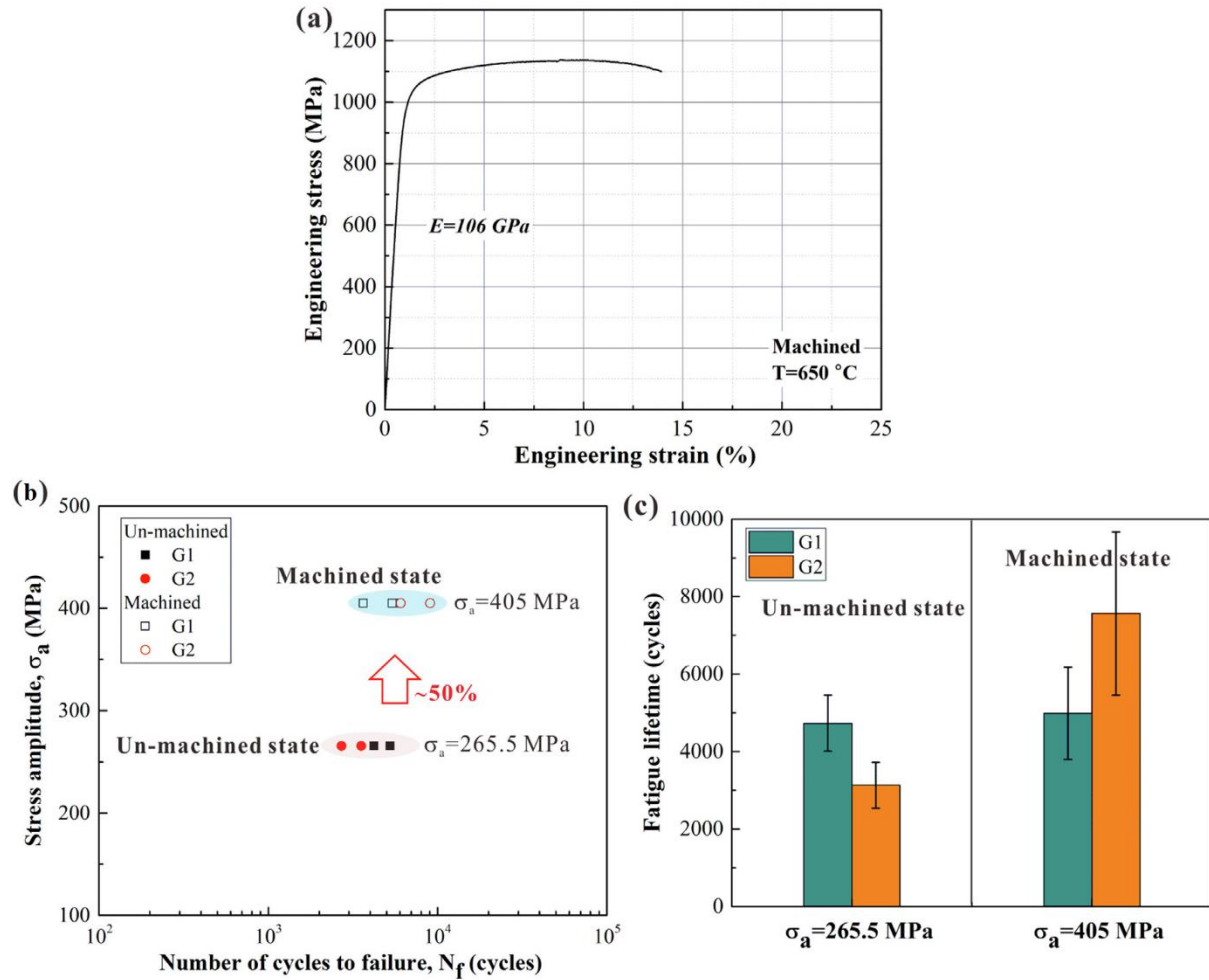


Figure 2.72 schematic illustration of (a) Engineering stress-strain curve for LPBF IN718 machined sample at 650 °C, (b) fatigue strength comparison of un-machined and machined samples and (c) fatigue life comparison of both G1 and G2 specimens [231].

Surface machining had a limited impact on improving the fatigue strength as it remained significantly lower than that of the reference material (50% failure probability at 107 cycles strength of 283 MPa compared to 600 MPa) [304]. The improved fatigue properties were attained when the stress relief and austenite decomposition heat treatment at 600°C were employed [306]. In general, the higher surface roughness caused by irregularly shaped defects e.g. voids, partially-melted /un-melted etc in LPBF processed samples are more sensitive to the fatigue life than their wrought counterparts. However, a relatively lesser number of defects were reported for the vertically built LPBF specimens [353]. The removal of residual stresses via stress relief (SR) heat treatment (5 h at 470 °C) does not necessarily improve the fatigue behaviour. Instead, the fatigue performance of LPBF-processed 316L steel was greatly enhanced by the removal of crucial crack

initiators using surface machining [1]. The obtained superior fatigue performance of machined samples with and without SR heat treatment was compared with conventionally produced 316L steels. SR treatment in conjunction with machining is recommended to achieve the desired fatigue performance when subjected to higher dynamic loading conditions [1]. Overall, the post-process treatments have a very minimal effect on the fatigue performance of LPBF-processed steels [328,347].

In addition to employing optimised parameters and other post-process treatments, the surface roughness can also be improved (especially the density of parts) by re-melting each layer [354-360]. The laser re-melting is generally applied for the last layer or the outer surface/skin of AM part; balling, porosities and other surface asperities can be reduced simultaneously improving the surface quality [354-357]. While maintaining the other process parameters constant, Metelkova et al. [354] investigated the edge effect of samples after the top surface had been re-melted one to ten times with varying hatch angles between each re-melting layer. The authors found that the height of the edges reduced and the edge length rose as the number of re-melting passes increased [354]. Ukar et al showed that the benefit of laser re-melting; the surface roughness (R_a) of AM part was reduced by ~80% from 7.8 μm to 1.49 μm [357]. Kruth et al. also reported the surface roughness (R_a) from 12 μm to 1.5 μm by adopting the laser surface re-melting (LSR) [358]. The impacts of the LSR method were further examined by Kruth et al. [359] with various process settings for twice melting the final 20 layers of the parts, and they found a notable improvement in surface roughness as well as an increase in microhardness and wear behaviour [359]. For titanium alloy, LSR in combination with optimised parameters for laser power and scan speeds resulted in improved surface roughness without inducing any edges at the contours of AM parts. Similarly, for 316L SS parts, the surface roughness was improved by 90% [359].

2.6 Summary

Based on an in-depth literature review of the state-of-the-art, the key findings related to the aims and objectives of this thesis are summarised below:

- LPBF process is widely used to fabricate metal AM parts but LPBF undergoes complex thermophysical phenomena that generate a very complex surface topography consisting of diverse metallurgical defects and surface asperities imparting poor surface quality.

- In addition, to processing parameters, the other factors responsible for the substandard surface quality are contour scan strategies, build inclination angles, build orientations, part location on the build platform, laser beam incidence angle and etc.
- The metallurgical defects and surface asperities are a large range of components over a large scale of spatial wavelengths – such as balling, porosities, cracks, staircase effect, spatters, and un-melted or partially melted particles.
- These defects and asperities present a new challenge for conventional surface texture measurement and characterisation.
- The measurement and characterisation of elaborate features of internal surfaces fingerprint is another major concern, while post-processing alone is not enough to improve the internal surface quality.
- The surface quality can be modified/tailored to desired roughness levels by optimising the critical process parameters using Taguchi DOE and various other optimisation methods. ANOVA is effective to quantify the impact of individual critical process parameter.
- The existing surface quality characterisation methods are only limited to surface texture height parameters (Ra/Sa) which gives only decent descriptions of vertical characteristics of the surface deviation. Ra/Sa are insensitive to differentiate peaks, valleys and the spacing of the various texture features.
- Ra/Sa fail to provide the general relation between the wavelength and amplitude properties of the surface or any changes occur either in amplitude or spacing.
- The available literature completely lacks to characterise, correlate and quantify the diverse metallurgical defects and asperities that emerge on various metal AM external and internal surfaces.
- It is non-viable to characterise and quantify the particle features individually with just Ra/Sa.
- With an inadequate understanding of complex metal AM surface topography (Ra/Sa information); it is impossible to optimise or tailor the surface quality to meet the desired roughness levels. In addition to surface texture characterisation, it is important to study the influence of different build orientations on microstructure, surface quality as they eventually determine the mechanical properties (ultimate tensile strength and fatigue life) of metal AM components.

Chapter 3. Surface texture characterisation of LPBF processed metal part built with varying surface inclinations

This chapter developed a novel surface texture characterisation toolbox used to systematically characterise the complex surface topographies comprised of diverse metallurgical defects and surface asperities emerge on various LPBF truncheon artefact built with varying inclination angles. The characterized defects and asperities of various up-skin and down-skin LPBF surfaces were then correlated with the suitable areal surface texture parameters as per ISO 25178-2. The newly developed one of its kind feature-based particle analysis was used to quantify the particle features emerged on various surfaces of Truncheon artefact. Finally, the experimental investigation and prediction model results successfully established a strong correlation between the resultant surface quality and the varying build inclination angles. A journal paper published, by the first author SR Narasimharaju, titled “*Surface Texture Characterization of Metal Selective Laser Melted Part with Varying Surface Inclinations*” [36]. This research work has also been presented as a poster at the conference as a primary author SR Narasimharaju, “*Surface irregularities of metal SLM part with different surface inclinations and their impact on surface texture characterization*”, Joint Special Interest Group meeting between EUSPEN and ASPE Advancing Precision in Additive Manufacturing Inspire AG, St. Gallen, Switzerland 2021.

As aforementioned, most of the researchers in the literature followed the general surface texture characterisation procedures to obtain the surface texture parameters but necessarily complied with ISO 4288 [216] and ISO 25178-3 [217]. It is interesting to note that different measurement lengths/areas and cut-off wavelengths (λ_c – the cutoff wavelength to separate the waviness from the roughness, λ_s – the cutoff wavelength to separate the roughness from the shorter wavelength components) were adopted and various surface texture parameters were studied [36]. The measurement area/length and cutoff wavelengths should be generally selected based on the surface roughness scale [31,220,221]. ISO 4288 recommended suitable sampling lengths and cutoff wavelengths corresponding to each roughness range [216]. However, the metal AM or LPBF surface topography displays a different nature from the conventionally machined surfaces. It is unsure whether the current ISO standards are applicable to metal AM surfaces. This leads to the attempts on choosing various measurement areas/lengths and cutoff wavelengths based on an individual’s knowledge and experience which is not acceptable. Also, the investigation in terms of the surface asperities such as staircase effect, spatters, and un-melted/partially-melted powder

particles present on the different surface inclinations and the selection of suitable parameters to characterize these features are very limited. Thus, this research is more focused on investigating the impact of distinct surface irregularities or asperities that form on the various surface inclinations of the LPBF component. The areal surface texture characterisation and the advanced features-based particle analysis mentioned in ISO 25178-2 were studied to quantify these formed surface asperities. Furthermore, an empirical model based on trigonometric modelling was examined to predict the real surface topographical features of the LPBF surface built with various inclination angles. This consolidated investigation would be beneficial to a better understanding of the surface texture characteristics of varying LPBF surfaces. Areal analysis of surface texture gives more opportunities as a representative of the functional surface than a study of 2D profiles.

3.1 Research methodology

3.1.1 Truncheon artefact design and fabrication

The bespoke truncheon artefact was built by using a Renishaw AM400 SLM machine using 316L stainless steel alloy powder. The 316L alloy is austenitic SS mainly iron alloyed and with the presence of other important elements like chromium, nickel, and molybdenum with a mass fraction of 18%, 14% and 3% respectively [353]. It is evident that as-received 316L alloy SS fine powder is dominantly regular in size mostly spherical-shaped particles with a diameter of 15-50 μm (see Figure 3.1a&b). The supplied free-flowing powder density is 7.94 g/cm^3 , the apparent density is 4.36 g/cm^3 and the reported tapped density is 5.01 g/cm^3 . Morphological analysis revealed the results in the vicinity of the 10th (D10), 50th (D50), and 90th (D90) percentile for particle size values are found to be 19.6 μm , 29.6 μm , and 44.1 μm respectively (see Figure 3.1c). The LPBF process parameters including general scan strategy employed is given in Table 3.1, the STRIPE hatching pattern was used for the core scanning. The Renishaw SLM machine is fitted with a fiber-laser that generates pulsed laser waves with a maximum power output of 400 W. The build chamber was filled with 99.99% purity level inert gas (argon), whereas oxygen content was maintained at less than 0.1 vol % during the LPBF process.

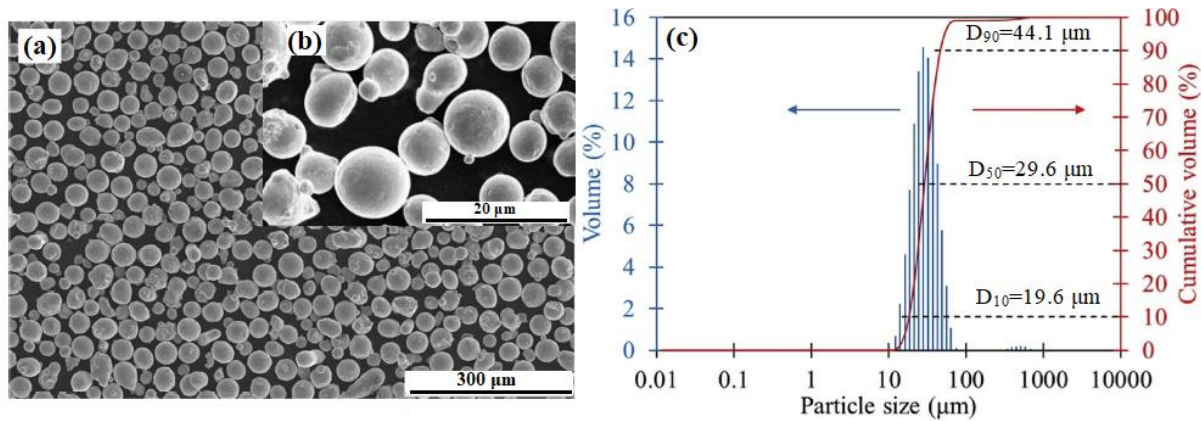


Figure 3.1 schematic illustration of (a) SEM image showing 316L SS powder, (b) higher resolution showing spherical powders (c) powder size distribution.

Table 3.1 Main LPBF process parameters adapted in this part of the research

Parameters	Values
Laser power (W)	110
Hatch spacing (μm)	110
Layer thickness (μm)	50
Point distance (μm)	20
Exposure time (μs)	100
General scan strategy	Meander

The truncheon artefact was built in a horizontal direction aligned perpendicular to the build direction (z-axis). The fabricated truncheon artefact consists of 31 square sections with various inclination angles from 0°-180° with increments of 3° (see Figure 3.2a). At 0° orientation, the surface is parallel to the horizontal plane; at 90° inclination, the surface is parallel to the build direction. The surfaces ranging from 0° to 90° inclination angles were considered as the up-skin, whilst the surfaces from 90° to 180° were deemed as down-skin. However, the down-skin surface measurement was restricted to a 132° position beyond which resulted in an extremely rugged surface damaged by supporting structures. The measurement readings for each incremental angle surface were taken at three different positions (see Figure 3.2b). Additionally, it is well known that the surface topography of the up-skin differs from the down-skin surfaces. As aforementioned, the main reason for these differed surface topographies is due to the presence of supporting structures which leads to significantly higher surface roughness rather impractical. In contrast, the lack of

sufficient supporting structures would result in the LPBF part being distorted or eventually lead to complete failure.

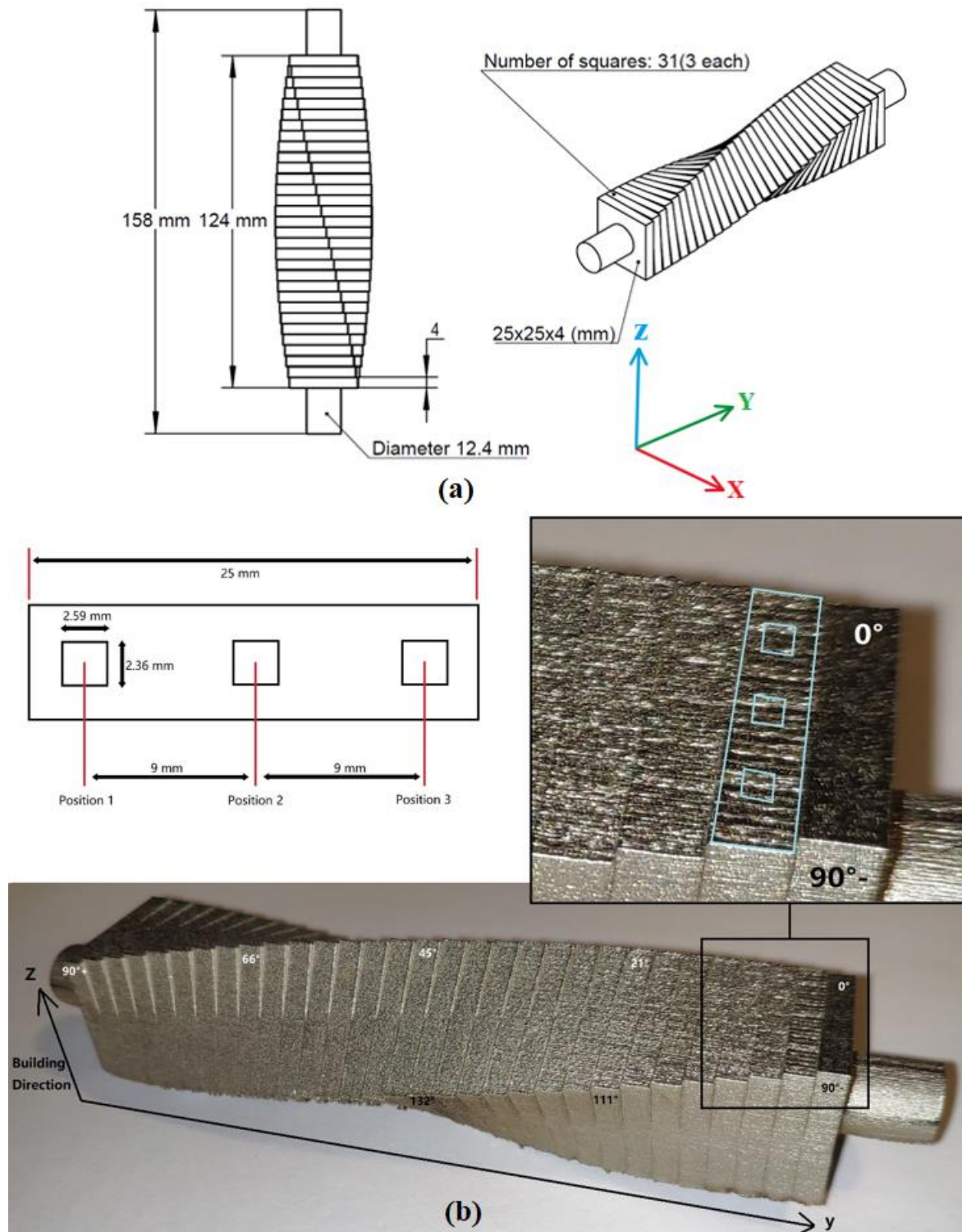


Figure 3. 2Truncation artefact (a) design drawing; (b) LPBF printed sample with measurement details being marked.

3.1.2 Measurement strategy

Alicona G4 FVM was employed to measure the areal surface topography of the truncheon artefact (see Figure 3.3). Non-destructive optical technology called the focus-variation measurement (FVM) is used to measure 3D surfaces at high resolution. Precision optics with a variety of lens systems that can be outfitted with different objectives make up its core part. In order to extract topographical and colour information from the fluctuation of focus, it combines the limited depth of focus of an optical system with vertical scanning. FVM is incredibly efficient because it simultaneously transmits information about a surface's form and roughness [361]. The FVM configuration parameters are listed in Table 3.2. The lateral resolution and magnification were adjusted in such a way that it could clearly capture the main surface topographical features, such as the staircase effect and other particle feature details existing on the surface. The selected measurement area was sufficient to analyze the surface texture parameters. The measurement readings for each incremental angle surface were taken at three different positions followed by the computation of the mean values and the standard deviation. The measurement taken at 0° was repeated four times to verify the repeatability error. The average deviation of Sa was found to be 3.85 nm with a standard deviation of 6.1 nm.



Figure 3. 3 Bruker Alicona focus varying measurement (FVM) system [362]

Table 3. 2 Configuration of FV measurement.

Magnification	20×
Illumination	Ring light
Lateral resolution	1 μm
Vertical resolution	0.7 μm
Sampling distance	0.878 μm (in both X and Y directions)
Measurement size	2.59 mm \times 2.36 mm (switched)

3.1.3 Data acquisition and processing strategy

Digital Surf MountainsMap commercial software [363] was used to analyze the gathered surface texture data. The analyzed surface texture results promote to the characterisation of the staircase effect and particle features. The imported measurement data is firstly processed by filling the non-measurement points, followed by least square levelling. The resulting data were then filtered by using the S-filter (the nesting index $5\text{ }\mu\text{m}$) to remove high-frequency noise. To separate the particle features from the underlying staircase surface, the robust Gaussian filter (with a nesting index of $80\text{ }\mu\text{m}$) was applied due to its robustness against outliers [364]. The data processing procedure is illustrated in Figure 3.4.

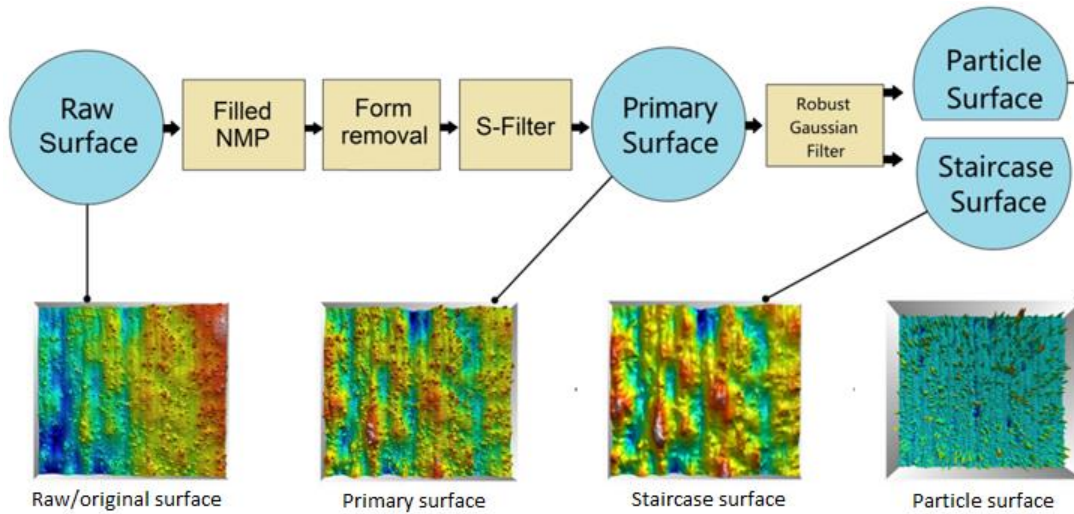


Figure 3. 4 Extraction of the primary surface, the staircase surface, and the particle surface by applying different filters.

3.1.4 Areal surface texture parameters characterisation

A spectrum of areal surface texture parameters employed in this research to characterize the surface topographical features of inclined AM surfaces are listed in Table 3.3. These targeted potentially useful parameters include height parameters (S_a , S_q , S_{sk} , S_{ku}), hybrid parameters (S_{dr} and S_{dq}), functional parameters (V_{mp}), and feature parameters (S_{pd}). Further information about particular surface texture parameters is found in ISO 25178-2:2012 [32]. The surface texture parameters characterisation is further facilitated by feature-based particle analysis by adopting the threshold segmentation approach [36].

Table 3. 3 Areal surface texture parameters explored in this research [36]

Categories	Surface texture parameters
Height Parameters	Sa (μm) -Arithmetical mean height of the scale-limited surface
	Sq (μm) -Root mean square height of the scale-limited surface
	Ssk -Skewness of the scale-limited surface
	Sku- Kurtosis of the scale-limited surface
Hybrid Parameters	Sdq -Root mean square gradient of the scale-limited surface
	Sdr (%) -Developed interfacial area ratio of the scale-limited surface
Functional parameters	Smr1 (%) -Material ratio related to the peak zone
	Vmp (mm ³ /mm ²) -Peak material volume of the scale-limited surface
Spatial Parameters	Sal (μm) -Autocorrelation length (fastest decay to 0.2)
	Str -Texture aspect ratio
Feature parameters	Spd (1/mm ²) (Density of peaks) number of peaks per unit area
Particles analysis	Particles number/density/coverage/projection area/Z-high

3.2 Surface roughness prediction model

A mathematical model based on trigonometric modelling of the staircase effect [365] is adopted to predict the real surface topographical features of the truncheon artefact built with various inclination angles. Here the trigonometry modelling functions for profile and areal surfaces are given by Equation (8) where L_t represents the layer thickness, and α indicates the inclination angle (with reference to the building surface and the edge of the stair). Computer-aided design (CAD) software was used to create the ideal 3D inclined surfaces based on the trigonometry model (see Figure 3.5). It is ensured that the layer thickness of 50 μm, i.e. the same value used while fabricating the LPBF test artefact. Since the ideal faces 0°-90° and 90°-180° have symmetrical features, therefore only the range of 0°-90° is considered with the increments of 3°. The areal surface texture parameters (Sa, Sq, Ssk, Sku and Sal) values of ideal surfaces are calculated and compared with the actual measurements [36].

$$\mathbf{Ra} = \frac{1}{L} \int_0^L |y(x)| dx = \frac{1}{4} L_t \cos(\alpha) \dots \dots \dots (8)$$

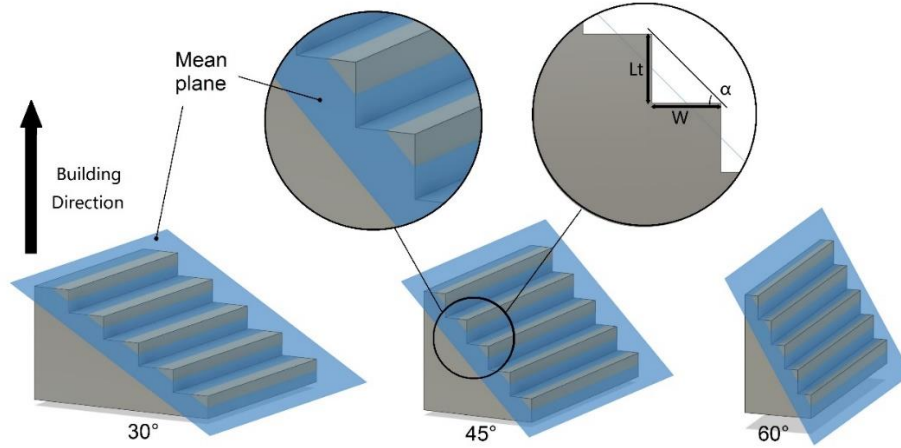


Figure 3. 5 3D representation of the prediction CAD model and the illustration of staircase computation.

3.3 Results and discussions

3.3.1 Visual inspection of truncheon artefact

Figure 3.6a illustrates the optical images of truncheon surfaces measured by a $5\times$ lens to gain a larger measurement area ($2\text{ mm}\times 10\text{ mm}$) for the visual inspection of surface patterns. It is important to note that the images were trimmed off to reduce their sizes for a better exhibition. At 0° , the surface exhibited a typical LPBF surface, with the presence of ripple characteristics caused by the fast-moving laser topped by a few unwanted particles (see Figure 3.6b). Moving forward to the inclined surfaces from 3° to 9° , the constituting stair-step (staircase effect) is clearly visible, which is related to the layer thickness and the inclination angles (see Figure 3.6c-e). Additionally, the chessboard pattern related to the laser scan strategy used during the building process can also be noticed. It is evident that un-melted/partially melted particles and spatters attach to the edges of the stair steps. Further increase in the inclination angle (12° - 15°) resulted in a gradual decrease in the width of the stair-steps, and the scan pattern that existed in previous inclinations is almost indistinguishable (see Figure 3.6f&g).

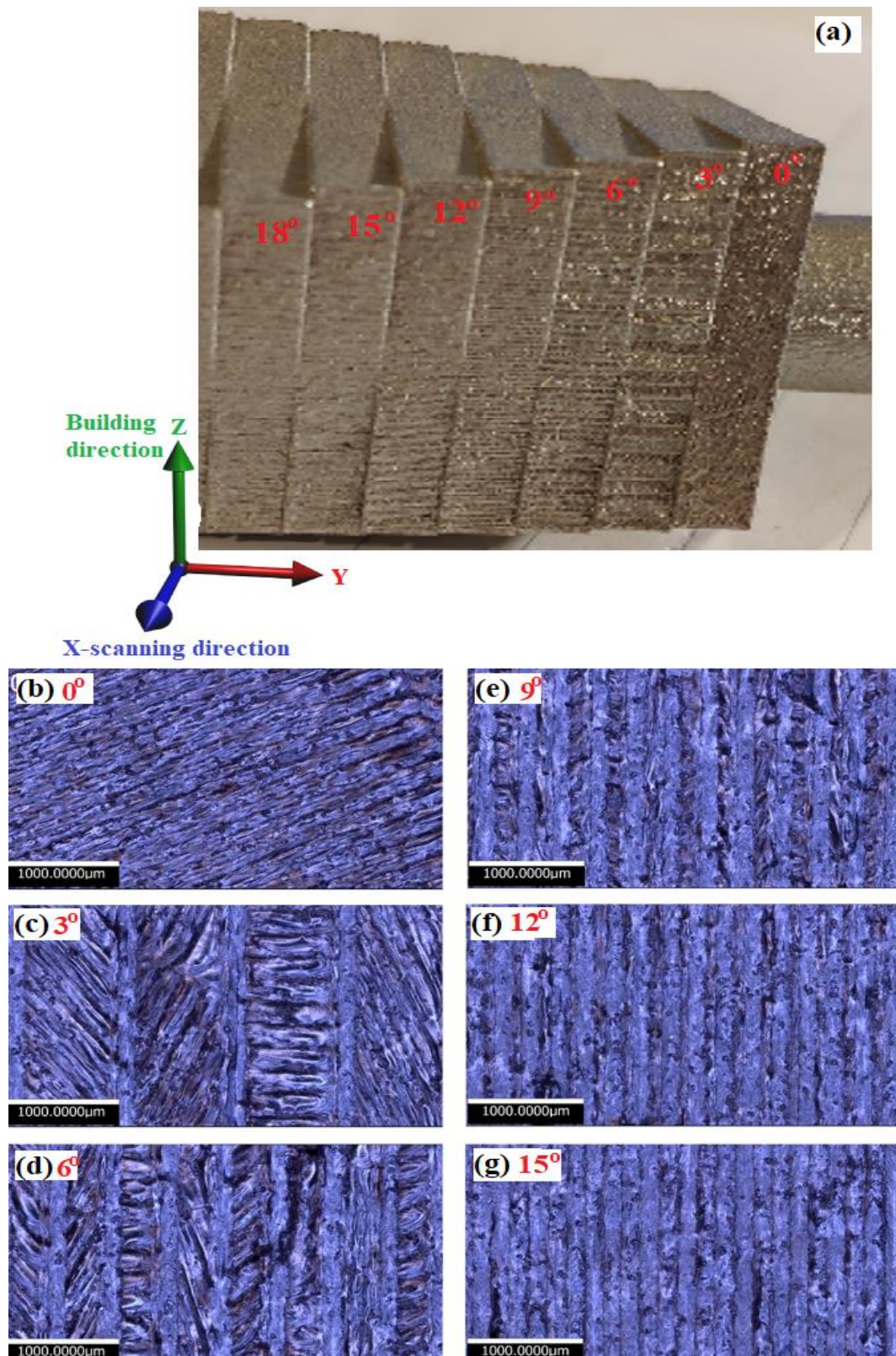


Figure 3. 6 Schematic illustrations of (a) 6 different truncheon surfaces, surface topography transitions between the inclination angles of (b)=0°, (c)=3°, (d)=6°, (e)=9°, (f)=12°, (g)=15°.

Figure 3.7 shows the comparison of the up-skin and down-skin surface pairs at the matching angles, 48° (132°), 60° (120°), 72° (108°), and 90° up-skin (90° down-skin; vertical built component has two side surfaces at 90° , i.e. the left and the right, marked as $90^\circ+$ and $90^\circ-$ hereafter). It is physically visible that the color of the fabricated down-skin surface has changed apparently as compared to the up-skin surfaces. With the change in inclination angle, the number of adhered particles on the up-skin surface have also changed significantly, however the down-skin surface showed very minimal change, regardless of the quantity of particles covering the surface area [36].

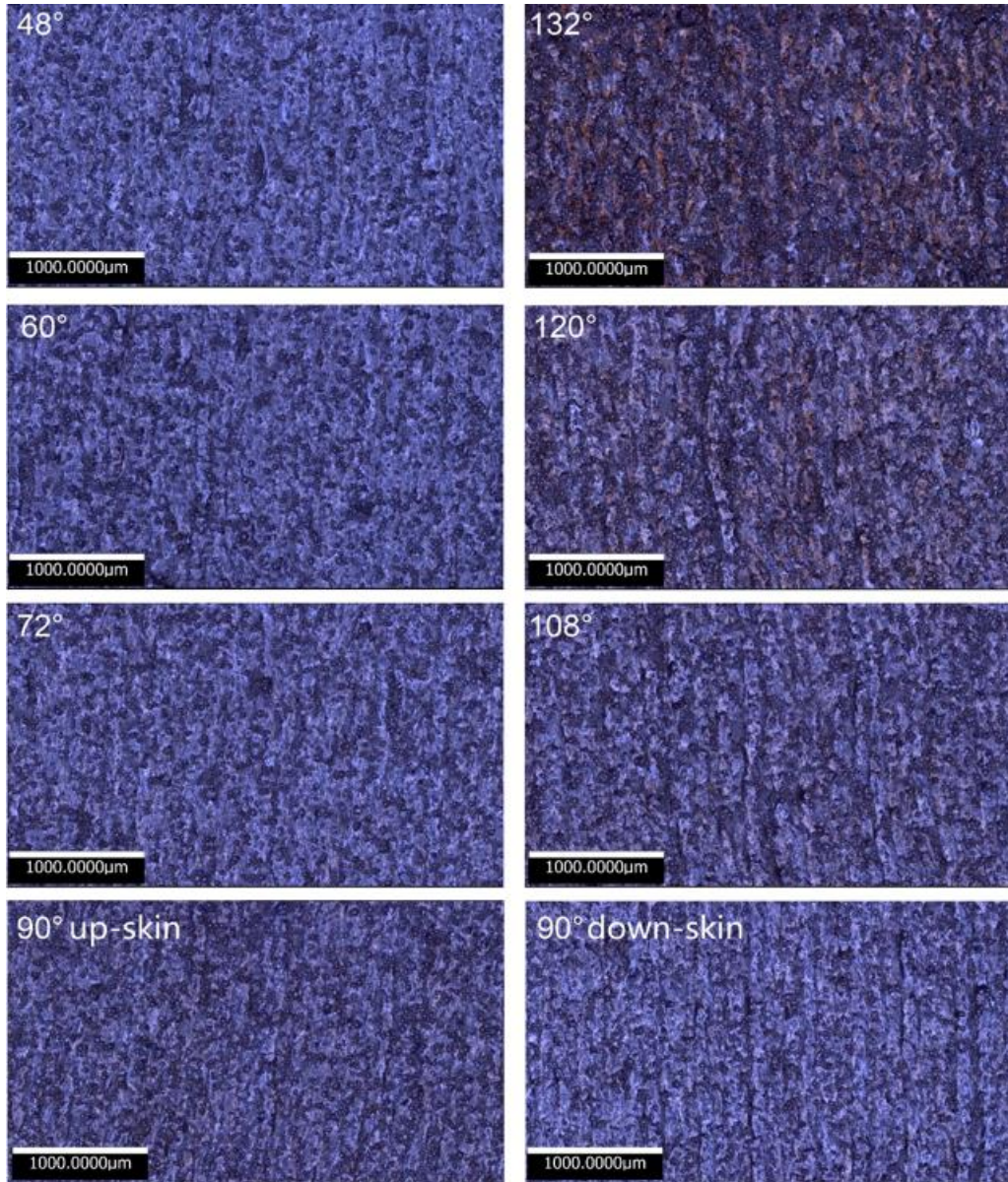


Figure 3. 7 Surface topography transition between the inclination angles of 48°, 60°, 72°, 90° up-skin, 90° down-skin, 108°, 120°, and 132°.

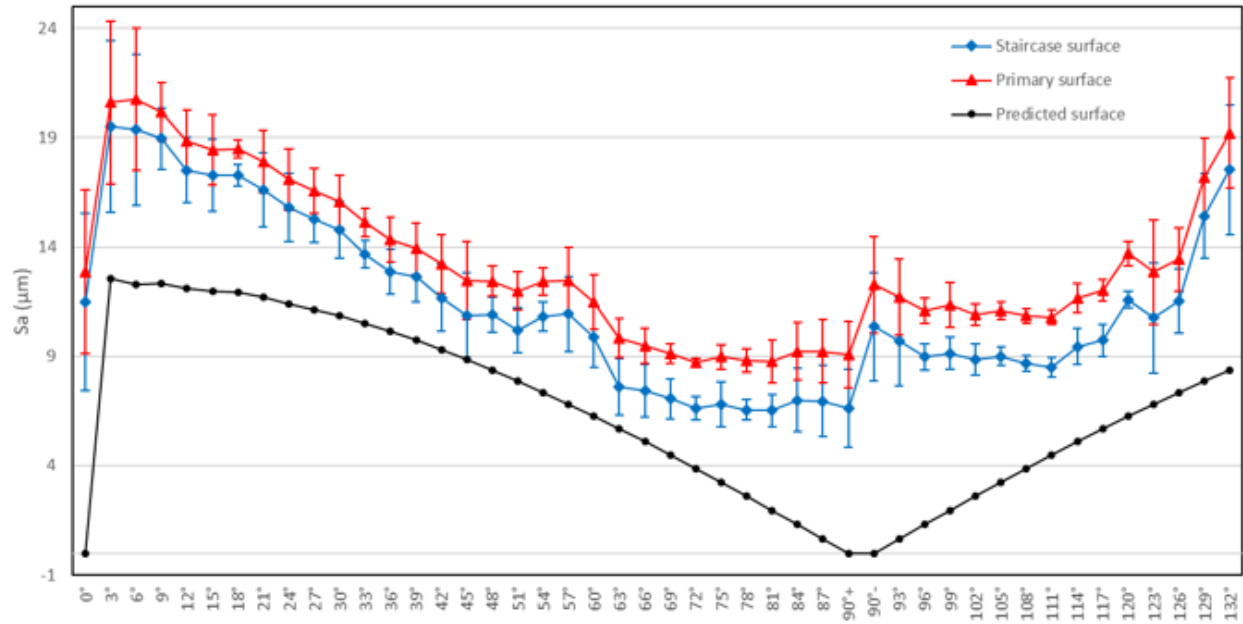
3.3.2 Height parameters

Sa, and Sq values of the primary, staircase and predicted surfaces for both up-skin and down-skin surfaces built with respect to different inclination angles are shown in Figure 3.8(a) & (b). The Sa and Sq displayed consistent trends for all the inclination angles [36]. As the surface inclination increases from first the measurement point (0°), an abrupt increase in both Sa and Sq was recorded (between 3° and 6°). This rapid rise in Sa and Sq values on the inclined surfaces is ascribed to the staircase effect [36]. In addition to the staircase effect, the LPBF process is designed in such a way

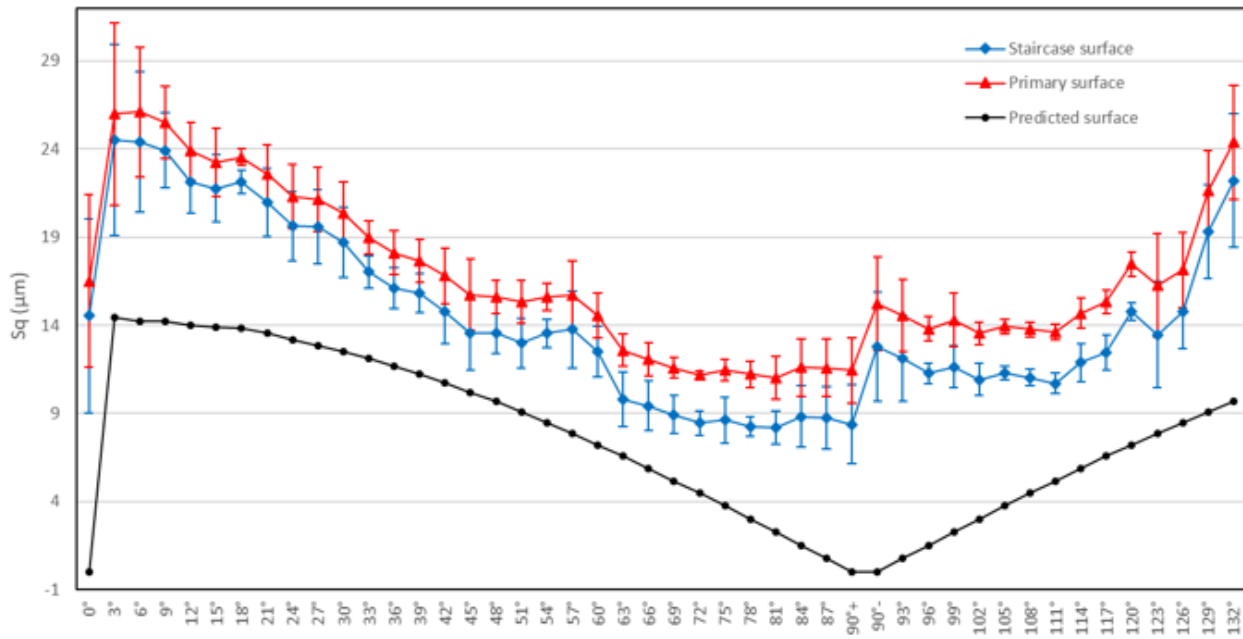
that the lasers melt/re-melt only the horizontal surfaces, but not the inclined ones [215]. Lack of laser re-melting leads to the formation of un-melted/partially-melted particles attaching to the inclined surfaces. The surface roughness decreases steadily between 6° - 45° surface inclinations, with a little increase between 51° - 60° , followed by a further decrease in surface roughness until it reaches 90° . The notable increase in roughness between 51° - 60° is still well below the roughness values obtained at 3° and 6° inclination angles. The staircase effect can be clearly observed between 3° - 45° ; above 45° the staircase effect slowly started to disappear, which was eventually replaced by particle features at 90° .

An interesting point to be noted here is the difference in measured Sa and Sq values are taken at 90° for both up-skin and down-skin surfaces. The observed surface roughness on the down-skin surfaces generally tends to be significantly higher than up-skin surfaces, e.g., about 140% higher than that of the up-skin surface at 90° location. On further exploring the 3D view of their surface topographies, it is found that there is an obvious accumulation of build-up stripes (perpendicular to the build direction) on the down-skin surface, whilst the build-up stripes on the upper surface are not obvious (see Figure 3.9(a) & (b)). The rationale behind this exploration is that the irregular heat dissipation through the inclined surfaces resulted in elevated temperatures in down-skin surfaces. These higher temperatures lead to the distortion and warping of down-skin surfaces. Additionally, the intermittent heat transfer along the down-skin surface contributes to the unnecessary adhesion of un-melted/partially-melted particles, ultimately leading to higher surface roughness. In fact, the obtained Sa and Sq of the down-skin surfaces are higher than the matching angles of the up-skin counterparts [36].

The sudden change of predicted Sa and Sq from 0° to 3° is caused by the transition from a purely flat surface to a strong staircase-presented surface, while a constant declining trend observed between 3° - 90° is attributed to the reducing strength of the staircase effect. This is followed by an increasing trend after 90° due to the re-formation of the staircase effect in the opposite direction. The Sa and Sq trends of the measurements for all cases tend to closely follow the theoretical mathematical model (see Figure 3.8 (a) and (b)). It was discovered by comparing the Sa and Sq values of the primary, staircase, and predicted surfaces that the staircase effect is predominantly responsible for the changes in Sa and Sq, with the impact of the particle characteristics having a less significant effect [36].



(a)



(b)

Figure 3. 8 S_a and S_q of the primary surface, the staircase surface, and the predicted surface with respect to surface inclination: (a) S_a ; (b) S_q .

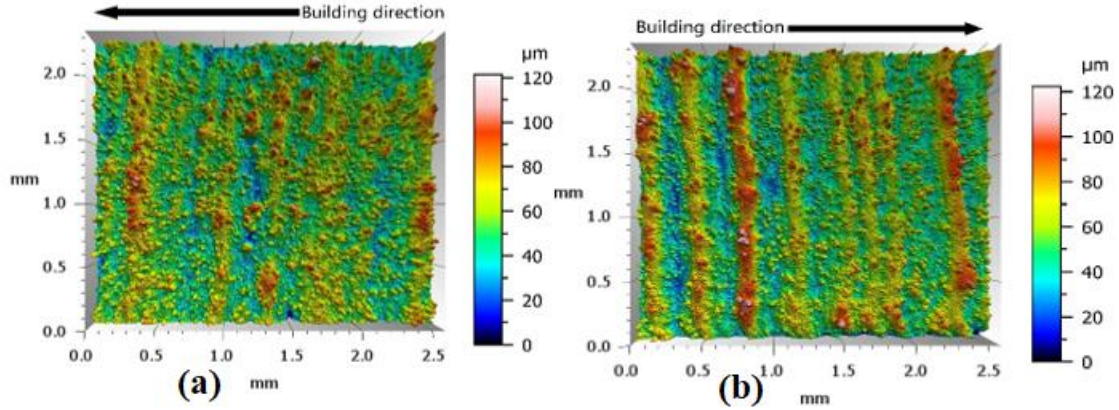


Figure 3.9 3D view of surface topography at 90°: (a) up-skin surface; (b) down-skin surface.

Ssk defines the unique distribution of height values above or below the mean plane, which is generally indicated by a positive or negative value, respectively [36]. Most of the recorded Ssk remained positive for all the up-skin surfaces. This signifies that the height distribution of the up-skin surfaces has a longer tail at the upper side of the mean/reference plane, indicating peaks dominate the surface, see Figure 3.10(a). The reason for the Ssk value close to zero at 24° and 45° surface inclinations could be related to the random deep valleys, but overall, the characteristics of the up-skin surface are mainly dominated by surface peaks. However, the noted Ssk trend for the down-skin surfaces (90°-132°) tends to be unstable. The Ssk becomes negative for all the down-skin surface inclinations beyond 114°. The unstable skewness is accredited to deep valley features and redundant peak features caused by the presence of a higher number of large protruded particles consisting of un-melted/partially-melted particles adhered to the down-skin surfaces [36]. A similar result can be found in the literature [219]. The Ssk of the primary surface is found to be larger than the staircase surface for almost all the surface inclinations, except for 3°, 6° and 9°, but the overall trend is almost the same for the primary and staircase surface. However, the predicted values of Ssk are close to zero, because the number of peaks and valleys are considered to be the same. The surfaces at 0°, 90° and 180° do not display any stair steps, thus, the resultant Ssk values are close to infinity [36].

Sku is described by the probability of distribution of height values [36]. It usually indicates whether the distribution of height values has sharp peaks ($Sku > 3$) or is small and widespread ($Sku < 3$). The calculated Sku value for all the surface inclinations was slightly above the nominal value of 3, see Figure 3.10(b). This gives a clear indication that the surface height distribution is basically normal distribution. It is also found that the Sku values of the staircase surface resemble that of the primary

surface, which only drops a little at a partial tilt angle, but almost all the results are greater than 3. The reported Sku value for all the surface inclinations of the predicted surface is lesser than 3 [36]. Similarly, there are no peaks and valleys at 0° , 90° , and 180° , therefore Sku is considered to be infinite in these cases [36].

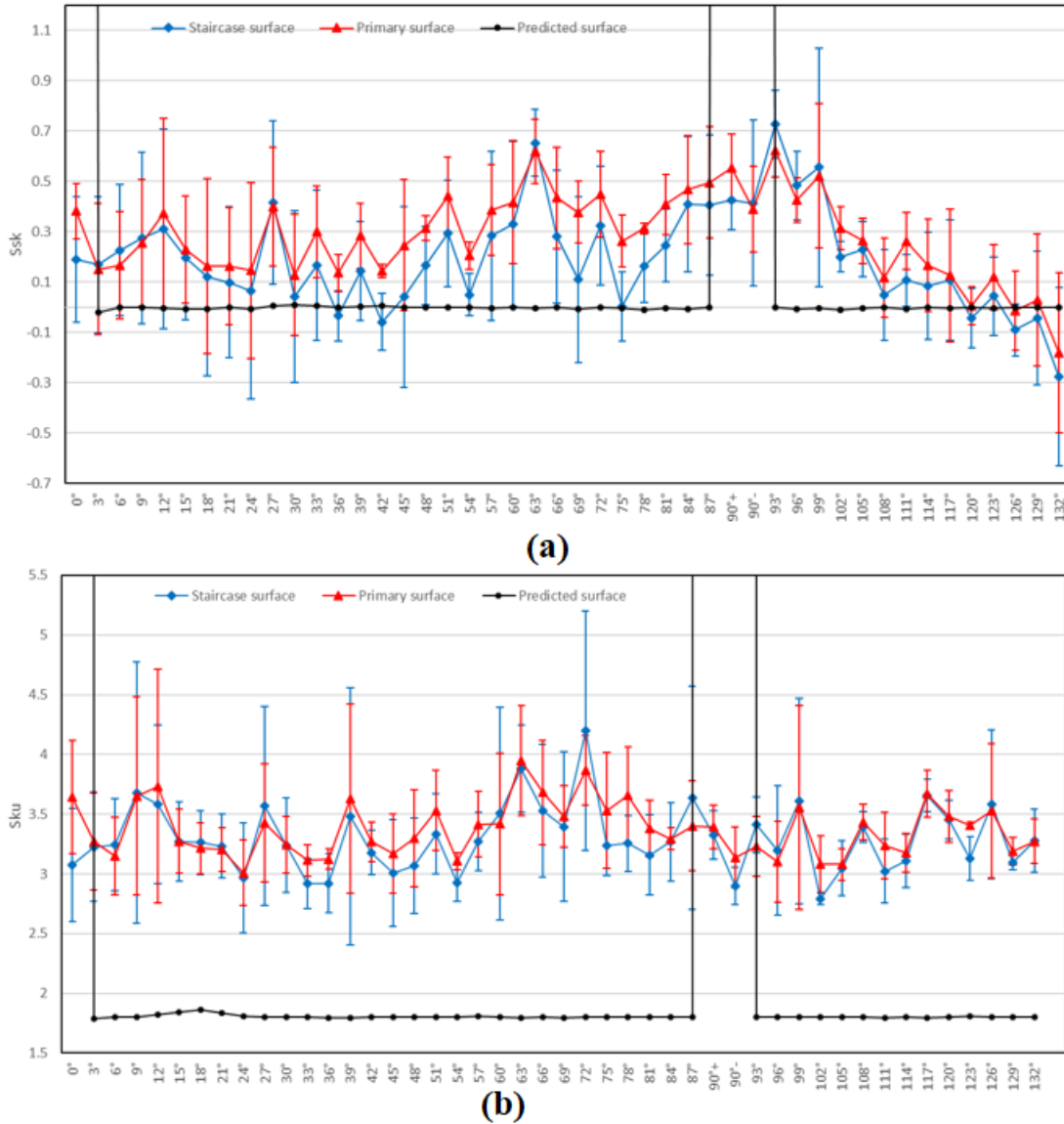


Figure 3. 10 Ssk and Sku of the primary surface, the staircase surface, and the predicted surface, with respect to surface inclination: (a) Ssk; (b) Sku.

Figure 3.11 a&b presents a further investigation of both Ssk and Sku by considering the surface height distributions at three different inclination angles, i.e. 0° , 90° and 132° . For 0° and 90° , the height distributions are skewed below the mean plane, see Figure 3.11(c)&(d), which implies positive Ssk values. In comparison, the height distribution of 132° appears to be skewed above the

mean plane, indicating a negative S_{sk} , see Figure 3.11(e). The shapes of the three height distributions were found shaper than that of the normal distribution, and thus their S_{ku} values are all positive, see Figure 3.11 (c-e). These findings are all consistent with the S_{sk} and S_{ku} values displayed in Figure 3.10.

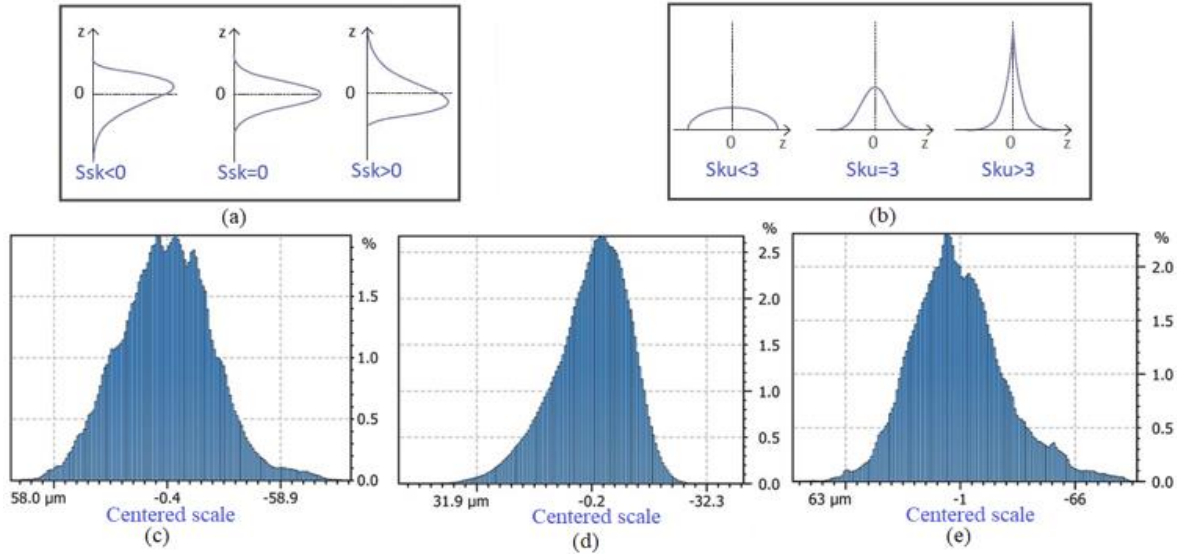


Figure 3. 11 Surface height distribution of three inclination angles: (a) significance of S_{sk} with respect to surface height distributions [308]; (b) significance of S_{ku} with respect to surface height distributions [157]; (c) surface height distribution of 0° ; (d) surface height distribution of 90° ; (e) surface height distribution of 132° .

3.3.3 Spatial parameters

The Sal parameter is defined by the minimal correlation length of the new location with respect to the original location. Sal is related to the periodicity of the surface, which is dominated by the melt track stripes (at 0°), and staircase effect (above 3°). Sal displays a general decline trend for the up-skin surfaces, and a strong rising trend for the down-skin surfaces, see Figure 3.12. This is in line with the staircase effect's characteristic. Figure 3.13 illustrates how the distance between stair step edges reduced as the angle of inclination increased. Overall, an undulating pattern can be seen in the Sal plot for the staircase surface, which could be related to the Sal 's sensitivity to short-wavelength periodic features [36]. If part of the particle features remains on the staircase surface, it can introduce significant turbulences to the Sal trend.

The predicted surface displays a very interesting Sal trend consisting of a sharp step peak at 3° , and a gradual decline to become flat at 90° . Based on the prediction model, Sal decreases with the inclination angle increase, which completely aligns with the reduction of the step width illustrated

in Figure 3.13. The predicted surface at 0° presents a purely flat surface (no consideration of melt tracks), thus the reported Sal value is zero. This is the same for 90° (no staircase at all). Sal of predicted down-skin surface maps the changing trend of the up-skin surface by reflection in terms of 90° [36].

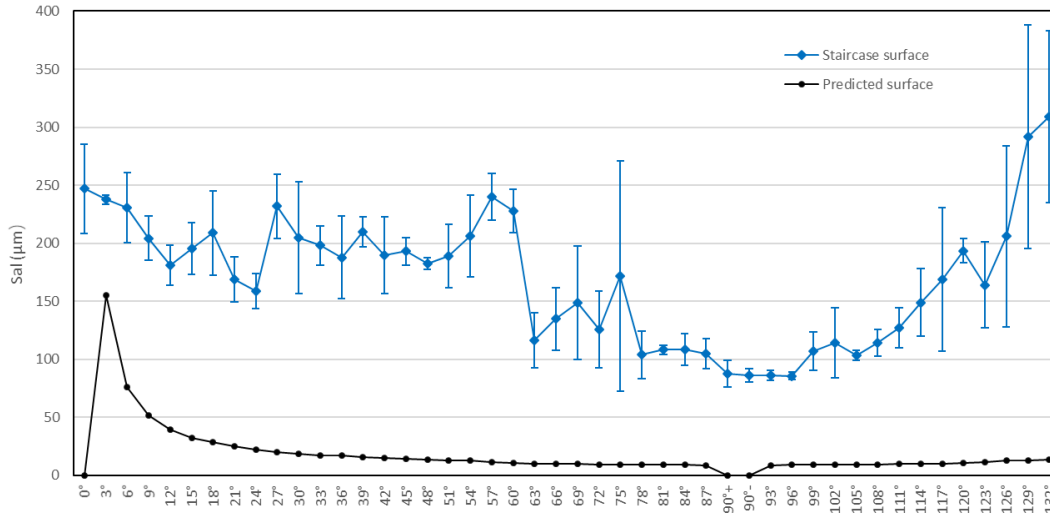


Figure 3. 12 Sal of the staircase surface, and the predicted surface, with respect to surface inclination.

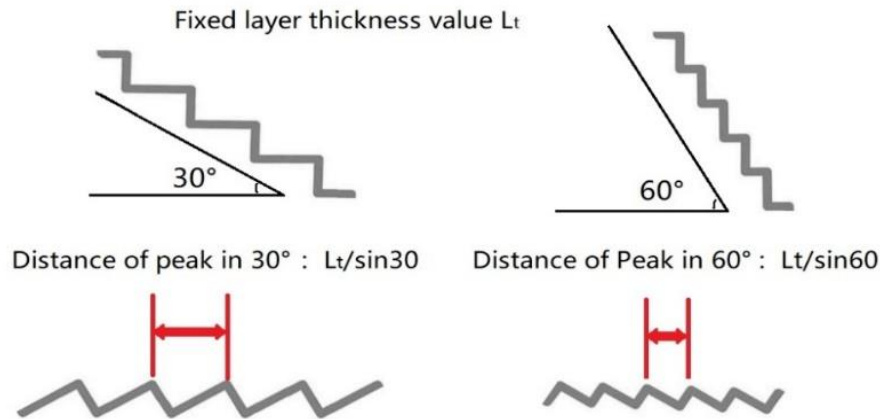


Figure 3. 13 Schematic to illustrate the variation in staircase width.

Str (texture aspect ratio) is a measure of uniformity of the surface texture [36,157]. Figure 3.14 illustrates the trend of Str with respect to different surface inclinations. The Str plot for particle surface displays a more or less stable trend overall (except between 0° - 27° surface inclinations) with the values approaching 1, which evidences the isotropic nature of particle features. In

comparison, the Str trends of the staircase surface and primary surface show numerous changes somewhat similar to Sal. Overall, Str for both staircase and primary surfaces is close to 0, indicating that these surfaces are anisotropic. The graph clearly shows that the staircase is the primary factor influencing Str [36].

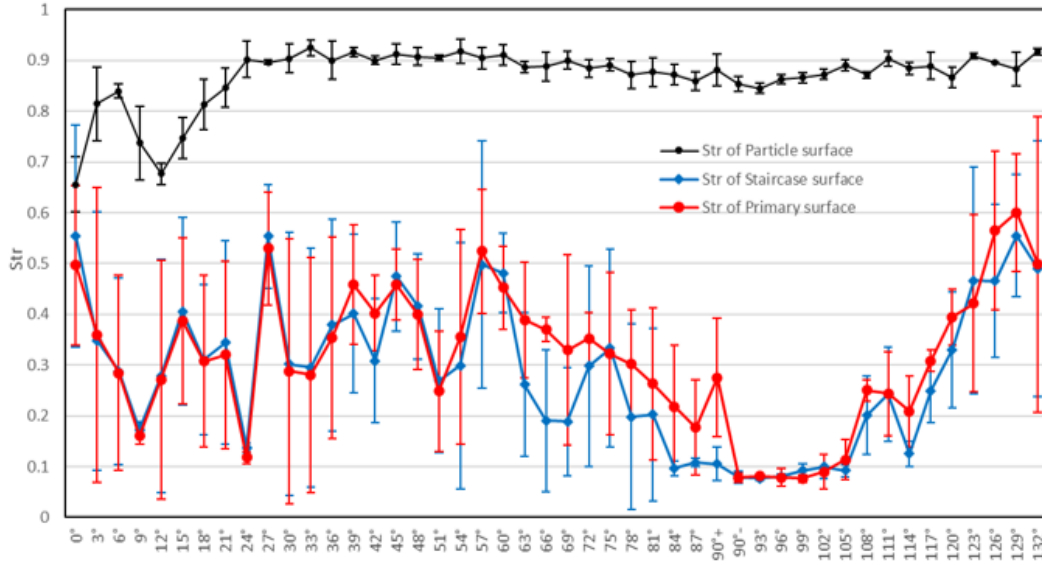


Figure 3. 14 Str of the primary surface, particle surface, and the staircase surface with respect to surface inclination.

3.3.4 Hybrid parameters

Sdr is useful in surface coating, adhesion, lubricant, heat exchanger applications etc., where the functional performances are highly linked with the surface area. Figure 3.15 displays Sdr values for up-skin and down-skin primary surfaces in relation to various inclination degrees. Sdr trend rises as the inclination angle increases. By comparing the Sdr results of primary surface and the staircase surface, it is discovered that their trends and specific values are extremely similar. This suggests that the staircase effect has less of an impact on Sdr. The attached particle features on the surface are the main factor influencing Sdr [36].

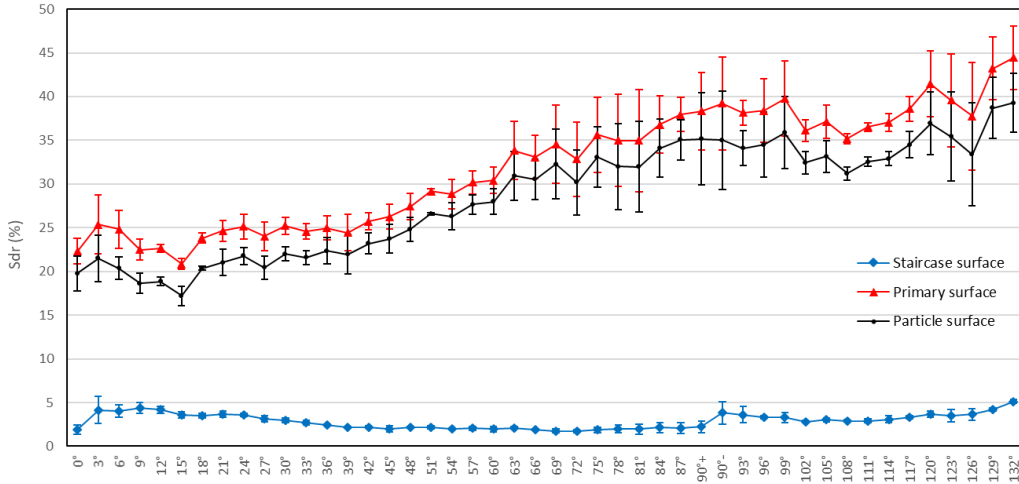


Figure 3. 15 Sdr of the primary surface, particle surface, and the staircase surface with respect to surface inclination.

Sdq is generally used to distinguish between the surfaces with similar roughness [36]. As displayed in Figure 3.8, the recorded changes for Sa and Sq values from 60°-90° and 90°-117° are relatively smooth. However, when comparing Sdq in the same regions, it is found Sdq displayed steady increase with the increase in inclination angle, see Figure 3.16 [36]. In general, Sdq in the range from 0° to 90° increases slowly in a minor oscillation pattern; In contrast, the down-skin surface exhibits a V-shaped trend between 90°-132°. Overall, the changing trend of the up-skin surface Sdq is relatively uniform, whereas the down-skin surface is more turbulent [36].

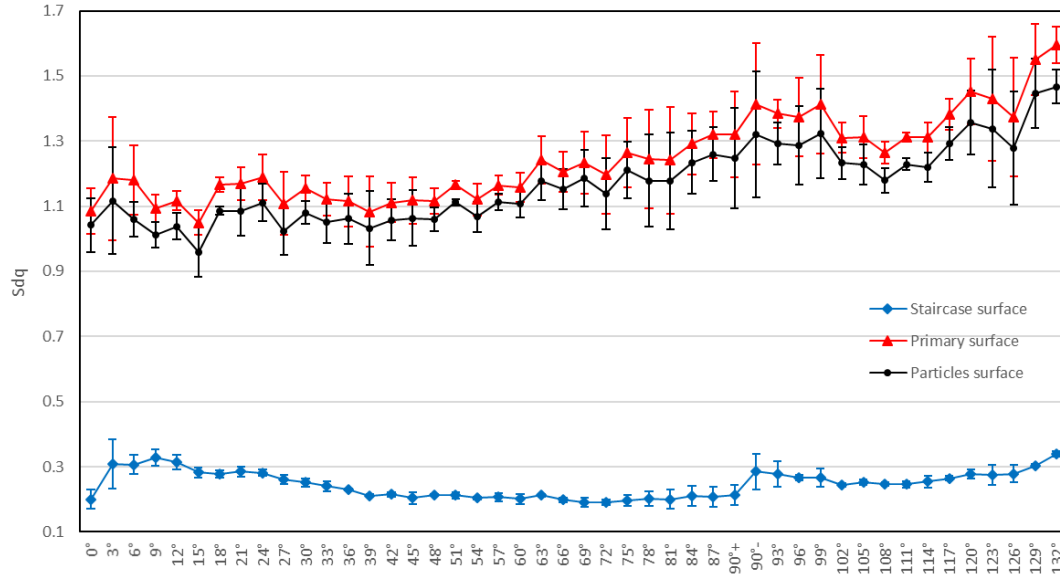


Figure 3. 16 Sdq of the primary surface, particle surface, and the staircase surface with respect to surface inclination.

3.3.5 Functional parameters

Functional parameters were developed to characterize common functional properties, such as wear and tribological-related characteristics. The volume parameters are obtained by splitting the material ratio curve into three zones by applying two material ratio thresholds Mr1 10% and Mr2 80%, with the default assumption that the peak materials embrace 0-10% of the material ratio whilst the core material/void ranges cover 10-80% and void valley range from 80% to 100% of the material ratio [36, 366-368]. It should be noted that Mr. 1 and Mr. 2 can be configured flexibly depending on the needs of a particular application. This study used the peak material volume parameter (Vmp) to examine the particle characteristics on the truncheon surface topography. It is discovered that the material ratio thresholds Smr1 and Smr2 obtained from the Sk parameters are more appropriate for the analysis of LPBF topographic characteristics (particles and subsurface pores), as opposed to employing the default Mr1 ratio of 10% [36,367,368].

Figure 3.17 shows the Vmp results with respect to Smr1. As the inclination angle increases, the Vmp of the up-skin surface generally increases, while the Vmp of the down-skin surface exhibits an irregular changing pattern. The steady increase in Vmp for all up-skin surfaces (0°-90°) is credited to the increase in the amount of un-melted/partially-melted particles and spatters attached to the edges of the steps. In comparison, the down-skin surfaces (90°-132°) do not show so many interesting facts, instead, the trend appears to be flat with a large standard deviation. This

phenomenon is attributed to the un-melted powders in the down-skin surface occupying the whole down-skin surface which presents a more irregular surface topography in comparison to the up-skin surface. The irregularity of the down-skin surface is even deteriorated by residual heat energy and the tendency of molten metal liquid moving downwards due to gravity effects. Similar results are also observed in particle analysis [36] (see section 3.3.7).

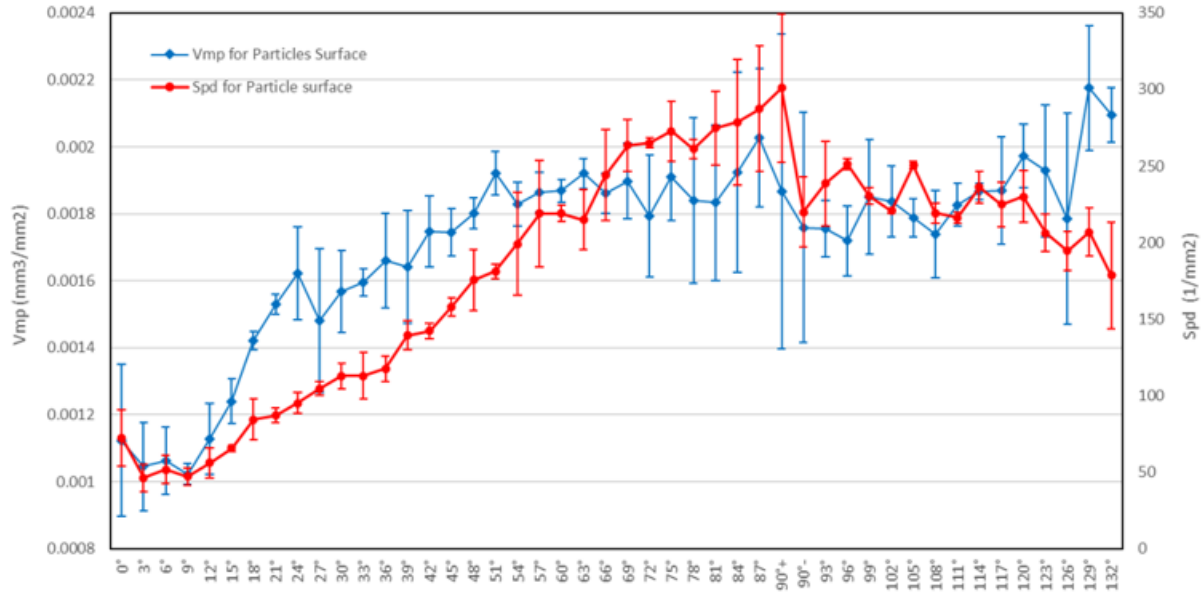


Figure 3. 17 Vmp and Spd for the particle surface with respect to surface inclination

3.3.6 Feature parameters

Spd indicates the density of peaks which is based on the watershed segmentation of surface topography with 5% Wolf pruning [32, 36]. The Vmp and Spd of the particle surface in relation to the inclination angles are shown in Figure 3.17. The number of peaks on the up-skin surfaces continuously increases between 3° and 90° as the inclination angle rises. It is important to remember that Spd dramatically drops between 0° and 3° [36]. This is ascribed to the presence of spatters attached to the surface at 0°. The down-skin surface presents a slow decrease of Spd, which forms a certain reflection symmetry to the up-skin surfaces but shows more variations due to the random nature of the down-skin surface topography. It is worth noting that by comparing the Spd and Vmp trends for down-skin surface: Spd drops when the down-skin inclination rises, whereas Vmp experiences the exact opposite. This means that there are more big particles or large protrusions appear on the bottom surface as down-skin tilt angle increases [36].

3.3.7 Particle analysis

Complimentary to Spd, a height threshold segmentation approach is applied to the particle surface (the staircase effect has been excluded). By comparing the surface height with a predetermined height threshold, the particles are recognized [36]. The surface portion is considered a particle feature if it is over this threshold. For the precise identification of particles, this threshold must be determined. In order to maintain the consistency of the particle volume density analysis in the case of Vmp, this threshold is chosen as the surface height corresponding to Mr1 of the material ratio curve, which is adopted to separate the peak zone from the core zone, (the peak zone represent the particle features) [36]. A similar comparable study can be found in [368]. Furthermore, the number of particles, the particle coverage, and the particle density are calculated respectively, to provide a quantitative characterisation of particles [36].

These three parameters basically show similar trends, see Figures 3.18 & 3.19. Six examples of particle identification and associated particle coverage ratio and numbers are illustrated in Figure 3.20. The three particle characterisation parameters of the up-skin surface rise slowly, while those of the down-skin surfaces show a flatter pattern. On the up-skin surface, the number of stair-steps increases as the inclination goes up, while the corresponding width of these steps gradually decreases. This causes a rising number of particles to adhere to the edges of the steps [36, 215]. On the contrary, the number of particles and the particle coverage rate on the down-skin surface remains relatively steady (see Figure 3.18). During the melting of the down-skin surface, the residual heat is accumulated, resulting in the expansion of melt pool; and melt metal liquid moves downward due to the gravity effect. All of these factors play a key role in the adherence of particle features and the unevenness of the down-skin surface [36].

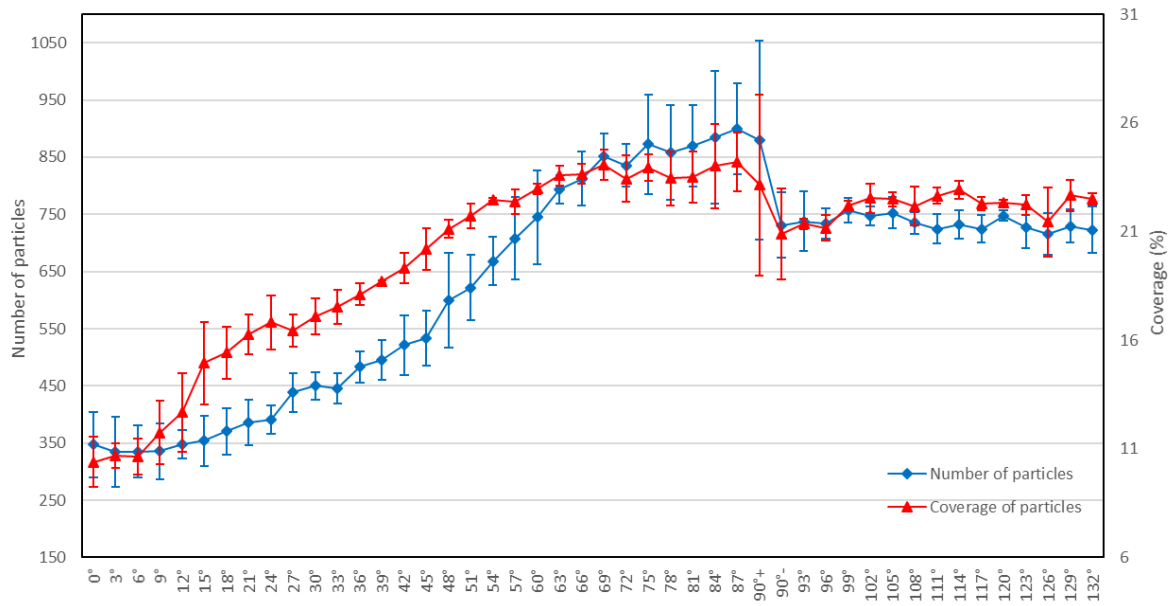


Figure 3. 18 Number of particles, particle coverage of the particle surface with respect to surface inclinations.

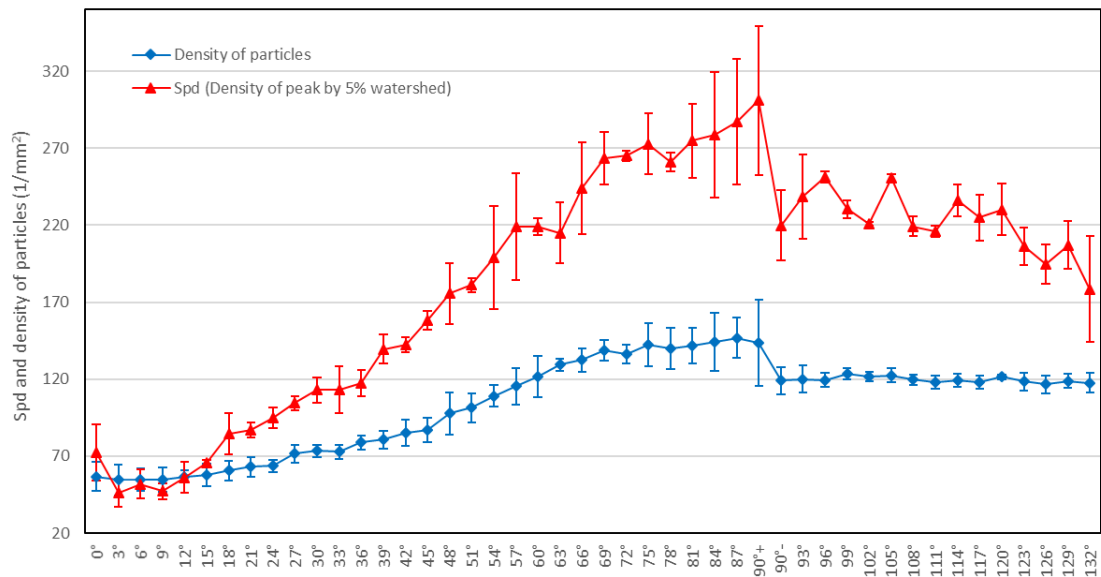


Figure 3. 19 Comparison of particle density and Spd of the particle surface with respect to surface inclinations.

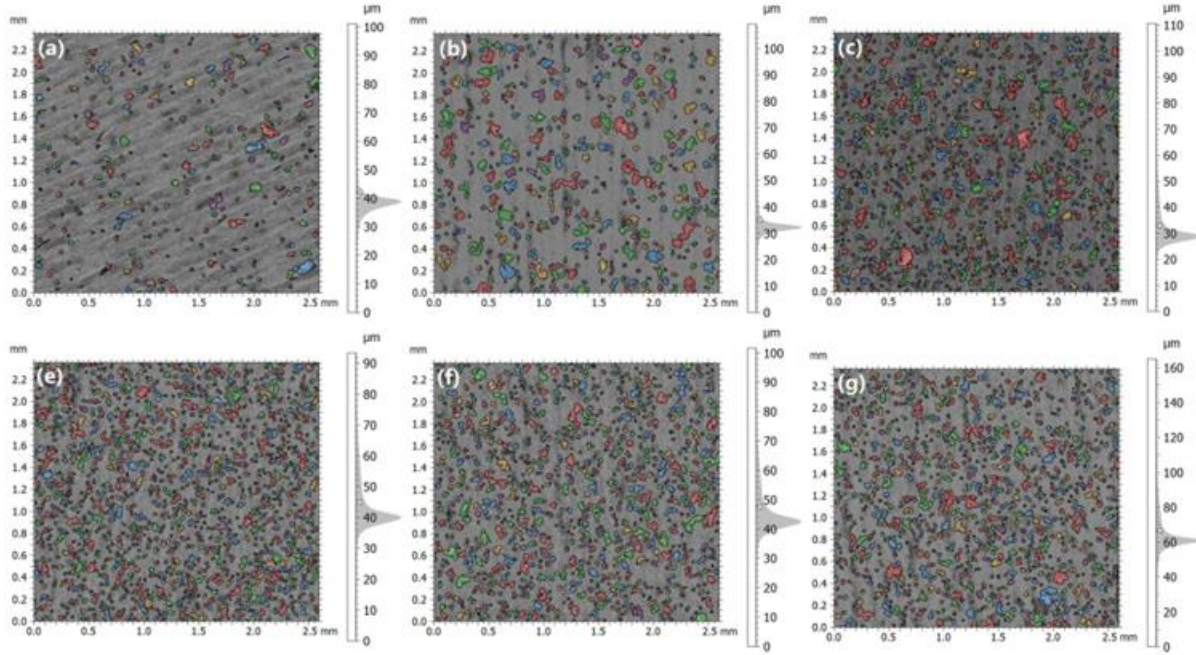


Figure 3. 20 Particles identification for six inclined surfaces: (a) 0° , 314 particles, 10.20 % coverage; (b) 30° , 394 particles; 18.34 % coverage; (c) 60° , 685 particles, 24.36 % coverage; (d) 90° , 848 particles, 27.28 % coverage; (e) 114° , 717 particles, 24.65 % coverage; (f) 132° , 707 particles, 24.33 % coverage.

3.4 Summary

The impact of different build inclination angles on the surface topography of the LPBF Truncation artefact is investigated. Additionally, a surface texture prediction model built on trigonometric functions was adopted to compare the outcomes of the measured and predicted surface texture parameter values. Suitable surface texture parameters were utilized to quantify the prevailing surface irregularities (staircase effect, spatters, and un-melted/partially melted particles) with respect to different surface inclinations [36].

- S_a and S_q of inclined surfaces are significantly influenced by the staircase effect, whereas the impact of the particles is less significant. For all the cases, S_a and S_q trends tend to closely resemble the predicted model. As a result of intermittent heat transfer, S_a and S_q of the down-skin surfaces often tend to be higher than those of the up-skin surfaces. Both up-skin and down-skin surfaces showed a similar pattern of S_{sk} , with the bulk of S_{sk} being positive, indicating the surface is dominated by peak features. S_{ku} was marginally higher than nominal value 3, indicating that the surface height distribution is basically a spiky-natured normal distribution [36].

- Sal displayed declining trend as the surface inclination approached 90° , which is consistent with the observation that the width of staircase decreased as the inclination angle increased. Sal is primarily controlled by the staircase effect, while any residual particle features portions on the staircase surface can also have an impact [36].
- Sdr and Sdq of the primary surface and the particle surface both exhibit sharp rising trends with an increase surface inclination. It is important to note that the increase in surface area and general surface slope were shown to be mostly caused by particle features, with the staircase effect having a negligible effect [36].
- Vmp is used to characterise the volume density of particle features, with the threshold ratio set to Smr1. Vmp generally exhibited rising tendency against the surface inclination, indicating that the surfaces with greater surface inclination have a larger volume of particles [36].
- The Spd of the particle surface showed a strong rising trend for the up-skin surfaces, signifying the increase of particle features, whereas the down-skin surfaces exhibit the opposite tendency [36].
- The values of the particle descriptors obtained from the particle analysis show an upward tendency for the up-skin surfaces, which is followed by a pattern that is largely stable for the down-skin surfaces. All descriptors exhibit the consistent general trend [36].

Chapter 4 Surface quality characterisation of external and internal surfaces of LPBF processed ball artefact built with varying inclination angles

The external surface quality of acetabular bone implants is rougher from outside and smoother from inside, whereas the tibial augments possess rougher internal surface and smoother outside. To design or tailor the different surface quality of same functional implants or components to the desired roughness levels, it is crucial to study the surface quality fingerprints that emerge on both external and internal surfaces built with varying inclination angles. In addition to the external surface quality, the surface texture metrology of AM internal geometries encompassing elaborate surfaces is extremely important. The complex geometry of internal surfaces poses a significant challenge for post-processing, and post-processing alone is not sufficient to improve the internal geometries' surface quality and thereby mechanical performance [12,38,33,226]. There is a decent amount of literature available pertaining to surface texture characterisation of external surfaces, but the research specific to surface texture characterisation of AM internal surfaces is scarce.

The surface characteristics of basic cubes, smaller size cylinders or standard artefacts have been studied so far, but the complex surface topographies emerge on bigger size artefacts comparable with the acetabular implants, tibial augments or the components of rocket engines has not been investigated. Hence, this comprehensive research is mainly focused to (i) visually inspecting the diverse defects and asperities, (ii) systematically characterise, correlate and quantify these defects and asperities with an suitable areal surface texture height parameters, hybrid parameters, and the features-based particle analysis based on ISO 25178-2 [32], (iii) establish the interrelationship between the emerging surface asperities as the function of different sloping angles and areal surfaces texture parameters of various longitudinal facets' external and internal up-skin and down-skin surfaces of LPBF ball artefact, including latitudinal facet external and internal surfaces (iv) examine the impact of location of ball artefact on the substrate and the laser beam incidence angle on the resultant surface quality, (v) comprehensively study the statistical significance of inclinations angles, build orientations, and the type of surfaces by statistical analysis of variance (ANOVA).

The ball artefact fabricated in this Chapter is comparable with an acetabular bone implant, and tibial augments of the knee of biomedical applications. Additionally, the ball artefact is similar to various aerospace applications like flow channels-integrated aerospike engine, liquid rocket

engines components; combustion chambers, thrusters, valves and line ducts, turbomachinery, cylinder liners, flow channel cooled nozzles, and uncooled nozzle extensions etc. [145,146,369]. A part of this research work has been presented as a poster “*Investigating the surface texture of internal and external metal AM surfaces built with varying inclination angles*”, at the International Conference of Metrology and Properties of Surfaces 2022, University of Strathclyde, Glasgow.

4.1 Research methodology

4.1.1 Ball artefact design and fabrication

The metal powder used for this experiment is Ti6Al4V (Grade 23 15-45 μ m) alloy supplied by Carpenter’s additive U.K. It is evident that as-received titanium fine powder is dominantly regular in size with mostly spherical-shaped particles. The supplied powder is free-flowing with good packing density, the apparent density is 2.6 g/cm³ and the reported tapped density is 2.9 g/cm³. The size distribution and powder morphology are shown in (Figure 4.1a&b), Morphological analysis revealed the results in the vicinity of the 10th (D10), 50th (D50), and 90th (D90) percentile for particle size values are found to be 21.3 μ m, 31.5 μ m, and 48.1 μ m respectively.

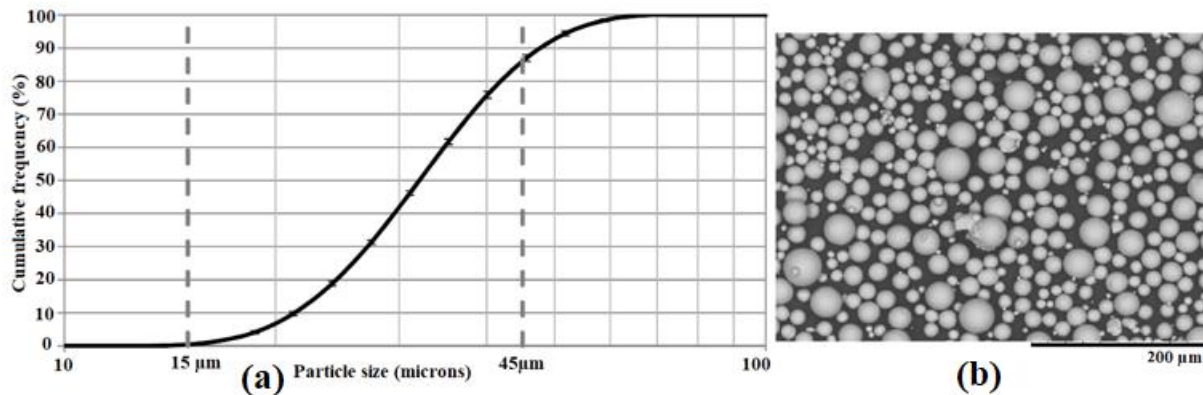


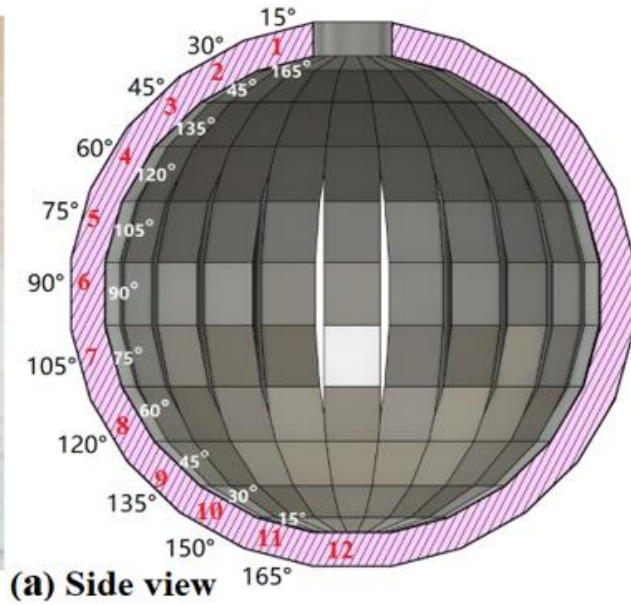
Figure 4. 1SEM image showing (a) size distribution and (b) characteristic morphology of the grade of Ti-6Al-4V powder

A Renishaw AM 500Q metal additive manufacturing machine has been used to fabricate a bespoke ball artefact at the MTC facility U.K. The AM 500Q machine is configured with a pulsed Nd: YAG laser with a wavelength of 1070 nm that generates a pulsed laser wave of high power of 500W. The AM machine is also equipped with two oxygen sensors to monitor the low oxygen (value below 0.1 vol%) content during the fabrication process. Before starting the process, itself, the build chamber is filled with 99.996 % pure Argon gas to avoid AM-built parts from oxidation. It must be ensured that the build chamber is continuously flooded with Argon gas during the

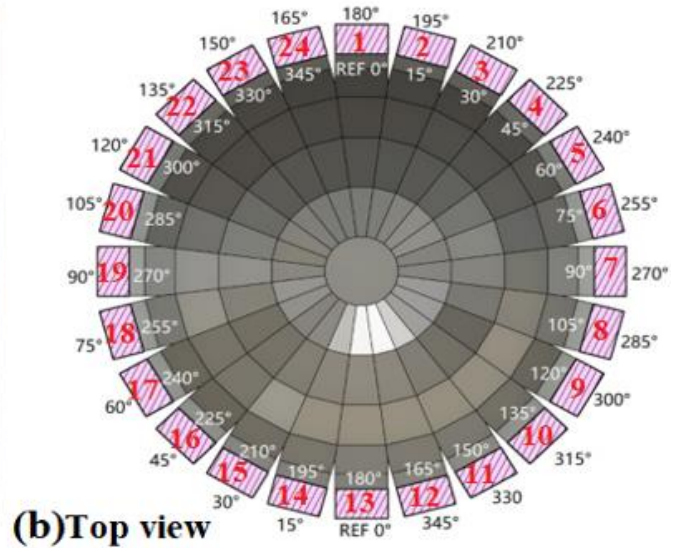
fabrication process to keep the oxygen content ~ 100ppm. A pure titanium base metal or substrate is used to build AM ball artefact. The base is polished to achieve good bonding of the titanium powder particles. The baseplate is heated to ~150°C and maintained at this temperature during the whole process until the AM ball artefact build is completed. The general scan strategy employed is mentioned in Table 4.1, while the STRIPE hatching pattern was used for the core scan strategy. The diameter of the ball artefact is 50mm, which is comprised of 24 facets, i.e. 24 latitudinal full-turn surfaces (0°-360°), 12 longitudinal surfaces (0°-180°) with an increment of 15° for each inclination angle (see Figure 4.2a & b).

Table 4. 1 Main LPBF process parameters adapted in this part of the research

Parameters	Values
Laser power (W)	320
Hatch spacing (µm)	95
Layer thickness (µm)	60
Point distance (µm)	60
Exposure time (µs)	90
General scan strategy	Meander



(a) Side view



(b) Top view

Figure 4. 2Schematic illustration of LPBF ball built with different inclination angles (a) side view & sectioned longitudinal facet to show external and internal surfaces and (b) top view & sectioned latitudinal facet to show external and internal surfaces.

4.1.2 Measurement strategy

All the surfaces of LPBF built ball artefact are measured using Bruker Contour LightSpeed™ (LS) focus variation measurement system (FVM) by adopting the following parameters mentioned in Table 4.2. Each location is measured simultaneously by switching between ring light and coaxial light illumination types, keeping the rest of the parameters unchanged. The ring light is helpful to capture a detailed 3D map of surface height data including deep valley terrain of the rough AM surfaces, while co-axial light is beneficial to visually capture images of surface asperities, and clearly distinguish particles and smooth terrain [370].

Table 4. 2 Focus variation measurement method configuration

Magnification	10x lens
Illumination type 1	Ring light (capture 2D½ topographical data)
Illumination type 2	Coaxial light (visual inspection)
Lateral resolution	1.11 µm
Vertical resolution	0.33 µm
Sampling distance	0.789 µm (both in X and Y directions)
Measurement (data) size	0.7 mm x 0.7 mm

The LPBF ball artefact mimicking the globe is built with different inclinations from 0° to 180° longitudinally, and 0°-360° latitudinally with 15° increments sloping angles. Out of all 24 facets, 7 facets composed of 12 surfaces covering 30% of the total ball artefact surfaces have been selected for the measurement of longitudinal external and internal surfaces. Longitudinal measurements are taken at one position from 15°-135° for external surfaces, and 15°-165° for internal surfaces respectively (see Figure 4.3a and b). For the latitudinal facet's external and internal surfaces, the measurements are taken at three positions starting from the reference (REF) surface covering full-turn (0°-360°:24 external & 24 internal surfaces) circumferentially at the equator as shown in Figure 4.3c. In addition, to verify the repeatability of the latitudinal measurement, five repeated measurements are performed on the full-turn latitudinal facet at 90° 1, 2, and 3 (see Figure 4.2c). The latitudinal facet measurement and characterisation are dedicated to investigating the uniformity of surface roughness.

The selected 7 external longitudinal facets comprised 63 surfaces in total: 42 surfaces are considered up-skin (US) surfaces (15°-90°), and the remaining 21 surfaces are regarded as down-

skin (DS) surfaces (105° - 135°). Similarly, the selected 07 internal facets measurement is comprised of 77 surfaces in total: 42 surfaces are designated as US surfaces (15° - 90°), and the rest 33 surfaces are identified as DS surfaces (105° - 165°). Overall, 188 surfaces have been measured in this research, in which longitudinal facets constituted 140 surfaces, while the latitudinal facets accounted for 48 surfaces measured in full-turn at the equator. At the end of the external facets' measurement, the ball artifact is sawed-off into small sections to ensure the right measurement of the internal surface face US and DS surfaces. Measurement at 0° surface is not considered as the whole surface turned out to be a small hole. The presence of support remnants on the remaining external surface inclinations made the areal measurement unfeasible, thus the surfaces beyond 135° are not considered.

4.1.3 Data acquisition and processing

The measured data is first processed by applying the least-square levelling operation. The levelled surface is directly used to calculate the surface texture parameters according to ISO 25178-2 [32]. Optical images are used to visually analyze the various surface topographical features. The analysed surface texture parameters results are beneficial for characterising and quantifying the various topographical asperities that exist on different surfaces of an AM ball artefact.

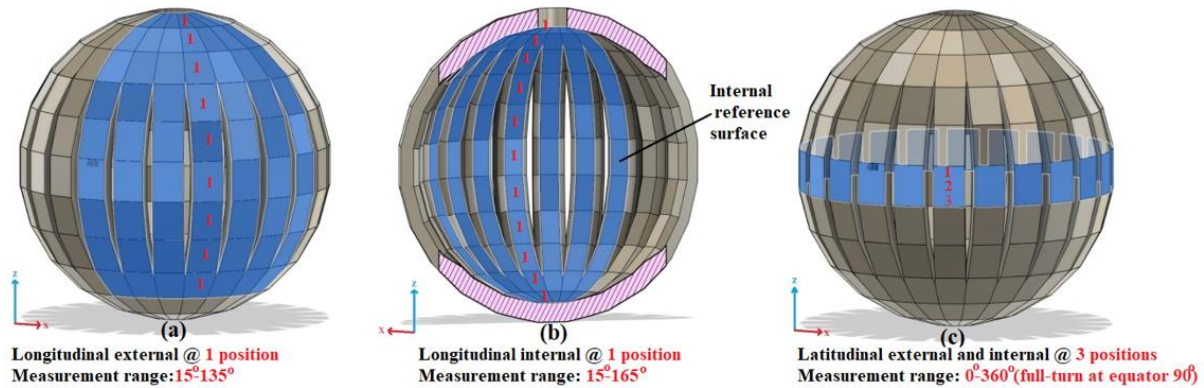


Figure 4. 3 Focus variation measurement scheme (a) 48 latitudinal facets in full-turn-24 external & 24 internal surfaces, (b) 07 longitudinal external facets, and (c) 07 longitudinal internal facets. Highlighted blue colour indicates the measured facets.

Conventional surface texture metrology is predominantly focused to characterize the overall surface topographical asperities data of the whole measured region by a limited number or set of scalar values. However, these conventional texture parameters are not intending to provide information about the individualities present on the surface. In saying those surface texture parameters are not capable to give details about the number of particles/asperities present on the

surface, nor their spatial distribution. Instead, these texture parameters would assist in capturing the overall or entire topographical data (for example, roughness Ra or Sa & Sq, etc.) of the surface of the region being measured. To overcome this limitation, feature-based particle analysis is carried out by adopting a spatially decomposing application of threshold segmentation, according to the Smr1 value. The captured surface measurement data consist of digital topographies which have been segmented to isolate partially-melted/un-melted particles and spatters from the surface that provides valuable quantification data, and the perception of the individual surface asperities which form during the LPBF process. Each individual segmented region is referred to as the feature that is then characterized related to its geometrical features. After separating, the leveled surface data is extracted into waviness surface and particles surface through Robust Gaussian filtering [36].

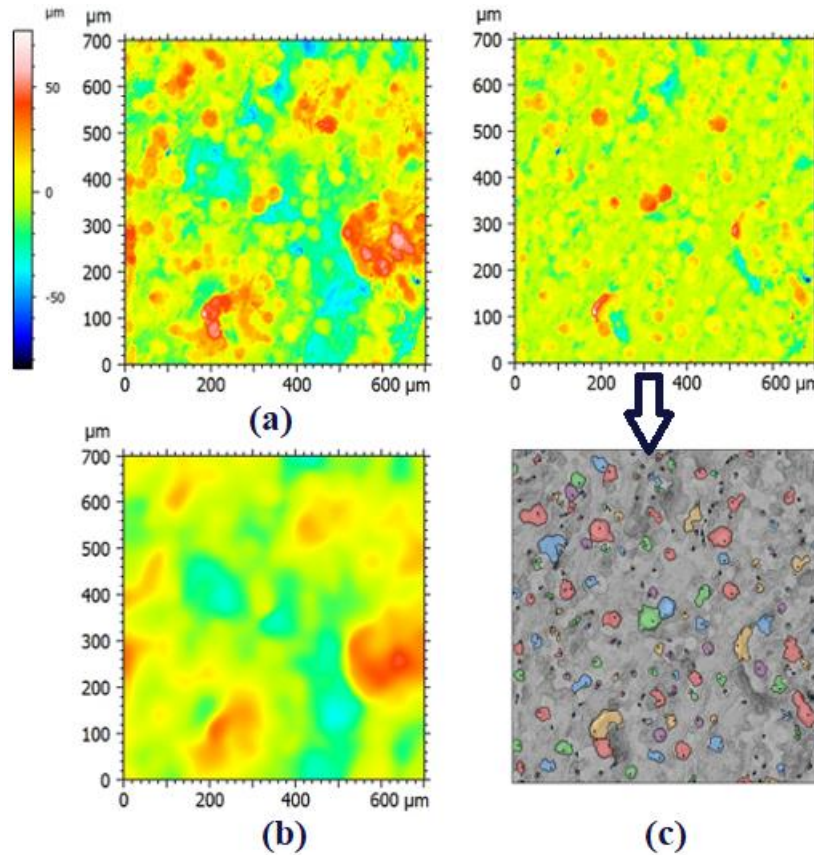


Figure 4. 4 Illustration of particle analysis, (a) raw data after leveling, (b) waviness surface, (c) particle surface and threshold particle.

A Robust Gaussian filter is well acknowledged to separate the surface particles and waviness surface [364]. The selected cut-off wavelength of 80 μm is used to separate the waviness surface

and particle surface, and the number of particles is calculated by using threshold segmentation method. The threshold height is set according to the S_{mr1} parameter of the surface [367]. The waviness surfaces are comprised of only higher peaks and the larger particles formed by the fusion of smaller particles minus spatters and un-melted/partially-melted particles, while the extracted particle surface mostly consists of spatters, un-melted/partially-melted individual particles information. The step-by-step data processing operation is represented in Figure 4.4a-c.

4.1.4 Areal surface texture parameters characterisation

A spectrum of areal surface texture parameters employed in this research to characterize the surface topographical features of inclined LPBF surfaces are listed in Table 4.3. These targeted potentially useful parameters include height parameters (S_a , S_q , S_{sk} , S_{ku}), hybrid parameters (S_{dr}). Further details of specific surface texture parameters can be found in ISO 25178-2:2012 [32]. The surface texture parameters characterisation was further complimented by feature-based particle analysis with the application of the threshold segmentation approach.

Table 4. 3 Areal surface texture parameters explored in this research

Categories	Surface texture parameters
Height Parameters	S_a (μm) - Arithmetical mean height of the scale-limited surface
	S_q (μm) - Root mean square height of the scale-limited surface
	S_{sk} - Skewness of the scale-limited surface
	S_{ku} - Kurtosis of the scale-limited surface
Hybrid parameter	S_{dr} (%) - Developed interfacial area ratio of the scale-limited surface
Particles analysis	Number of particles and particles coverage ratio

4.2 Results and discussions

4.2.1 Visual inspection of longitudinal facet external up-skin surfaces

The emergence of the staircase or stair-stepping effect is clearly visible between 15° – 60° up-skin surfaces Figure 4.5(a-d). Traces of ripples created by a fast-moving laser beam is obvious on the

surface at a 15° sloping angle. At very low surface inclinations the influence of adhered particles on the stair-step edges is less significant as the width of the staircase is considerably higher than the particle size; indicating that adhered particles proved to be the least contributors to the surface roughness. It is worth noting that between 75°- 90° sloping angles, the staircase effect started to become invisible, accumulation of particle features caused by un-melted and partially melted particles dominated all the inclined surfaces after 60°: which could be referred to as the transition zone from staircase dominated surface to particles featured surface, and other surface abnormalities (spatters, cracks) acclimated surfaces. The width of the staircase effect subsided as the inclination of sloping angles increased, generating a significant increase in the concentration of several surface abnormalities apparent. The diminution of staircase width is identified between 15°- 60°, beyond this sloping angle the staircase slowly began to disappear till the surface inclination reached 90°. At this point, the entire surface is mostly replaced by particle features and other surface abnormalities Figure 4.5(e, f). It is important to note that measurement and characterisation along the horizontal axis or the top surface will only consider just one layer, whereas the measurement of the vertical axis takes account across multiple melted track layers. These intermetallic multiple layers correlation can potentially lead to the increased roughness of side surfaces. It is interesting to note that the adhered particles on up-skin surfaces mainly resided between the boundaries of each melt track (see Figure 4.5(a-d)). Therefore, the main contribution towards the surface roughness of up-skin is confined to the staircase effect, which ascertains the size of each staircase and the gap between neighbouring staircases.

4.2.2 Visual inspection of longitudinal facet external down-skin surfaces

All the down-skin surfaces merely displayed particle features and other surface abnormalities, it is highly unlikely to distinguish the existence of the staircase effect. However, it is almost certain that the emergence of staircase effect in reverse direction on all the down-skin surfaces, but it turned out to be impossible to visually inspect as all the down-skin surfaces are completely occupied by the particle features and other surface irregularities. Also, it is intriguing to reveal that agglomeration of un-melted particles, partially-melted particles and spatters into a dross formation and bigger island-like protruded structures at a higher inclination (>105°) angle Figure 4.5(g-i). The rationale behind the emergence of higher number of surface asperities on the metal AM down-skin surfaces is attributed to the increased accumulation of particle features and agglomeration of dross deposition. The domination of the particle features and the dross formation are ascribed to

the combination of intermittent heat transfer (conduction) across the inclined parts melting tracks, lack of laser re-melting, and finally, the absence of a solid/rigid continuous support from the loose powder bed or from the supporting structures as compared to the strong persistent support provided by substrate/base plate or from the already solidified melt track layer(s). The absence of continuous support for down-skin surfaces results in heat transfer through the neighboring powder particles with low thermal conductivity which embrace a strong tendency of heat accumulation and induce liquid (molten melt pool) flow, consequently attracting a greater number of particles into molten melt pool (see position 1 in Figure 4.6a). The heat conduction through the solidified melting tracks or through the substrate/ base plate tends to be apparently higher when compared to the loose powder bed, contributing to the fewer number of particles attraction (see position 2 in Figure 4.6a and Figure 4.6b). At the same time the higher laser fluence absorptivity in powder particles as compared to the solid substrate or the base metal or from the previously solidified layers [35]. The number of adhered particles on up-skin surfaces is easily outnumbered by the adhered particles on down-skin surfaces. For up-skin surfaces, heat conduction occurs partly through the already solidified underlying melt track layers as well as through the loose powder particles, resulting in less adherence to particle features as compared to down-skin surfaces (see position 3 in Figure 4.6a). It is fair to note that build inclination angles exhibit a pronounced effect on balling and other forms of defects, owing to the accumulation of layer thickness and aggravated wetting characteristics at the melt track interface [34].

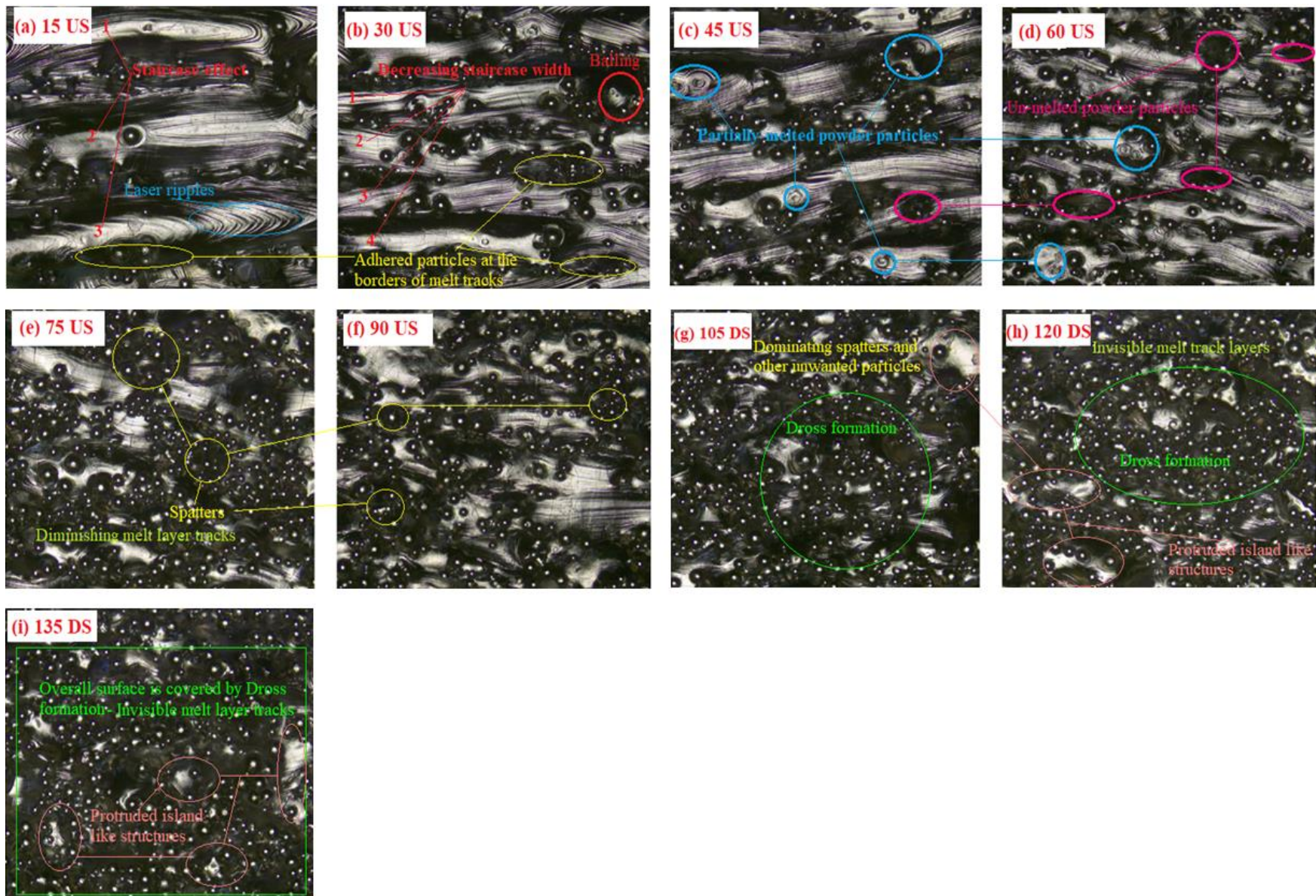


Figure 4. 5 Schematic illustration of longitudinal facet external surfaces, (a-f) up-skin surfaces, (g-i) down-skin surfaces

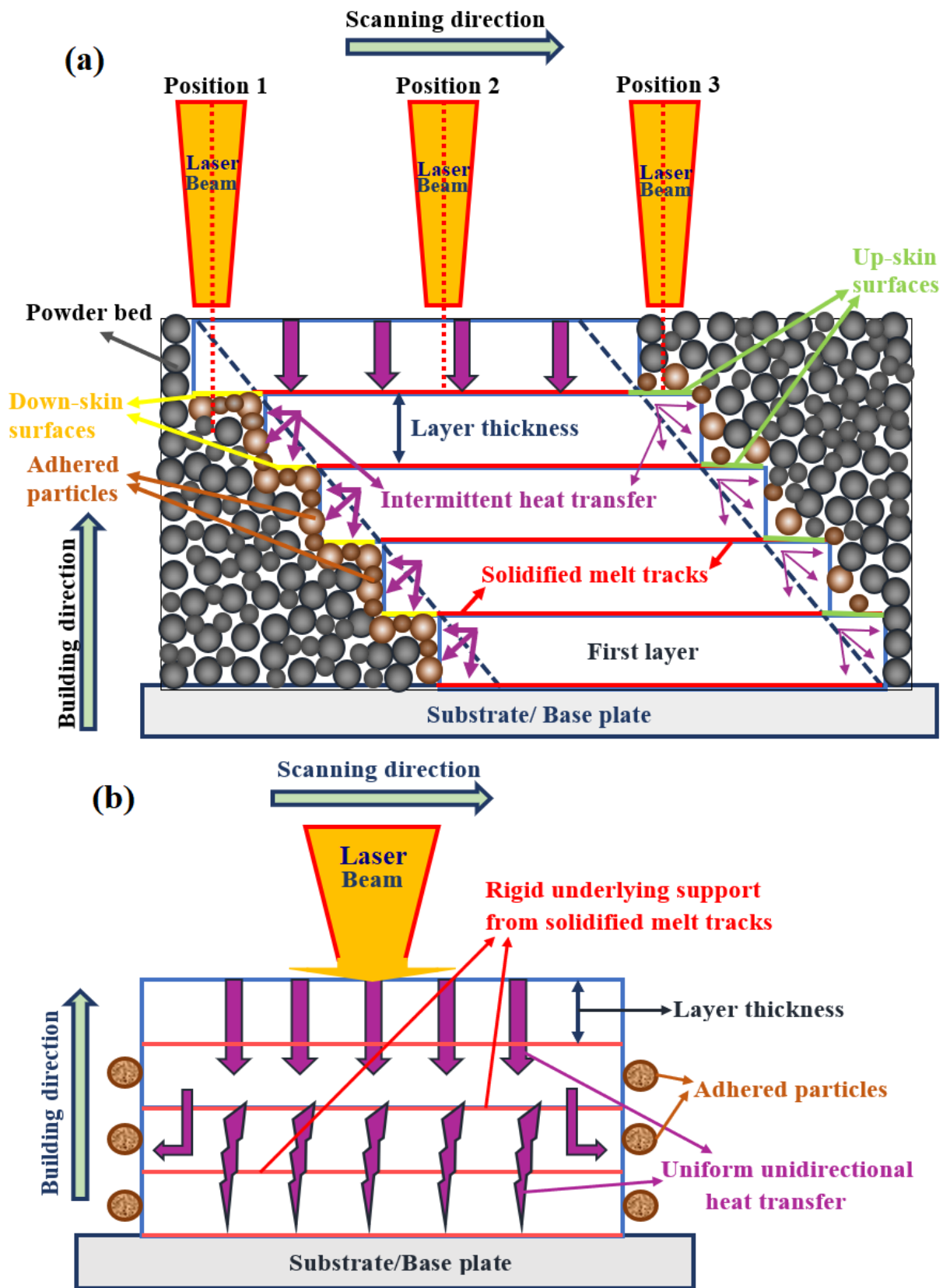


Figure 4. 6 Schematic illustration showing (a) rationale behind intermittent heat transfer, and (b) rigid underlying support from solidified melt track layers;

4.2.3 Visual inspection of longitudinal facet internal down-skin surfaces

It is imperative to understand that the external up-skin surface corresponds to the internal down-skin surface and vice versa, for example, the external 15° up-skin surface inclination angle is equivalent to the 165° down-skin sloping angle of the internal surface. To maintain the same cohesiveness with already described external surfaces; internal down-skin surfaces are first scrutinized for the simple reason that a 165° internal down-skin surface corresponds to a 15° external up-skin surface. The general perception related to visual inspection of internal surfaces is mostly similar to already discuss external surfaces with a bit more conviction. Figure 4.7(a-e) represents the internal down-skin surfaces at 165° - 105° sloping angles. The 165° down-skin surface reveals the extreme dross formation spread across the whole surface without any visible sign of melt track layers underneath. Moving further down to 150° surface presents island-like protruded structures, but the dross formation is significantly immanent. Spatters and other un-wanted particle features dominate the 135° and 120° inclined surfaces with minuscule visibility of melt track layers or staircase effect in the reverse direction. An equal percentage of particle features and melt track layers are evident on a 105° surface. The inclination angle defines the quantity of loose powder with a lower thermal conductivity that is present above the previous solidified melt track layer and then becomes solidified. The images taken between 165° - 135° display the shift between larger agglomerated particles and the bigger size island kind of structures caused due to spatters and dross formation. In spite of down-skin surfaces printed on top of the loosely dispersed powders which lacked continuous rigid support from underneath, the surfaces which had less steep sloping angles attracted fewer particles as compared to the greater number of adhered particles to steep inclination angle surfaces. This phenomenon is attributed to the partial heat transfer through the bulk material resulting in a smaller overheating zone. In contrast, more heat energy is transferred into the powder-bed leading to the formation of a larger molten melt pool and thereby dross formation in case of steeply angled surfaces [24]

4.2.4 Visual inspection of longitudinal facet internal up-skin surfaces

Figure 4.7(f-k) shows the internal up-skin surfaces for 90° - 15° inclination angles. Molten melt pool splash is clearly visible for 90° up-skin surface, in addition to inherent particles feature fingerprints. Sloping angles of 75° - 60° are considered as a kind of transition zones where unwanted particle characteristics slowly subside, and the simultaneous staircase effect begins to appear. The staircase effect becomes more significant displaying increased width between the stair steps as the inclination angle is further decreased from 45° - 15° . In the meantime, a

drastic decrease in un-wanted particle features attached at the borders of melt tracks is observed for these surface inclinations. Only a few countable particles feature are attached to a 15° surface. Laser ripples created from the rapid-moving laser beam are clearly evident at 30° up-skin surface.

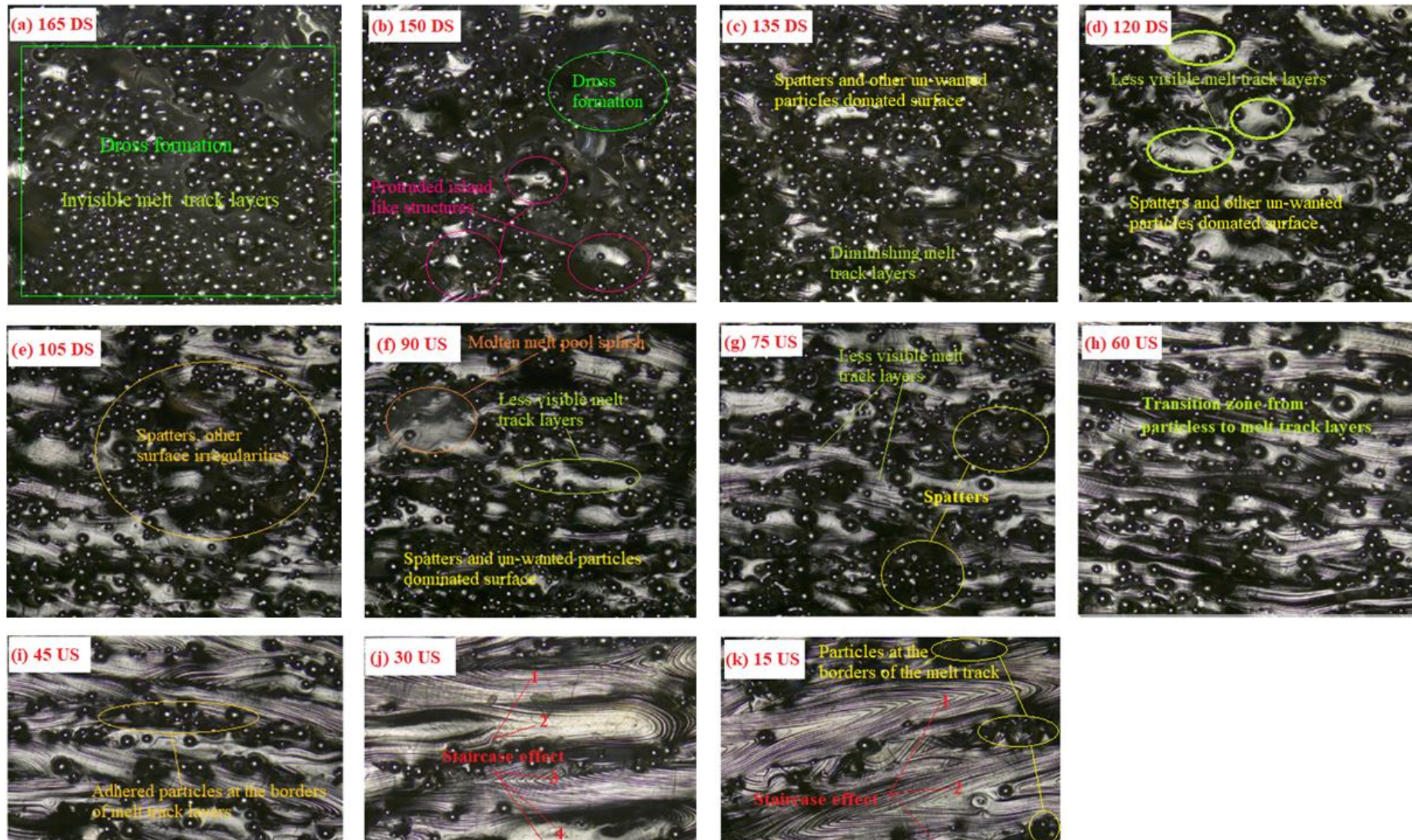


Figure 4. 7 Schematic illustration of longitudinal facet internal surfaces, (a-f) down-skin surfaces, (g-i) up-skin surfaces

4.2.5 Visual inspection of latitudinal facet external and internal surfaces

The visual inspection of the latitudinal facet is only limited to external surfaces, as there is minimal or no significant difference between the external and internal surfaces for full-turn inclination angles (0° - 360°) measured at the equator. Figure 4.8 (a-x) in appendix presents the external surfaces of 24 facets. It is not surprising to note that identical outcomes of latitudinal facet external and internal surfaces are obtained compared to longitudinal external and internal surfaces analyzed at 90° inclined surface. All 24 full-turn facets of external surfaces exhibited indistinguishable topographical characteristics consisting of less visible melt track layers in the background of dominant un-wanted particle features. A comparatively higher number of adhered particle features are registered especially at 285° , 315° , and 345° surfaces (Figure 4.8 (l-t, v & x)), which is an exception as compared to all other surfaces. This higher attraction of particles (~ 30 particles) is attributed to the intermittent heat transfer at the corners which is also confirmed by the particle analysis (see Figure 4.26). Almost all surfaces greater than 300° angle recorded a significantly higher concentration of particles adherence, however, this increase is not linear. A considerable number of spatters redeposition are only evident at higher inclination angles. The incidence of spatters varies with build inclination angles, signifying randomness of the spatters redeposition. Spatters formation are related to vapor jet or gas (outlet) flow which is presumably affected by other stochastic elements such as gas flow variations that takes place during LPBF process [143]. The suitable justification given for this event could be related to the increased radial distance of the laser fluence with respect to the centre of the build platform. Figure 4.9 shows the position of AM ball artefact placed away from the laser window and/or close to the boundary build platform during the fabrication process. Another more suited explanation is the angle of laser beam incidence which is not exactly perpendicular to build platform or printing chamber [371], resulting in the emergence of a higher number of surface irregularities including dross formation (see Figure 4.10). It is common knowledge for logical reasons the laser window is usually placed at the centre of the LPBF machine build platform. And for geometrical considerations, laser fluence melts the powder in a circular area at the centre (circular aspect ratio equal to unity), and in the rest of the locations especially at the borders or corners, it tends to melt in an elliptical area (elliptical aspect ratio higher than one) [372]. To overcome this shape warping or dimensional errors, most of the commercial LPBF machines (including Renishaw AM 500Q used in this research) are integrated with optical lens. These optical lenses help to focus the incident laser beam from a few millimetres

in diameters where it exits the fibre, down to a narrow waist where it intersects with the flat plane (build platform) [373]. If the focus is inaccurate and away from the true focal point then the laser spot diameter will double and energy density will fall 50%, leading to incomplete melting [373]. The prediction of surface quality related to the position of the build platform is extremely difficult as it is critical to control the alignment optical lens to the optical axis to ensure the accurate focusing and positioning of the laser beam spot.

In general, the surface topography is not uniform for latitudinal facet full-turn external and internal surfaces even though the ball artefact is fabricated using the same process parameters. As a result of varying surface topography, the resultant surface roughness is not uniform which is potentially related to contrasting laser beam incidence angles with respect to an external and internal surface. It is clear from Figure 4.1 1a, that the external surface lies in front of the fast scanning laser beam implying a front-light surface. It is anticipated that this surface receives sufficient laser irradiation by almost circular-shaped laser fluence, as it is situated somewhat closer to the centre of the build platform with acute angle laser beam incidence. On the other hand, the internal surface experience lower laser irradiation, as it is situated far away from the centre of the build platform with obtuse angle laser beam incidence. Elliptical shaped laser irradiation prompts insufficient melting at the borders/corners of the build platform resulting in greater number of un-melted/partially-melted particle features adherence and thus induces residue formation implying back-light surface resulting in higher or uneven surface roughness (see Figure 4.1 1b). In addition, to the laser beam incidence angle, and location of AM part on the platform, inaccuracies in laser optics also play an equally important role in determining the final surface roughness



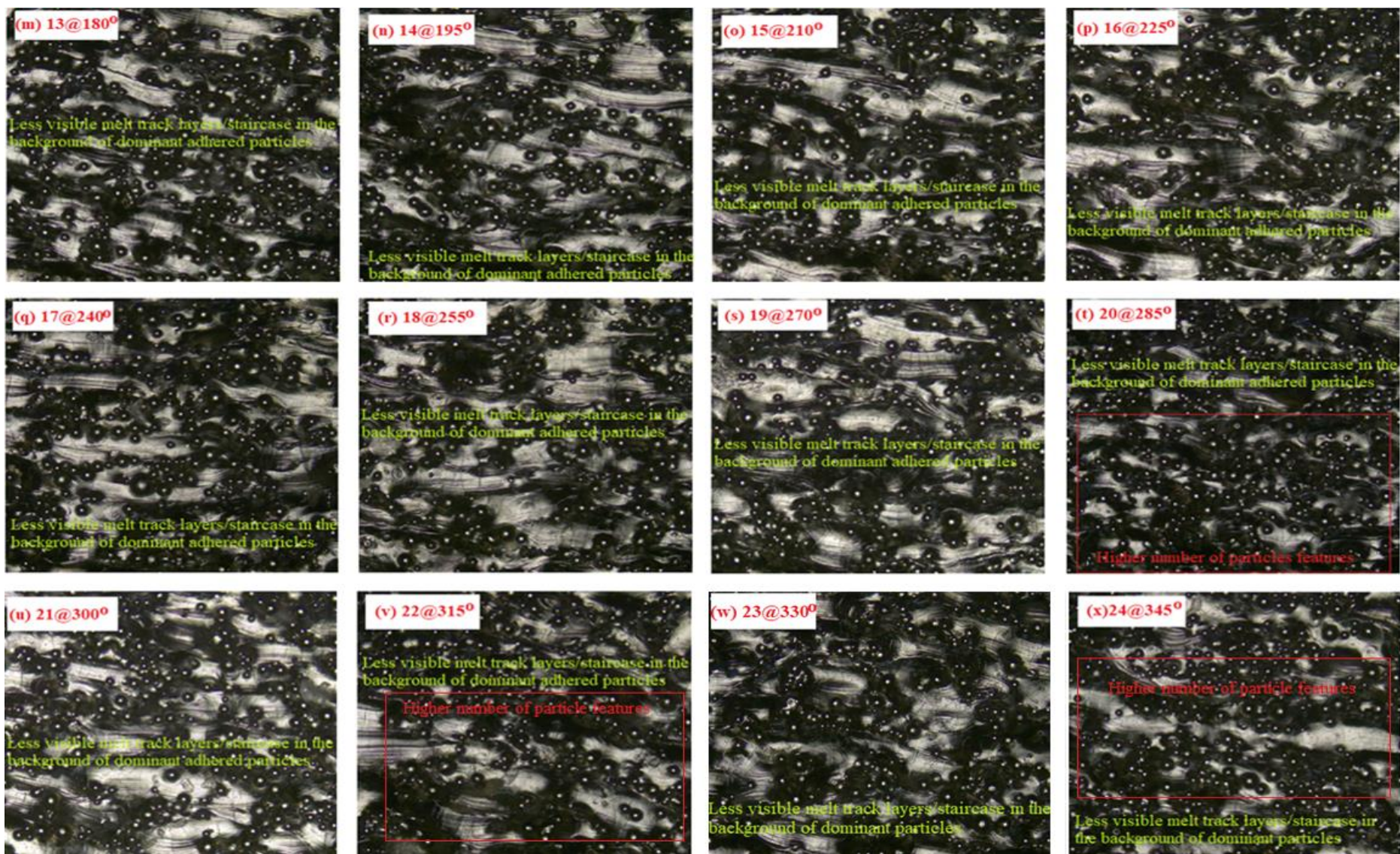


Figure 4. 8 Schematic illustration of latitudinal external surfaces, (a-x) 24 facets full-turn inclination angles (0°-360°) measured at equator

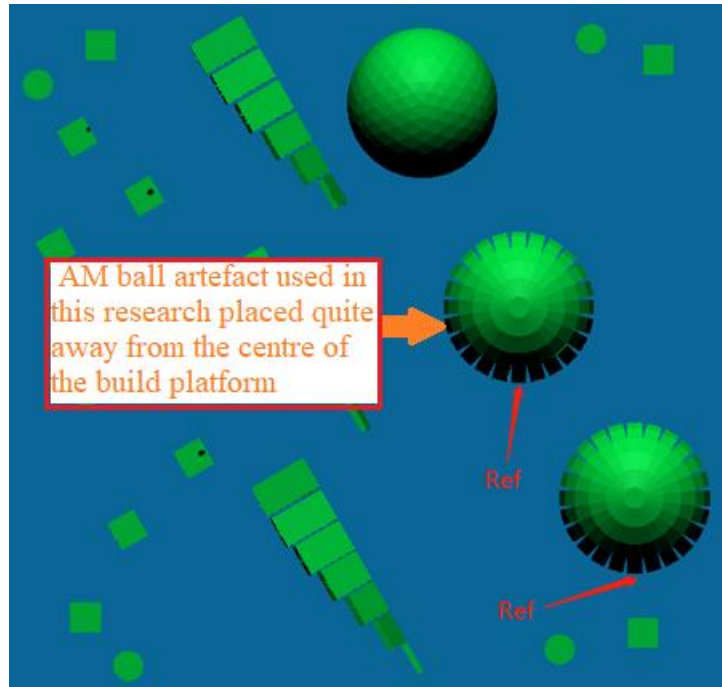


Figure 4. 9 Schematic illustration of AM ball artifact position during fabrication

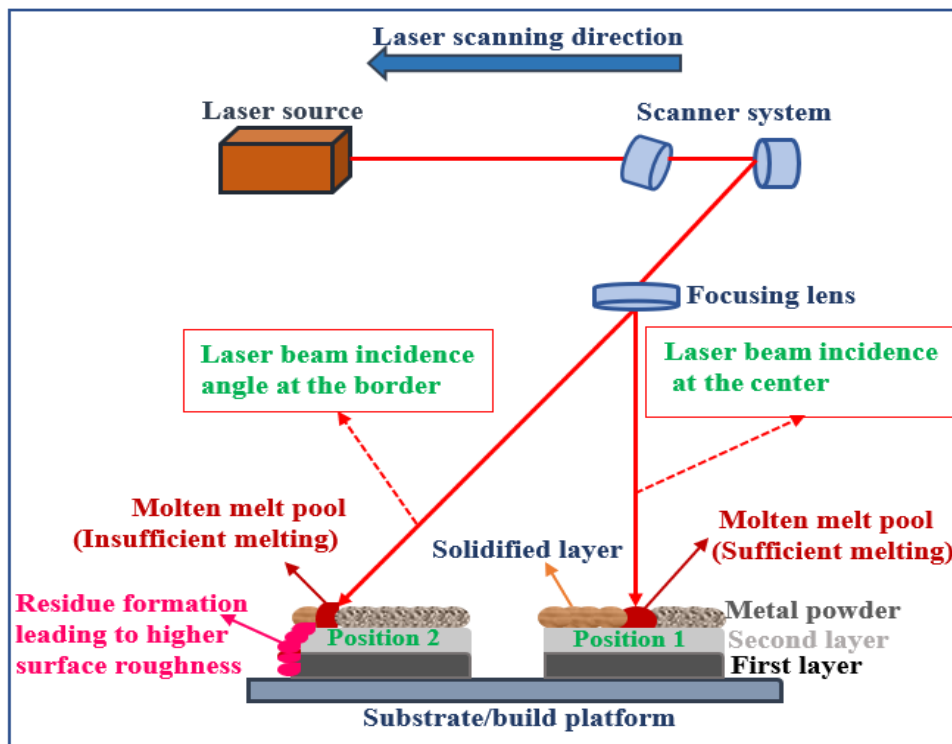


Figure 4. 10 Schematic of the laser beam incidence angle: (a) position-1 laser perpendicular to the build platform, (b) position-2 laser incidence not perpendicular or away from centre of the build platform.

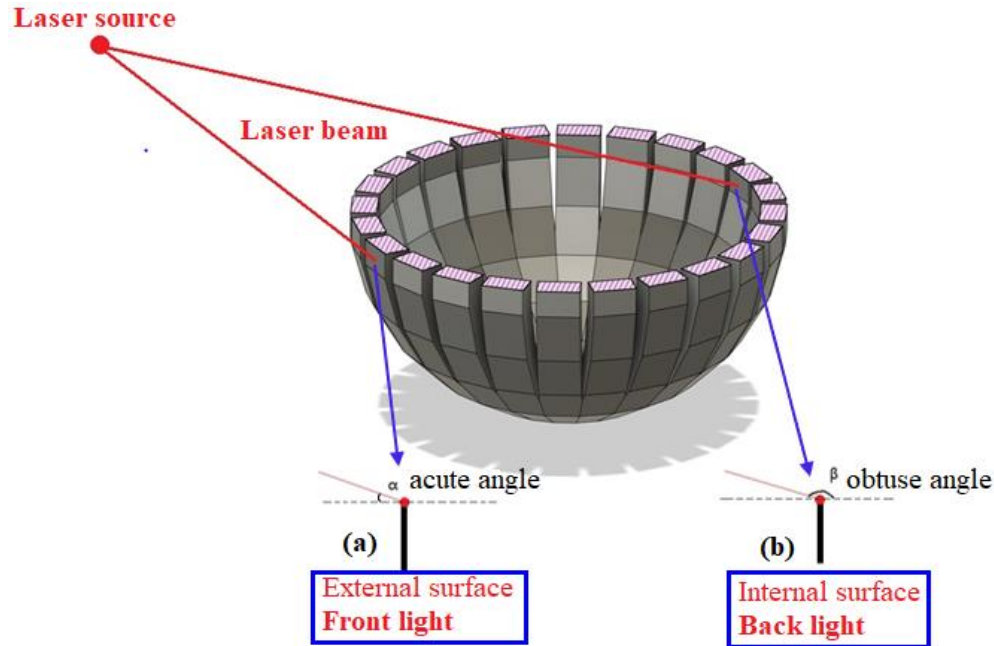


Figure 4. 11 Schematic illustration of (a) front light and (b) back light caused by laser beam incidence angle for latitudinal facet external and internal surface

4.3. Surface texture characterisation of longitudinal facets

The longitudinal surface texture analysis is aimed to examine the following aspects;

- (i) The variety of surface asperities that emerge on various up-skin and down-skin surfaces of longitudinal facets external and internal surfaces built with different inclination angles.
- (ii) The impact of these emerging surface asperities on the resultant surface roughness metrics height parameters and feature-based particles analysis.
- (iii) Is there any significant difference in resultant surface roughness between longitudinal facet external and internal surfaces?

To distinguish between the longitudinal facet external and internal surfaces, the relative sloping angle of the internal surface is inverted, some examples are given below;

- Longitudinal facet external up-skin surface at 30° is inverted to 150° internal down-skin surface.
- Similarly, the longitudinal facet external down-skin surface at 150° is inverted to 30° internal up-skin surface.

4.3.2 Height parameters

Sa and Sq texture height parameters generally represent the significant deviations in the texture characteristics comprising the surface. Sa and Sq roughness metrics are usually insensitive to higher peaks or deep valleys and the spacings of the various texture features [374]. The surface texture height metrics Sa, Sq, Ssk, and Sku are calculated from the leveled surface. Sa, Sq, Ssk, Sku height parameters, Sdr hybrid parameter, particles analysis, and particles coverage ratio plots for internal surfaces are indicated by green markers, while the external surfaces are indicated by orange markers on line charts with error bars. As a result of individual build melt track layers, staircase effect, and laser ripples, the surface roughness metrics Sa and Sq trend between 15°-45° inclination angles display salient large wavelength features which are often in loose clusters (see Figures 4.12 and 4.13). The observed larger wavelength features are credited to insufficient redistribution of mass or heat transfer (by a laser fluence) from the adhered un-melted, partially melted powder particles during the re-melting process by the virtue of inclined angles. As the angle of inclination increases, the relative increase in heat accumulation is also apparent during the building process giving rise to an increased number of un-melted and partially-melted particles adherence resulting in higher surface roughness. The surface inclinations beyond 75° show a higher number of closely packed un-melted, partially particles adhered to the surface, which is ascribed to the ability of laser fluence to complete mass redistribution thereby, reducing the large wavelength features.

The reported surface roughness Sa values for external up-skin at 15° and corresponding internal down-skin surfaces are 20.6 µm and 14.7 µm, and the recorded Sq values are 25.7 µm and 18.8 µm respectively. With a further increase in inclination angle, the corresponding Sa values decrease to 12.8 µm and 13.8 µm (Sq values decrease to 16.2 µm and 17.1 µm) for external up-skin and internal down-skin surfaces until it reaches a 45° inclined angle. A continuous and steady Sa trend in the range of 14.5 µm to 12.3 µm, and an equivalent Sq trend in the range of 18.4 µm to 15.5 µm is evident for both external and internal surfaces between 45°-90° inclination angles. Surface roughness is not very sensitive to these inclined angles as both Sa and Sq values remained constant at an average of ~13.4 µm and ~17 µm. Beyond 105° inclined angle, Sa and Sq values for both external and internal surfaces increased significantly. The unsatisfactory roughness Sa=36.5 µm and Sq=46.1 µm are recorded at 135° inclination angle for the external down-surface, whereas the worst Sa value of 68.3 µm, and Sq=84.3 µm is recorded at 165° inclined angle for the internal

down-skin surface. The unacceptable Sa values noted for external and internal surfaces are 172% (by 23.1 μm) and 410% (by 54.9 μm) higher than the average Sa value $\sim 13.4 \mu\text{m}$ observed between 45°-90° inclination angles (Figure 4.12).

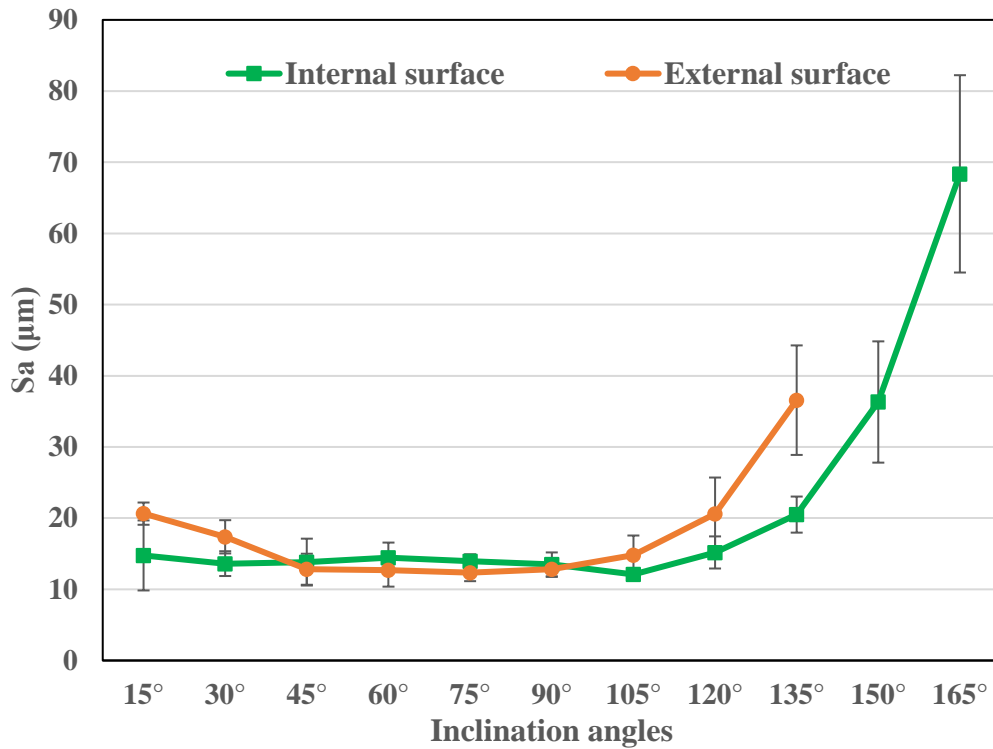


Figure 4. 12 Line graph for longitudinal external and internal Sa against various inclination angles. Similarly, the unacceptable Sq values noted for external and internal surfaces are 171% (by 29.1 μm) and 396 % (by 67.3 μm) higher than the average Sq value $\sim 17 \mu\text{m}$ observed between 45°-90° inclination angles (see Figure 4.13). The rationale behind higher Sa and Sq values of down-skin surfaces is already detailed in the visual inspection sections 5.1 and 5.2. Overall Sa and Sq metrics followed a similar trend for all the internal and external surfaces. A rapid increase of Sa and Sq values for both internal and external surfaces are evident for all the inclination angles beyond 90°. The higher surface roughness of down-skin surfaces is credited to the combined interaction of inclination angle and intermittent heat input [178]. It is obvious the computed surface roughness metric Sa values are lower than the obtained Sq values for all the inclination angles, due to the fact Sa values are expressed in terms of absolute value, the difference in height of each peak or highest point compared to the arithmetical mean height of the surface, whereas, Sq values are extracted from the root mean square values of ordinate value within the sampling length.

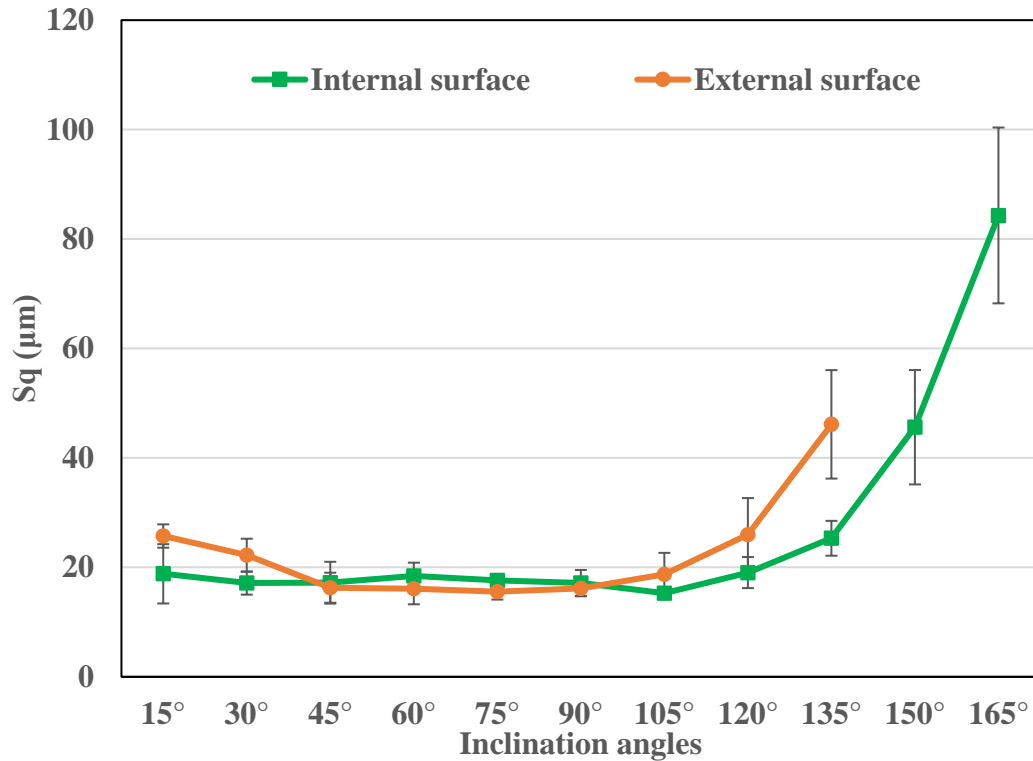


Figure 4. 13 Line graph for longitudinal external and internal Sq against various inclination angles. Skewness (Ssk) can be either positive or negative value. Ssk value of zero signifies random or Gaussian height distribution which shows a symmetrical surface topography. Ssk value for most of the internal surface except 15° inclined angle tend to be positive; indicating that surface is mostly dominated by higher local peaks above the mean line describing positive skewness (see Figure 4.14). Similar to the internal surface, besides the 15° inclined surface, all other remaining inclined surfaces displayed positive skewness values including 60°-90° where Ssk values are close to zero, signifying the surface is predominantly comprised of normal Gaussian height distribution. A greater number of higher protruded-like structures and random lower deep valley singular creatures are ascribed to spatters and other particle anomalies like re-entrant features attached to the sample top surface.

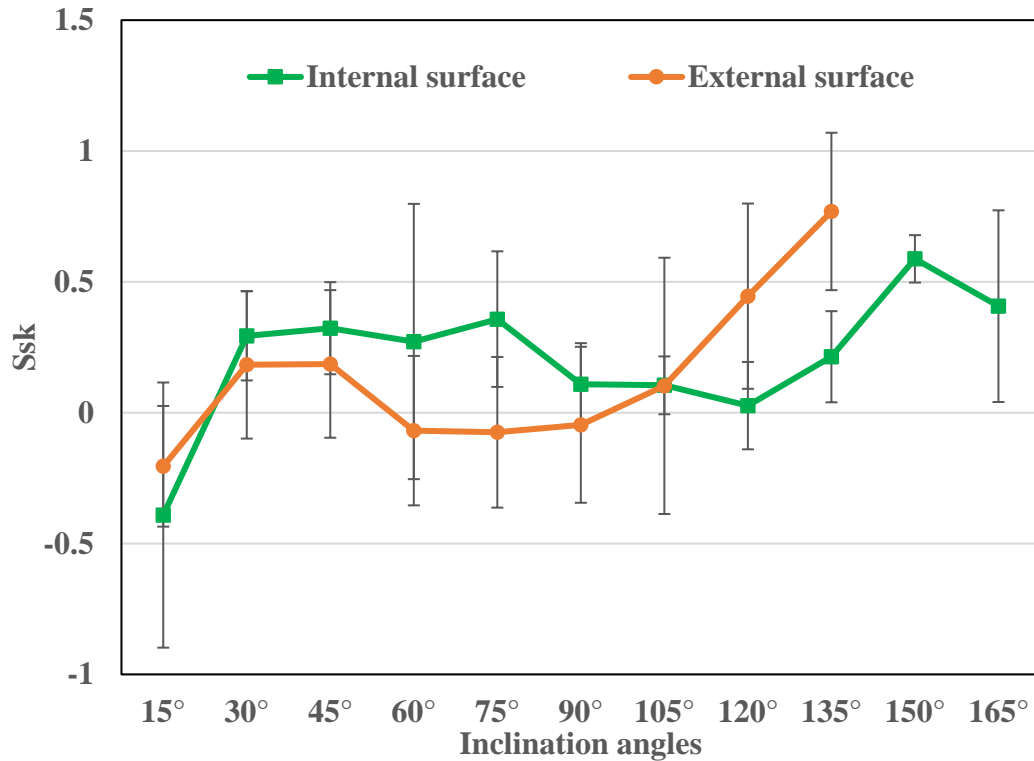


Figure 4. 14 Line graph for longitudinal external and internal Ssk against various inclination angles

Kurtosis (Sku) generally determines the nature of the surface height distribution; spiky or bumpy natured surface. The majority of the Sku values for the external surface remained to be steady for all the inclination angles except for the occasional rise observed at 30° and 120° surfaces, and a slight dip at 90° inclined angle which is insignificant (see Figure 4.15). However, kurtosis continued to be above nominal value 3 for both external and internal surfaces. The higher Sku values of the internal surface visible at 15° and 60° inclined angles signify the surface is spiky natured, whereas the observed Sku dip at 135° describes the bumpy natured surface height distribution. Significant dispersion of Sku value is obvious between external and internal surfaces for all the inclination angles. The most relevant explanation given is the presence of a plethora of surface abnormalities that emerged on different surface inclinations which is confirmed by the Sku values greater than nominal value 3. And most of the sporadic spikes present on both external and internal surfaces are evenly distributed, also comply with normal Gaussian height distribution.

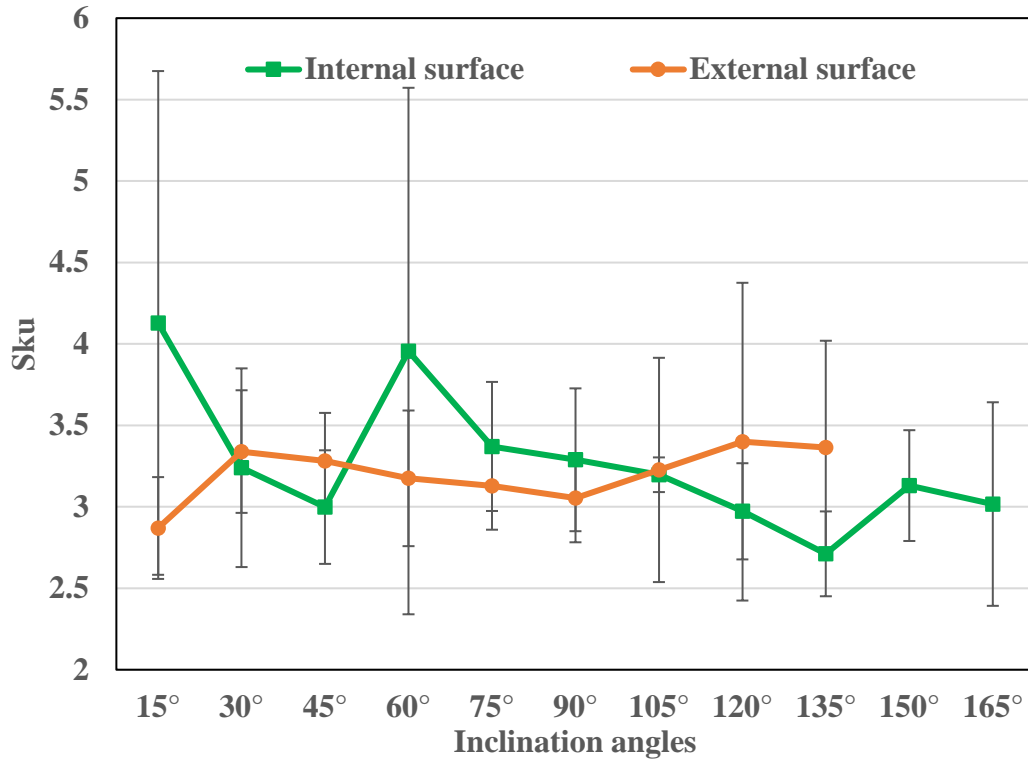


Figure 4. 15 Line graph for longitudinal external and internal Sku against various inclination angles

4.3.3 Hybrid parameter (Sdr)

Developed interfacial ratio (Sdr) enables quantifying the complexity of the surface on all three axes present due to the comparison of the curvilinear surface and the support surface and also provides the details about the percentage of the additional surface area contributed by the texture [60,64,68]. Sdr line plot for external surface displays a declining trend between 15° (105%) and 45° (80%) up-skin surfaces, followed by a stable level continuous increasing trend up to 135° (151%) down-skin surface (See Figure 4.16). All the external up-skin surfaces (i.e. 15°- 90°) do not exhibit any notable discrepancies with a mere difference of ~15%. The smaller Sdr values are credited to the wider spatial texture of the surface. However, the difference between external up-skin surface at 90°, and down-skin surface at 135° is ~60% viz quite high, which is a typical random surface texture characteristic of AM surfaces.

Sdr line plot for internal surface presented a constantly rising trend from 15° (50%) to 90° (99%) up-skin surfaces, but the recorded Sdr values for 15°-45° internal surfaces are smaller (average ~36%) than that of external surfaces for the same inclination angles range. A quick rise in Sdr values is seen for all the internal surface down-skin surfaces from 105° (91%) to 165° (258%) inclination angles (See Figure 4.16). Overall, external surfaces presented fewer substantial

discrepancies even though the difference is ~46% between 15° and 135° inclination angles, while the internal surfaces exhibited a bigger discrepancy with a massive difference of ~202% between the least recorded Sdr value at 15° up-skin (50%) surface and the highest witnessed Sdr value at 165° (258%) down-skin surface. The higher Sdr values of internal surface are ascribed to finer spatial intricacy of the texture generated by a higher concentration of particle features that present extremely complex geometries of metal AM surfaces. The higher Sdr values noted here are similar to higher Sa values registered for internal down-skin surfaces, signifying that surfaces with a rough characteristic demonstrate a larger curvilinear area than the smoother ones [29,227].

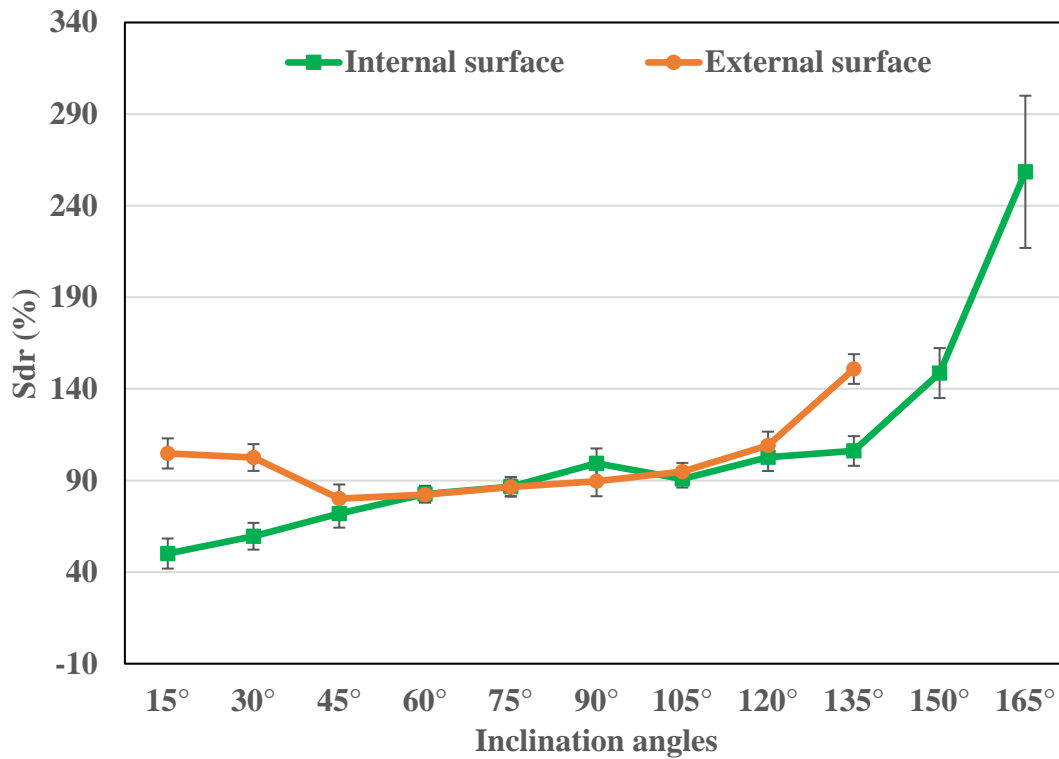


Figure 4. 16 Line graph for longitudinal external and internal Sdr against various inclination angles

4.3.4 Particle analysis

The number of adhered particles is calculated from the particle surface. The mean number of particles vs various inclination angles is illustrated in Figure 4.17. The external surface particles plot exhibits a symmetrical pattern; the number of particles increases as the inclination angle increased till it reaches 60° (~157 particles). A slight decrease between 60°-75° (~151 particles) is attributed to the transition zone mainly consisting of re-entrant features; which are difficult or impossible to capture using an optical FVM system [3]. Similarly, decreased adhered number of particles trend is apparent in the same way as it increased previously upon further increasing the

inclination angles from 90° (~158 particles) to 135° (~116 particles) sloping surfaces with bigger size particles agglomerated into island-like protruded structures as already explained. For internal surfaces at a 15° inlined angle, it is visible that the particles trend slowly rises till it reaches its first maximum at 90° (~153 particles), followed by a slight decline at 105° (~149 particles), and finally reaching its peak at 120° (~155 particles) sloping surface. The number of particles decreases as further increases in inclined angle to reach ~122 particles at 165° surface. Particles analysis of both internal and external surfaces for all the inclination angles display identical trends to some degree. Likewise, in particle analysis, particle coverage ratio plots of both external and internal surfaces displayed identical trends in general for all the surface inclinations (see Figure 4.18). The particles coverage ratio of the external surface shows a rising trend at the beginning from 15° (~14%) to 45° (~18%) up-skin surfaces and 15° (~12%) to 60° (~21%) inclined angles for the internal surface. The approximate overall difference of 2% is noticed between the particle coverage ratio trends of external and internal surfaces. The observed rising trends of external surfaces (15°- 45°) and internal surfaces (15°-60°) are attributed to the increased number of spatters, and adherence of un-melted/ partially melted particles onto the surface as the slope of inclination angle increases. Overall, external up-skin surfaces witnessed an average of ~12 particles attached as compared to internal surfaces in the same region. Similarly, an average of ~8 particles are less attracted to the external down-skin surfaces in comparison with their counterparts.

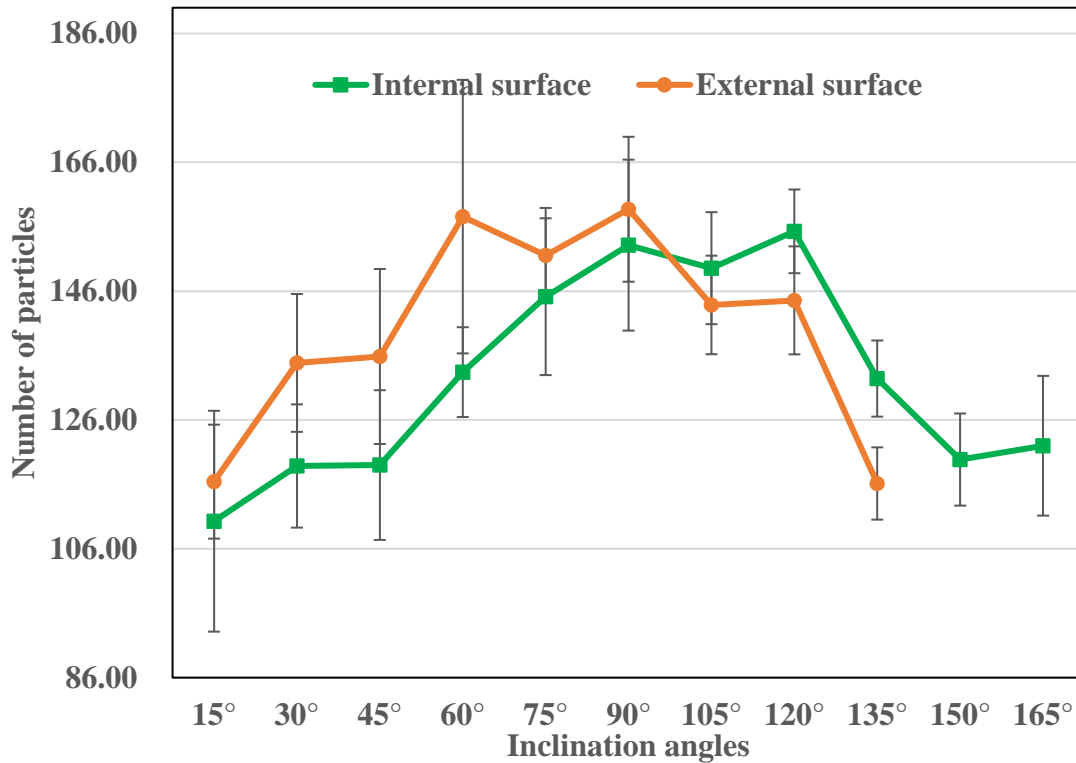


Figure 4. 17 Line graph for longitudinal external and internal surfaces number of particles against various inclination angles

However, instead of displaying notable rising trends for all sloping angles beyond 60°, particle analysis, and particle coverage ratio line plots for all down-skin surfaces display an interesting opposite declining trend. The most suitable reason for this circumstance is that accumulation of particle features is mostly at the boundaries of melt track layers, and the number of adhered particles at the lower sloping angles 15°-60° up-skin surfaces are naturally low as compared to higher sloping angles beyond 60° and down-skin surfaces. This is attributed to the width of the staircase effect which is related to the distance between each melt track layer. For up-skin surfaces starting from 15°, the distance between each melt track layer/staircase effect is higher, therefore the corresponding number of particles adherence at the melt track boundaries is less. It is well acknowledged that an increase in sloping angles marks a decrease in distance between the width of melt track layers/staircase effect leading to a simultaneous increase of particles accumulation up to a 90° inclined angle. The appearance of staircase effect in the reverse direction for all down-skin surfaces 105° and beyond witness an increase in width of the staircase or distance between the melt track layers which gives rise to the lower number of smaller size particles adherence, in addition to the bigger size agglomerated island-like protruded structures and cross formation

which are difficult to identify or segment by Robust Gaussian filter with the cut off wavelength of 80 μm . The smaller number of detected adhered particles represents the decreasing trend in particle analysis and particle coverage ratio for both external and internal down-skin surfaces (Figures 4.17 and 4.18).

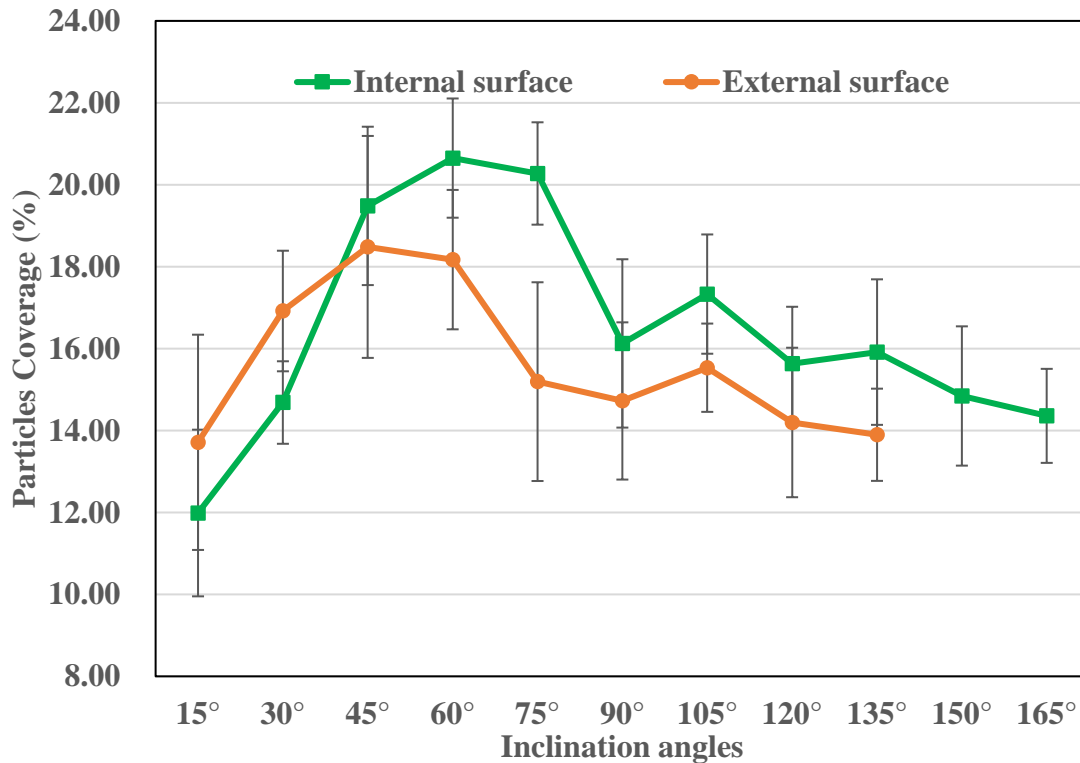


Figure 4. 18 Line graph for longitudinal external and internal surfaces particles coverage ratio against various inclination angles

4.3.5 Longitudinal facet particles descriptors analysis

For the purpose of understanding, the individual surface particle descriptors label comprised of an adhered number of particles with their relative particle coverage ratio analyzed at position one (out of 03) for both external and internal surfaces are shown in Figures 4.19 (a-i) and 4.20 (a-i). From individual particles descriptors labels of longitudinal facet external and internal surfaces, it is evident that the irregular shaped bigger size particle features dominated the starting angles between 15°-60° with miniature particles at the background. As the inclination angles increased the number of irregular shaped particles slowly tend to turn in to mostly circular or oval shaped particles. A significantly high number of closely packed circular or oval shaped particles features are apparent till the inclination angle reaches 90° up-skin surface. In contrast, the shape of these particles slowly

starts to shift back to irregular shape from the circular or oval shaped features starting from 105° surfaces. During this transition, a remarkable reduction in these number of irregular particles features are also noted. The up-skin surfaces between 15°-60° inclinations showed the higher percentage of largest size irregular particles, while 75° and 90° surfaces displayed the medium size particles. Finally, the down-skin surfaces between 105°-135° exhibited intermediate size particles. The particles features are loosely packed for 15°,30°,120° and 135° surfaces, and densely packed for the remaining surfaces. The suitable reasons for these phenomena are that even though a greater number of particles are attached beyond a 60° inclined angle, these particles would agglomerate into a big island like protruded structures and eventually form bigger size dross for 105° and beyond inclined surfaces, leaving only a fewer smaller size particles (below 80 µm size) resulting in a lower number of particles and lower particles coverage ratio in individual particles descriptors Figures 4.19(a-i) and 4.20(a-i). Overall, individual particle descriptors labels of longitudinal facet external and internal surfaces coincide with already described particle analysis and particles coverage ratio line chart plots (Figures 4.17 & Figures 4.18).

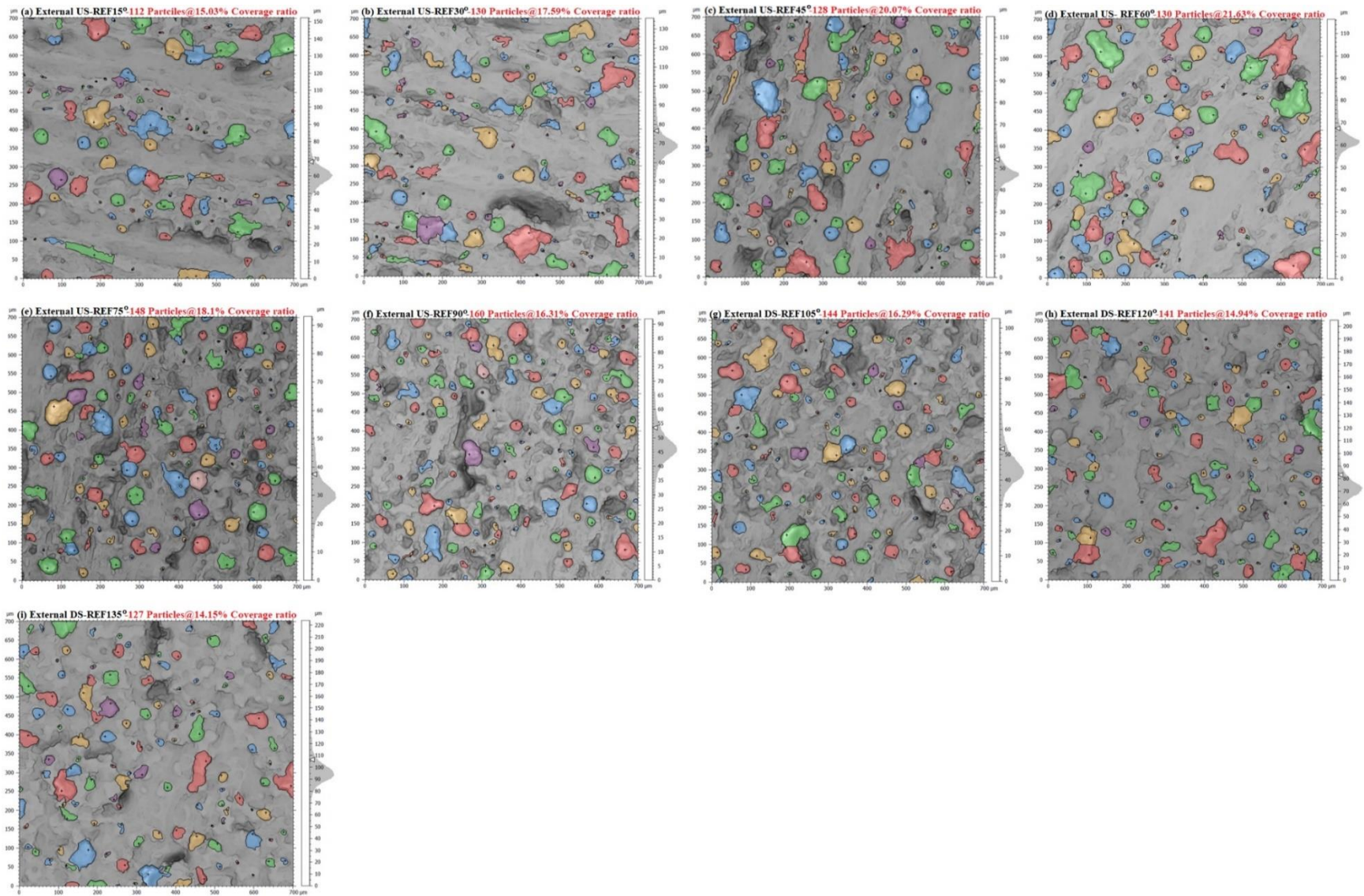


Figure 4. 19(a-i) Schematic representation of individual particles descriptors and particles coverage ratio labels for longitudinal facet external surface against inclination angles

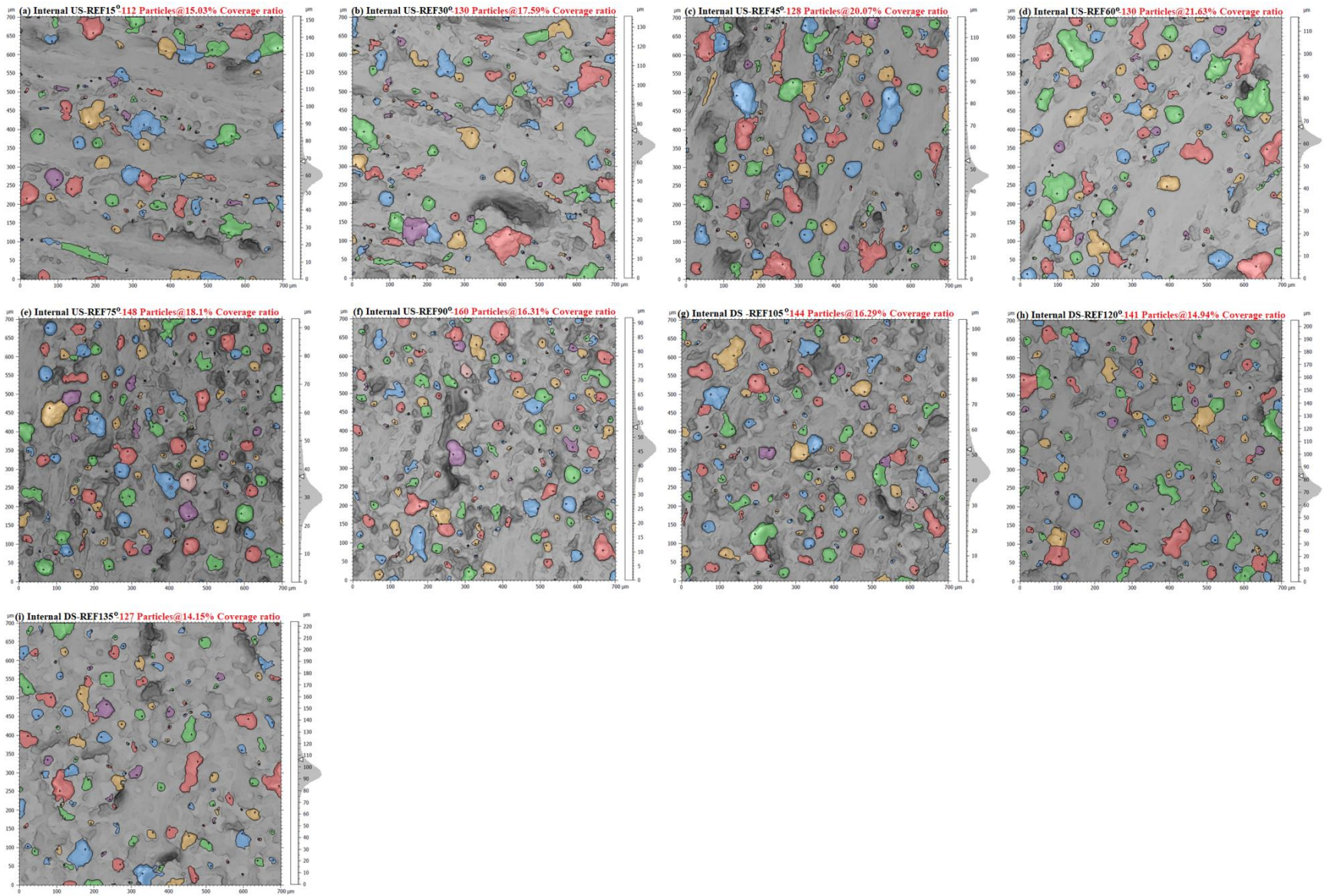


Figure 4. 20(a-i) Schematic representation of individual particles descriptors and particles coverage ratio labels for longitudinal facet internal surface against inclination angles

4.4 Surface texture characterisation of latitudinal facets

The aim of latitudinal surface texture analysis is to identify the following aspects;

- (i) Is there any difference in resultant surface roughness analyzed full-turn (0° - 360°) at the equator?
- (ii) Is there any difference in resultant surface roughness between external and internal surfaces analyzed full-turn (0° - 360°) at the equator?

Owing to the difference in laser beam interaction with different full-turn inclination angles of the latitudinal facet, it is anticipated to achieve diverse surface texture characteristic fingerprints. In order to nullify this variance, and to match the laser beam incidence angle between external and internal surfaces of latitudinal facet full-turn angles, the internal surface sloping angle is inverted, to ensure both external and internal surfaces face the same direction, for example;

- Latitudinal facet external surface at 30° is inverted to 210° latitudinal facet internal surface.
- Latitudinal facet internal surface at 210° is inverted to 30° latitudinal facet external surface.

4.4.1 Height parameters

The commonly used surface roughness metric Sa average standard deviation is found to be 43nm and Sq is 52nm for latitudinal facet. The polar plots are prepared without error bars to illustrate Sa, Sq, Ssk, Sku surface texture height metrics, Sdr hybrid parameter, and particle analysis including particle coverage ratio investigation. The internal surface is denoted by green markers, while orange markers are used to denote the external surface. The Sa and Sq values for the external surface exhibited alternative increasing and decreasing trends for every 15° starting from the reference (Ref) 0° angle (see Figures 4.21 and 4.22). The recorded Sa and Sq values at 0° are $12.8\text{ }\mu\text{m}$ and $16\text{ }\mu\text{m}$, followed by a slight increase at 15° to (Sa) $13.9\text{ }\mu\text{m}$ and Sq to $17.5\text{ }\mu\text{m}$ respectively. Sa and Sq values witnessed a further declining pattern at 30° (Sa= $13.3\text{ }\mu\text{m}$, Sq= $16.7\text{ }\mu\text{m}$) and 45° to Sa= $12.8\text{ }\mu\text{m}$ and Sq= $16.1\text{ }\mu\text{m}$. The steady trends for both Sa and Sq are observed between 60° - 75° (Sa \sim $13.7\text{ }\mu\text{m}$, Sq \sim $17.5\text{ }\mu\text{m}$), 105° - 120° (Sa \sim $12.4\text{ }\mu\text{m}$, Sq \sim $15.6\text{ }\mu\text{m}$), and 285° - 300° (Sa \sim $12.7\text{ }\mu\text{m}$, Sq \sim $15.8\text{ }\mu\text{m}$) correspondingly. The best external surface roughness Sa value of $9.8\text{ }\mu\text{m}$ and Sq value of $12.5\text{ }\mu\text{m}$ is achieved at 195° , while the worst Sa= $13.9\text{ }\mu\text{m}$ is recorded at a 15° angle, likewise the worst Sq value of $17.6\text{ }\mu\text{m}$ is noted at 75° angle. Overall, the external surface displayed consistent Sa and Sq trends without displaying any significant disordered oscillations (see Figures 4.21 and 4.22).

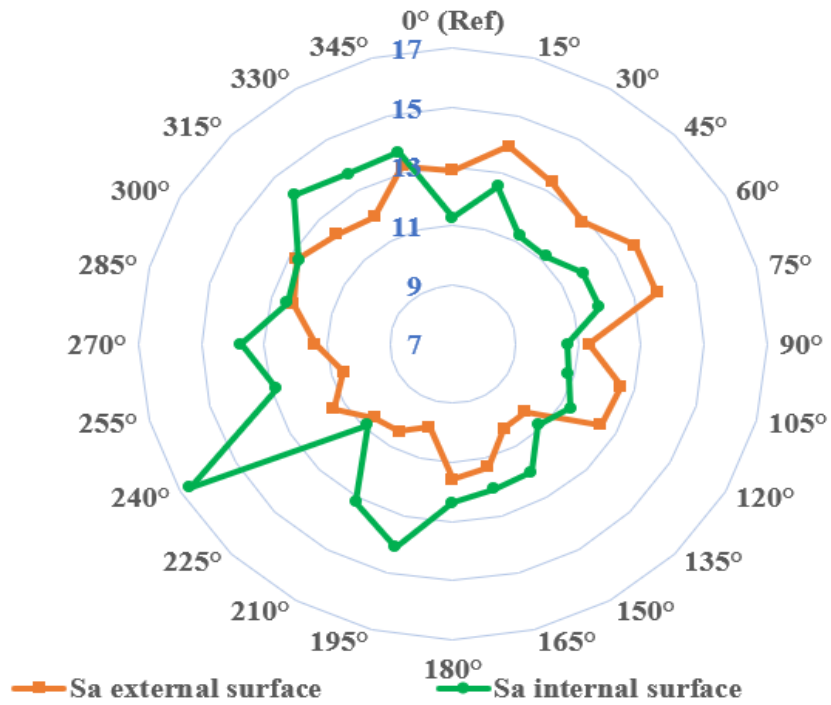


Figure 4. 21 Polar plot for latitudinal full-turn external and internal Sa against various inclination angles

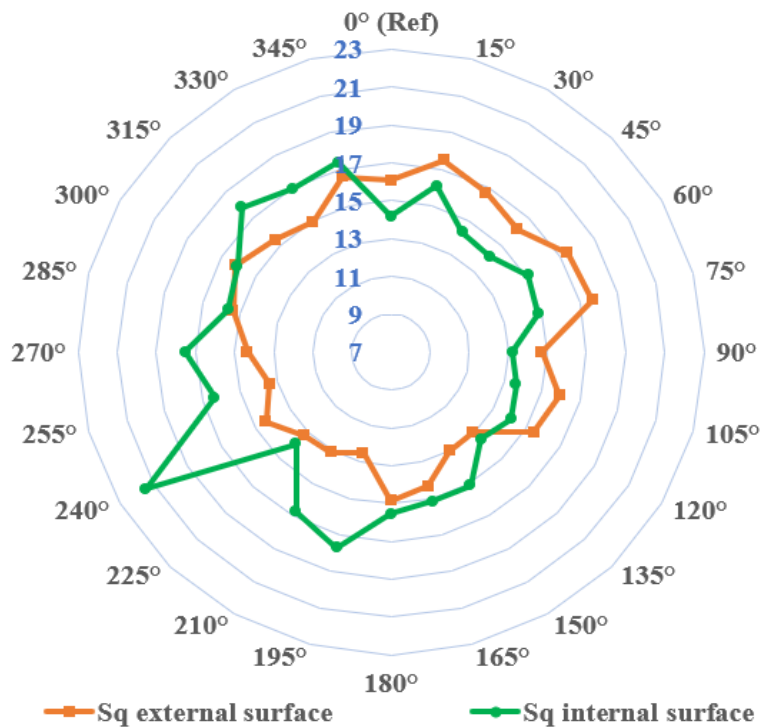


Figure 4. 22 Polar plot for latitudinal full-turn external and internal Sq against various inclination angles

The Sa and Sq values for internal surfaces follow a similar pattern as external surfaces except for a sharp rise in the form of some outlier is noted at 240° which is coincidentally a worst Sa value of 16.6 μm and Sq=21.4 μm . The least or the best surface roughness metrics Sa ~10.6 μm and Sq ~13.2 μm are noted at a 90° angle. From the latitudinal analysis, it is important to note that the recorded Sa and Sq trends for the internal surface are comparatively higher than the external surface. The obtained (best and worst) Sa value for the external surface is in the range of 9.8-13.9 μm , whereas this range for the internal surface lies between 10.6 – 16.6 μm which is approximately in the range of ~8- ~19% increase in surface roughness metric Sa for the internal surface (see Figure 4.21). Similarly, the obtained (best and worst) Sq value for the external surface is in the range of 12.5 μm -17.6 μm , whereas this range for the internal surface lies between 13.2 μm – 21.4 μm which is approximately in the range of ~5.5% - ~21% increase in surface roughness metric Sq for the internal surface (see Figure 4.22). The rationale behind higher Sa and Sq values of internal surfaces placed away from the centre of the build platform is already detailed in the visual inspection section 4.2.5.

The obtained Skewness (Ssk) value with respect to various full-turn surface angles at the equator is illustrated in Figure 4.23. Similar to longitudinal analysis, skewness Ssk values for both external and internal surfaces remained to be positive; signifying the normal height distribution with the overall surface is predominantly covered by localized peaks. The random deep valley features observed between 255°-300° inclined angles of the external surface resulted in negative skew, which is less significant. Overall, the Ssk value ~0 (zero) is noted for both external and internal surfaces representing symmetrical surface topography.

Figure 4.24 illustrates different kurtosis values vs various full-turn inclination angles. The kurtosis is always a positive value, which often determines the sharpness of surface height distribution. The sharp peaks well above the nominal value of 3 denote the spiky nature of the surface that are evident at 90°, 180°, and 300° inclination angles for external surfaces, and 30°, 60°, 225°, and 240° for internal surface sloping angles respectively. Similarly, lower Sku values merely below the nominal value of 3 are apparent between 315°-30°, and 120° angles for external surfaces, and 0°, and 135° angles for internal surfaces describing the bumpy natured surface height distribution. Overall, both external and internal surfaces predominantly display the spiky natured surface, which is again similar to that of longitudinal analysis.

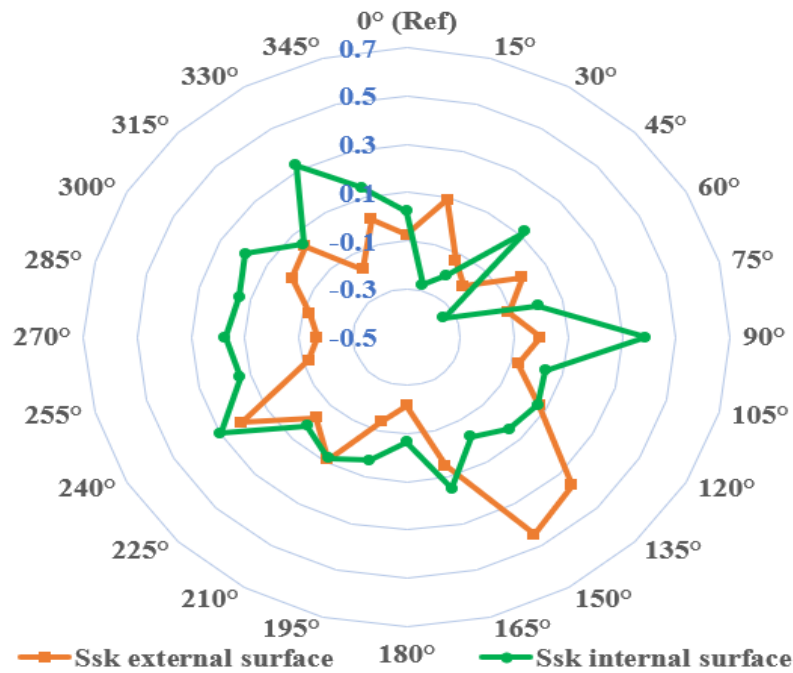


Figure 4. 23 Polar plot illustrating full-turn external and internal Ssk against various inclination angles

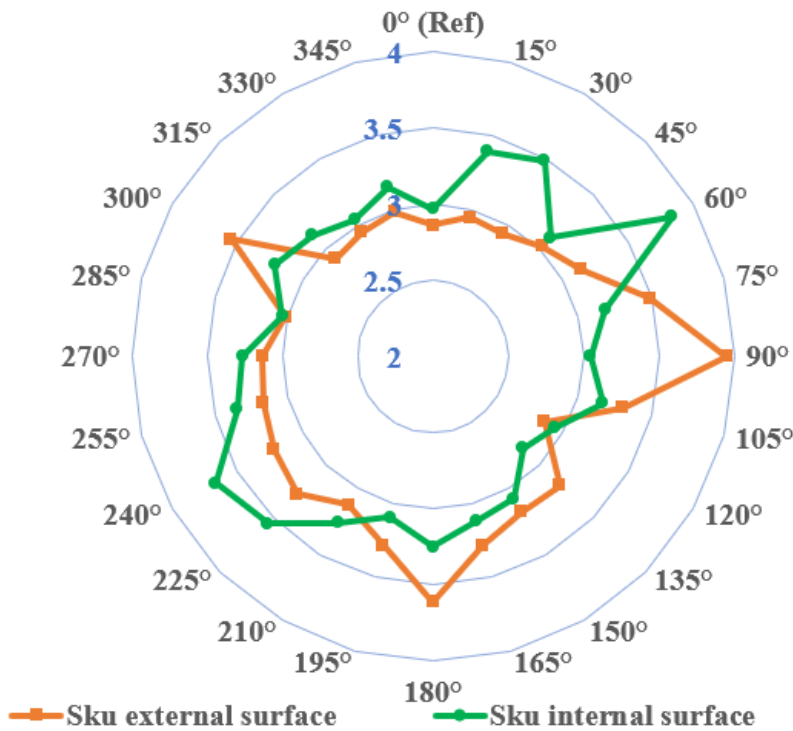


Figure 4. 24 Polar plot for latitudinal full-turn external and internal Sku against various inclination angles.

4.4.2 Hybrid parameter (Sdr)

The Sdr values for the first half section of the latitudinal internal surface reveal an unvarying trend from 15° (~88%) to 180° (~88%) with a mere difference of ~2% (see Figure 4.25). The zig-zag shaped trend is evident throughout the second half-section of the latitudinal facet internal surface comprising 195°-360° inclinations, with the minimum Sdr value noted at 210° (82.96%) and maximum one at 240° (101%). Similarly, the Sdr plot for the latitudinal facet external surface displays an oscillating trend for most of the sloping angles, except 165° (87%) to 255° (~83%), where a constant declining trend is observed. The lowest Sdr value for the external surface is noticed at 45° (~69%), while the highest value is witnessed at 30° (~92%).

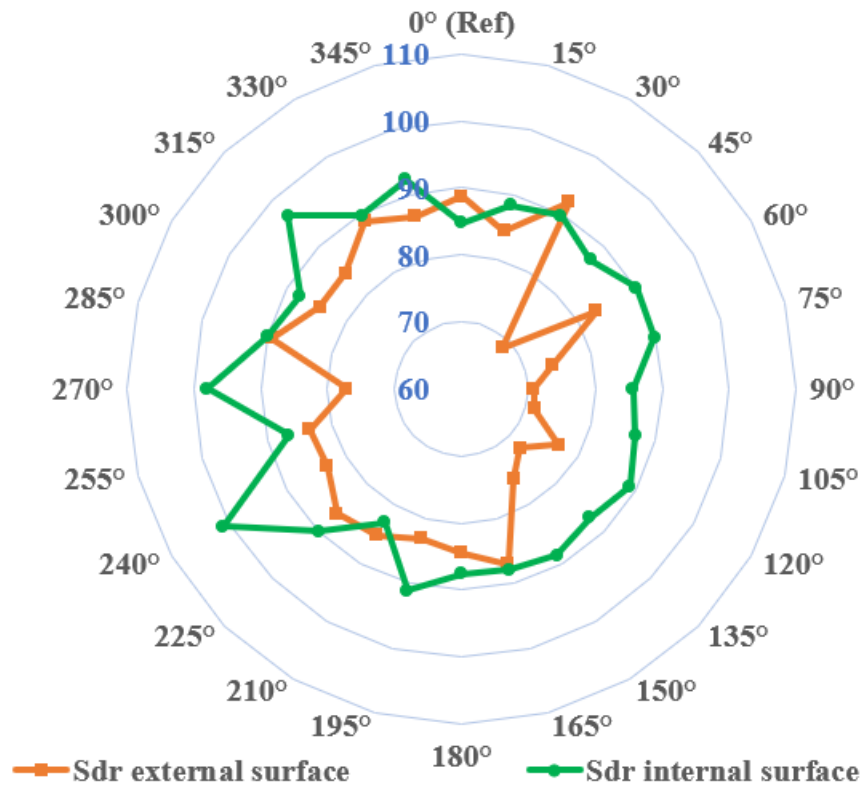


Figure 4. 25 Polar plot for latitudinal full-turn external and internal Sdr against various inclination angles

Overall, the Sdr parameter of the external surface for all sloping angles demonstrated lower Sdr values than the internal surface. The erratic trend with higher Sdr values is attributed to the finer spatial disparities that exist on the surface caused by intermittent heat transfer, laser beam incidence angle, and the position of AM part on the build platform. As laser beam incidence angle increases there is a higher likelihood of insufficient heat energy supplied, which lacks to completely melt the powder particles. These incompletely melted layer tracks would attract the

loose powders from the next layer and bind them together onto the surface forming a batwing-like structure with a weaker contour that is ascribed to the filleting effect [213]. The filleting effect would result in finer spatial anomalies.

4.4.3 Particle analysis

The mean number of particles that emerged on various external surface full-turn inclination angles is illustrated in Figure 4.26. The number of particles for external surfaces unveiled a continuous descending and ascending trend with an average of ~27 particles from 0° to 60° angles. The highest number of adhered particles 170, 174, and 185 are observed at 0°, 165°, and 285° angles respectively for external surfaces. While the least number of adhered particles are detected at 45° (122 particles) and 105° (124 particles). A constant rising plot from 300° (160 particles) to 0° (170 particles), a steady declining trend from 165° (174 particles) to 255° (153 particles), and a combination of marginal increase and the decreasing pattern is clearly visible for external surface from 75° (139 particles) to 105° (141 particles). A consistent steady particle (151-160 particles) trend is observed for all the inclination angles of the internal surface.

The particle coverage ratio for both external and internal surfaces showed homogeneous trends (see Figure 4.27). Apart from 0° (~21%) and 285° (~22%) angles, all other internal surfaces exhibited a higher (by ~2%) proportion of particle coverage ratio than the external surfaces. The highest particle coverage ratio ~24% is apparent at 285° for the external surface, and ~26% at 315° for the internal surface. Similarly, the lower particle coverage ratio (~18%) at 270° and ~21% at 0° is registered for external and internal surfaces simultaneously. The higher percentage of particle coverage ratio at 285° is ascribed to the higher number of adhered particles for the external surface. From the latitudinal particle analysis, it is fair to culminate that there is not a significant difference in surface roughness Sa and Sq values, nor there is any remarkable distinction in adherence of a number of particles and the particles coverage ratio between the internal and external surfaces, unlike longitudinal analysis.

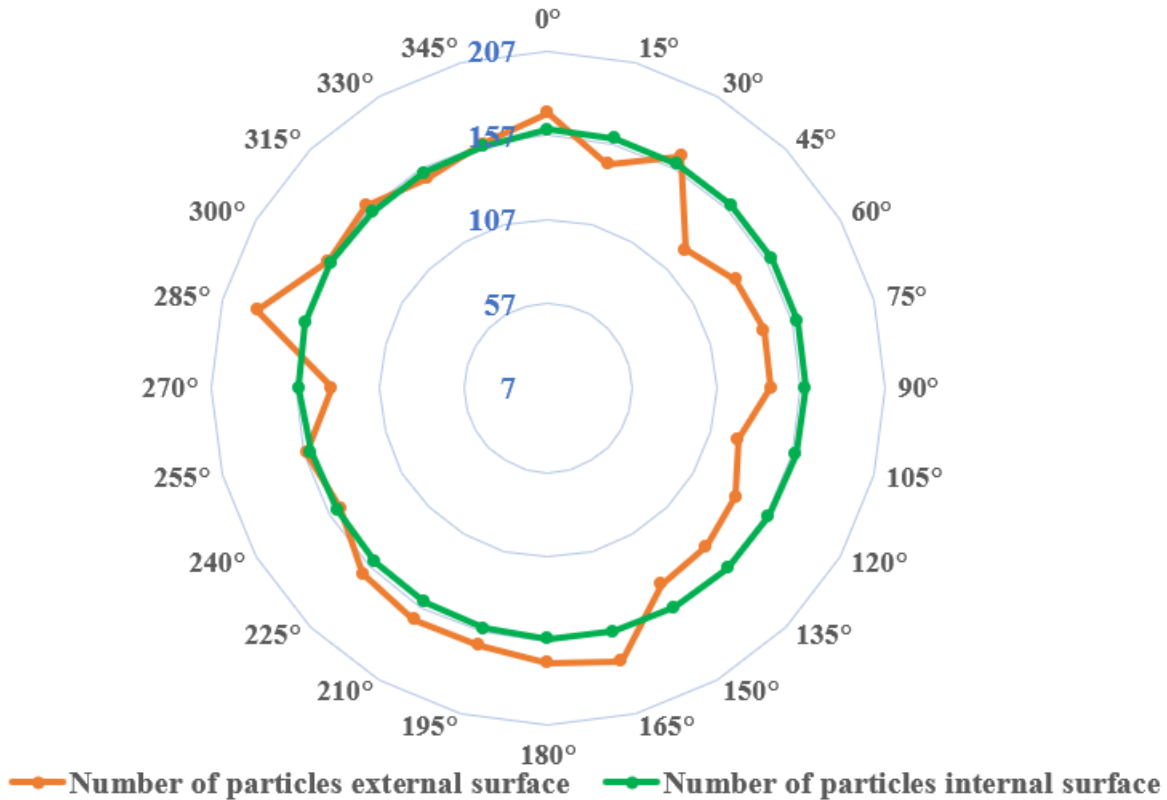


Figure 4. 26 Polar plot for latitudinal facet full-turn external and internal number of particles against various inclination angles

4.4.4 Latitudinal facet particles descriptors analysis

The individual particle descriptors of latitudinal facet external and internal surfaces comprised of adhered particles with their relative particle coverage ratio analyzed at position one is shown in Figures 4.28(a-x) 4.29 (a-x). For full-turn external surfaces 15°-75°,105°,240°-345°, it is evident that at least one or more number of adhered particle(s) is huge in size with irregular shape. The surfaces 0°,165°,180°,225°-255°,285° and beyond displayed densely populated (>165) particles. Likewise, 15°,45°,60°,90°-120° surfaces showed lower number (120-135) of irregular shaped loosely packed particles adherence, rest of the surfaces exhibited 140-160 number of particles with intermediate packing. The internal surfaces 345°-315°,285°-225° revealed one or more massive sized irregular shaped particle(s). A uniformly packed mostly with circular or oval shaped particles are apparent between 180°-15° surfaces. A significant irregular shaped unevenly packed particles features are mostly noted for the 345°-195° internal surfaces. Overall, higher percentage of regular shaped adhered (circular or oval) particles are evident for the internal surfaces, whereas the irregular shaped particles dominates the external surfaces. Although, the shape of adhered may be

slightly different between full-turn external and internal surfaces, but there is no significant difference between the number of particles or the particles packing factor.

The most relevant justifications for the higher number of particles adherence are potentially due to the laser beam incidence angle, elliptical shape of laser beam focus, the position of AM ball artifact on the build platform, and also height from the printer bed to the AM surface. Another valuable reason for the higher particle accumulation is due to spatters, which are generally associated with the ejection of gas plumes, it is important to note that the gas flow (transfers the spatters) conditions vary along the substrate or the build platform is position-dependent. Additionally, the angle of incidence of the laser beam with powder is also position-dependent because it is responsible for the gas flow conditions, which simultaneously influence the resultant surface roughness [375]. The impact of spatters and the laser fluence incidence are contingent on individual printing machines as each AM machine is configured to its personalized settings. Overall, individual particle descriptors labels of full-turn external and internal surfaces coincide with afore-described particle analysis and particles coverage ratio polar plots (Figures 4.26 and 4.27)

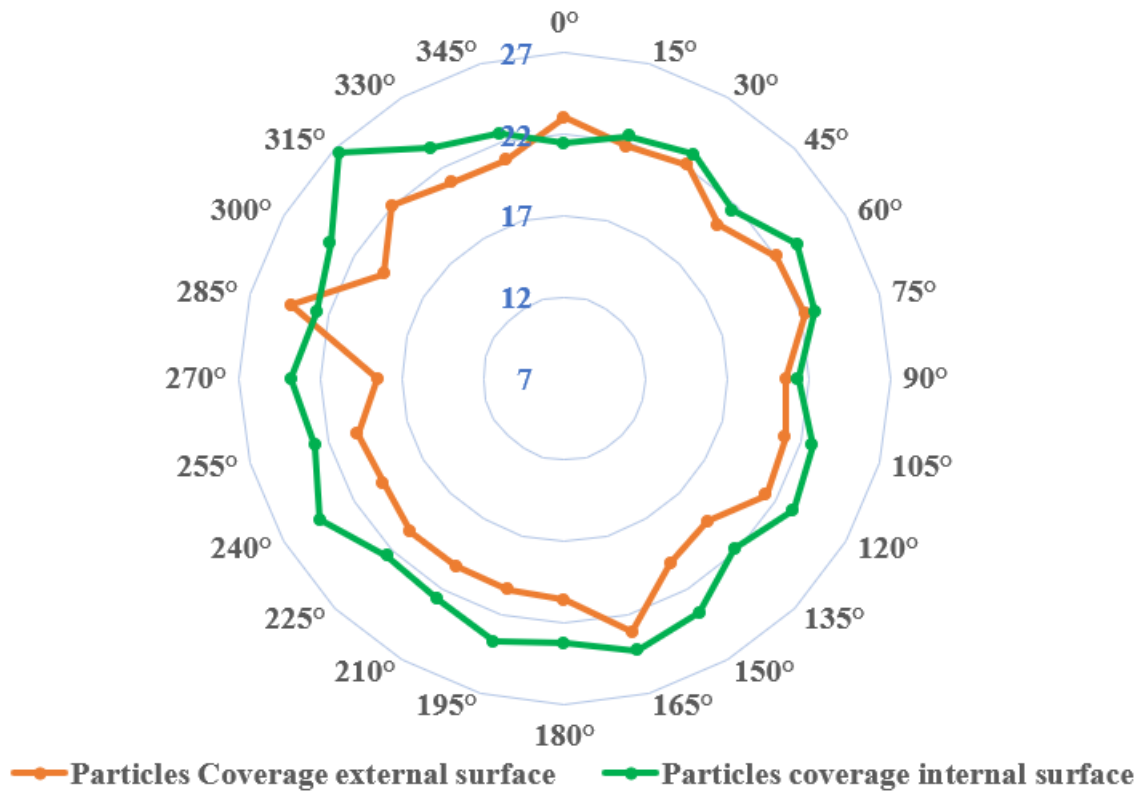
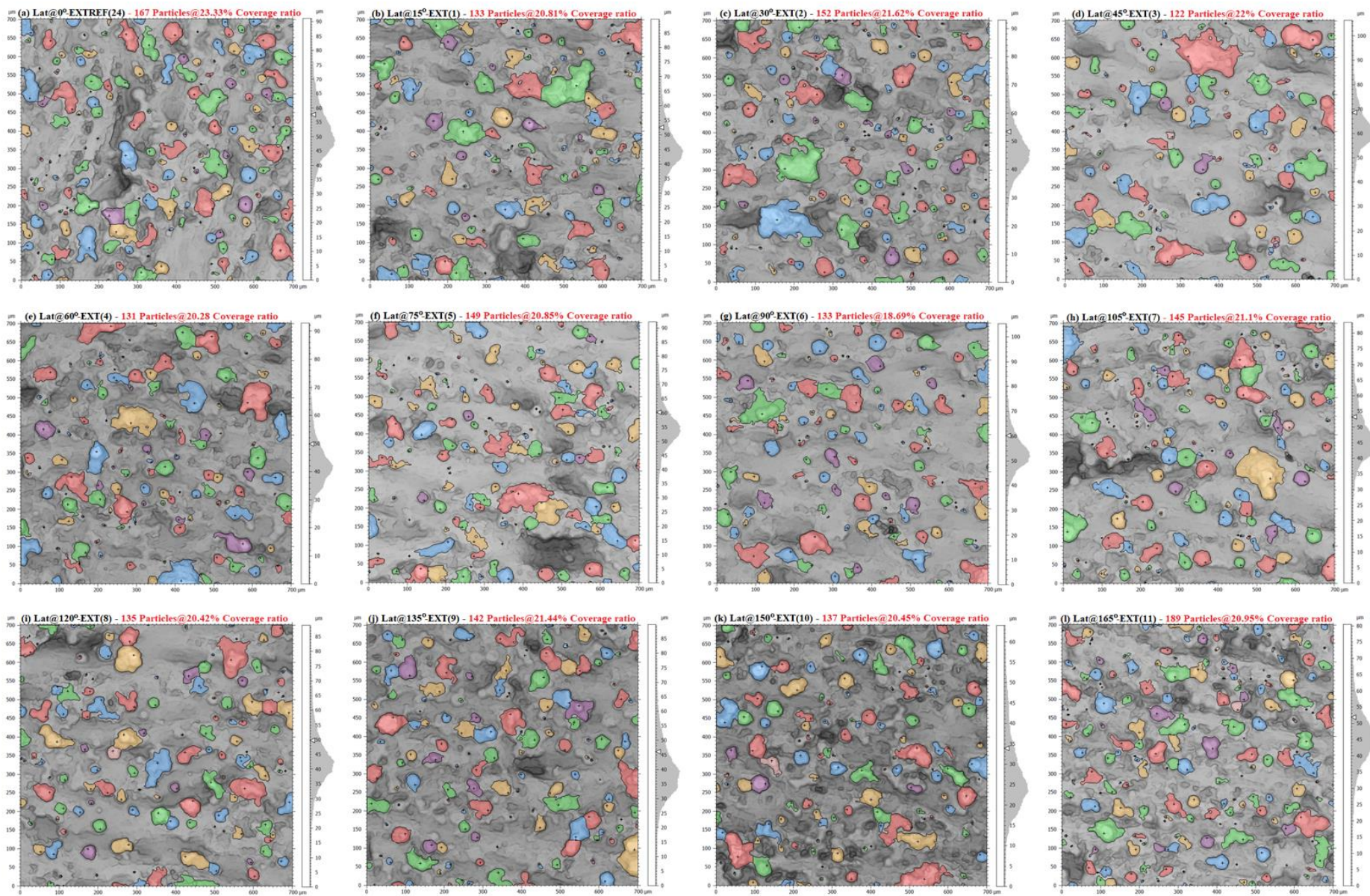


Figure 4. 27 Polar plot for latitudinal full-turn external and internal particles coverage ratio against various inclination angles



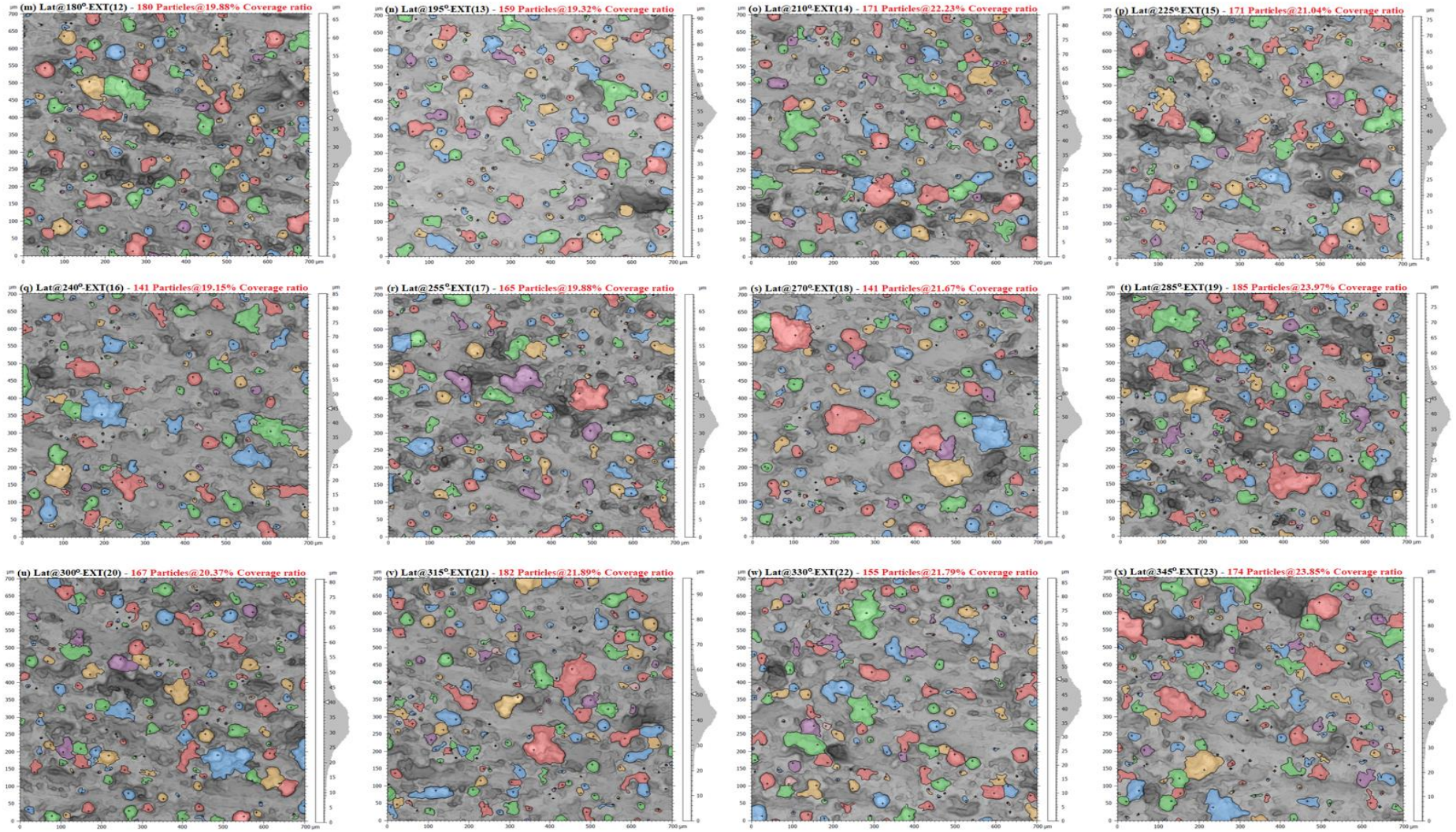
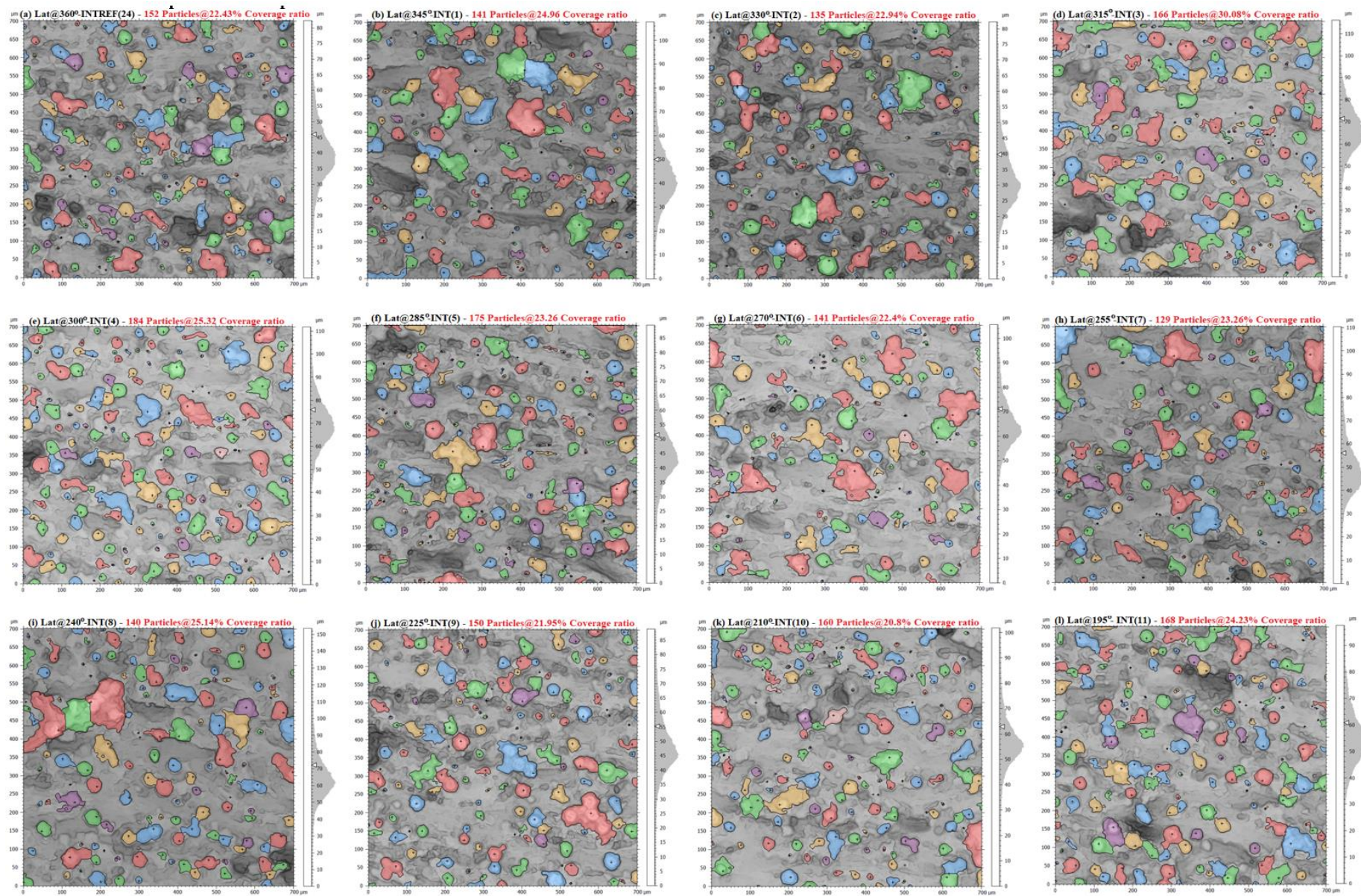


Figure 4. 28 (a-x). Individual particles descriptors and particles coverage ratio labels for latitudinal facet external surface against inclination angles



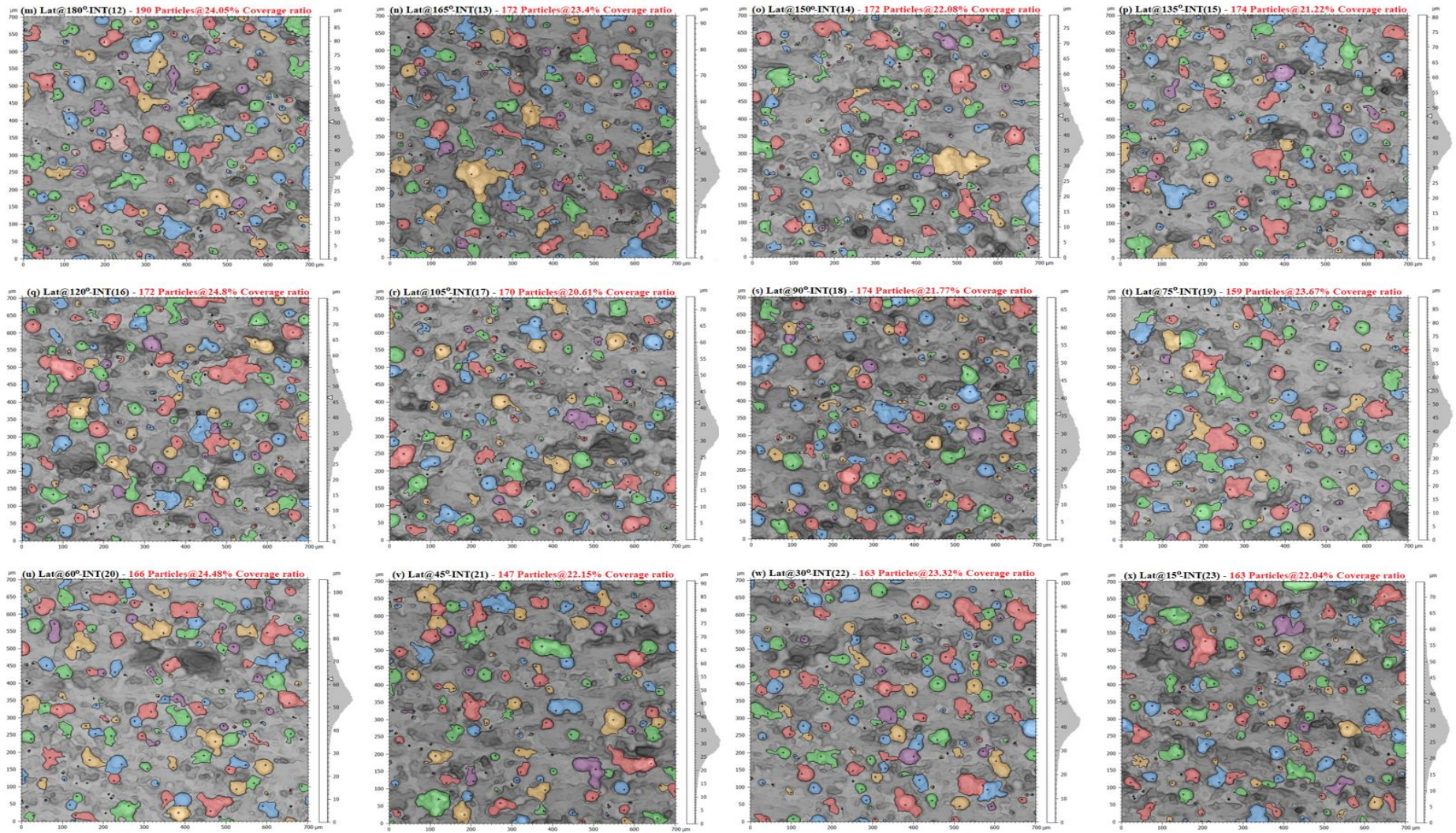


Figure 4. 29 (a-x). Individual particles descriptors and particles coverage ratio labels for latitudinal facet internal surface against inclination angles

4.5 Statistical analysis of variance (ANOVA)

Analysis of variance (ANOVA) is accustomed to identify whether there is any statistically significant difference between two or more samples. The main purpose of statistical ANOVA is to analyse and characterize the impact of different control factors and their interactions on the experimentally obtained surface roughness [212]. A comprehensive statistical analysis of variance is carried out to evaluate the impact of inclinations angles, build orientations, and the type of surfaces on the resultant surface roughness [212,376]. The significance threshold or risk level is usually set at $\alpha=0.05$. The following statistical questions are considered:

- (i) Is there any significant impact of inclination angles on resultant surface roughness?
- (ii) Is there any systematic difference between build orientations; longitudinal facet up-skin and down-skin surfaces?
- (iii) Is there any systematic difference between longitudinal facet external and internal surfaces?

4.5.1 Impact of inclination angles on resultant surface roughness

To investigate the impact of various inclination angles, obtained longitudinal facets S_a values are classified into four sets corresponding to their inclination angles namely external down-skin, external up-skin, internal down-skin, and internal up-skin surfaces. ANOVA statistical tool is applied for each individual set displayed that the calculated F values are greater than F -critical (except for internal down-skin surface), with significance threshold (α) value set to 0.05, concluding that the build inclination angles significantly influence the resultant surface roughness (see Table 4.4 to Table 4.7).

Table 4. 4 ANOVA-Impact of inclination angles on external up-skin surfaces

<i>Source of Variation</i>	<i>SS</i>	<i>df</i>	<i>MS</i>	<i>F</i>	<i>F critical</i>
External Up-skin	412.69	5.00	82.54	35.02	2.53
Longitudinal external facets	52.94	6.00	8.82		
Error	70.71	30.00	2.36		
Total	536.346	41			

Table 4. 5 ANOVA-Impact of inclination angles on external down-skin surfaces

<i>Source of Variation</i>	<i>SS</i>	<i>df</i>	<i>MS</i>	<i>F</i>	<i>F critical</i>
External Down-skin	891.52	1	891.5	17.68	5.99
Longitudinal external facets	207.87	6	34.64		
Error	302.60	6	50.43		
Total	1402.01	13			

Table 4. 6 Impact of inclination angles on internal down-skin surfaces

<i>Source of Variation</i>	<i>SS</i>	<i>df</i>	<i>MS</i>	<i>F</i>	<i>F critical</i>
Internal Down-skin	12027.66	3	4009.22	54.15	3.16
Longitudinal internal facets	324.5268	6	54.08781		
Error	1332.733	18	74.04071		
Total	13684.92	27			

Table 4. 7 ANOVA-Impact of inclination angles on internal up-skin surfaces

<i>Source of Variation</i>	<i>SS</i>	<i>df</i>	<i>MS</i>	<i>F</i>	<i>F critical</i>
Internal Up-skin	8.36	5.00	1.67	0.20	2.53
Longitudinal internal facets	29.38	6.00	4.90		
Error	248.37	30.00	8.28		
Total	286.115	41			

4.5.2 Statistical difference between build orientations; up-skin and down-skin surfaces

To investigate this statistical question, first external surfaces are considered. The obtained S_a values of longitudinal facets external surface up-skin and down-skin orientations are addressed. ANOVA analysis reveals that the computed F value is greater than the F -critical for both up-skin and down-skin orientations of external surfaces. This signifies that there is a significant difference present between up-skin and down-skin orientations of external surfaces (see Table 4.8).

Table 4. 8 ANOVA- statistical difference between external up-skin and down-skin surfaces

<i>Source of Variation</i>	<i>SS</i>	<i>df</i>	<i>MS</i>	<i>F</i>	<i>F critical</i>
External Up-skin and Down-skin	3380.62	8.00	422.58	35.14	2.14
Longitudinal external facets	102.38	6.00	17.06		
Error	577.29	48.00	12.03		
Total	4060.29	62			

Similarly, to investigate the internal surfaces, obtained Sa values of longitudinal facets internal surface up-skin and down-skin orientations are counted. An ANOVA analysis reveals that the computed F value is greater than the F-critical for both up-skin and down-skin orientations of internal surfaces. This signifies that there is a significant difference present between up-skin and down-skin orientations of internal surfaces (see Table 4.9).

Table 4. 9 ANOVA- statistical difference between internal up-skin and down-skin surfaces

<i>Source of Variation</i>	<i>SS</i>	<i>df</i>	<i>MS</i>	<i>F</i>	<i>F critical</i>
Internal Up-Skin and Down-skin					
skin	20169	10	2017	67.53	1.99
Longitudinal internal 07 facets	145.34	6	24.22		
Error	1792.07	60	29.87		
Total	22106.48	76			

4.5.3 Statistical difference between the type of surfaces; external and internal surfaces

To investigate this statistical question, first up-skin surfaces are considered. The obtained Sa values of longitudinal facets external and internal up-skin surfaces are analyzed. From ANOVA it is evident that the computed F value is greater than the F-critical for both external and internal up-skin surfaces. This signifies that there is a significant difference present between external and internal up-skin surfaces (see Table 4.10).

Table 4. 10 ANOVA- statistical difference between external up-skin and internal up-skin surfaces

<i>Source of Variation</i>	<i>SS</i>	<i>df</i>	<i>MS</i>	<i>F</i>	<i>F critical</i>
External Up-skin, Internal Up-skin	432.76	11.00	39.34	7.81	1.94
Longitudinal external and internal facets	69.16	6.00	11.53		
Error	332.26	66.00	5.03		
Total	834.1742	83			

Similarly, to investigate down-skin surfaces, obtained Sa values of longitudinal facets external and internal down-skin surfaces are explored. From ANOVA it is apparent that the calculated F value is greater than the F-critical for both external and internal down-skin surfaces. This signifies that there is a significant difference present between external and internal down-skin surfaces (see Table 4.11).

Table 4. 11 ANOVA-statistical difference between external and internal down-skin surfaces

<i>Source of Variation</i>	<i>SS</i>	<i>df</i>	<i>MS</i>	<i>F</i>	<i>F critical</i>
External Down-skin, Internal Down-skin					
	17322.51	7	2474.64	52.86	2.24
Longitudinal external and internal facets	249.44	6	41.57		
Error	1966.23	42	46.82		
Total	19538.18	55			

4.6 Summary

Surface quality characterisation and quantification are considered 3D micro and nanoscale analyses that provide essential information to understand, control and optimise the functional behaviour of AM surfaces used in heat exchanger internal cooling channels, and other wear and tribological applications. The experimental results revealed the existence of strong intertwining interrelationship between the varying surface inclination angles and distinct defects and surface asperities emerged on both external and internal AM surfaces. From the analysed surface roughness metrics height parameters, it was found that Sa, Sq, Ssk, Sku, trends interspersed between the surfaces dominated by spatters, un-melted and partially-melted powder particles, and the surfaces

dominated by laser ripples and staircase effect from the re-solidified melt tracks at lower inclination angles.

Longitudinal facet external and internal surfaces

- As a result of individual build melt track layers, staircase effect and laser ripples, the surface roughness (Sa, Sq) metric trends between 15°-45° inclination angles display salient large wavelength features which are often loose clusters. The observed larger wavelength features are credited to insufficient redistribution of mass or heat transfer (by laser beam) from the adhered un-melted, partially melted powder particles during the re-melting process by the virtue of inclined angles.
- The surface inclinations beyond 75° showed a higher number of closely packed adhered un-melted, partially particles onto the surface with each other, which is ascribed to the ability of laser fluence to the complete redistribution of heat transfer thereby, reducing the large wavelength features.
- The surface roughness of longitudinal facets up-skin surfaces is linearly dependent on build inclination angles, while the surface roughness of down-skin surfaces is affected by the adherence of a higher number of particle features caused by intermittent heat transfer. Internal down-skin surfaces revealed quite a strong correlation between hybrid parameter Sdr and inclination angles (105°-165°).
- The number of particles analysis plot for external up-skin and down-skin surfaces presented a symmetrical fashion. Internal up-skin surfaces showed a consistently increasing trend while the down-skin surfaces followed a steady descending path; somewhat identical but less symmetrical as compared to the external surface. Overall, external up-skin surfaces revealed an average of ~12 particles more attached to the surface as compared to internal surfaces for the same region. Similarly, an average of ~8 particles are less attracted to the external down-skin surfaces in comparison with their counterparts.
- The particles coverage ratio graphs of external and internal surfaces for all the sloping angles demonstrated a homogeneous style, with a mere 2% higher particles coverage ratio identified for internal surfaces.

Latitudinal facet external and internal surfaces

- Sa and Sq values for latitudinal facet internal surface are approximately higher (6%-20%) than that of the external surface.

- A consistent continuous and steady particle (151-160 particles) trend is observed for all full-turn angles (0° - 360°) at the equator for internal surfaces.
- The external surfaces followed a consistent steady trend for all inclination angles, except 285° where the higher number of particles (~30 particles) are registered; which is ascribed to angle of incidence of the laser beam and the position of AM part/artefact on the build platform. The particle coverage ratio for both external and internal surfaces showed homogeneous trends.
- From the latitudinal facet surface texture parameters characterisation and particles analysis, it is fair to conclude that there is no significant difference between internal and external surface roughness. However, the position of AM part on the substrate and laser beam incidence angle significantly affect the final surface roughness.
- All in all, it is clearly evident from the experimental results and statistical significance analysis that build inclination angles have a significant impact on the surface roughness of longitudinal facets up-skin and down-skin orientation as well as external and internal surfaces. Meanwhile, the build inclination angles demonstrate a less significant effect on latitudinal facets on external and internal surfaces.

Chapter 5. Statistical optimisation and impact of critical parameters on top and side surface quality of LPBF processed 316L SS hexagon artefacts

Targeting to achieve lower roughness in most of the functional parts is useful. However, it is important to note that optimising or tailoring the surface quality to the desired (higher) roughness levels greater than 4 μm (up to 100 μm in dentistry) has proven to be more beneficial in certain osseointegrated implants of biomedical applications. The rougher surface aid biocompatibility and support higher load-bearing capacity. Similar higher roughness has favoured the heat transfer for cooling and maintain the structural integrity in liquid rocket engines of aerospace applications. Also, rougher surface helps to retain more oil and results in smaller wear and friction of cylinder liners and marine applications. Optimising or tailoring the surface quality to achieve lower or desired roughness levels is a challenge. To tailor the desired surface quality, it is vital to have a thorough understanding of complex surface topographical features that emerge on different metal AM surfaces. The novel surface texture characterisation toolbox developed in Chapters 3&4 provided essential information on complex topographies of various AM surfaces. Hence, this chapter aims to design or achieve lower or desired top and side surface quality of 316L SS hexagon artefacts by optimising LPBF critical parameters using Taguchi design of experiments. ANOVA was used to identify the impact (percentage contribution) of individual parameters on the resultant surface quality. Finally, 25 different top, and 25 side surfaces topographies were systematically characterised.

A conference paper has been published by the first author SR Narasimharaju, titled *“Influence of critical process parameters on surface roughness and statistical optimization of LPBF 316L stainless steels”* [12]. Summer Tropical Meeting: Advancing Precision in Additive Manufacturing-2022. American Society for Precision Engineering (ASPE).

The surface quality of an AM part is vital in determining the dimensional accuracy, and post-process treatments, also enhance the functional performance of the final products [233]. The surface quality of a load-bearing engineering part is crucial in industrial applications, with certain applications requiring surface roughness of 0.8 μm or more to avoid premature failure from the surface-initiated cracking [234]. However, it is highly unlikely to improve the surface quality infinitely as it is exceedingly difficult to reduce the surface roughness value to $<1 \mu\text{m}$ by optimizing the LPBF process alone [165,235]. Despite having the vast advantages of indefinite geometrical freedom and minimal material waste, LPBF still suffers from poor surface quality.

It is necessary to have a strong understanding of AM parameters' influence on the resultant surface quality [236]. A comprehensive knowledge of AM enables the fabrication of load-critical parts with enhanced surface integrity [61,138,236,238]. For example, complex thermo physical phenomena that occur rapidly in microscopic scales during laser powder-bed interplay are crucial as they define the final surface quality of the LPBF parts [35]. The existing research found that satisfactory surface quality can be achieved by controlling the critical AM process parameters [236,]. Amongst all, the critical LPBF process parameters deemed mainly responsible for surface quality are laser power (LP), hatch spacing (HS), layer thickness (LT), point distance (PD), and exposure time (ET) [36,238]. These five parameters deliver the required energy by a pulsed laser beam to a volumetric unit of powder material.

Many researchers in the public literature have fabricated only a few basic cubes and/or existing standard artefacts using a limited set of parameters while evaluating the surface characteristics and parametric optimization of the metal AM process [34-38]. Also, there has been very little open access literature on statistical optimization of LPBF process critical parameters concerned with surface texture prediction and characterisation of both top and side surfaces of bespoke artefacts built in one run. Hence, this research is focused on statistical optimization of the LPBF critical parameters by Taguchi DOE to predict the optimal parametric combination that helps to achieving the best or desired top and side surface quality of 25 hexagon artefacts. The impact of these critical parameters and their interactions are established by analysing the parametric significance using statistical analysis of variance (ANOVA). Furthermore, the correlation between various surface anomalies and the surface texture parameters S_a is studied. Finally, verification experiments are conducted to validate the statistically predicted parametric combinations. This research aims to provide valuable insight into the surface quality of LPBF components, which defines the functional performance in the long term. For instance, to select the optimal manufacturing workflow, one must have in-depth knowledge about the surface capabilities of that specific AM process. This research will also promote enhanced understanding and conviction of statistical optimisation, fabrication of multiple artefacts-two surfaces, and the emergence of various surface anomalies concerning multiple parametric combinations and surface texture parameters. The flowchart of this research is given in Figure 5.1

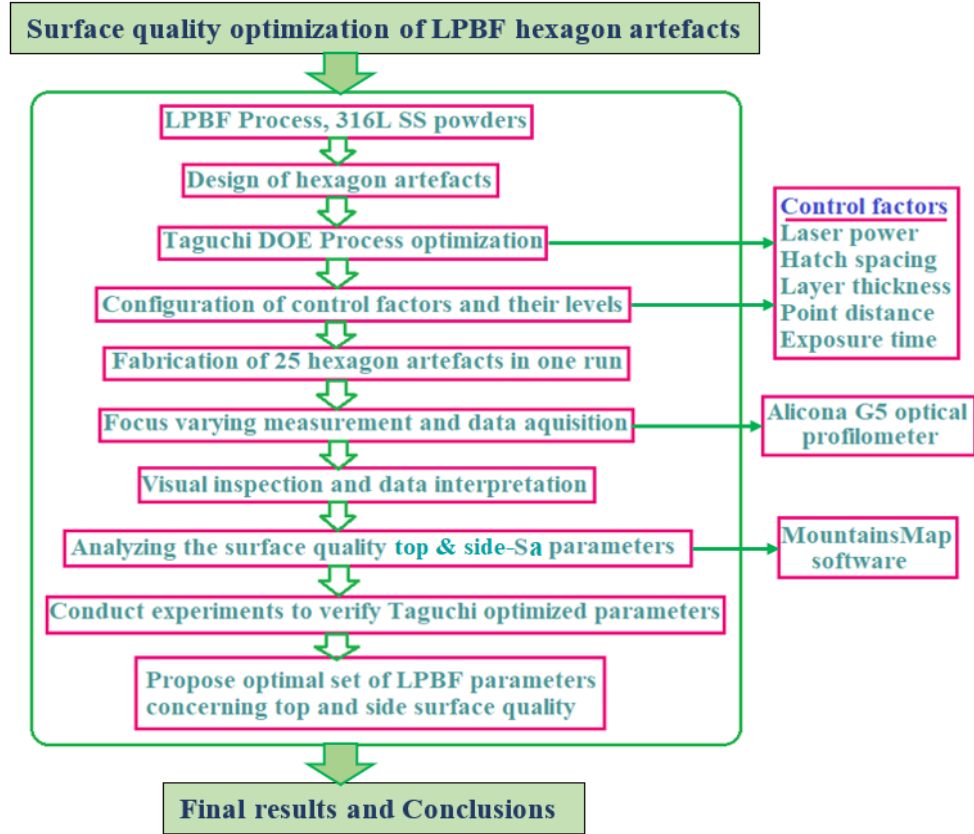


Figure 5. 1 Flowchart of this research

5.1 Hexagon artefacts design and fabrication

Figure 5.2a shows the dimensions of the hexagon artefacts produced by the Renishaw AM400 selective laser melting machine. LPBF process parameters chosen in this research are given in Table 5.1. Gas atomized mostly spherical-shaped 316L SS powder supplied by Renishaw U.K plc is used to fabricate 25 hexagon artefacts. The AM machine is fitted with high-stability fiber lasers of pulsed Nd:YAG (wavelength 1070 nm) capable of delivering maximum average laser power of 400 W. The substrate size was 280 mm x 280 mm x 365 mm. The build chamber is ensured to be constantly pumped with protective atmospheric gas (argon) during the process, to maintain an oxygen content of less than 0.1%, which helps to keep the LPBF parts free from oxidation. The powder morphologies, scanning patterns employed in this research is same as already mentioned in the previous chapters.

Table 5. 1 LPBF critical parameters used for parametric optimization

Parameters	Values	Levels
Laser power (W)	100 125 150 175 200	5
Hatch spacing (μm)	25 50 75 100 125	5
Layer thickness (μm)	30 60 90 120 150	5
Point distance (μm)	20 40 60 80 100	5
Exposure time (μs)	40 80 120 160 200	5

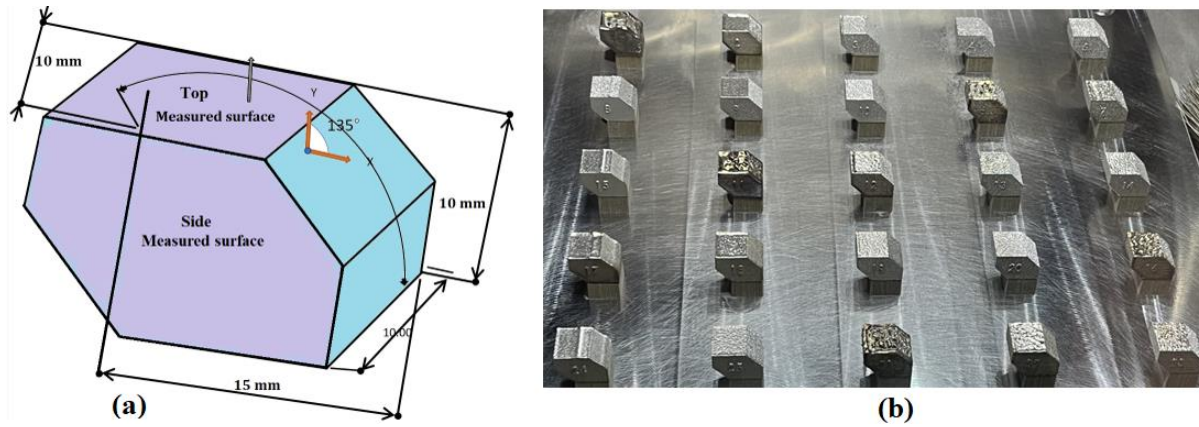


Figure 5. 2 schematic illustration of (a) dimensions of the hexagon artefacts, and (b) LPBF built 25 hexagon artefacts using Taguchi DOE optimization

5.2 Measurement and data processing strategy

Alicona G5 infinite focus variation measurement (FVM) system has been used to capture the areal topography of LPBF artefacts. The FVM configuration adopted is tabulated in Table 5.2. DigitalSurf MountainMaps commercial software is used to analyze the surface topographical data. Only levelling is applied and no other filtration operations are performed to void losing surface information. The analysed surface topographical data is helpful to characterize and correlate the emerging surface anomalies concerning surface texture parameter S_a as per ISO 25178-2 [32]. Furthermore, the captured FVM images are used to visually inspect and interpret the varieties of surface anomalies originating from 25 parametric combinations.

Table 5. 2 Focus variation measurement method configuration

Magnification	10x lens
Illumination type	Ring light (capture topographical data)
Lateral resolution	2 μm
Vertical resolution	1 μm
Sampling distance	0.878 μm (X and Y directions)
Measurement size	size 8 mm x 8 mm (stitched)

5.3 Taguchi design of experiments and ANOVA

The research relating to the surface quality optimisation presented in the literature section have mainly employed the Taguchi DOE using orthogonal arrays and S/N ratio analysis to determine the optimal parametric combinations of metal AM parameters that reduce the response variable [156-158,192,193]. Five control factors at five levels are prepared using MINITAB-19 software based on the orthogonal array of L25 (5x5). The experimental top quality (Sa) results correspond to the L25 orthogonal array are shown in Table 5.3. The Taguchi DoE method is adopted because it gives a reduced variance for the LPBF experimentation process to achieve the least possible or best surface roughness (Sa) result under the optimal settings for the five crucial control parameters, and determines their impact on the experimentally obtained top and surface roughness of hexagon artefacts [213]. The 25 LPBF printed artefacts using Taguchi DoE can be seen in Figure 5.2b. The top and side surfaces of the hexagon artefacts are measured at four different locations, and the mean was computed.

As already mentioned ANOVA is a statistical decision-making tool that determines the differences in average performance and helps to analyse the significance of all the control factors of Taguchi DOE. In simple terms ANOVA is basically used to study the significance of process parameters on the output characteristics [212,213]. ANOVA in this chapter is employed to understand and analyse the complex experimental data interactions between the five critical LPBF parameters and the resultant top and side surface roughness values. In addition, ANOVA is helpful to establish a meaningful correlation of the Taguchi predicted results, and how much percentage contribution each control factor caused on the resultant top and side surface quality [213].

5.4. Results and discussions

The final surface quality of the LPBF part is primarily determined by the aforementioned five critical process parameters (LP, LT, HS, PD and ET), which decide the overall specific energy density or common term energy input per unit volume of the build [241,247]. It is acknowledged that Renishaw AM400 operates with discrete laser spot/point exposures. An analogous scan speed is calculated based on exposure time, point distance, point jump speed (PJS), jump delay time (JDT) and point jump time (PJT). PJS is usually set to 5000 mm/s and JDT at 0 [241,247,377]. The energy density (ED) is given by equation (9).

$$ED = \frac{LP * ET}{LT * HS * PD} J/mm^3 \dots\dots\dots (9)$$

The impact of these critical parameters is analysed by visually inspecting the FVM images. A sincere effort has been invested in establishing the correlation between the varieties of surface anomalies that emerged on all 25 hexagon artefacts' top and side surfaces fabricated using 25 different experimental parametric designs.

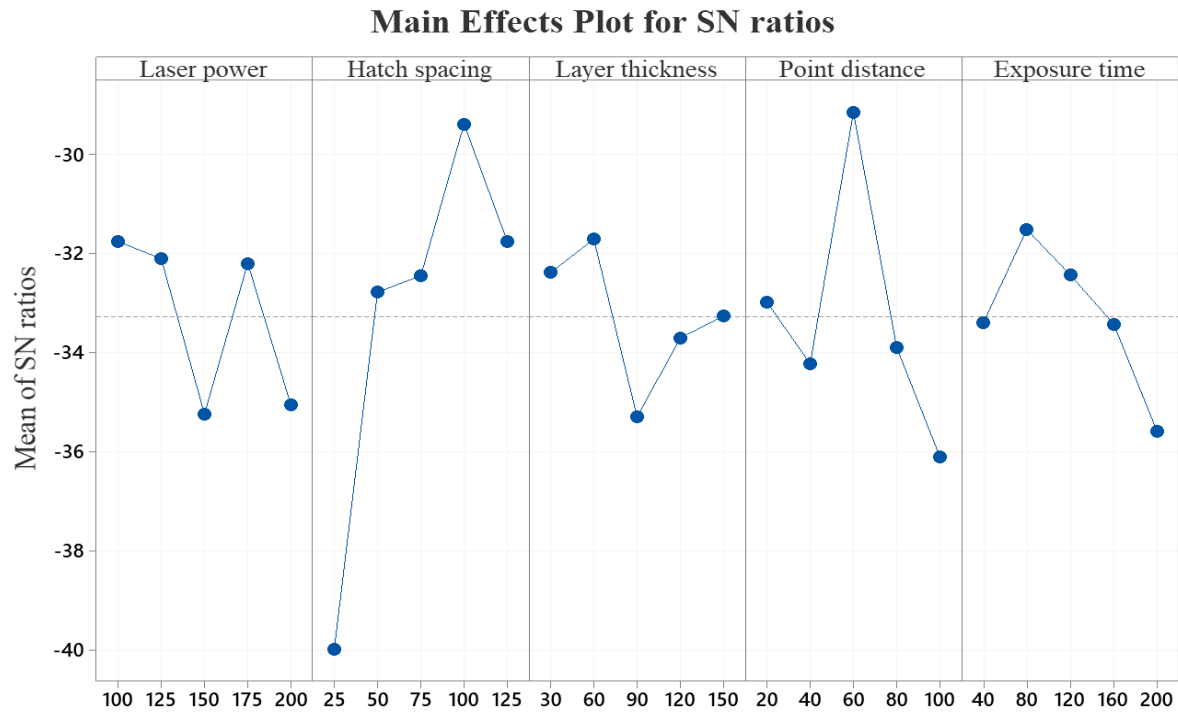
Table 5. 3 L25 Orthogonal array by Taguchi DoE and their resultant top surface Sa values

Serial no	LP (μm)	HS (μm)	LT (μm)	PD (μm)	ET (μm)	Top Sa (μm)
1	100	25	30	20	40	76
2	100	50	60	40	80	38
3	100	75	90	60	120	21
4	100	100	120	80	160	34
5	100	125	150	100	200	42
6	125	25	120	40	120	33
7	125	50	150	60	160	69
8	125	75	30	80	200	74
9	125	100	60	100	40	17
10	125	125	90	20	80	37
11	150	25	60	60	200	214
12	150	50	90	80	40	36
13	150	75	120	100	80	61
14	150	100	150	20	120	37
15	150	125	30	40	160	37
16	175	25	150	80	80	113
17	175	50	30	100	120	29
18	175	75	60	20	160	21
19	175	100	90	40	200	28
20	175	125	120	60	40	58
21	200	25	90	100	160	163
22	200	50	120	20	200	57
23	200	75	150	40	40	65
24	200	100	30	60	80	37
25	200	125	60	80	120	26

5.4.1 Taguchi DOE optimisation and ANOVA for top surface quality

The proper combination/selection of critical parameters determines the LPBF process reliability. The different levels of critical process parameters window, maximum and minimum range are selected based on the existing literature on PBF SS316L (Renishaw metal AM machines). The main objective of this Taguchi DOE optimization is to (i) investigate the 25 different combinations of critical process parameters on the resultant top and side surface quality and systematically characterise, correlate with the suitable areal surface texture parameters, (ii) find out the optimum set of LPBF parameters to achieve the best or desired top and side surface quality (iii) validate Taguchi predicted optimum critical parameters for top and side surface quality by carrying out confirmation experiments and (iv) compare and draw the meaningful conclusions between the resultant top and side surface quality S_a values obtained from Taguchi predicted parameters with Renishaw AM-400 default industrial settings. Finally, the impact of individual critical process parameters was effectively analysed by using ANOVA.

To identify the most efficient process parameters for the top surface quality S_a , the Taguchi analysed S/N ratio response table obtained from Minitab 19 software tool is given in Table 5.4. The *Delta* value represents the difference between the maximum and minimum S/N ratio for the levels of each control factor. The higher the *Delta* value, the greater significance of that specific control factor. The most dominant control factor is ranked based on its efficacy. Hatch spacing emerged as the top-ranked influential control factor, followed by point distance, laser power, and exposure time. Layer thickness is the least significant controlling factor or parameter in analysis. Based on the Taguchi DOE, with the selected objective, smaller-the-better, optimum LPBF parameters to achieve the best top surface quality are found to be laser power at 100W, hatch spacing at 100 μm , layer thickness at 60 μm , point distance at 60 μm , and exposure time at 80 μs (see Figure 5.3 and Table 5.5). These optimized parameters can be represented as $\text{LP}_1\text{-HS}_4\text{-LT}_2\text{-PD}_3\text{-ET}_2$, i.e., laser power at level 1, hatch spacing at level 4, layer thickness and exposure time both at level 2, and finally, point distance at level 3.



Signal-to-noise: Smaller is better

Figure 5. 3 Schematic label of S/N ratio plots for LPBF critical parameters for top surface quality

Table 5. 4 Taguchi response for S/N ratios for top surface-*Smaller-the-better*

Level	LP	HS	LT	PD	ET
1	-33.40	-39.98	-31.75	-32.98	-32.38
2	-31.51	-32.77	-32.10	-34.22	-31.71
3	-32.42	-32.45	-35.23	-29.15	-35.29
4	-32.42	-29.38	-32.19	-33.89	-33.70
5	-35.59	-31.75	-35.06	-36.10	-33.25
Delta	4.07	10.60	3.48	6.96	3.59
Rank	3	1	5	2	4

Table 5. 5 Taguchi DOE predicted LPBF parameters for top surface quality

LP1 (W)	HS4 (μm)	LT2 (μm)	PD3 (μm)	ET2 (μs)
100	100	60	60	80

The percentage contribution of each control factor or process parameter that influences the performance characteristics is determined by analysis of variance (ANOVA) for the S/N ratio, which is illustrated in Table 5.6 and Figure 5.4. From the ANOVA table, the highest percentage contribution on the top surface quality Sa is identified as hatch spacing (46 %), followed by point distance (19 %), laser power (8.6 %), exposure time (6.6 %). Layer thickness is found as the least percentage contributed control factor towards the top surface quality at 5.4 %.

Table 5. 6 ANOVA for S/N ratios for top surface quality

Source	DF	Seq SS	Adj SS	Adj MS	F	% C
Laser power	4	59.42	59.42	14.856	0.58	8.6
Hatch spacing	4	316.84	316.84	79.211	3.07	46
Layer thickness	4	37.55	37.55	9.388	0.36	5.4
Point distance	4	132.08	132.08	33.020	1.28	19
Exposure time	4	46.03	46.03	11.507	0.45	6.6
Residual Error	4	103.26	103.26	25.815		
Total	24	695.19				

Note: DF-degree of freedom, Adj. SS-adjusted sum of squares, Adj. MS-adjusted mean squares.

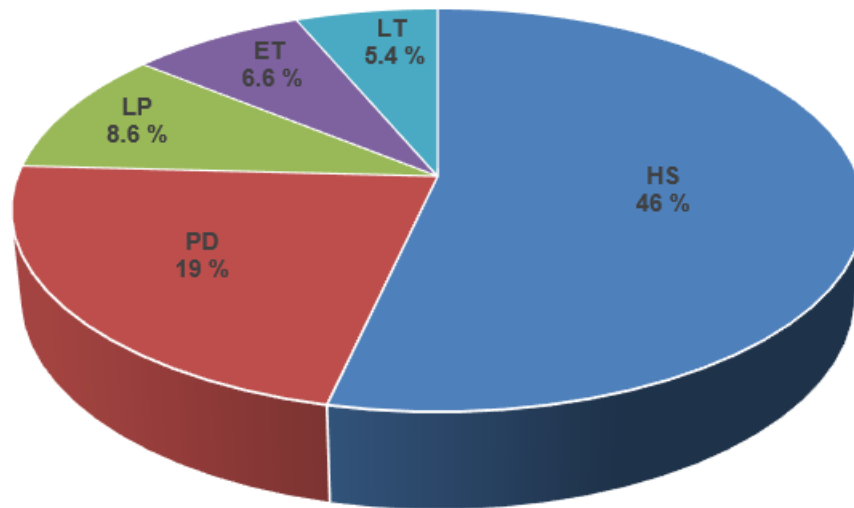


Figure 5. 4 Percentage contribution of the control factors for top surfaces

5.4.2 Visual inspection of top surface quality

Figure 5.5(a-y) depicts the top surface topography of all the 25 LPBF hexagon artefacts. It is interesting to note that artefacts #1, #6, #11, #16, and #21 (Figure 5.5-a,f,k,p,u) displayed fascinating identical bigger crater-like defects that cover a major part of the surface at different scales. For example, artefact #1 displayed a wider smoother crater-like defect, whereas the other four artefacts showed more rigorous and torturous kinds of crater defects. It is intriguing to note that all these defects appeared at the first-level shift of each set of process parameters. As mentioned, five parameters at five levels are accounted for in this research. Similar crater-like defects occurred on a number of other artefacts surfaces such as #7, #12, #13, #14, #19, #20, #22, and #23 (Figure 5.5-g, l, m, n, s, t, v and w). However, these crater defects are either smaller or shallower or very few in number compared to the previously discussed ones. The artefact surfaces seen in Figure 5.5(n), (t) and (w) exhibited almost equal amounts of crater defects and porosities. Artefact #8 (Figure 5.5h) surface showed prevalent LPBF process-related defects like balling, spatters, and porosities. Artefacts surfaces #3, #9, and #18 accounted for a minimum of/or fewer porosities (Figure 5.5b, c, i, r); these surfaces are mostly covered with uniform and continuous molten melt track layers. Artefacts #4 and #10 presented reasonable porosities (see Figure 5.5-d, j), and no other defects are visually visible, whereas the surface of #5 unveiled a higher number of porosities (Figure 5.5e). Artefact #15 primarily displaced molten melt track layers (Figure 5.5-o), while #17 showed fewer occasional porosities and cracks (Figure 5.5-q). Finally, artefact surface #24 displayed molten melt track layers along with a random step towards the right side of the surface (Figure 5.5-x).

5.4.3 Surface texture characterisation of top surfaces

From Figure 5.6, it is apparent that artefact # 9 displayed the best surface quality (S_a 17 μm), with its parameter's combination of LP-125W, HS-100 μm , LT-150 μm and PD-20 μm , and ET-80 μs . The best S_a value (~ 17 μm) is credited to the surface mainly consisting of molten melting track layers without any visible defects. The next best S_a values are recorded for artefacts #3 and #18 (S_a 21 μm), ascribed to the uniform molten melt track layers with fewer porosity defects. The worst S_a value (214 μm) is recorded for artefact #11. This is attributed to the bigger, wider and deeper crater-like defects covered over the entire surface. The following two worst S_a values (163 μm and 113 μm) are obtained for artefacts #21 and #16, respectively, which is again related to the presence of crater-like defects all over these surfaces. The presence of balling, porosities, and

spatters on the surface of artefact #8 leads to a higher Sa of 74 μm . Except for #1 (76 μm), #7 (69 μm), #13 (61 μm), #20 (58 μm), #22 (57 μm) and #23 (65 μm), Sa values of all other artefacts were in the range of 26-42 μm .

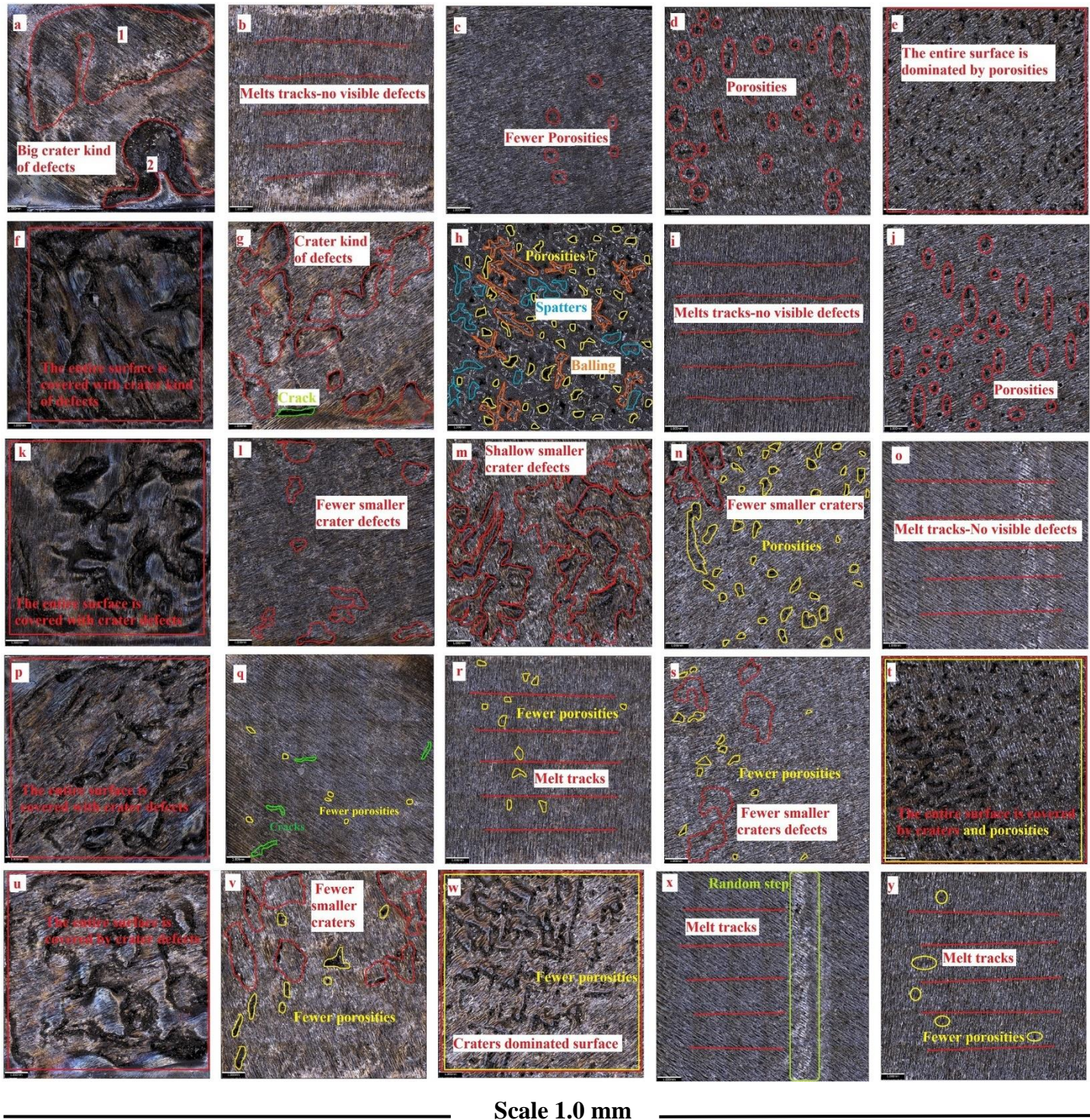


Figure 5. 5 visual inspection of the top surface of 25 artefacts [12] scale for all the images is 1 mm

The rationale behind the formation of crater-like defects is likely due to the following reasons: (i) shift of parameters level from one combination set (5th to 6th, 10th to 11th, 15th to 16th, 20th to 21st) to the other set level; (ii) evaporation of alloying elements caused by overheating of the molten melt pool and (iii) the overheated melt pool tends to evaporate, the about-to evaporate molten melt pool stuck just above the powder-bed is brushed, and dragged back by the re-coater/wiper all over the already deposited melt track layers potentially causing crater-like defects at different sizes and different scales. The emergence of other defects, such as balling, porosities, spatters, and cracks, is inevitable on the flat top surfaces in the LPBF process [12]. The formation of these defects can be reduced by choosing the optimized parametric combinations, but they are highly unlikely to be eradicated from forming [1].

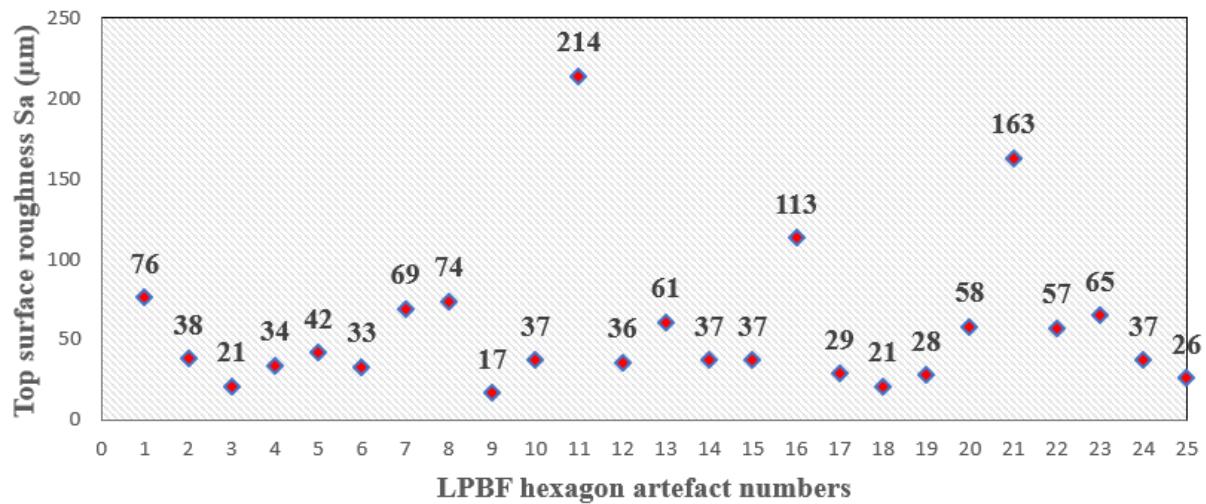


Figure 5. 6 Experimentally obtained top surface quality Sa values for 25 hexagon artefacts

5.4.4 Interaction plot of critical LPBF parameters on top surface quality

The interaction plots between each of the critical process parameters or control factors and the resultant surface quality of LPBF processed parts are shown in Figure 5.7. It is important to note that there is no interrelation between the critical parameters if the lines in the interaction plot are parallel. Meanwhile, the fewer parallel lines dispersed far away from one another in the interaction plots or the greater the degree of lines intersection of the control factors signify a greater interaction or correlation between the critical parameters. From Figure 5.7, it is anticipated that better or higher surface quality can be achieved for laser power ranging between 150-200 W, which generally shows more significant interaction overall concerning smaller hatch spacing at 25 μm. However, a more significant and stronger interaction can be observed for 150 W laser power with 90 μm

layer thickness, 100 μm point distance, and 80 μs exposure time. A similar higher degree of interaction plot for smaller hatch spacing is apparent, corresponding to 90 μm layer thickness, 100 μm point distance, and 80 μs exposure time. Layer thickness between 90-150 μm displayed complex correlation, but the highest interaction can be found at 90 μm layer thickness. Point distance and exposure time trends followed a similar interaction trend.

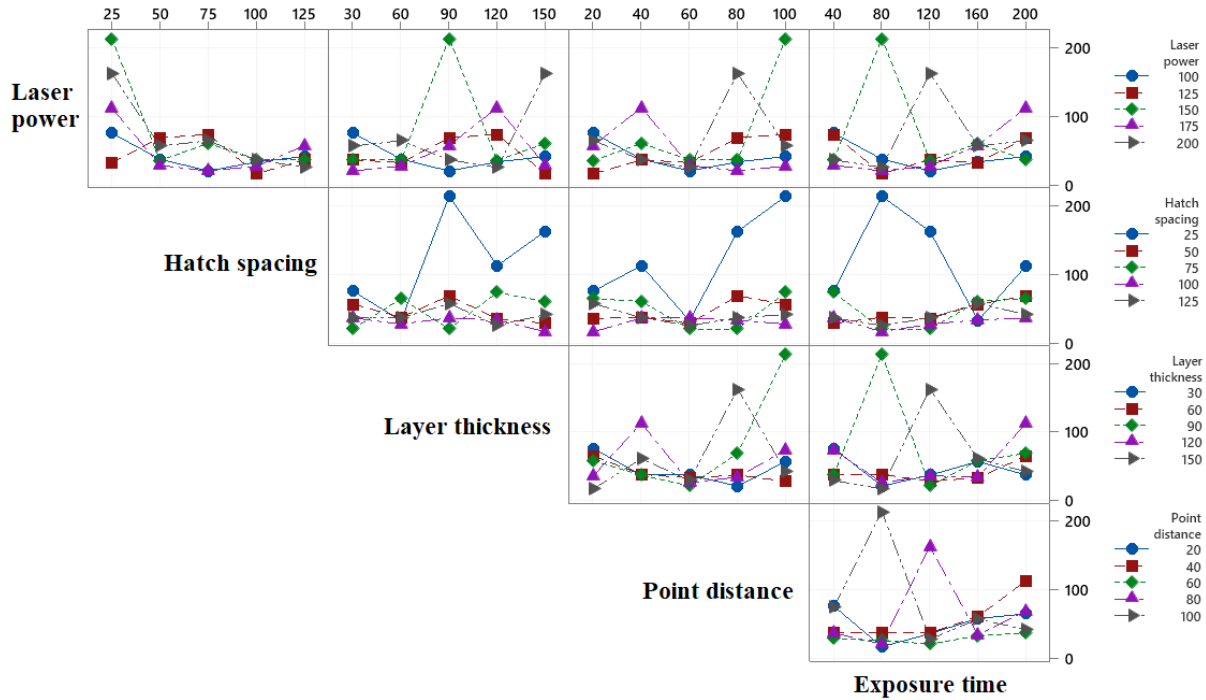


Figure 5. 7 Interaction plot for top surface quality from the critical LPBF parameters

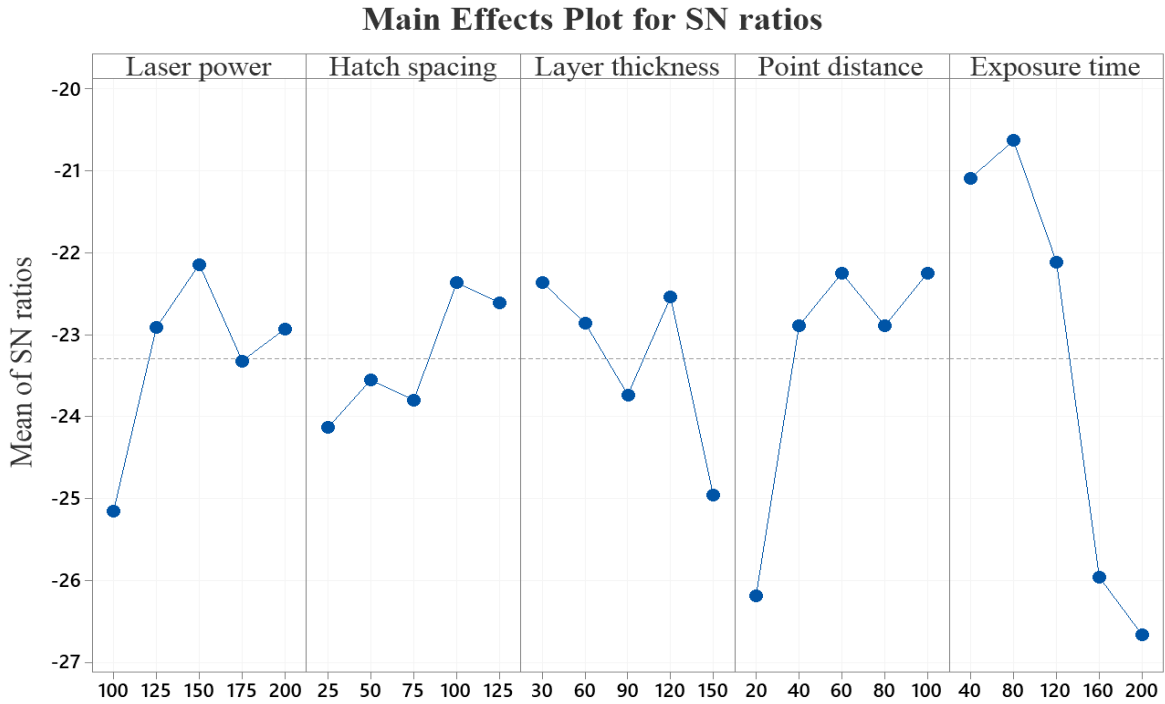
5.5 Taguchi DOE optimisation and ANOVA for side surface quality

The Taguchi optimization for the L25 orthogonal array and their corresponding side surface resultant Sa values are given in Table 5.7. The most significant critical process parameters influencing the side surface quality Sa is determined by Taguchi analyzed S/N ratio response Table 5.8 obtained from Minitab 19 software. Based on the Taguchi DOE, with the selected objective, smaller-the-better, optimum LPBF parameters to achieve the best side surface quality are found to be laser power at 150 W, hatch spacing at 100 μm , layer thickness at 30 μm , point distance at 60 μm , and exposure time at 80 μs (see Figure 5.8 and Table 5.9). Out of five critical parameters, exposure time is found to be the dominant control factor, followed by point distance, laser power, and layer thickness. Hatch spacing is identified as the least prominent controlling factor in the case of side surface quality. These optimized parameters can be represented as LP₃-HS₄-LT₁-PD₃-ET₂, i.e., laser power and point distance both at level 3, hatch spacing at level 4, layer thickness at level

1, and finally, exposure at level 2.

Table 5. 7 L25 Orthogonal array by Taguchi DoE and their resultant side surface quality Sa values

Serial no	LP (μm)	HS (μm)	LT (μm)	PD (μm)	ET (μm)	Side Sa (μm)
1	100	25	30	20	40	20
2	100	50	60	40	80	12
3	100	75	90	60	120	15
4	100	100	120	80	160	20
5	100	125	150	100	200	27
6	125	25	120	40	120	18
7	125	50	150	60	160	22
8	125	75	30	80	200	9
9	125	100	60	100	40	15
10	125	125	90	20	80	10
11	150	25	60	60	200	10
12	150	50	90	80	40	15
13	150	75	120	100	80	22
14	150	100	150	20	120	13
15	150	125	30	40	160	9.5
16	175	25	150	80	80	20
17	175	50	30	100	120	13
18	175	75	60	20	160	10
19	175	100	90	40	200	10
20	175	125	120	60	40	26
21	200	25	90	100	160	15
22	200	50	120	20	200	15
23	200	75	150	40	40	30
24	200	100	30	60	80	10
25	200	125	60	80	120	9



Signal-to-noise: Smaller is better

Figure 5. 8 Schematic label of S/N ratio plots for LPBF critical parameters for side surface quality

Table 5. 8 Taguchi response for S/N ratios for side surface-*Smaller-the-better*

Level	LP	HS	LT	PD	ET
1	-25.15	-24.13	-22.36	-26.18	-21.09
2	-22.91	-23.55	-22.86	-22.89	-20.63
3	-22.14	-23.80	-23.73	-22.25	-22.11
4	-23.32	-22.36	-22.54	-22.89	-25.96
5	-22.93	-22.61	-24.96	-22.25	-26.66
Delta	3.01	1.77	2.60	3.93	6.03
Rank	3	5	4	2	1

Table 5. 9 Taguchi DOE predicted LPBF parameters for side surface quality

LP3 (W)	HS4 (μm)	LT1 (μm)	PD3 (μm)	ET2 (μs)
150	100	30	60	80

The percentage contribution of each control factor or process parameter that influences the side surface quality characteristics is determined by analysis of variance (ANOVA) for the S/N ratio Table 5.10, which is also illustrated in Figure 5.9. From the ANOVA table, the highest percentage contribution on the side surface quality Sa is identified as exposure time with 58 %, followed by point distance (20 %), laser power (9.2 %), and layer thickness (8.3 %). Hatch spacing has a minor percentage contributed control factor towards the top surface quality at 4.3 %.

Table 5. 10 ANOVA for S/N ratios for side surface quality,

Source	DF	Seq SS	Adj SS	Adj MS	F	% C
Laser power	4	25.342	25.342	6.3356	12.15	9.2
Hatch spacing	4	11.794	11.794	2.9485	5.66	4.3
Layer thickness	4	22.937	22.937	5.7343	11.00	8.3
Point distance	4	54.248	54.248	13.5619	26.02	20
Exposure time	4	158.954	158.954	39.7386	76.23	58
Residual Error	4	2.085	2.085	0.5213		
Total	24	275.361				

Note: DF-degree of freedom, Adj. SS-adjusted sum of squares, Adj. MS-adjusted mean squares.

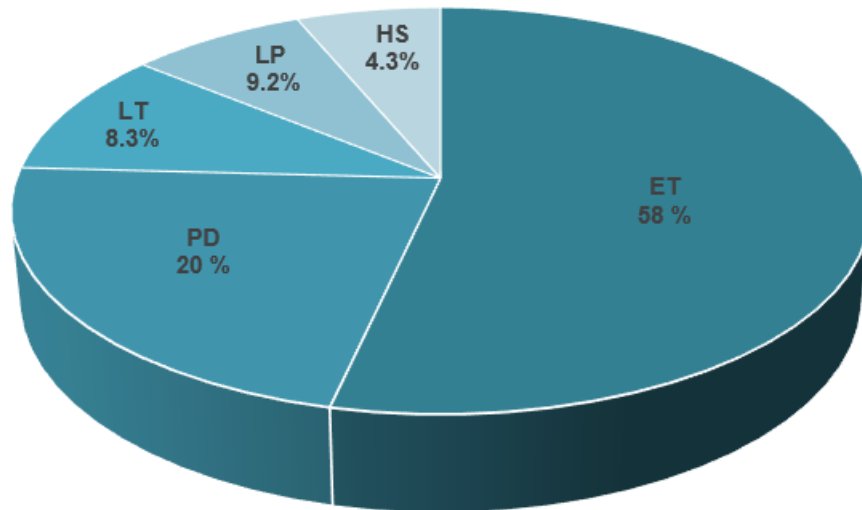


Figure 5. 9 Percentage contribution of the control factors for side surfaces

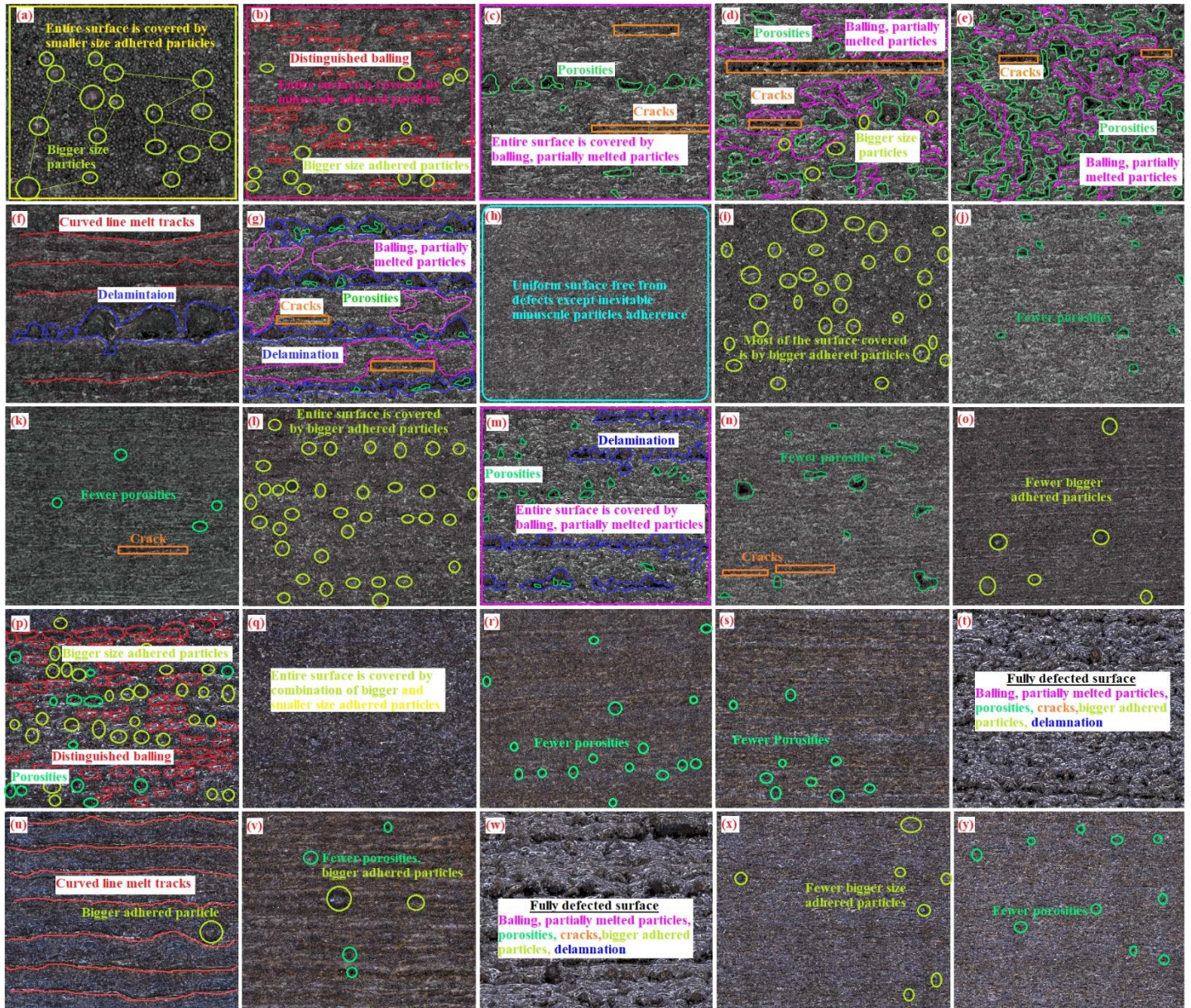
5.5.1 Visual inspection of side surface quality

Figure 5.10 (a-y) give the side surface topography of all the 25 LPBF hexagon artefacts. Unlike the top surface, none of the side surfaces displayed any form (bigger/smaller/wider/shallower) of

crater-like defects. Side surface quality is predominantly influenced by the adhered particle features derived from partially-melted/un-melted powder particles, which are well documented in the public literature [36,215]. The other contributing factors to the poor surface finish of side surfaces specific include the balling, spatters, porosities, cracks, and delamination [34,378]. It is evident that artefacts #23, #5, and #20 considered entirely defective surfaces, comprised all the indistinguishable surface anomalies mentioned earlier; spatters, balling, porosities, cracks, delamination, and other adhered particle features (Figure 5.10-w,e,t). The combination of bigger size and smaller size adhered particles covered the entire surface of artefact #1 (Figure 5.10-a). The presence of partially-melted particles, distinguished balling, porosities, cracks and bigger size adhered particles have contributed to artefact #4 and #16 surfaces (Figure 5.10-b,d,p). Artefact #6 exhibited delamination and curvy melt track layers (Figure 5.10-f). A plethora of anomalies like delamination, balling, partially-melted particles, cracks, and porosities are obvious in artefacts #7 and #13 surfaces (Figure 5.10-g,m). A uniform surface, fewer porosities, and fewer adhered particles are visible on the artefacts #15, #25 and #8 surfaces (Figure 5.10-o,y,h). Simultaneously, artefacts #10, #11, #18, #19, and #24 demonstrated limited surface topographical defects (Figure 5.10-j,k,r,s,x). The remaining artefacts #3, #9, #12, #14, #17, #21, and #22 revealed reasonable porosities, adhered particle features, cracks, and balling surface anomalies (Figure 5.10-c,i,l,n,q,u,v). The rationale behind the high proportion of particle adherence to the side surface is mainly due to (i) the complex thermophysical phenomena and intermittent heat transfer occurring during the LPBF process, (ii) the lack of laser re-melting of side surfaces in the state-of-art metal AM machines and (iii) absence of continuous support for the side surfaces unlike the top surface receives the rigid underlying support from the already solidified melt track layers or the substrate/solid base plate. The rigid support in LPBF offers faster heat conduction, whereas the heat transfer of the side surfaces occurs through the loose powder-bed support. The conduction of heat through the loose powder bed is normally slow, and part of it is accumulated within, which attracts more powder particles. However, this partially accumulated heat is not sufficient for the complete melting, leading to the adherence of more particle features on side surfaces, causing a rougher surface or substandard surface finish [12,36,215]. There is always continuous room for the reduction of other inevitable defects concerning the LPBF process, but implausible to nullify. Similarly, delamination and cracking on side surfaces can be minimized by selecting smaller layer thickness, particularly with other optimized parameters.

5.5.2 Surface texture characterisation of side surfaces

From Figure 5.11, most of the side surfaces exhibited stable and closely associated Sa values within the range of 10-20 μm .



Scale 1.0 mm

The best surface roughness value of Sa 0 μm is recorded for artefacts #9 and #25, resulting from Figure 5. 10 Visual inspection of the side surface of 25 artefacts, scale for the all images is 1 mm

The best surface roughness value of Sa-9 μm is recorded for artefacts #8 and #25, resulting from a uniform surface with fewer surface anomalies. The respective parametric combinations are LP-125W, HS-75 μm , LT-120 μm and PD-100 μm , ET-40 μs , and LP-200W, HS-125 μm , LT-120 μm and PD-60 μm , and ET-80 μs . The next best Sa-9.5 μm is found for artefact #15, followed by artefacts #10, #11, #18, #19, and #24 with their corresponding Sa-values 10 μm . The completely defected artefact surfaces #23, #5, and #20 resulted in the worst Sa values of 30 μm , 27 μm and 26 μm . Delamination played a major role in the poor surface quality of artefacts #6 (Sa-18 μm), #7, and #13, both recording a Sa value of 22 μm . The remaining artefacts' Sa values are in the range of 12 μm -20 μm , owing to various inevitable surface anomalies at different sizes and scales. Although the side surfaces are more prone to the adherence of particle features, they do not contribute significantly towards the substandard surface quality compared to the top surface quality, which is greatly compromised mainly due to the formation of crater-like defects at different sizes and different scales.

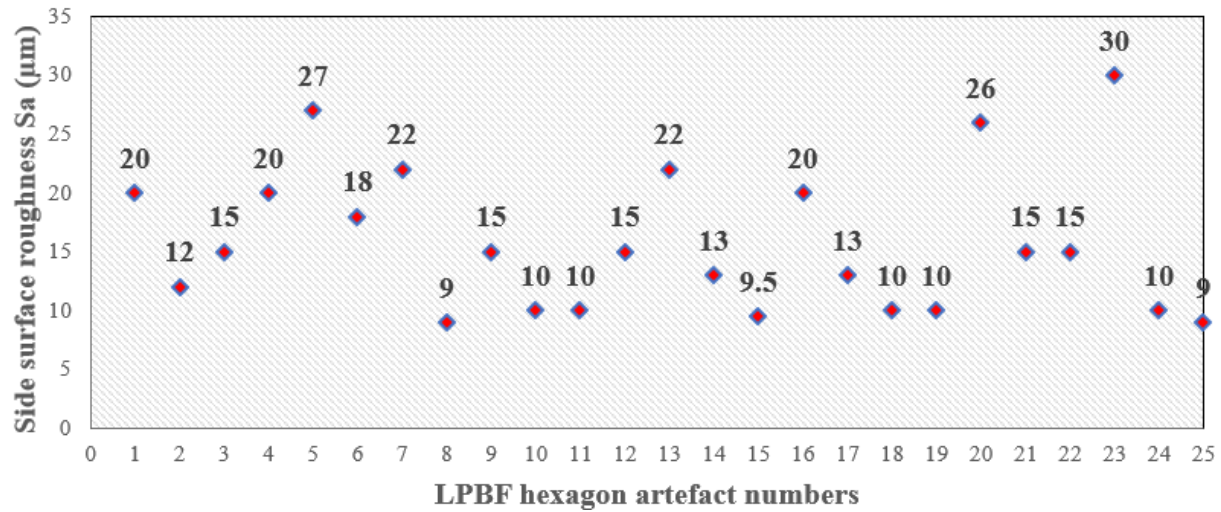


Figure 5. 11 Experimentally obtained side quality Sa values for 25 hexagon artefacts

5.5.3 Interaction plot of critical LPBF parameters on side surface quality

Fig. BBB illustrates the complex interaction plot between the five critical process parameters and the resultant side surface quality of LPBF hexagon artefacts. Unlike the top surface, where only a few levels of each critical parameter displayed complex interaction, the interaction plot for the side surface quality displays an entirely different, very strong and fascinating interaction between all the five critical process parameters (see Figure 5.12). It is hard to figure out any parallel lines in the side surface interaction plot. Instead, a rigorous intertwining interaction between all the five

levels of the five critical parameters is clearly visible. Although all levels exhibited a meaningful interaction, laser power levels 100 W, and 200 W particularly revealed significant interactions for hatch spacing levels 75 μm and 125 μm ; layer thickness levels 60 μm and 150 μm ; point distance levels 20 μm and 100 μm ; and finally, exposure time levels at 200 μs . A similar trend was followed for the other critical process parameters at all levels. Based on the side surface interaction plot, it is highly likely to achieve the best side surface quality for the laser within the above-mentioned range/levels of the critical parameters.

The main reason for this sophisticated, appealing interaction plot could be related to the close range or evenly distributed obtained resultant side surface quality Sa values (9-30 μm) for all the 25 hexagon artefacts. Conversely, the resultant top surface quality Sa values were unevenly distributed and widely dispersed from 17 μm to 214 μm for all 25 hexagon surfaces. Hence, it is fair to infer that the interaction plot for the top surface quality displayed a weaker correlation between fewer selected levels of each critical process parameter. Overall, the side surface interaction plot exhibited reliable and effective interactions compared to the top surface quality plot.

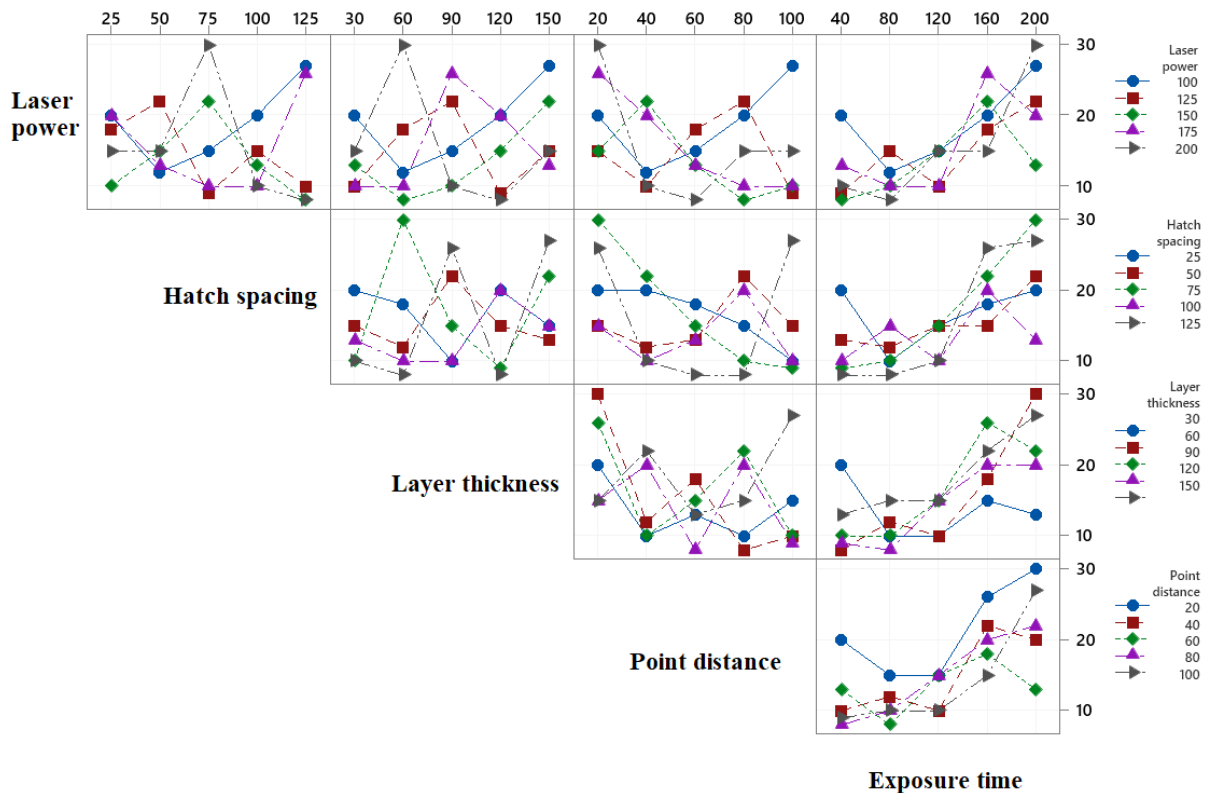


Figure 5. 12 Interaction plot for side surface (Sa) from the critical LPBF parameters

5.6 Verification experiments

The verification experiments are carried out to validate the Taguchi design predicted optimum process parameters. Instead of selecting a random result as most authors followed in the public literature [379], the best surface quality result is selected from the L25 orthogonal experimental design arrays and compared with the Taguchi optimized top and side surface quality Sa results. In addition, these two Sa results are also compared to the results obtained from the Renishaw AM-400 machine default parameters settings. It is interesting to note that the top surface quality from Taguchi DOE resulted in an improved Sa value (13 μm) by 4 μm when compared with the best surface quality result Sa (17 μm) obtained from the L25 orthogonal arrays (see Table 5.11). Similarly, the side surface quality was improved by 1 μm for Taguchi optimized parameters (Sa 8 μm) as compared to the best surface quality result Sa (9 μm) obtained from the L25 orthogonal arrays, which is not a significant improvement but still reasonable (see Table 5.12). Finally, the Renishaw default settings obtained a slightly better top surface quality (Sa 10.5 μm), while the Taguchi design predicted optimum parameters resulting in excellent side surface quality of Sa 8 μm compared to its counterparts. The top surface topography of the hexagon artefact built using the Renishaw default AM parameters setting confirms the achieved best top surface quality with the presence of fewer countable porosities and balling defects (see Figure 5.13a), whilst a small number of adhered particles are visible on the side surface (see Figure 5.13b). Overall, the Taguchi DOE parametric optimization has been successful in achieving the best side surface quality, even better than default parameters settings, while the top surface quality optimization process was almost close to the default settings.

Table 5. 11 Top surface Sa values for default, best Sa achieved from L25 array, and Taguchi predicted/optimised parameters

Process parameters	Default (top surface)	Best Sa (top surface)	Optimal/predicted (top surface)
Laser power (W)	110	125	100
Hatch spacing (μm)	110	100	100
Layer thickness (μm)	50	150	60
Point distance (μm)	20	20	60
Exposure time (μs)	100	80	80
Sa (μm)	9.5	17	13

Table 5. 12 Side surface Sa values for default, best Sa achieved from L25 array, and Taguchi predicted/optimised parameters

Process parameters	Default (side surface)	Best Sa (side surface)	Optimal/predicted (side surface)
Laser power (W)	110	125	150
Hatch spacing (μm)	110	75	100
Layer thickness (μm)	50	120	30
Point distance (μm)	20	100	60
Exposure time (μs)	100	40	80
Sa (μm)	9.5	9	8

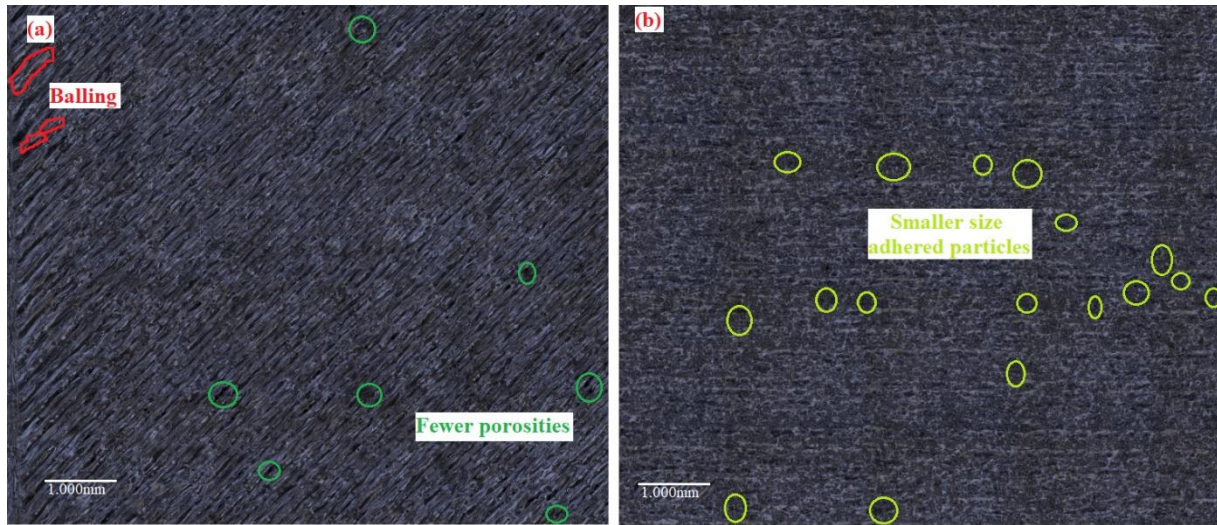


Figure 5. 13 Visually inspected (a) top and (b) side surfaces built with Renishaw AM-400 default parameters settings

5.7 Summary

The critical LPBF process parametric optimisation by Taguchi DOE, and ANOVA to identify the impact of these critical process parameters on the resultant surface quality of both top and side surfaces were studied.

Top surface quality

- More prominent crater-like defects were reported for artefacts #1, #6, #11, #16 and #21, which resulted in poor surface roughness values. The best Sa value (17 μm) was recorded for the #9 artefact, while the worst surface Sa (214 μm) was reported for artefact #11.
- The formation of smaller-size crater defects and typical LPBF defects like balling, porosities, cracks and spatters induced poor Sa values ranging between 60 μm – 80 μm for artefacts #1, #7, #8, #13, and #23. The obtained Sa values for the rest of the artefacts were in the range of 26 μm – 42 μm .
- ANOVA analysis found that the hatch spacing (46%) is the most influential parameter that affected the top surface quality of the LPBF artefacts, followed by point distance (19%), laser power (9%), exposure time (7%) and layer thickness (5%).
- The Taguchi DOE optimised parameters (LP₁: 100 W, HS₄: 100 μm , LT₂: 60 μm , PD₃: 60 μm , ET₂: 80 μs) were validated by conducting the verification experiments with the

objective “of smaller is better”. The verified experiments effectively justified achieving the best top surface quality Sa value of 13 μm (reduced by 4 μm).

Side surface quality

- Unlike top surfaces, side surfaces did not display any (bigger/smaller/wider/shallower) crater-like defects. Side surface quality is predominantly influenced by the adhered particle features derived from partially-melted/un-melted powder particles. Artefacts #23, #5, and #20 considered fully defective surfaces (Sa values 26-30 μm) comprised all of the indistinguishable surface anomalies (spatters, balling, porosities, cracks, delamination).
- Delamination played a significant role in the poor surface quality of artefacts #6 (Sa-18 μm), #7, and #13 both recording a Sa value of 22 μm .
- The best Sa value (9 μm) was recorded for artefacts #8, and #25. Artefacts #10, #11, #18, #19, and #24 exhibited the second-best Sa value of 10 μm , whereas the remaining artefacts’ Sa values are in the range of 12 μm -20 μm , owing to the occurrence of various inevitable surface anomalies at different sizes and different scales. Most of the side surfaces exhibited stable and closely associated Sa values within the range of 10-20 μm .
- ANOVA analysis found that the exposure time (58 %) is the most influential parameter that affected the side surface quality of the LPBF artefacts, followed by point distance (20 %), laser power (9 %), and layer thickness (8 %), and hatch spacing (4 %).
- The Taguchi DOE optimised parameters (LP₃: 150 W, HS₄: 100 μm , LT₁: 30 μm , PD₃: 60 μm , ET₂: 80 μs) were validated by conducting the verification experiments with the objective “of smaller is better”. The verified experiments effectively justified achieving the best side surface quality Sa value of 8 μm (reduced by 1 μm).
- Overall, the Taguchi DOE optimisation showed that the lower or desired surface quality can be successfully tailored or achieved by optimising the LPBF critical parameters (but not infinitely). ANOVA demonstrated that the impact or percentage contribution of individual critical parameter can be effectively quantified while the interaction of all five critical parameters can be easily analysed.

Chapter 6. Impact of build orientation on surface quality, microstructure and mechanical properties of LPBF 316L SS parts

As already mentioned in previous chapters LPBF has proved to have greater potential to substitute conventional fabrication techniques in certain aerospace and biomedical functional applications. However, the anisotropic microstructure and substandard surface quality induced by inevitable metallurgical defects and surface asperities result in poor mechanical properties, which eventually have significant implications for the advancement of LPBF's widespread functional applications. In addition to the LPBF critical parameters optimisation, the building orientation is one of the important aspects that need to be carefully selected as it determines the anisotropic microstructure, complex surface topography and mechanical properties. The complex surface topography consists of diverse metallurgical defects and surface asperities representing the final surface quality has been systematically characterised and quantified with a suitable array of areal surface texture parameters as per ISO-25178-2 (Chapters 3-5). Furthermore, it has also been shown that desired surface quality could be achieved or tailored by optimising the critical LPBF critical process parameters (Chapter 5). Based on this strong foundation, it is paramount to investigate the impact of different build orientations on the final quality of LPBF components. The unique anisotropic microstructure and the complex surface topography are generally associated with the LPBF building orientations. The importance of studying the impact of different build orientations is to identify the optimal build angle or orientations. The optimised build angle or orientation minimizes the occurrence of defects and asperities on the complex surface topography of LPBF components. The rougher surface mostly affects the fatigue life. Oftentimes, the rougher surface consists of more peaks and valleys created by surface defects and asperities. However, fatigue life is mostly driven by the valleys on the surface as they behave like higher stress concentration regions that could lead to early crack initiation and easy propagation through the material before failing at the lower fatigue loads. Hence, this complimentary chapter is aimed to study the impact of four different build orientations on the final microstructure (defects and asperities), surface quality, tensile and fatigue performance of LPBF 316L steel dog-bone samples.

6.1. Research methodology

6.1.1 Dog-bones samples design and fabrication

The dog-bone samples were designed according to ASTM E8 [380], and their dimensions are presented in Figure 6.1. The schematic illustration of four building orientations adopted in this

research is given in Figure 6.2 The total 24 dog-bone samples were fabricated in four build orientations i.e., horizontal (H), vertical (V), horizontal inclined (HI) and vertical inclined (VI), see Figure 6.3.

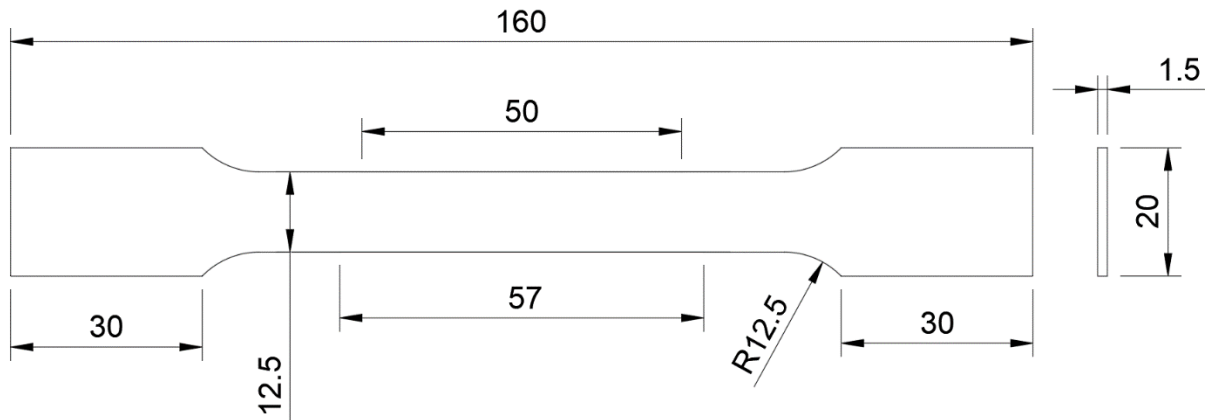


Figure 6. 1 Dimensions (in mm) of LPBF printed dog-bone samples.

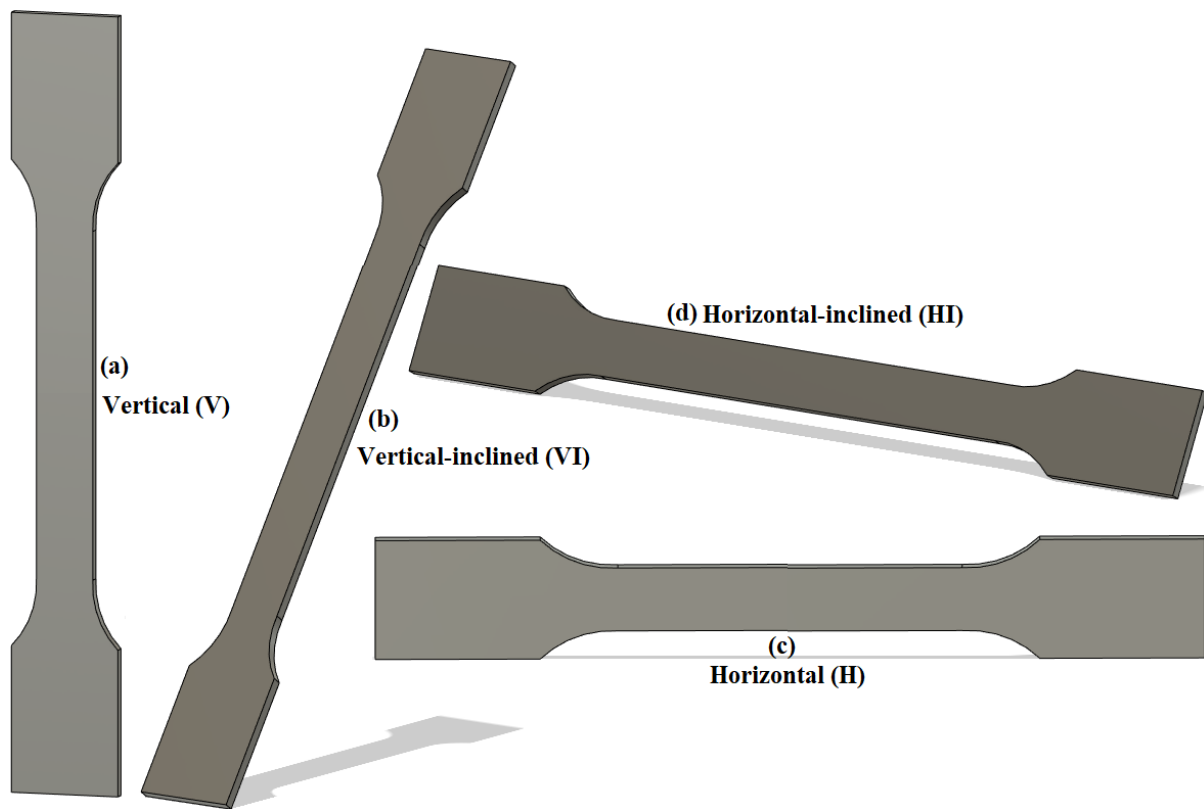


Figure 6. 2Schematic illustration of LPBF dog-bone samples built in four build orientations.

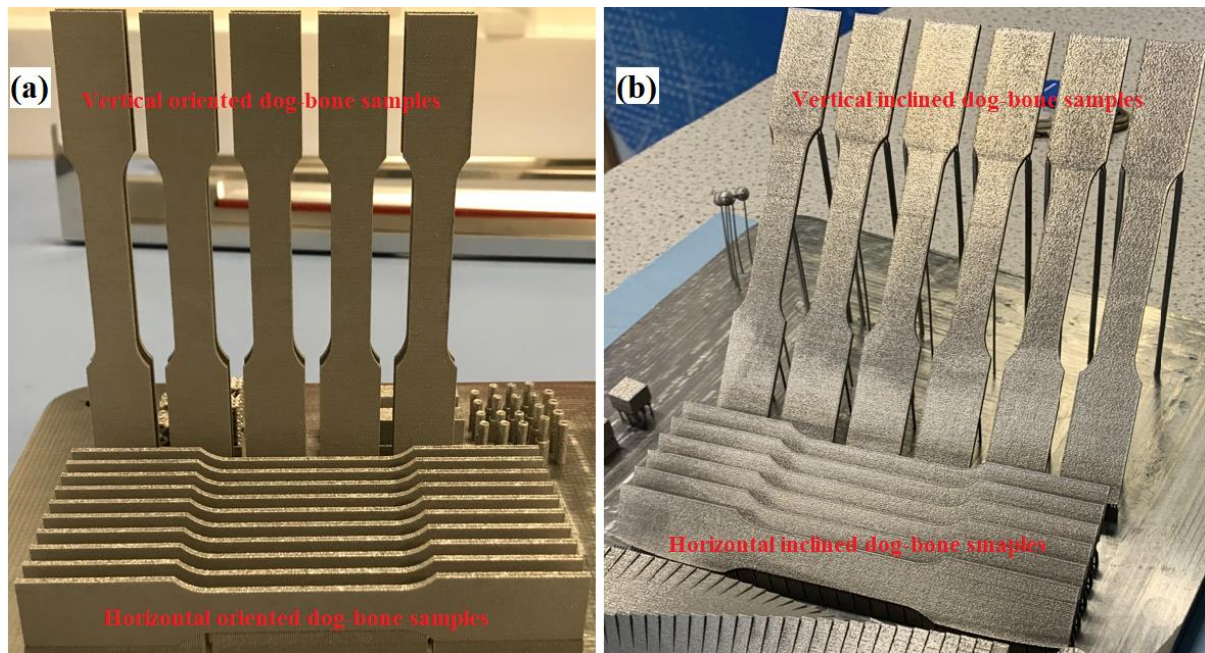


Figure 6.3 LPBF printed samples (a) horizontal and vertical oriented dog-bones, and (b) horizontal-inclined and vertical-inclined (at 45 degrees) dog-bones (other samples are not part of this research)

The dog-bone samples were built by a Renishaw AM400 LPBF machine using 316L stainless steel alloy powder. The commercially available 316L alloy stainless steel powder with particles mostly spherical in shape (supplied by Renishaw plc Stone Staffordshire U.K) was utilised. The 316L alloy is austenitic stainless steel (SS), mainly iron alloyed along with the presence of other important elements like chromium, nickel, and molybdenum with a mass fraction of 18%, 14% and 3% respectively [353]. The Renishaw LPBF machine is fitted with a fiber laser that generates pulsed laser waves with a maximum power output of 400 W. The following default process parameters were employed; laser power 110 W, scan speed 500 mm/s, hatch spacing 110 μm and layer thickness 50 μm . The build chamber was filled with 99.99% purity level inert gas (argon), whereas oxygen content was maintained at less than 0.1 vol % during the LPBF process. The powder details and the scanning patterns employed is same as already mentioned in the previous chapters.

6.1.2 Surface quality measurement strategy and data analysis

The surface topographical measurements were carried out using Bruker Contour LightSpeed™ (LS) FVM by adopting the measurement parameters listed in Table 6.1. Four dog-bone samples built in four built orientations were measured along four locations, and the surface texture height

parameters were calculated. The measured data was analysed using Mountainsmaps premium version 7.4 software. Non-measured points (NM) were filled in, and a polynomial filter of the order of 2 was selected to remove the form. A Robust Gaussian filter was used to extract surface texture from the measured data such as the roughness component with cut-off λ_s 0.8 mm [36,364]. The analysed surface texture height parameters result of as-built conditions concerning four build orientations were compared and analysed. The areal surface roughness component is the primary subject of interest and is often used to calculate the surface texture height parameters S_a , S_q , S_{ku} and S_{sk} based on ISO 25178-2 [32].

Table 6. 1 FVM measurement configurations

Magnification	10x lens
Illumination type 1	Coaxial light
Lateral resolution	1.57 μm
Vertical resolution	0.71 μm
Sampling distance	0.89 μm (both in X and Y directions)
Measurement (data) size	1.4 mm x 1.4 mm

6.1.3 Microstructure analysis

State-of-the-art microstructure characterisation techniques were performed using Quanta 200 scanning electron microscope (SEM) (formerly produced by FEI), which is a flexible and easy-to-operate instrument that was operated by using a regular high-vacuum. The electron beam generated in this instrument is a conventionally produced tungsten filament electron source. The SEM can resolve features as small as up to 3 nm. The Quanta 200 SEM is also equipped with a standard backscatter electron (BSE) detector, secondary electron (SE), energy dispersive spectrometer (EDS) and an internal television camera. The accelerating voltage used in this research was in the range of 20-30 KV, and at varying scales between 5 -500 μm at different magnifications of 100-12000x levels.

The SEM-EDS was used to capture high-quality surface topographical images, which were useful to study and characterise the metallurgical defects, impurities, and various alloying elements that form part of anisotropic microstructure features in four building orientations of dog-bone samples. However, the phase composition, grains orientation and crystallographic structure analysis were not carried out as they are out of this research scope. This microstructure characterisation is a

yardstick to correlate the impact of different build orientations on the final surface quality and mechanical performance. In addition, this research would be helpful as a stepping stone to gain insights about the process-structure-property relationship of metal AM components fabricated with different build orientations, along with a newly developed novel surface texture characterisation toolbox (chapters 3-5) and tailoring the desired surface quality by optimising the LPBF critical parameters (chapter 5).

6.1.4 Tensile testing

The LPBF-printed 316L SS dog-bone samples were subjected to tensile testing to evaluate the tensile performance. Ultimate tensile strength (UTS) was calculated based on the stress-strain curve. Samples were tested at room temperature of 25° with a constant crosshead displacement rate of 3 mm/min using a 50 KN universal tensile testing machine, with a 50-mm extensometer attached (see Figure 6.4). The extensometer was used to measure the elongation of the dog-bone test samples which helps to characterise the strain.



Figure 6. 4 Tensile testing rig of 316L SS sample (ASTM E8 dog-bone) with extensometer attached [323]

6.1.5 Fatigue testing

Fatigue is the condition whereby material fails as a result of cyclic stresses applied below the ultimate strength of the material. Fatigue testing was performed on a 100 KN capacity servo-hydraulic testing machine using a sinusoidal loading waveform with a frequency of 30 Hz and stress loading ratio $R=0.1$. Test samples were loaded into the machine with stress amplitudes

ranging from 100 MPa-400 MPa until failure or 10^6 cycles were achieved. The output of the test is plotted in terms of the stress amplitude range against the number of cycles to failure. Fatigue test frequencies were adjusted for each test so that the strain rate remains approximately the same for all fatigue tests.

6.2. Results and discussions

6.2.1 Surface quality analysis of dog-bone samples

The analysed results from the Mountainsmap7 software are discussed in this sub-section. Interestingly, a considerable difference in areal surface texture parameters was evident between all the samples. The areal surface texture height parameter values for as-built conditions in four build orientations are tabulated in Table 6.2.

Table 6. 2 Average Sa, Sq, Ssk and Sku values obtained for as-built conditions from four build orientations

Building Orientations	Sa (μm)	Sq (μm)	Sku	Ssk
As-built-horizontal (AB-H)	14	19	10	0.3
As-built-vertical (AB-V)	11	16	14	0
As-built-horizontally inclined (AB-HI)	9	13	11	0.4
As-built-vertically inclined (AB-VI)	11	15	9	0.9

From Figure 6.5, the Sa and Sq values display decreasing and increasing trends for all four build orientations. A closer look into Sa, the Sq plot of AB-H displayed the highest Sa ($14 \mu\text{m}$) and Sq ($19 \mu\text{m}$) values. Whereas the AB-HI recorded the least Sa ($9 \mu\text{m}$) and Sq ($13 \mu\text{m}$) values out of all as-built categories. A slight increase of $2 \mu\text{m}$ for both Sa ($11 \mu\text{m}$) and Sq ($15 \mu\text{m}$) values was evident for an as-built vertical-inclined category. The rapid rise in roughness values for the AB-VI sample was attributed to the combination of adhered particle features and the staircase effect. However, the staircase effect predominantly appears below 45° [36], but the as-built vertical inclined sample has been tilted at 45° orientation; thus, the underlying staircase effect cannot be distinguished clearly (particle features start to dominate the surface inclination at 45°) even though it poses a considerable impact on the final surface quality. Additionally, LPBF systems are designed for laser melt/re-melt of horizontal surfaces but not inclined surfaces. Lack of laser re-melting leads to the adherence of more particle features on the inclined surfaces [36,215].

Overall, the obtained Sa values were in the range between 9-14 μm irrespective of the build orientations. The reason for the higher (rougher) surface roughness Sa (14 μm) for horizontally oriented samples is due to the fact that higher residual stresses are formed during LPBF fabrication of the larger cross-section parts, as these larger parts (or longer in this case) tend to have longer melting tracks and the laser beam has to travel more distance over which the shear forces can act. These formed residual stresses could lead to surface cracks at various scales and other surface asperities which are more likely to become destructive, especially in the layered fabrication of the LPBF process [1]. Simultaneously, the higher standard deviation for as-built horizontal samples in Sa and Sq values were observed, which is attributed to the combination of inevitable balling and ripple effect features induced by the fast-moving laser beam, in addition to the presence of solidified melting tracks stripes and powder spatters [36].

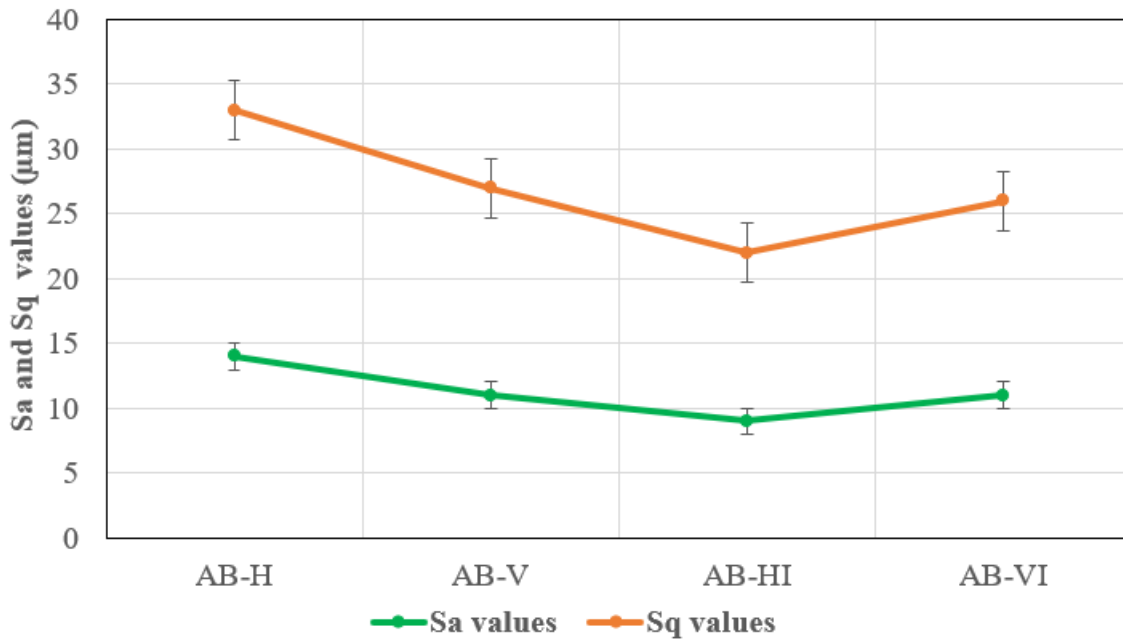


Figure 6. 5 Sa Sq plot for as-built processed samples for four different build orientations

The Sku, Ssk plots are shown in Figure 6.6. The calculated Sku value was above the nominal value of 3, for all the build orientations. This clearly indicates that the surface roughness height distribution is dominated by strong peaks with smaller edge radii caused by particles-features, signifying the overall surface height distribution is basically spiky-natured normal distribution. Also, the obtained kurtosis values reveal the presence of randomness of the surface heights present on typical metal AM surfaces, which plays a significant role in premature failure of the functional part (see Figure 6.7). The recorded Ssk value is positive ($Ssk > 0$) for all the measured surfaces.

This signifies that degree of skew or symmetry of peaks and valleys of the average surface at the centre is predominantly downward and dominated by peaks relative to the Centre line. The reported Ssk value close to zero for the AB-V surface could be related to the presence of random deep valleys, but overall, the characteristics of all surfaces are mainly dominated by surface peaks (Figure 6.7).

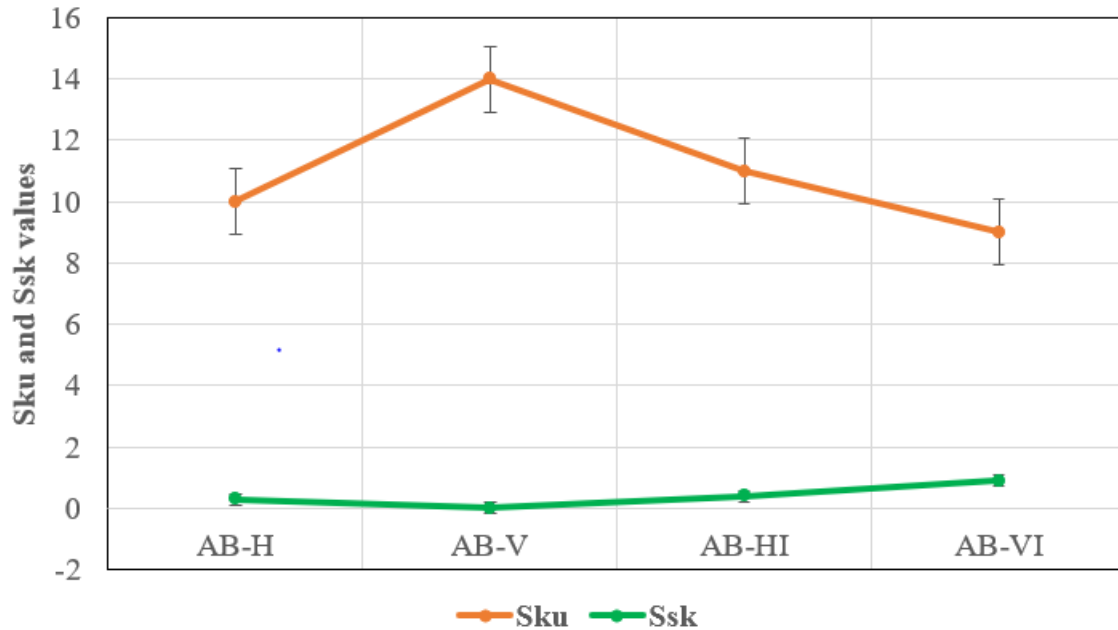


Figure 6. 6 Sku Ssk plot for as-built processed samples for four different build orientations

The accumulation of bigger-size agglomerated particle features comprised of balling and spatters on the as-built horizontal surface resulted in higher Sa and Sq values (Figure 6.8a). The presence of comparatively smaller size particle features on the as-built vertical and as-built horizontal inclined surfaces yielded reasonably lower surface roughness values (Figure 6.8b&c. The formation of a larger island-like protruded structure visible on the as-built vertical inclined surface gave rise to moderately higher Sa and Sq values (see Figure 6.8d), but was still well below that of the as-built horizontal surface roughness.

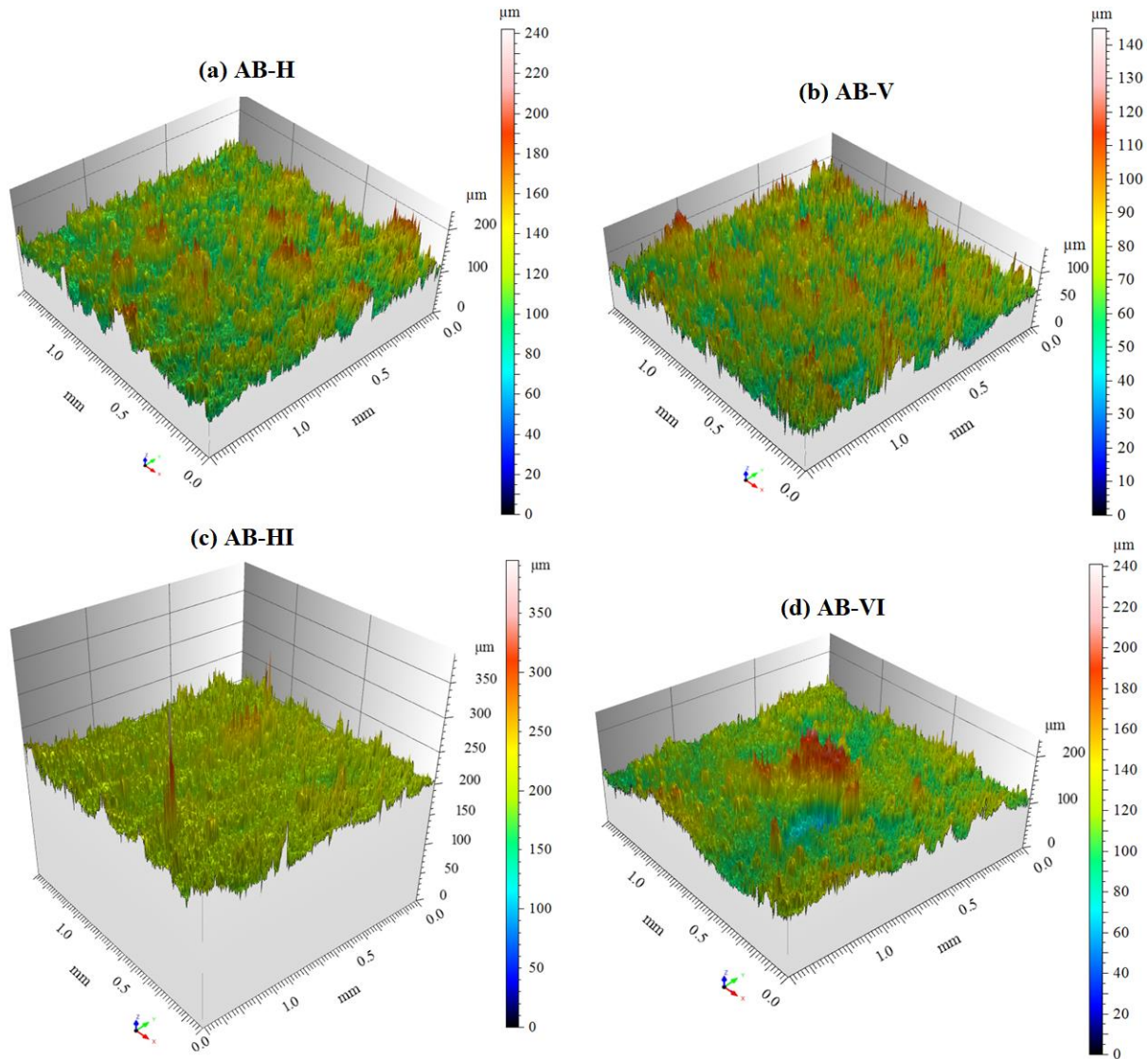


Figure 6. 7 height map for as-built LPBF (a) horizontal, (b) vertical, (c) horizontal-inclined and (d) vertical-inclined oriented sample

The analysed as-built samples for all four orientations consist of a directionally situated series of peaks and valleys in the laser scanning direction. However, the surface asperities in the form of particle features were distributed in the random path and at different sizes. This randomness can be ascribed to the typical anisotropic microstructure characteristics (consisting of diverse metallurgical defects and surface asperities) of the LPBF fabrication that undergoes complex thermophysical phenomena of material flow and solidification during the building process.

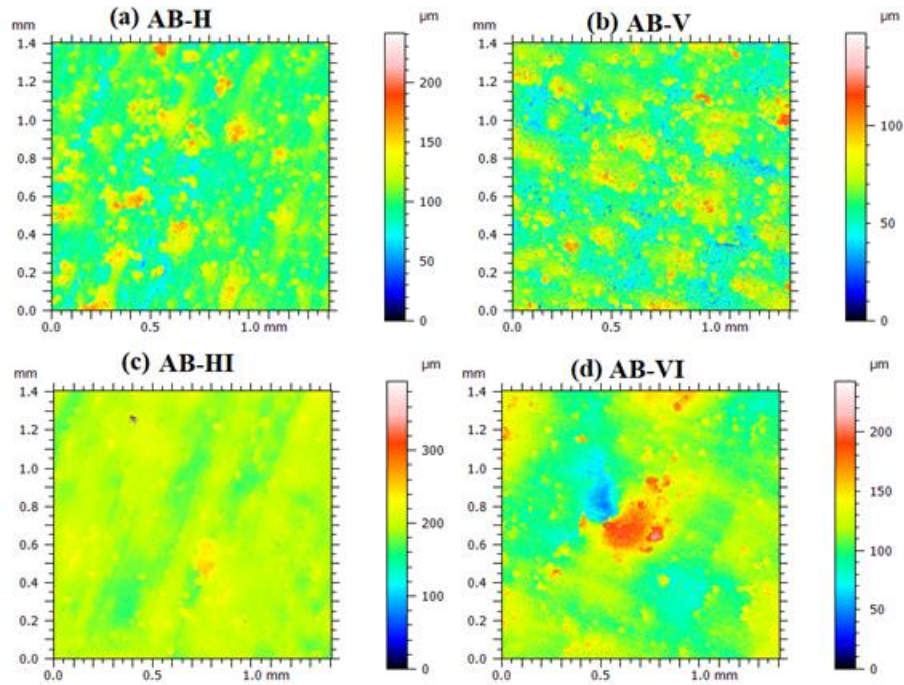


Figure 6. 8 Schematic illustrations of surface topography observed from FVM (a) horizontal, (b) vertical, (c) horizontal-inclined and (d) vertical-inclined oriented sample for as-built conditions

6.2.2 Microstructure and tensile property

As aforementioned the various defects, surface asperities, impurities, and alloying elements that form part of the microstructure which eventually defines the final mechanical properties of LPBF steels have been investigated in this subsection. The tensile testing results for as-built conditions of LPBF dog-bone samples fabricated in four build orientations were given the Table 6.3. The corresponding stress-strain curves were shown in Figure 6.9.

Table 6. 3 Tensile testing results for as-built LPBF dog-bone samples in four orientations

Build orientation	As-built-UTS (MPa)	As-built-Elongation (%)
Horizontal (H)	582	10
Vertical (V)	528	10
H-Inclined	566	13.5
V-Inclined	554	14.5

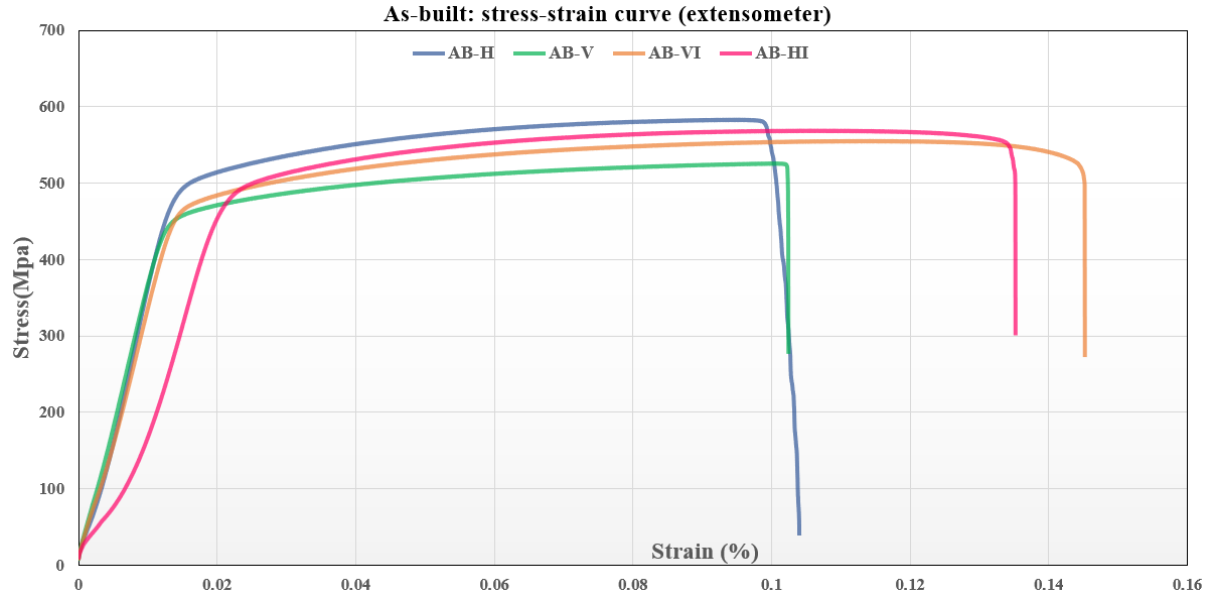


Figure 6. 9 Stress-strain curves of LPBF dog-bone samples for as-built conditions in four orientations

From Figure 6.9, it was interesting to note that the as-built horizontal sample reported the highest ultimate tensile strength (UTS) of 582 MPa within all as-built conditions, while the as-built vertical sample recorded the least UTS of 528 MPa. Both as-built horizontal and vertical samples exhibited an identical lower elongation of about 10 %; implying the least tough samples. The anisotropic microstructure consisting of defects, surface asperities, impurities, and alloying elements of as-built LPBF dog-bone samples in four build orientations were observed using SEM-EDS. The microstructural features of tensile fractography images concerning four build orientations were given in Figures 6.10. The microstructure characteristics correlation with the tensile testing results at fracture was helpful to understand the rationale behind different tensile fracture modes. The SEM micrographs taken at the fracture surface at different magnifications were shown in Figure 6.10a-d. A closer look at the fracture surface of the as-built horizontal sample revealed finer dimples (5-10 μm) undergoing significant plastic deformation before the failure. The presence of smaller and fewer porosities defects posed minimal influence on the tensile behaviour, resulting in higher UTS with ductile fracture (see Figures 6.9 and 6.10a). Finer microstructure dimples are able to withstand higher applied loads, as it requires breaking more grain boundaries before the final fracture. Although the as-built vertical sample demonstrated decent dimples (8-10 μm); the emergence of a bigger void and numerous porosities gave rise to premature failure at lower applied

loads without undergoing any local deformation (see Figures 6.9 and 6.10b). The as-built vertical sample was regarded as the weakest out of all.

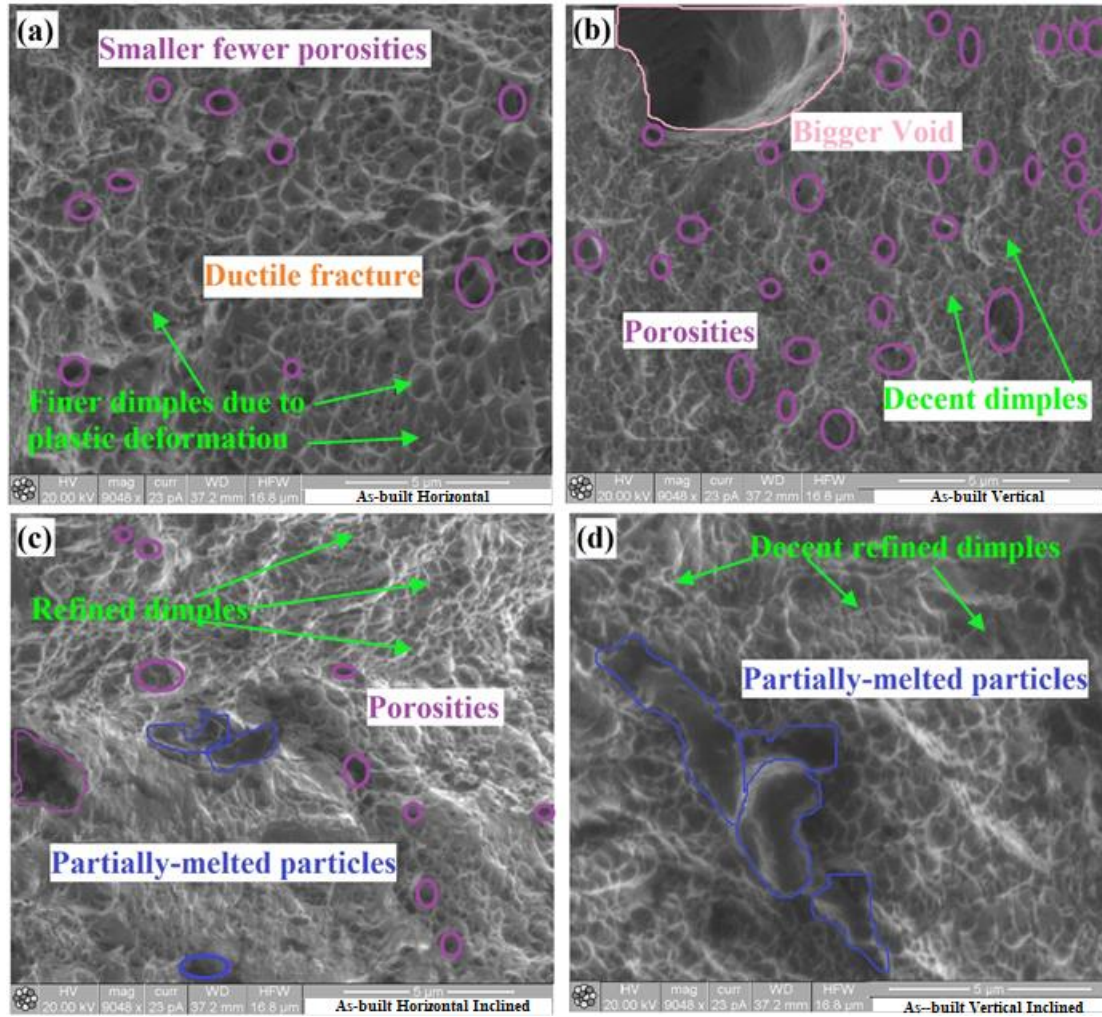


Figure 6. 10 SEM microstructure features of as-built LPBF dog-bone samples built in four orientations

The as-built horizontal inclined sample microstructure presented refined dimples (5-10 μm), smaller partially-melted particles and fewer porosities. The refined microstructure resisted considerably higher tensile loads before fracturing at relatively higher UTS (566 MPa), with a decent elongation of 13.5% (see Figures 6.9 and 6.10c). The as-built vertical inclined sample exhibited modest refined microstructure dimples (8-10 μm) but the presence of bigger partially-melted particles gave way at a reasonable tensile load before fracturing at moderate UTS (554 MPa) whilst at higher elongation of 14.5% (see Figures 6.9 and 6.10d). Based on the tensile

performance results, the as-built horizontal-oriented sample was considered the strongest, while the as-built vertical-inclined sample was the toughest.

The rationale behind the horizontal oriented sample being the strongest is due to the fact that the sample experiences multiple cycles of laser heating and re-melting for a longer period of time during the deposition of subsequent layers as compared to the other build orientations. The laser reheating and re-melting lead to higher cooling rates thereby refining the microstructure grains which eventually withstand higher applied loads before failure. Lack of laser reheating and re-melting in vertical build orientation induces shorter cooling rates eventually leading to coarser microstructure and incomplete melting (leads to voids, porosities and other defects and asperities). It is obvious that only a small amount of energy is required to break a lesser number of larger grain boundaries (coarser microstructure). Also, the presence of diverse defects and asperities could easily give away at lower tensile loads resulting in early failure.

Further microstructure analysis was carried out using SEM-EDS to identify the presence of alloying elements and the existence of any possible impurities within the tensile fractured surfaces of the as-built horizontal and vertical oriented samples (see Figure 6.11 and Figure 6.12). The formation of various carbides, nitrides and oxide inclusions/impurities is most common during the LPBF process of 316L steels. From EDS analysis, it was obvious to see the typical alloying elements like iron (Fe), carbon (C), nickel (Ni) and chromium (Cr) at various weight percentages in both as-built horizontal and vertical oriented samples (Figure 6.11a-g, (Figure 6.12d&i). There were no signs of the presence of oxide phases in the as-built horizontal-oriented sample. Whereas the oxide inclusions in the as-built vertical sample were evident in Figure 6.12a,b&c. It was particularly worth noting the presence of oxygen (O) content greater than 0.6% within the fractured surface of the as-built vertical-oriented sample (Figures 6.12a&b) which was further confirmed by the EDS analysis ((Figure 6.12e).

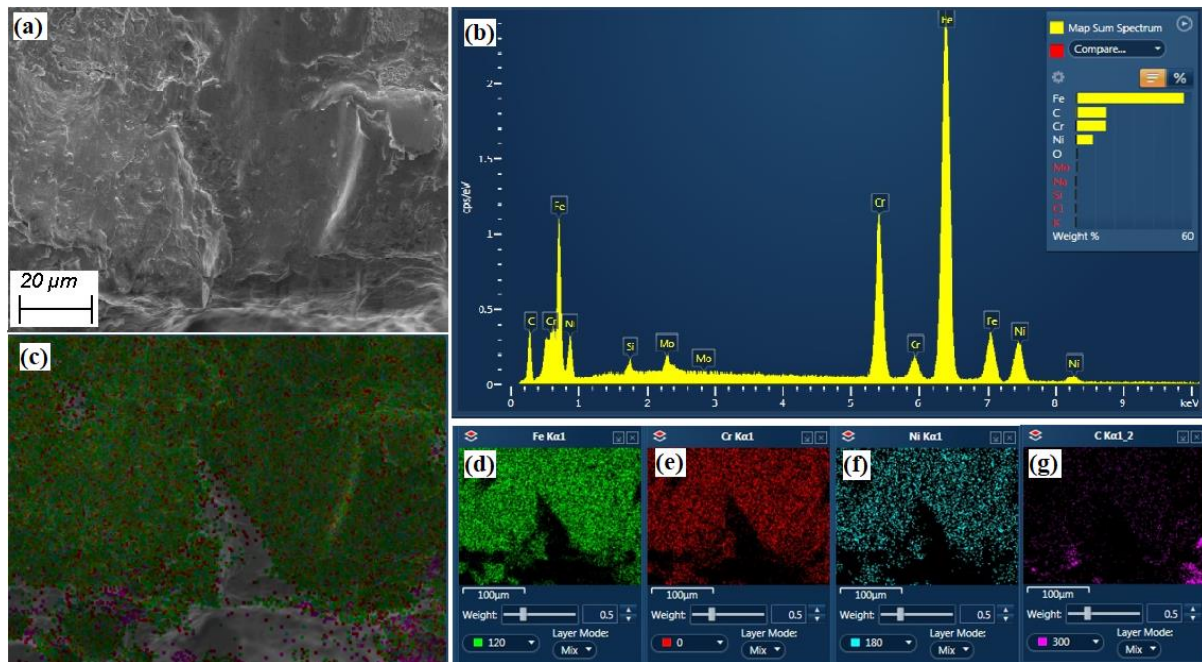


Figure 6. 11 SEM-EDS analysis of LPBF as-built horizontal oriented dog-bone sample showing various alloying elements (no sign of oxides).

This higher content of oxide is attributed to the formation of liquid oxides at the beginning of the molten melt pool (trapped between the powder particles) and further crystallised into certain oxide phases by means of hydrodynamic forces during LPBF melting and solidification [181]. Moreover, the interfacial energy and melt pool convection and buoyant forces significantly influence the evolution of nanoscale oxides into bigger microscale oxide inclusion [182]. As a typical characteristic of metal powder feedstock materials, there is a high likelihood that oxygen could be pick-up during the powder atomisation process, or due to powder surface oxidation during powder handling, or while long-term storage in non-ideal conditions [1]. The oxygen content has a higher affinity to attract with other alloying elements present in 316L alloy powder and could easily form oxide inclusions [1]. The formation of bigger oxide inclusions could easily result in other forms of defects and asperities such as voids, porosities, spatters etc [381]. These formed defects or asperities combined with oxide inclusions could impart substantial adverse effects on the laser heating, melting, and fusion of powder particles eventually affecting the stability of the molten melt pool, final microstructure and mechanical performance (tensile strength and fatigue life) of LPBF components [1]. It is evident from the SEM-EDS analysis of the vertical-oriented sample's fractured surface that oxide inclusions played a key role to achieve lower UTS. In contrast, uniform microstructure, fewer defects and absence of oxide inclusions resulted in higher UTS of horizontal

oriented sample (see Figure 6.9). This could possibly be attributed for two reasons, (i) lack of laser reheating and re-melting in vertical build orientation induces shorter cooling rates which may present insufficient time for oxides to escape from the molten melt pool, and (ii) the bigger oxides inclusions might get trapped inside molten melt pool during intense intermixing and solidification [1]. The formation of oxide layers in the nanoscale range can be quickly evaporated during vigorous mixing and stirring of molten melt pool by a laser beam, resulting in minimal damage to LPBF parts [1]. On the other hand, micrometre range oxides films (10-100 μ m) of irregular geometry formed cannot be completely vaporized by the stirring action of the laser beam and Marangoni flow. The oxide layer can grow thicker with increasing oxygen content in the atmosphere, at the same time as the layer re-melting. When the re-melting of a new layer begins, the oxide film formed previously breaks down, and part of this oxide hovers on top of the newly formed layer, with the rest trapped inside the LPBF fabricated component. The trapped oxide leads to the formation of oxide inclusion [124,127,128]. Some of the un-melted or partially-melted particles can easily get trapped in these oxide inclusions. The stability of the molten melt pool can be significantly impacted by the oxide residues' and pose adverse effects on the heating, melting, and fusing of powder particles [1,124]. Thick oxide inclusions increase the surface tension effects, limit the absorption of the laser energy and wetting of substrate, and obstruct molten pool flowability. These oxide inclusions also result in the formation of metallurgical defects such as balling, insufficient melting between powder particles, reduces part densification, induces cracking and consequently lowers mechanical properties [125-127]. It is worth noting that any pickup of moisture from the environment by the feedstock powders paves the way for the introduction of oxygen content into the LPBF system [129].

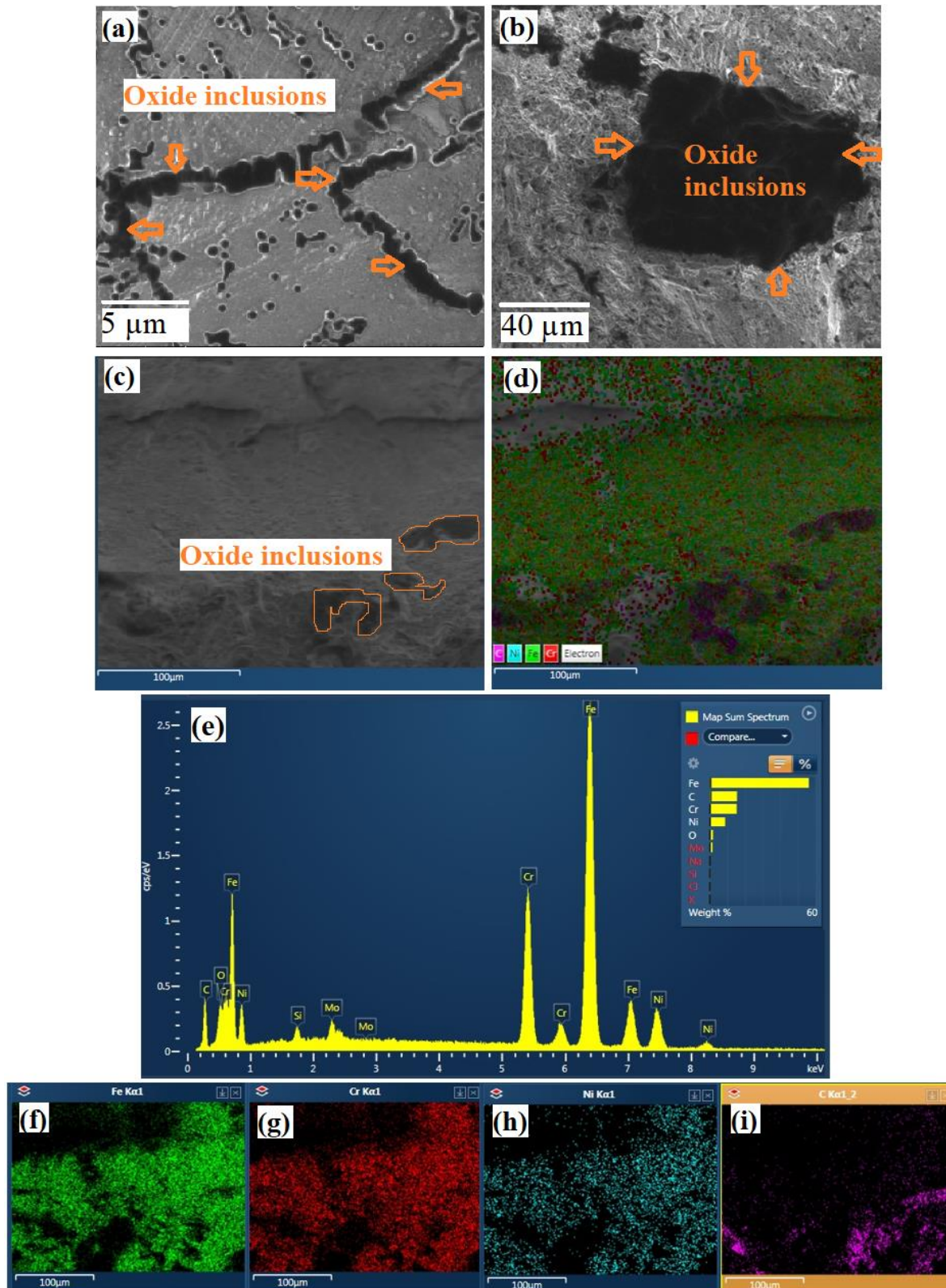


Figure 6. 12 SEM-EDS analysis of LPBF vertical oriented dog-bone sample showing various alloying elements and impurities like oxide inclusions.

6.2.3 Microstructure and fatigue life

The fatigue life of as-built dog-bone samples built in four orientations was given in Table 6.4. The stress amplitudes versus the number of cycles to failure diagram is shown in Figure 6.13. All of the as-built dog-bone samples exhibited significantly higher fatigue life in all four build orientations (see Figure 6.13). As-built horizontal-orientated in particular sample displayed an excellent fatigue life (178,440 cycles at a higher stress amplitude (214 MPa). AB-HI showed the second-best fatigue life (149,047 cycles but at the same higher stress amplitudes 214 MPa. In contrast, the as-built vertical sample displayed the least fatigue life (102,548 cycles) and at a lower stress amplitude of 187 MPa. The vertical-inclined oriented sample performed rather poorly (11228 cycles) but at a fairly higher stress amplitude of 213 MPa.

Table 6. 4 Fatigue life of as-built dog-bone samples in four different orientations

Build orientation	Number of cycles to failure (As-Built)	Stress amplitude (MPa)
H	178440	214
V	102548	187
HI	149047	214
VI	112228	213

It is worth noting that the difference between the fatigue lives decreases when the applied stress amplitude decreases. The impact of the stress gradient of the as-built horizontal sample that displayed excellent fatigue life at lower stress amplitudes may not be significant compared to other samples with lower fatigue life at higher stress amplitudes. This is because the larger proportion of fatigue life at lower stress amplitudes was governed by the crack initiation and crack growth stages induced by the cyclic stress gradient which is often not effective in enhancing fatigue resistance [382]. The highest fatigue life obtained for AB-H was 43% higher than the worst-performed AB-V among other as-built oriented samples.

It is well recognized that process-induced inevitable metallurgical defects and other surface asperities act as sites for crack initiation in LPBF components. These defects are sensitive to higher stress concentration under cyclic loading conditions which eventually have detrimental effects on

fatigue performance. The “general term” particle features herein are used to describe the surface asperities, namely balling, spatters, and unmelted/partially melted particles, which are sometimes difficult to distinguish individually. The impact of these metallurgical defects and surface asperities on the fatigue life of as-built dog-bone samples in four orientations was inspected by characterizing their surface topographical characteristics observed by SEM at the fractured surface (Figure 6.14a-d), and at the outer/top surface (see Figure 6.15a-e).

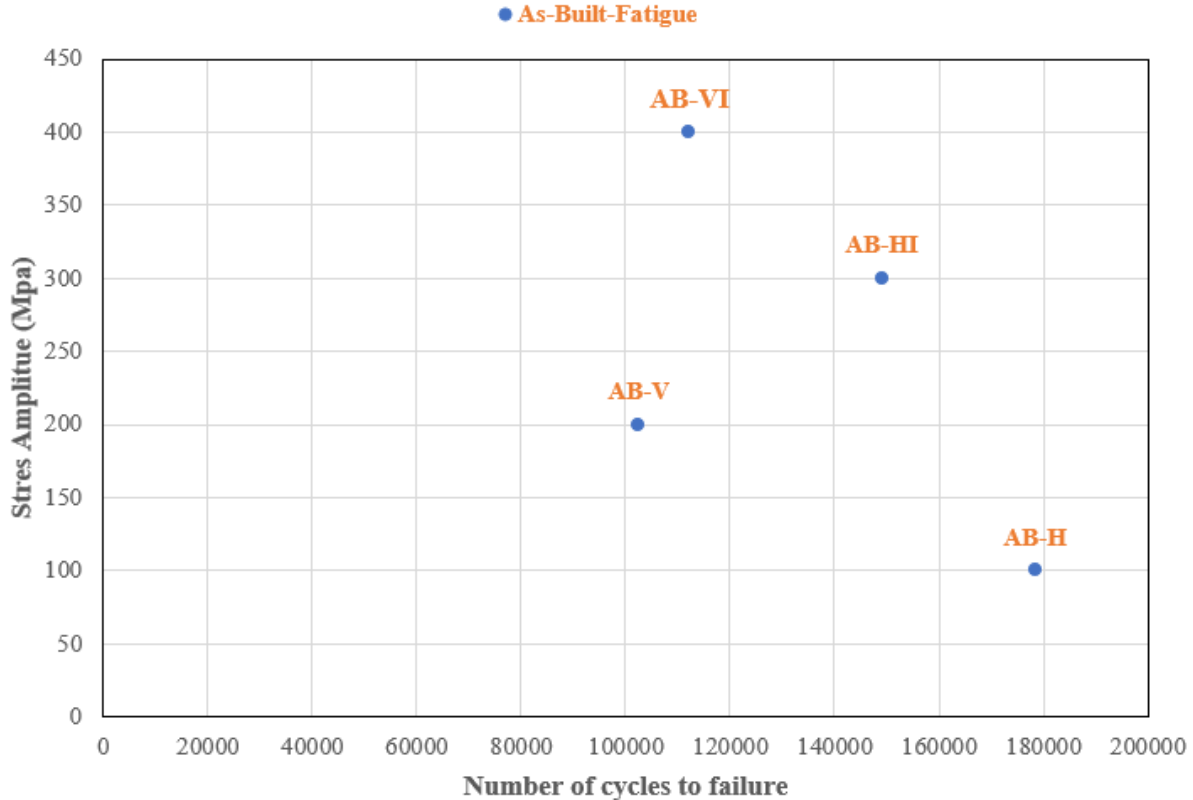


Figure 6. 13 S-N diagram for as-built dog-bone samples in four orientations

Very few un-melted/partially melted powders particles were visible at the fractured surface, while the uniform-size loosely dispersed particle features attached along the equidistant melt-track layers were evident on the top surface interface of the AB-H sample (see Figures 6.14 & 6.15a). The presence of a surface crack initiated from the left top side of the as-built horizontal surface passing through the particle features was evident in the higher magnification image of the top surface (see Figure 6.15b) but this surface crack was not apparent at the fractured surface (Figure 6.14a), signifying that AB-H’s fatigue cracks initiated from the top surface. Even though the external surface of AB-H contains a crack, it showed a very good fatigue life (see Figure 6.13). This was attributed to the effect of the lower stress gradient being more significant than the size of the defect

(see Figure 6.15a). The AB-V surface was mostly dominated by a plethora of defects including cracks, delamination, porosities, and other particle features that led to the lowest fatigue life (see Figures 6.13, & 6.15d&e). The individual or combination of these defects and particle features contributed to the sites of higher stress concentrations that eventually lead to faster fatigue crack growth and eventually induce premature fatigue failure (Figures 6.14c&d). As a result of fewer particle features emergence at the fractured interface (Figure 6.14e), and on the top surface of AB-HI, reasonably sound fatigue life was achieved (Figures 6.13, & 6.15f). The presence of fewer finer cracks, porosities and un-melted powders was observed at the fractured interface of the AB-VI sample (Figure 6.14g). The agglomerated particle features were apparent on the AB-VI top surface (Figures 6.13 & 6.15h), which resulted in failure at moderate fatigue life cycles under cyclic loading conditions.

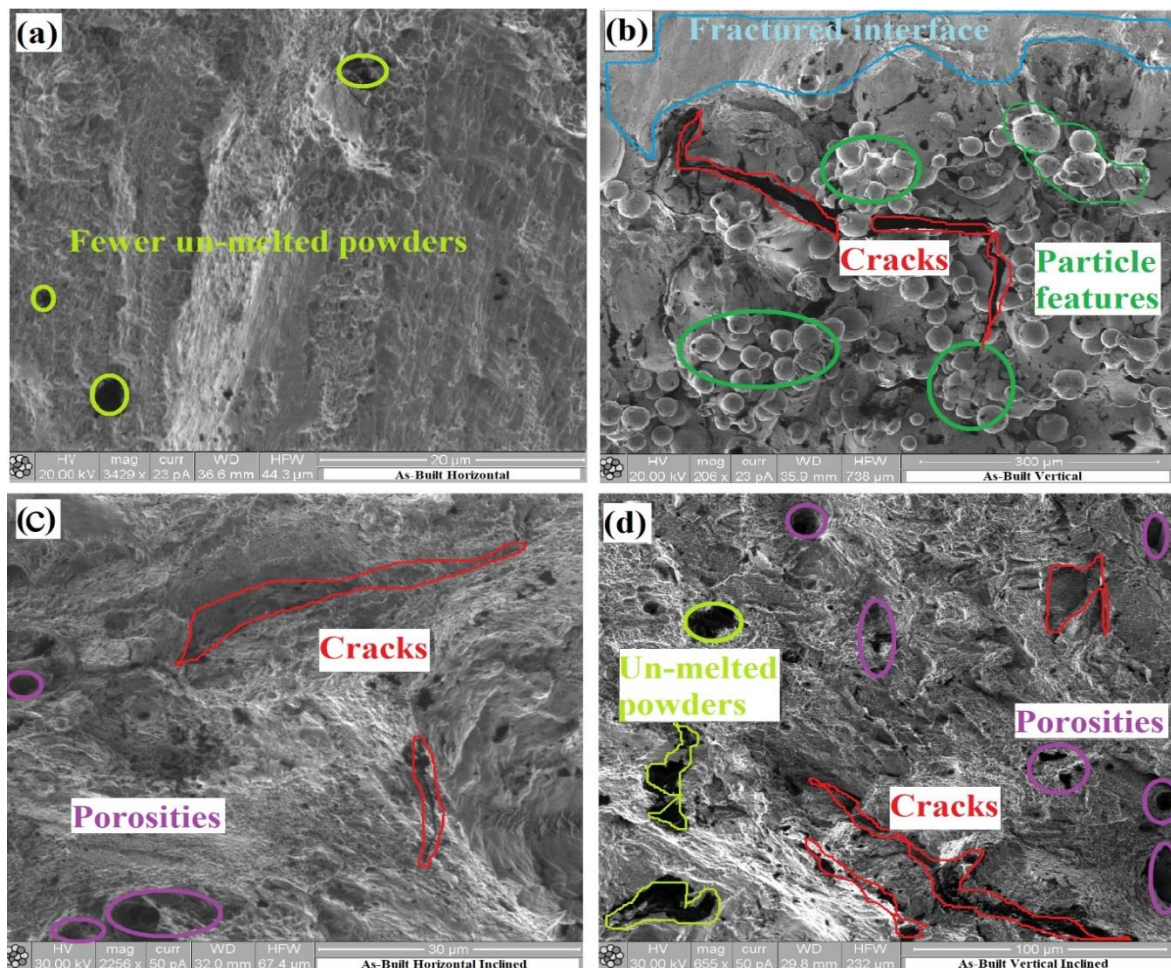


Figure 6. 14 SEM images at the fractured interface of as-built dog-bone samples built in four orientations.

In general, the fatigue life of LPBF components depends on the build orientations, as it governs the size, shape and orientation of metallurgical defects and surface asperities. The rationale behind the slightly better fatigue life of horizontal-orientated samples compared to the vertical-oriented samples was due to the fact that metallurgical defects and surface asperities were aligned parallel to the applied stress direction during cyclic loading conditions. Additionally, the horizontal-oriented sample was exposed to longer inter-time intervals and experienced higher cooling rates and faster solidification rates. Thus, forming finer microstructure and distribution of small-scale defects/asperities causes less stress concentration, thereby resulting in higher fatigue life [1,327]. In vertical-oriented samples, the stress concentrations were higher due to weak interfacial bonding between the successive layers (lack of laser re-melting; coarser microstructure), which induces bigger scale defects and surface asperities that were aligned perpendicular to the applied stress direction. The perpendicular alignment provides easy access paths for the cracks to grow faster leading to early fatigue failure at a lower number of cycles [1].

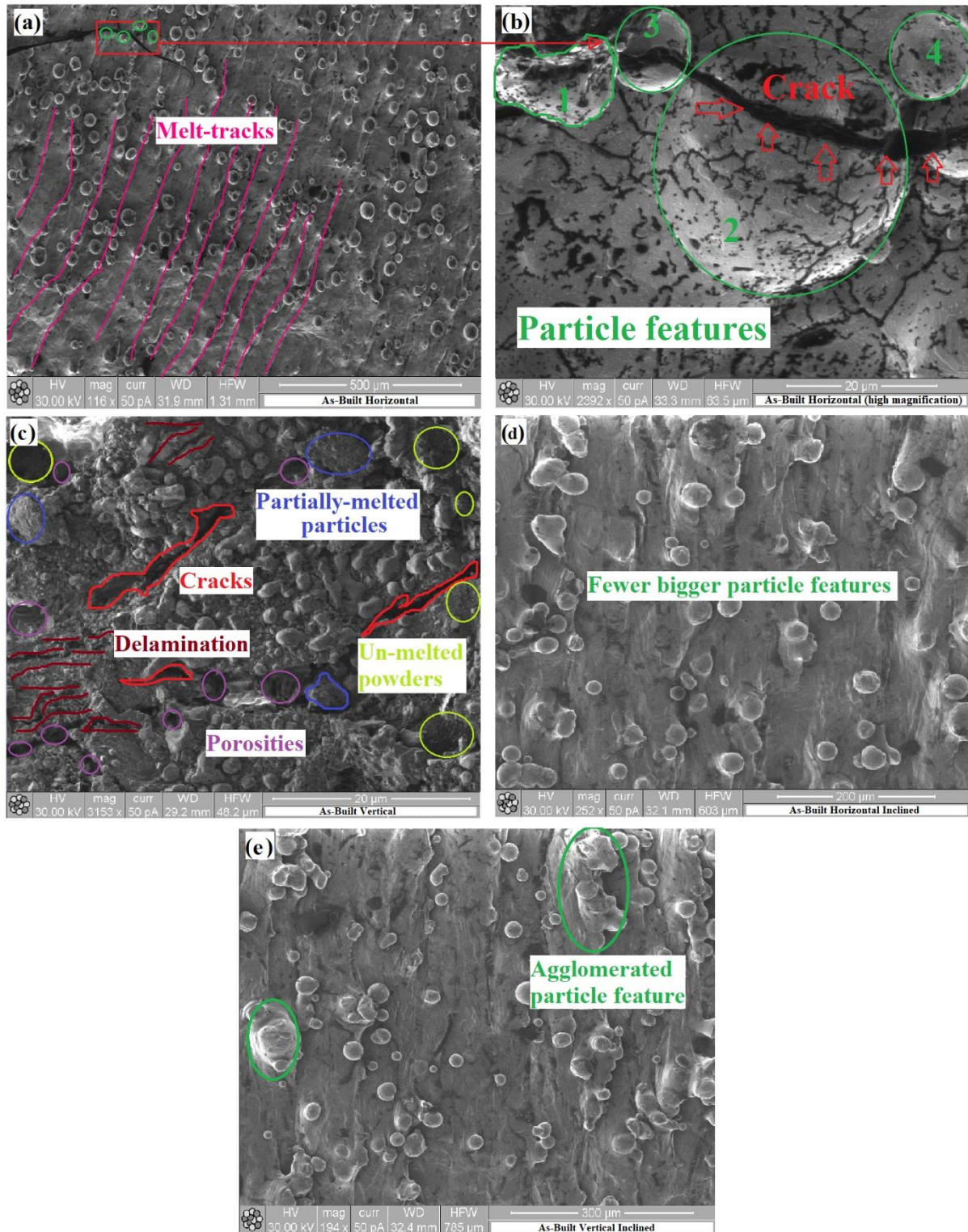


Figure 6. 15 Schematic illustration of various metallurgical defects and surface asperities observed on surface of as-built LPBF dog-bone samples built in four orientations.

6.3 Summary

The impact of four build orientations on surface quality, microstructure (metallurgical defects, surface asperities) and mechanical properties has been investigated.

Impact of build orientations on surface quality

- The AB-H oriented surface recorded a highest Sa value of 14 μm , this was credited to higher residual stresses during LPBF fabrication of the larger cross-section parts.
- The formed residual stresses could lead to surface cracks at various scales and other surface asperities which played a vital role in higher Sa value.
- Both AB-V and AB-VI orientation samples demonstrated similar Sa values of 11 μm , signifying the least impact of build orientation between them.
- The AB-HI orientation sample displayed the best Sa of 9 μm among all four orientations.

Impact of build orientations on microstructure and tensile property

- The AB-H oriented sample was regarded as the strongest with the highest UTS of 582 MPa.
- As a result of the sheer domination of various metallurgical defects and particle features, the AB-V-oriented dog-bone sample recorded the least UTS of 528 MPa. But both AB-H and AB-V oriented exhibited a lower elongation of 10%, implying the least tough samples.
- The presence of oxide inclusions, defects, and asperities lead to the early failure of the AB-V sample.
- AB-VI showed the highest elongation of 14.5% in combination with decent UTS of 554 MPa; signifying the toughest sample.

Impact of build orientations on microstructure and fatigue life

- Fatigue life results followed a similar trend to tensile properties. Irrespective of the build orientations,
- The best fatigue life obtained for the AB-H (178440 cycles) sample was 43 % higher than the worst-performed AB-V (102548 cycles) oriented sample.
- The poor fatigue life of AB-V oriented sample is credited to the higher stress concentrations due to weak interfacial bonding between the successive layers and the alignment of bigger size defects and asperities perpendicular to the applied stress which becomes an easy path for crack initiation and propagation before failing at the lower number of cycles.

- The finer microstructure and distribution of small-scale defects/asperities in horizontal-oriented sample caused less stress concentration, thereby resulting in higher fatigue life.
- Overall, this research has found a significant impact of different build orientations on surface quality, microstructure and mechanical properties (both tensile and fatigue) of LPBF dog-bone samples. However, irrespective of the build orientations, metal AM or LPBF steels are susceptible to dynamic loading conditions.

Chapter 7 Conclusions and future work

7.1 Conclusions

AM is not able to completely replace the conventional methods with one of the many reasons being substandard surface quality. The surface quality is vital in determining part functionality which can pose significant problems if it is not counted. The complex surface topographies of AM present a greater challenge to conventional surface texture metrology techniques as the surface quality of AM surfaces is not trivial like conventional surfaces. The AM surface differs from processes, parameters, materials, geometries, build inclination angles and orientations etc. The available conventional surface characterisation methods are generally two-dimensional (R_a), but some of the researchers who attempted to study three-dimensional surface texture characterisation are mostly limited to an average height parameter (S_a). Conventional surface texture metrology is predominantly focused to characterize the overall surface topographical asperities data of the whole measured region by a limited number or set of scalar values. However, R_a/S_a lacks characterising the diverse surface topographical features (metallurgical defects and surface asperities) and fails to interpret the functional performance. Also, the conventional texture parameters (R_a/S_a) are not intending to provide information about the individualities present on the surface. In saying that conventional parameters are not capable of providing the details about the number of particles/asperities present on the surface, nor their spatial distribution. Instead, these conventional parameters would assist in capturing the overall or entire topographical data (for example, roughness R_a/S_a & R_q/S_q , etc.) of the surface of the region being measured. To overcome this limitation, a feature-based particle analysis was employed by adopting a spatially decomposing application of threshold segmentation, according to the S_{mr1} value. The captured surface measurement data consist of digital topographies which have been segmented to isolate partially-melted/un-melted particles and spatters from the surface that provides valuable quantification data and the perception of the individual surface asperities which form during the LPBF process. Each segmented region is referred to as the feature that is then characterised related to its geometrical features. Establishing an advanced surface texture characterisation tool for AM surfaces is a prerequisite. This newly developed novel surface texture characterisation toolbox can be used as a guideline (i) to systematically characterise and quantify the diverse defects and asperities that emerge on various metal AM external and internal surfaces built with varying inclination angles and correlate them with suitable surface texture parameters as per ISO-25178-2

(ii) to design/tailor or optimise the metal AM process to achieve lower or desired roughness levels, (iii) to effectively determine the influencing factors (individual process parameters, inclination angles, laser beam incidence angle, AM part location on the build plate, building orientations, type of surface, etc) representing a complex AM surface quality that suits the required functional performance of end-use parts.

In addition, the basic profile characterisation method (Ra) is not suitable to characterise the unique surface asperities like re-entrant features, sub-surface porosities and deep notch-like crater defects as the tip of the stylus cannot reach the depth sub-surface or intricate non-vertical shape of re-entrant features and crater-defects. Sa and Sq are suited to characterise the surface topography of metal AM surfaces whilst Ssk is suited to distinguish between up-skin and down-skin surfaces which mostly comprised of peaks from particle features (balling, spatters, and unwanted/partially-melted particles) stuck on the metal AM surface. The spatial parameter Sal is beneficial to study (staircase effect) the change in the autocorrelation length of a new location with respect to the original length. The areal surface texture height parameters fail to provide information about individual particle features, the newly developed feature-based particle analysis is appropriate to characterize, quantify these features individually. Functional parameters are used to characterise the functional properties of wear and tribological components. The Vmp parameter is helpful to study the volume density of particle feature characteristics of different metal AM surfaces. It is also important to note that volume parameters are obtained by dividing the material ratio curve into three zones by applying two material ratio thresholds Mr1 10% and Mr2 80% with default peak material 0-10%. However, Mr1 and Mr2 can be adjusted flexibly depending on particular applications. The material ratio thresholds Smr1 and Smr2 from the Sk parameters are more suited to analyse particle features compared to adopting the default Mr ratio of 10%. The feature parameter Spd is useful to examine the density (smaller or bigger) of the particle features.

The external surface quality of acetabular bone implants is rougher from the outside and smoother from the inside, whereas the tibial augments possess a rougher internal surface and smoother outside. Therefore, it is crucial to study both external and internal surfaces (quality) built with varying inclination angles. It is also challenging to design or tailor to achieve the lower/ desired surface quality of functional components used in flow channels-integrated aerospike engines, liquid rocket engine components; cylinder liners, orthopaedic and dental implants.

Taguchi DOE was found to be successful to achieve the lower or desired top and side surface quality by optimising the LPBF critical parameters. The ANOVA was effective to identify the impact of individual critical parameters on the resultant top and side surface quality, whilst the 25 different top and side surface were systematically characterised.

Based on this strong foundation of advanced surface texture characterisation and LPBF process optimisation to achieve lower or desired surface quality, it is paramount to investigate the impact of different build orientations on the final quality of LPBF components. The importance of studying the impact of different build orientations is to identify the optimal build angle or orientations. The optimised build angle or orientation minimizes the occurrence of defects and asperities on the complex surface topography of LPBF components. The rougher surface mostly affects the fatigue life due to the presence of more peaks and valleys created by surface defects and asperities. However, fatigue life is mostly driven by the valleys on the surface as they behave like higher stress concentration regions that could lead to early crack initiation and easy propagation through the material before failing at the lower fatigue loads.

This novel characterisation approach can be applied to study the surface quality of functional components of liquid rocket engines in aerospace applications, osseointegrated ortho and dental implants of biomedical applications, cooling channels, piston cylinder liners, wind turbines and marine applications.

The research achievements accomplished in this thesis are listed below.

Objective 1: Chapter 3 is dedicated to study the emergence of different metallurgical defects and various surface asperities (staircase effect, balling, spatters, un-melted/partially-melted particles) on the LPBF Truncheon artefact built with varying inclination angles.

The novel surface texture toolbox was developed to systematically characterise the prevailing defects and asperities, and correlate with the suitable array of areal surface texture parameters as per ISO 25178-2, and the newly proposed particle analysis to quantify particle features. Simultaneously, the surface texture prediction model based on the trigonometric functions was adopted to compare the analysed texture parameters results with the predicted ones.

The results confirmed that height parameters S_a and S_q , and the spatial parameter S_{al} were predominantly influenced by the staircase effect, and S_a and S_q trends tend to closely follow the prediction model. The hybrid parameters S_{dr} and S_{dq} revealed that the particle features were the major contributors to the increase of surface area and general surface slope, while the impact of

the staircase effect is insignificant. The functional parameter, V_{mp} showed that the surfaces with higher inclination have a larger total volume of particles. Similarly, the feature parameter, Spd and particle analysis revealed particle features have a significant impact on the varying build inclination angles. The experimental investigation and predicted results found a strong correlation between the resultant surface quality and the various build inclination angles.

Objectives 2 and 3: Chapter 4 examined the emergence of different metallurgical defects and various surface asperities on both longitudinal and latitudinal facets external and internal up-skin and down-skin surfaces of a bespoke ball artefact built with varying inclination angles.

The novel surface texture characterisation method was then applied to characterise, correlate and quantify diverse defects and asperities formed on both longitudinal and latitudinal facets external and internal up-skin and down-skin surfaces of a ball artefact.

Established a strong relationship between various build inclination angles and the final surface quality. Determined the statistical significance of various inclination angles, build orientations, and types of surfaces with respect to resultant surface quality by ANOVA.

Longitudinal facet external and internal surfaces

The results confirmed that surface roughness metrics height parameters (S_a and S_q) trends interspersed between the surfaces dominated by spatters, un-melted and partially-melted powder particles at higher inclination angles due to insufficient redistribution of mass or heat transfer by laser beam, while the laser ripples, staircase effect from the re-solidified melt tracks dominated at lower inclination angles. The surface roughness of longitudinal facets up-skin surfaces was linearly dependent on build inclination angles, while the surface roughness of down-skin surfaces was affected by the adherence of a higher number of particle features caused by intermittent heat transfer.

Internal down-skin surfaces revealed quite a strong correlation between hybrid parameter S_{dr} and downward surface inclinations. The number of particle analysis plots for the longitudinal facet external up-skin surface revealed an average of ~12 particles more attached as compared to internal surfaces for the same region. Similarly, an average of ~8 particles are less attracted to the external down-skin surfaces than the internal down-skin surfaces. It was interesting to note that there was no significant difference in particles coverage ratio between longitudinal external and internal surfaces; with a mere 2% higher particle coverage ratio identified for internal surfaces.

Latitudinal facet external and internal surfaces

Sa and Sq values for the latitudinal facet internal surface were approximately higher (6%-20%) than the external surface. A consistent continuous and steady particle (151-160 particles) trend was observed for all the latitudinal internal surfaces. All the external surfaces, except 285° where the higher number of particles (~30 particles) were observed which is ascribed to the angle of incidence of the laser beam and the farther position of AM ball artefact on the build platform. From the latitudinal facet surface texture characterisation and particles analysis, it is fair to conclude that there is no significant difference between internal and external surface quality. However, the position of AM part on the substrate and laser beam incidence angle significantly affect the final surface roughness.

All in all, it is clearly evident from the experimental results and statistical significance analysis that build inclination angles have a significant impact on the surface roughness of longitudinal facets up-skin and down-skin orientation as well as external and internal surfaces. Meanwhile, the build inclination angles demonstrate a less significant effect on latitudinal facets on external and internal surfaces.

Objective 4: Chapter 5 reported the LPBF critical parameters optimisation by Taguchi DOE to achieve or tailor the lower or desired top and side surface quality of bespoke hexagon artefacts built with 25 different parametric combinations. The percentage contribution of the individual critical parameter was calculated by ANOVA. The confirmation experiments were carried out to validate the Taguchi predicted surface quality and compared with the default industrial settings and lowest (achieved) surface quality parametric combinations. The results confirmed that the top surface quality was affected by the metallurgical defects like crater-defects, spatters, balling, porosities, cracks, and side surface quality was affected by various surface asperities such as delamination partially- melted, un-melted particles.

Top surface quality

More prominent crater-like defects were reported for artefacts #1, #6, #11, #16 and #21, which resulted in poor Sa values. The best Sa value (17 µm) was recorded for the #9 artefact, while the worst surface Sa (214 µm) was reported for artefact #11. The formation of smaller-size crater defects and typical LPBF defects like balling, porosities, cracks and spatters induced poor Sa values ranging between 60 µm – 80 µm for artefacts #1, #7, #8, #13, and #23. The obtained Sa values for the rest of the artefacts were in the range of 26 µm – 42 µm. ANOVA analysis found that the hatch spacing (46%) was the most influential parameter that affected the top surface quality

of the LPBF artefacts, followed by point distance (19%), laser power (9%), exposure time (7%) and layer thickness (5%). The Taguchi DOE optimised parameters (LP₁: 100 W, HS₄: 100 μm , LT₂: 60 μm , PD₃: 60 μm , ET₂: 80 μs) were validated by conducting the verification experiments with the objective “of smaller is better”. The top surface quality from Taguchi DOE resulted in an improved Sa value (13 μm) by 4 μm compared to the lowest-achieved surface quality result Sa (17 μm) obtained from the L25 orthogonal arrays.

Side surface quality

Unlike top surfaces, side surfaces did not display any (bigger/smaller/wider/shallower) crater-like defects. Side surface quality was predominantly influenced by the adhered particle features derived from partially-melted/un-melted particles. Artefacts #23, #5, and #20 considered fully defective surfaces (Sa values 26-30 μm) comprised all the indistinguishable surface anomalies (spatters, balling, porosities, cracks, delamination). Delamination played a significant role in poor surface quality of artefacts #6 (Sa-18 μm), #7, and #13 both recording a Sa values of 22 μm . The best Sa value (9 μm) was recorded for artefacts #8, and #25. Most of the side surfaces exhibited stable and closely associated Sa values within the range of 10-20 μm , owing to the occurrence of various inevitable surface anomalies at different sizes and different scales. ANOVA analysis found that the exposure time (58 %) is the most influential parameter that affected the side surface quality of the LPBF artefacts, followed by point distance (20 %), laser power (9 %), and layer thickness (8 %), and hatch spacing (4 %). The Taguchi DOE optimised parameters (LP₃: 150 W, HS₄: 100 μm , LT₁: 30 μm , PD₃: 60 μm , ET₂: 80 μs) were validated by conducting the verification experiments with the objective “of smaller is better”, the side surface quality was improved by 1 μm for Taguchi optimised parameters (Sa 8 μm) as compared to the best surface quality result Sa (9 μm) obtained from the L25 orthogonal arrays, which was not a significant improvement but still reasonable. Although the side surfaces were more prone to the adherence of particle features, they do not contribute significantly towards the substandard surface quality as compared to the top surface quality, which was greatly compromised mainly due to the formation of crater-like defects at different sizes and different scales. Overall, Taguchi DOE parametric optimisation has been successful in achieving the lower or desired surface quality, even better than default AM parameters settings, while the top surface quality optimisation process was effectively close to the default settings.

Objective 5: Chapter 6 investigated the influence of build orientations on the final surface quality, microstructure characteristics, and mechanical properties of LPBF dog-bone samples.

Impact of build orientations on surface quality

The AB-H oriented surface recorded a worst Sa value of 14 μm , this was likely credited to the higher residual stresses induced surface defects and asperities at various scales covering the entire surface which were generated during the LPBF fabrication of longer cross-section horizontal oriented parts. Both AB-V and AB-VI orientation samples demonstrated identical Sa signifying the least impact of build orientations. AB-HI orientation sample displayed the best Sa of 9 μm among all four orientations.

Impact of build orientations on microstructure and mechanical properties

The AB-H oriented sample emerged as the strongest with the highest UTS of 582 MPa which is attributed to the minimal defects and refined microstructure. The presence of various metallurgical defects including oxide inclusions and particle features in the AB-V-oriented dog-bone sample resulted in the least UTS of 528 MPa. But both AB-H and AB-V oriented exhibited a lower elongation of 10%, implying the least tough samples. AB-VI showed the highest elongation of 14.5% in combination with decent UTS of 554 MPa; signifying the toughest sample.

Fatigue life results followed a similar trend to tensile properties. The best fatigue life was obtained for the AB-H (178440 cycles) sample which is 43 % higher than the worst-performed AB-V (102548 cycles) oriented sample. The poor fatigue life of AB-V oriented sample is ascribed to the higher stress concentrations regions due to weak interfacial bonding between the successive layers and the alignment of bigger size defects and asperities perpendicular to the applied stress which becomes an easy path for crack initiation and propagation before failing at the lower number of cycles. The uniform distribution of small-scale defects/asperities aligned parallel to applied stress in horizontal-oriented sample surface caused less stress concentration regions, thereby resisting for longer period that resulted in higher fatigue life.

Overall, this part of the research has found a significant impact of different build orientations on surface quality, microstructure and mechanical properties (both tensile and fatigue) of LPBF dog-bone samples. However, irrespective of the build orientations, metal AM or LPBF components are susceptible to dynamic loading conditions.

7.2 Contributions to the field

This PhD thesis makes the following contributions,

1. Developed a novel surface texture characterisation toolbox which is used to systematically characterise diverse metallurgical defects and surface asperities emerge on different external and internal metal AM surfaces built with varying inclination angles, and correlate them with the suitable array surface texture parameters described in ISO-25178-2. For example, Sa, Sq, Sal parameters were suitable to study staircase effect of metal AM curved or inclined surfaces. Ssk is able to differentiate between up-skin and down-skin surfaces. Sdr Sdq parameters can be applied to study particle-features (see Chapters 3-6).
2. Also, the newly developed feature-based particle analysis is effective to quantify the individual particle features like balling, spatters, un-melted or partially melted particles) (see Chapters 3 & 4).
3. Established a strong relationship between various build inclination angles and the final surface quality (see Chapters 3 & 4)
4. Determined the statistical significance of various inclination angles, build orientations, and types of surfaces with respect to resultant surface quality by ANOVA (see Chapter 4).
5. Discovered the dependence of laser beam incidence angle and the location of AM part on the build platform with final surface quality (see Chapter 4).
6. Demonstrated that lower or desired surface quality can be achieved or tailored (introducing intentional porosity if necessary) by optimising LPBF critical parameters using Taguchi DOE, and the percentage contribution of individual critical parameter was successfully quantified using ANOVA. Importantly, diverse surface topographical features emerged on 25 different top and 25 side surfaces were systematically characterised (see Chapter 5).
7. Finally, found that different build orientations have a significant impact on the final surface quality, microstructure and mechanical properties of metal AM components. The optimised build angle or orientation helps to minimize the occurrence of defects and asperities on the complex surface topography of LPBF components (see Chapter 6).

7.3 Future work

Further detailed research addressing the other surface irregularities like sub-surface porosities, re-entrant features, and the staircase effect occurring in the reverse direction beyond 90° surface inclination will be crucial to get insights into the complete surface quality of metal AM/LPBF surfaces built with varying inclination angles. Another key future work is to investigate the inhomogeneity of surface roughness across various locations on the same inclined surface.

In addition to the LPBF process optimisation of external top and side surfaces, it is essential to optimise the surface quality of different inclined surfaces. Simultaneously surface texture prediction modelling and the surface quality optimisation of internal surfaces with respect to varying inclination angles will be very intriguing research that needs further investigation. Expanding the surface quality optimisation beyond surface texture height metrics (S_a , S_q , S_{sk} , and S_{ku}) will be beneficial for the comprehensive understanding of the surface quality of LPBF surfaces.

It has been successfully demonstrated that Taguchi DOE can effectively optimise the LPBF process parameters to achieve lower or desired surface quality. However, it is essential to explore other advanced tools like machine learning technology, e.g., artificial neural networks (ANN), for the same. Investigating the impact of laser beam incidence angle/position of building part on the resultant (uniformity) LPBF surface quality is another unexplored aspect for future study.

References

- [1] Narasimharaju, S. R., Zeng, W., See, T. L., Zhu, Z., Scott, P., Jiang, X., & Lou, S. (2022). A comprehensive review on laser powder bed fusion of steels: Processing, microstructure, defects and control methods, mechanical properties, current challenges and future trends. *Journal of Manufacturing Processes*, 75, 375-414.
- [2] Mueller, B. (2012). Additive manufacturing technologies–Rapid prototyping to direct digital manufacturing. *Assembly Automation*.
- [3] Townsend, A. (2018). Characterisation of the Surface Topography of Additively Manufactured Parts (Doctoral dissertation, University of Huddersfield).
- [4] Srivatsan, T. S., & Sudarshan, T. S. (Eds.). (2015). Additive manufacturing: innovations, advances, and applications.
- [5] DebRoy, T., Wei, H. L., Zuback, J. S., Mukherjee, T., Elmer, J. W., Milewski, J. O., ... & Zhang, W. (2018). Additive manufacturing of metallic components–process, structure and properties. *Progress in Materials Science*, 92, 112-224.
- [6] Diaz, A. (2019). Surface texture characterisation and optimisation of metal additive manufacturing-produced components for aerospace applications. In *Additive manufacturing for the aerospace industry* (pp. 341-374). Elsevier.
- [7] Behera, M. P., Dougherty, T., & Singamneni, S. (2019). Conventional and additive manufacturing with metal matrix composites: A perspective. *Procedia Manufacturing*, 30, 159-166.
- [8] Brandt, M. (Ed.). (2016). *Laser additive manufacturing: materials, design, technologies, and applications*.
- [9] Khodabakhshi, F., Farshidianfar, M. H., Bakhshivash, S., Gerlich, A. P., & Khajepour, A. (2019). Dissimilar metals deposition by directed energy based on powder-fed laser additive manufacturing. *Journal of Manufacturing Processes*, 43, 83-97.
- [10] Abe, T., & Sasahara, H. (2016). Dissimilar metal deposition with a stainless steel and nickel-based alloy using wire and arc-based additive manufacturing. *Precision Engineering*, 45, 387-395.
- [11] Gibson, I., Rosen, D., Stucker, B., & Khorasani, M. (2014). *Additive manufacturing technologies* (Vol. 17, p. 195). New York: Springer.
- [12] Narasimharaju, S. R., Zeng, W., See, T. L., Zhu, Z., Scott, P., Jiang, X., & Lou, S. (2022). Influence of critical process parameters on surface roughness and statistical optimization

of LPBF 316L stainless steel. In *2022 ASPE and euspen Summer Topical Meeting on Advancing Precision in Additive Manufacturing* (Vol. 77, pp. 113-118). American Society for Precision Engineering, ASPE.

[13] Gockel, J., Sheridan, L., Koerper, B., & Whip, B. (2019). The influence of additive manufacturing processing parameters on surface roughness and fatigue life. *International Journal of Fatigue*, 124, 380-388.

[14]<https://www.metal-am.com/articles/advancing-rocket-propulsion-through-3d-printing-novel-surface-finishing-technologies-and-public-private-partnerships/>

[15] Nobles, K. P., Janorkar, A. V., & Williamson, R. S. (2021). Surface modifications to enhance osseointegration—Resulting material properties and biological responses. *Journal of Biomedical Materials Research Part B: Applied Biomaterials*, 109(11), 1909-1923.

[16] Kerstens, F., Cervone, A., & Gradl, P. (2021). End to end process evaluation for additively manufactured liquid rocket engine thrust chambers. *Acta Astronautica*, 182, 454-465.

[17] Hassanin, H., ElShaer, A., Benhadj-Djilali, R., Modica, F., & Fassi, I. (2018). Surface finish improvement of additive manufactured metal parts. *Micro and Precision Manufacturing*, 145-164.

[18] Kokkonen, P., Salonen, L., Virta, J., Hemming, B., Laukkanen, P., Savolainen, M., ... & Welling, J. (2016). Design guide for additive manufacturing of metal components by SLM process.

[19] Fox, J. C., Moylan, S. P., & Lane, B. M. (2016). Effect of process parameters on the surface roughness of overhanging structures in laser powder bed fusion additive manufacturing. *Procedia Cirp*, 45, 131-134.

[20] Delgado, J., Ciurana, J., & Rodríguez, C. A. (2012). Influence of process parameters on part quality and mechanical properties for DMLS and SLM with iron-based materials. *The International Journal of Advanced Manufacturing Technology*, 60(5-8), 601-610.

[21] Miyoshi, K. Chapter 16 “Surface Analysis and Tools.” *Tribology of Mechanical Systems: A Guide to Present and Future Technologies*. Ed. Vižintin, J, Kalin, M, Dohda, K, & Jahanmir, S. ASME Press, 2004.

[22] Maleki, E., Bagherifard, S., Bandini, M., & Guagliano, M. (2020). Surface post-treatments for metal additive manufacturing: Progress, challenges, and opportunities. *Additive Manufacturing*, 101619.

[23] Nagarajan, B., Hu, Z., Song, X., Zhai, W., & Wei, J. (2019). Development of micro selective laser melting: The state of the art and future perspectives. *Engineering*, 5(4), 702-720.

- [24] Ni, C., Shi, Y., & Liu, J. (2018). Effects of inclination angle on surface roughness and corrosion properties of selective laser melted 316L stainless steel. *Materials Research Express*, 6(3), 036505.
- [25] Sahoo, P., & Barman, T. K. (2012). ANN modelling of fractal dimension in machining. In *Mechatronics and manufacturing engineering* (pp. 159-226). Woodhead Publishing.
- [26] Blind, A. (2014). A Different Slice of Surface Finish. *Quality*, 53(9), 30.
- [27] <https://amfg.ai/wp-content/uploads/2019/08/The-Additive-Manufacturing-Landscape-2019-Whitepaper.pdf>
- [28] Leach, R. (Ed.). (2011). *Optical measurement of surface topography* (Vol. 8). Berlin Heidelberg, Germany: Springer Berlin Heidelberg.
- [29] Grimm, T., Wiora, G., & Witt, G. (2015). Characterisation of typical surface effects in additive manufacturing with confocal microscopy. *Surface topography: metrology and properties*, 3(1), 014001.
- [30] Ek, R. K., Rännar, L. E., Bäckström, M., & Carlsson, P. (2016). The effect of EBM process parameters upon surface roughness. *Rapid Prototyping Journal*.
- [31] Whitehouse, D. J. (2004). *Surfaces and their Measurement*. Gulf Professional Publishing. London. U.K.
- [32] ISO 25178-2, 2012, *Geometrical Product Specifications (GPS)—Surface Texture: Areal—Part 2: Terms, Definitions and Surface Texture Parameters*. International Standards Organization: Geneva, Switzerland.
- [33] Whip, B., Sheridan, L., & Gockel, J. (2019). The effect of primary processing parameters on surface roughness in laser powder bed additive manufacturing. *The International Journal of Advanced Manufacturing Technology*, 103(9), 4411-4422.
- [34] Y. Bai, C. Zhao, J. Yang, J. Y. H. Fuh, W. F. Lu, C. Weng, & H. Wang (2020). Dry mechanical-electrochemical polishing of selective laser melted 316L stainless steel. *Materials & Design*, 193, 108840.
- [35] Fathi-Hafshejani, P., Soltani-Tehrani, A., Shamsaei, N., & Mahjouri-Samani, M. (2022). Laser incidence angle influence on energy density variations, surface roughness, and porosity of additively manufactured parts. *Additive Manufacturing*, 50, 102572.

- [36] Narasimharaju, S. R., Liu, W., Zeng, W., See, T. L., Scott, P., Jiang, X. J., & Lou, S. (2021). Surface texture characterization of metal selective laser melted part with varying surface inclinations. *Journal of Tribology*, 143(5).
- [37] Casalino, G., Campanelli, S. L., Contuzzi, N., & Ludovico, A. D. (2015). Experimental investigation and statistical optimisation of the selective laser melting process of a maraging steel. *Optics & Laser Technology*, 65, 151-158.
- [38] Snyder, J. C., & Thole, K. A. (2020). Understanding laser powder bed fusion surface roughness. *Journal of Manufacturing Science and Engineering*, 142(7), 071003.
- [39] L.E. Murr, E. Martinez, S.M. Gaytan, D.A. Ramirez, B.I. Machado, P.W. Shindo, J.L. Martinez, F. Medina, J. Wooten, D. Ciscel, U. Ackelid, R.B. Wicker. Microstructural architecture, microstructures, and mechanical properties for a nickel-base superalloy fabricated by electron beam melting, *Metall. Mater. Trans. A* 42 (2011)3491–3508.
- [40] W.E. Frazier, "Metal additive manufacturing: a review." *Journal of Materials Engineering and performance* 23, no. 6 (2014): 1917-1928
- [41] L Song, J Mazumder. "Real-time implementation of generalized predictive algorithm for direct metal deposition (DMD) process control." U.S. Patent 9,044,827, issued June 2, 2015.
- [42] Zhang J, Liou F, Seufzer W, et al. A coupled finite element cellular automaton model to predict thermal history and grain morphology of Ti-6Al-4V during direct metal deposition (DMD). *Additive Manufacturing*, 2016, 11: 32–39
- [43] G.N Levy, R Schindel & J.P Kruth. Rapid Manufacturing and rapid tooling with layer manufacturing (LM) Technologies, State of the Art and Future Perspectives. *CIRP Ann. -Manuf. Technol.* 52(2003), 589–609.
- [44] Amt B.S. "EN ISO/ASTM 52900: 2017-Additive manufacturing. General principles." Terminology
- [45] Wohlers Report 2020, Wohlers Associates
- [46] N. Guo, M.C. Leu Additive manufacturing: technology, applications and research needs *Front. Mech. Eng.*, 8 (2013), pp. 215-243
- [47] S.H. Khajavi, J. Partanen, J. Holmström Additive manufacturing in the spare parts supply chain *Comput. Ind.*, 65 (2014), pp. 50-63

- [48] D. Cong, H. Zhou, Z. Ren, Z. Zhang, H. Zhang, C. Meng, C. Wang The thermal fatigue resistance of H13 steel repaired by a biomimetic laser remelting process Mater. Des., 55 (2014), pp. 597-604
- [49] https://www.slmsolutions.com/fileadmin/user_upload/SLM_Solutions_Group_AG_Annual_Report_2018.pdf
- [50] <https://www.netl.doe.gov/sites/default/files/eventproceedings/2017/utsr/general/Grylls.pdf>
- [51] <https://www.smartechpublishing.com/news/metal-am-report-2018/>
- [52] <https://www.metal-am.com/introduction-to-metal-additive-manufacturing-and-3d-printing/metal-additive-manufacturing-processes/>
- [53] Wohlers report 2019: 3D printing and additive manufacturing state of the industry. Wohlers Associates, 2019
- [54] Y. Liu, Y. Yang, S. Mai, D. Wang, C. Song "Investigation into spatter behavior during Selective laser melting of AISI 316L stainless steel powder." Materials & Design 87 (2015): 797-806
- [55] J.P. Kruth, L. Froyen, J.V. Vaerenbergh, P. Mercelis, M. Rombouts, B. Lauwers. Selective laser melting of iron-based powder." Journal of materials processing technology 149, no. 1-3 (2004): 616-622
- [56] J.P. Kruth, G. Levy, F. Klocke, T.H.C. Childs, Consolidation phenomena in laser and powder-bed based layered manufacturing." CIRP annals 56, no. 2 (2007): 730-759
- [57] B. Stucker. Additive Manufacturing Technologies: Technology Introduction and Business Implications. Frontiers of Engineering 2011: Reports on Leading-Edge Engineering from the 2011 Symposium, pages 19–21, 2012.
- [58] H. W. Lee, K.H. Jung, S.-K. Hwang, S.H. Kang, D.K. Kim. Microstructure and mechanical anisotropy of CoCrW alloy processed by Selective laser melting. Materials Science & Engineering A 749(2019) 65–73.
- [59] L.E. Murr, E. Martinez, K.N. Amato, S.M. Gaytan, J. Hernandez, D.A. Ramirez, P.W. Shindo, F. Medina, R.B. Wicker, Fabrication of metal and alloy components by additive manufacturing: examples of 3D materials science, J. Mater. Res. Technol. 1 (2012) 42–54.
- [60] S.N Patil, A.V Mulay, B.B Ahuja. Development of experimental setup of metal rapid prototyping machine using selective laser sintering technique. Journal of the Institution of Engineers (India): Series C, 2018, 99(2): 159–167

- [61] K. Mumtaz and N. Hopkinson. Top surface and side roughness of Inconel 625 parts processed using Selective laser melting. *Rapid Prototyping Journal*, Volume 15, Number 2, 2009, pp. 96-103(8)
- [62] C. Casavola, S. Campanelli, C. Pappalettere. Preliminary investigation on distribution of residual stress generated by the Selective laser melting process. *Journal of Strain Analysis for Engineering Design*, 2009, 44(1): 93–104.
- [63] M.A Quader, S. Ahmed, R.A.R Ghazilla, S. Ahmed, and M. Dahari. A comprehensive review on energy efficient CO₂ breakthrough technologies for sustainable green iron and steel manufacturing. *Renewable and Sustainable Energy Reviews*, 50(2015), pp.594-614
- [64] D. Peckner, I.M. Bernstein, *Handbook of stainless steel*, McGraw-Hill, 1977.
- [65] J. Pellegrino, and K. Jamison, 2015. US DOE Roundtable and Workshop on Advanced Steel Technologies: Emerging Global Technologies and R&D Opportunities. No. ORNL/TM-2015/742. Oak Ridge National Lab. (ORNL), Oak Ridge, TN (United States), 2015.
- [66] <https://www.thebalance.com/steel-grades-2340174>.
- [67] D. Herzog, V. Seyda, E. Wycisk, and C. Emmelmann, "Additive manufacturing of metals." *Acta Materialia* 117 (2016): 371-392
- [68] C.N. Hsiao, C.S. Chiou, J.R. Yang, "Aging reactions in a 17-4 PH stainless steel." *Materials Chemistry and Physics* 74, no. 2 (2002): 134-14
- [69] H. Fayazfar, M. Salarian, A. Rogalsky, D. Sarker, P. Russo, V. Paserin, E. Toyserkani, A critical review of powder-based additive manufacturing of ferrous alloys: process parameters, microstructure and mechanical properties, *Mater. Des.* 144 (2018) 98–128.
- [70] C. Donate-Buendia, P. Kurnsteiner, F. Stern, M. B. Wilms, R. Streubel, I. M. Kusoglu, J. Tenkamp, E. Bruder, N. Pirch, K. Durst, J.H. Schleifenbaum, F. Walther, B. Gault, and B. Gokce "Microstructure formation and mechanical properties of ODS steels built by Laser Additive Manufacturing of nanoparticle coated iron-chromium powders." *Acta Materialia* (2020): 116566.A
- [71] W.D. Jr. Callister .*Materials Science and Engineering: An Introduction*, 8th Edition
- [72] K. Özsoy, "Examining mechanical properties of profiles manufactured aluminum extrusion dies using powder bed fusion." *Measurement* 177 (2021): 109266.

- [73] S. AM Tofail, E. P. Koumoulos, A. Bandyopadhyay, S. Bose, L. O'Donoghue, and C. Charitidis. "Additive manufacturing: scientific and technological challenges, market uptake and opportunities." *Materials today* 21, no. 1 (2018): 22-37.
- [74] E.O. Correa. Weldability of Iron Based Powder Metal Alloys Using Pulsed GTAW Process, Arc Welding, Prof. Wladislav Sudnik (Ed.). (2011)
- [75] C. Selcuk, S. Bond and P. Woollin Metallurgy, Corrosion & Surfacing Technology Group, TWI Ltd, Granta Park, Great Abington, Cambridge
- [76] B.Song, X. Zhao, S. Li, C. Han, Q. Wei, S. Wen, J. Liu, Y. Shi. Differences in microstructure and properties between Selective laser melting and traditional manufacturing for fabrication of metal parts: A review, *Frontiers of Mechanical Engineering*.2015(10)
- [77] W.K Brooks, S. Tsopanos, R. Stamp, C.J Sutcliffe, W.J Cantwell, P. Fox., J. Todd.. The production of open cellular lattice structures using Selective laser melting. 6th National Conference on Rapid Design, Prototyping, and Manufacturing, Buckinghamshire Chilterns University College, June 2005
- [78] X. Li, Y.H. Tan, H.J. Willy, et al., Heterogeneously tempered martensitic high strength steel by Selective laser melting and its micro-lattice: Processing, microstructure, superior performance and mechanisms, *Materials & Design*,
- [79] W. Li, K.Yang, S. Yin, X. Yang, Y. Xu, R. Lupoi. "Solid-state additive manufacturing and repairing by cold spraying: A review." *Journal of materials science & technology* 34, no. 3 (2018): 440-457
- [80] H. Alipooramirabad, A. Paradowsk, R. Ghomashchi, M. Reid. Investigating the effects of welding process on residual stresses, microstructure and mechanical properties in HSLA steel welds, *Journal of Manufacturing Processes* 28 (2017) 70–81,
- [81] Deng Q L, Xie A N, Ge Z J, et al. Experimental researches on rapid forming full compacted metal parts by Selective laser melting. *Materials Science Forum*, 2006, 532–533: 428–431.
- [82] M. Yakout, M.A. Elbestawi, S. C. Veldhuis. Density and mechanical properties in Selective laser melting of Invar 36 and stainless steel 316L. *Journal of Materials Processing Tech.* 266 (2019) 397–420
- [83] Y. Hong, C. Zhou, Y. Zheng, L. Zhang, J. Zhen, X. Chena, Bai. Formation of strain-induced martensite in Selective laser melting austenitic stainless-steel *An. Materials Science & Engineering A* 740–741 (2019) 420–426

- [84] S.Sun, T. Ishimoto, K. Hagihara , Y. Tsutsumi ,T. Hanawa , T. Nakano. Excellent mechanical and corrosion properties of austenitic stainless steel with a unique crystallographic lamellar microstructure via laser powder bed fusion Scripta Materialia 159 (2019) 89–93
- [85] U.S Bertoli, B.E. MacDonald, J. M. Schoenung. Stability of cellular microstructure in laser powder bed fusion of 316L stainless steel. Materials Science & Engineering A 739 (2019) 109–117
- [86] Q.B. Nguyena, Z. Zhua, F.L. Nga, B.W. Chuua, S.M.L. Naia, J. Wei. High mechanical strengths and ductility of stainless steel 304L fabricated using Selective laser melting. Journal of Materials Science & Technology 35 (2019) 388–394
- [87] V G Smelov, A V Sotov, A V Agapovichev and T.M Tomilina. Selective laser melting of Metal Powder of Steel 316L. Materials Science and Engineering 142 (2016) 012071
- [88] J. Sande, J. Hufenbach, L. Giebeler , H.Wendrock , U. Kühn, J. Eckert. Microstructure and properties of FeCrMoVC tool steel produced by Selective laser melting. Materials and Design 89 (2016) 335–341.
- [89] D. Gua, H. Chen Selective laser melting of high strength and toughness stainless steel parts: The roles of laser hatch style and part placement strategy. Materials Science & Engineering A 725 (2018) 419–427
- [90] A. Bandar, G.Dariusz, B.Tushar, Y. Jenn-Ming. Densification behavior, microstructural evolution, and mechanical properties of TiC/316L stainless steel nanocomposites fabricated by Selective laser melting. Materials and Design 138 (2018) 119–128.
- [91] H. Chen, D. Gu, D. Dai, C. Ma, Mujian Xi. Microstructure and composition homogeneity, tensile property, and underlying thermal physical mechanism of Selective laser melting tool steel parts. Materials Science & Engineering A 682 (2017) 279–289.
- [92] A V Agapovichev, A V Sotov V G Smelov, V S Sufiiarov, D V Masaylo. The investigation of microstructure and mechanical properties of tool steel produced by Selective laser melting technology, Mater. Sci. Eng. 441(2018) 012003
- [93] W.M. Tucho , V. H. Lysne , H. Austb , A. Sjolyst-Kverneland ,V. Hansen Investigation of effects of process parameters on microstructure and hardness of SLM manufactured SS316L,. Journal of Alloys and Compounds 740 (2018) 910-925
- [94] B. Zhang, Y. Li, Q. Bai. Defect formation mechanisms in Selective laser melting: A Review. Chin. J. Mech. Eng. (2017) 30:515–527

- [95] R.Morgan, C. J Sutcliffe, W. O’neill. Density analysis of direct metal laser re-melted 316L stainless steel cubic primitives, *Journal of materials science* 39 (2004) 1195 – 1205
- [96] M. Yakout, M.A. Elbestawi, S.C. Veldhuis. A study of thermal expansion coefficients and microstructure during, Selective laser melting of Invar 36 and stainless steel 316L. *Additive Manufacturing* 24 (2018) 405–418
- [97] Y.F. Shen, D. Gu and Y.F. Pan. Balling Process in Selective Laser Sintering 316 Stainless Steel Powder, 315-3162006) pp 357-360
- [98] S. Das. Physical Aspects of Process Control in Selective Laser Sintering of Metals. *Advanced Engineering Materials*, 5(10) (2003):701–711.
- [99] P. tang, S. wang, H. duan, M. long, Y. li, S.fan and D. chen. The formation of humps and ripples during Selective laser melting of 316L stainless steel. *JOM*, Vol. 72, No. 3, 2020
- [100] E. Liverani, S. Toschi, L. Ceschini, A. Fortunato. Effect of Selective laser melting (SLM) process parameters on microstructure and mechanical properties of 316L austenitic stainless-steel, *Journal of Materials Processing Tech.* 249 (2017) 255–263
- [101] Y. Kaynak, O. Kitay. Porosity, Surface Quality, Microhardness and Microstructure of Selective Laser Melted 316L Stainless Steel Resulting from Finish Machining. *J. Manuf. Mater. Process.* 2018, 2, 36;
- [102] W.E. King, H.D. Barth, V.M. Castillo, G.F.Gallegos, J.W. Gibbs, D.E. Hahn, C. Kamath, A.M. Rubenchik. Observation of keyhole mode laser melting in laser powder-bed fusion additive manufacturing. *Journal of Materials Processing Technology* 214 (2014) 2915–2925
- [103] D.Wang, C.Song, Y.Yang, Y. Bai. Investigation of crystal growth mechanism during Selective laser melting and mechanical property characterization of 316L stainless steel parts *Materials and Design* 100 (2016) 291–299
- [104] J. Wang, W.J Wu, W. Jing, X. Tan, G.J Bi, S.B Tor, K.F Leong, C.K Chu, E. Liu, Improvement of densification and microstructure of ASTM A131 EH36 steel samples additively manufactured via Selective laser melting with varying laser scanning speed and hatch spacing. *Materials Science & Engineering A* 746 (2019) 300–313
- [105] Z. Sun, X. Tan, S.B Tor, W.Y Yeong. Selective laser melting of stainless steel 316L with low porosity and high build rates. *Materials and Design* 104 (2016) 197–204

- [106] M. Xia, D. Gu, G. Yu, D. Dai, H. Chen, Q. Shi, "Porosity evolution and its thermodynamic mechanism of randomly packed powder-bed during Selective laser melting of Inconel 718 alloy." *International Journal of Machine Tools and Manufacture* 116 (2017): 96-106.
- [107] H. Choo, K.L Sham, J. Bohling , A. Ngo, X. Xiao, Y. Ren, P. J. Depond, M. J. Matthews, E. Garlea. Effect of laser power on defect, texture, and microstructure of a laser powder bed fusion processed 316L stainless steel. *Materials and Design* 164 (2019) 107534
- [108] H. Zheng, H. Li, L. Lang, S. Gong, Y. Ge. Effects of scan speed on vapor plume behavior and spatter generation in laser powder bed fusion additive manufacturing. *Journal of Manufacturing Processes* 36 (2018) 60–67
- [109] L. Mugwagwa , D. Dimitrov, S. Matope, I. Yadroitsev. Influence of process parameters on residual stress related distortions in Selective laser melting. *Procedia Manufacturing* 21 (2018) 92–99
- [110] C. Li, C.H. Fu, Y.B. Guo, F.Z. Fang, A multiscale modeling approach for fast prediction of part distortion in Selective laser melting *Journal of Materials Processing Technology* 229 (2016) 703–712
- [111] F. Feuerhahna, A. Schulzb, T. Seefeldt , F. Vollertsena. Microstructure and properties of selective laser melted high hardness tool steel *Physics Procedia* 41 (2013) 843 – 848
- [112] P. Mercelis, J.-P. Kruth, Residual stresses in selective laser sintering and Selective laser melting, *Rapid Prototyp. J.* 12(2006) 254–265.
- [113] T. Simson, A. Emmel, A. Dwars, J. Böhm Residual stress measurements on AISI 316L samples manufactured by Selective laser melting. *Additive Manufacturing* 17 (2017) 183–189
- [114] K. Kempen, B. Vrancken, S. Buls, L. Thijs. Selective laser melting of Crack-Free High Density M2 High Speed Steel Parts by Baseplate Preheating. *Journal of Manufacturing Science and Engineering* 136(6) (2014)
- [115] <https://link.springer.com/content/pdf/10.1007%2Fs11837-003-0137-4.pdf>
- [116] N.J. Harrison, I. Todd, and K. Mumtaz. Reduction of micro-cracking in nickel superalloys processed by Selective laser melting: A fundamental alloy design approach. *Acta Materialia* 94 (2015) 59–68
- [117] Y. Chen, F. Lu, K. Zhang, P. Nie, S.R Elmi Hosseini, K. Feng, Z. Li. Dendritic microstructure and hot cracking of laser additive manufactured Inconel 718 under improved base cooling. *Journal of Alloys and Compounds* 670 (2016) 312-321

- [118] Y.Chen, K. Zhang, J. Huang, S.R Elmi-Hosseini, Z. Li. Characterization of heat affected zone liquation cracking in laser additive manufacturing of Inconel 718. *Materials and Design* 90 (2016) 586–594
- [119] S. Kou *Welding metallurgy* 2nd edition by John Wiley & Sons (2003)
- [120] L.N. Carter, C. Martin, P.J. Withers, M.M. Attallah. The influence of the laser scan strategy on grain structure and cracking behaviour in SLM powder-bed fabricated nickel superalloy. *Journal of Alloys and Compounds* 615 (2014) 338–347.
- [121] M. Garibaldi, I. Ashcroft, M. Simonelli, R. Hague. Metallurgy of high-silicon steel parts produced using Selective laser melting. *Acta Materialia* 110 (2016) 207-216
- [122] J. Yu, M. Rombouts, G. Maes. Cracking behavior and mechanical properties of austenitic stainless-steel parts produced by laser metal deposition, *Mater. Des.* 45(2013) 228–235.
- [123] S. Cheruvathur, E.A. Lass, C.E. Campbell. Additive manufacturing of 17-4 PH stainless steel: post-processing heat treatment to achieve uniform reproducible microstructure, *JOM* 68 (2016) 930–942
- [124] M. Simonelli, C. tuck, N.T. Aboulkhair, I. Maskery, Ian Ashcroft, R.D. Wildman, and R. Hague, A study on the laser spatter and the oxidation reactions during Selective laser melting of 316l stainless steel, al-si10-mg, and ti-6al-4v. *the minerals, metals & materials society and asm international* (2015).
- [125] <http://sffsymposium.engr.utexas.edu/Manuscripts/1999/1999-030-Hauser.pdf>
- [126] J. Krell, A. Röttger, K.Geenen, W.Theisen. General investigations on processing tool steel X40CrMoV5-1 with Selective laser melting. *Journal of Materials Processing Tech.* 255 (2018) 679–688
- [127] Q. Jia, D. Gu. Selective laser melting additive manufactured Inconel718 superalloy parts: High-temperature oxidation property and its mechanisms. *Optics & Laser Technology* 62(2014)161–171
- [128] Thijs, L., Van Humbeeck, J., Kempen, K., Yasa, E., Kruth, J. P., & Rombouts, M. (2011). Investigation on the inclusions in maraging steel produced by Selective Laser Melting. *Innovative Developments in Virtual and Physical Prototyping*, 297-304.
- [129] D. Galicki, F. List, S.S. Babu, A. Plotkowski, H.M. Meyer III, R. Seals and C. Hayes. Localized Changes of Stainless-Steel Powder Characteristics During Selective laser melting Additive Manufacturing, *Metallurgical and Materials transactions A* 50A (2019)1582-1605

- [130] <https://pdfs.semanticscholar.org/31fe/7c1b0344856e09bd5a7460781820c61362c3.pdf>
- [131] Q. Guo, C. Zhao, L. I Escano, Z. Young, L. Xiong, K. Fezzaa, W. Everhart, B. Brown, T. Sun, L. Chen..Transient dynamics of powder spattering in laser powder bed fusion additive manufacturing process revealed by in-situ high-speed highenergy x-ray imaging., *Acta Materialia* 151 (2018) 169-180.
- [132] M.J. Matthews, G. Guss, S.A. Khairallah, A.M. Rubenchik, P.J. Depond, W. E. King Denudation of metal powder layers in laser powder bed fusion. *Acta Materialia* 114 (2016) 33-42.
- [133] S. A. Khairallah, A.T. Anderson, A. Rubenchik, W.E. King. Laser powder-bed fusion additive manufacturing: Physics of complex melt flow and formation mechanisms of pores, spatter, and denudation zones. *Acta Materialia* 108 (2016) 36-45
- [134] A. V. Gusarov and E. P. Kovalev. Model of thermal conductivity in powder beds. *Physical Review B - Condensed Matter and Materials Physics*, 80(2) (2009):16–20
- [135] B. Zhang, L. Dembinski, C. Coddet. The study of the laser parameters and environment variables effect on mechanical properties of high compact parts elaborated by Selective laser melting 316L powder, *Materials Science & Engineering A* 584(2013)21–31.
- [136] M. Rombout, J.P. Kruth, L. Froyen and P. Mercelis, *Fundamentals of Selective laser melting of alloyed steel powders*. *CIRP Annals* 55(2006)187-192
- [137] Tang, P., Wang, S., Duan, H., Long, M., Li, Y., Fan, S., & Chen, D. (2020). The Formation of Humps and Ripples During Selective Laser Melting of 316l Stainless Steel. *JOM*, 72(3), 1128-1137.
- [138] Triantaphyllou, A., Giusca, C. L., Macaulay, G. D., Roerig, F., Hoebel, M., Leach, R. K., ... & Milne, K. A. (2015). Surface texture measurement for additive manufacturing. *Surface Topography: Metrology and Properties*, 3(2), 024002.
- [139] Lalehpour, A. (2017). *Modelling, inspection, and post-processing of layer-based additive manufacturing surfaces to maintain product quality* (Doctoral dissertation).
- [140] Barari, A., Kishawy, H. A., Kaji, F., & Elbestawi, M. A. (2017). On the surface quality of additive manufactured parts. *The International Journal of Advanced Manufacturing Technology*, 89(5-8), 1969-1974.
- [141] Frank, D., & Fadel, G. (1995). Expert system-based selection of the preferred direction of build for rapid prototyping processes. *Journal of Intelligent Manufacturing*, 6(5), 339-345.

- [142] Attarzadeh, F., Fotovvati, B., Fitzmire, M., & Asadi, E. (2020). Surface roughness and densification correlation for direct metal laser sintering. *The International Journal of Advanced Manufacturing Technology*, 107(5), 2833-2842.
- [143] Schwerz, C., Raza, A., Lei, X., Nyborg, L., Hryha, E., & Wirdelius, H. (2021). In-situ detection of redeposited spatter and its influence on the formation of internal flaws in laser powder bed fusion. *Additive Manufacturing*, 47, 102370.
- [144] Young, Z. A., Guo, Q., Parab, N. D., Zhao, C., Qu, M., Escano, L. I., ... & Chen, L. (2020). Types of spatter and their features and formation mechanisms in laser powder bed fusion additive manufacturing process. *Additive Manufacturing*, 36, 101438.
- [145] Gradl, P. Advanced and Additive Manufacturing Technologies for Liquid Rocket Engine Components. In *Liquid Rocket Engines: Emerging Technologies in Liquid Propulsion*.
- [146] Gradl, P. R., Greene, S. E., Protz, C., Bullard, B., Buzzell, J., Garcia, C., ... & Cooper, K. G. (2018). Additive manufacturing of liquid rocket engine combustion devices: a summary of process developments and hot-fire testing results. In *2018 Joint propulsion conference* (p. 4625).
- [147] Ho, J. Y., Leong, K. C., & Wong, T. N. (2020). Additively-manufactured metallic porous lattice heat exchangers for air-side heat transfer enhancement. *International Journal of Heat and Mass Transfer*, 150, 119262.
- [148] Kuhns, M. M., Nuechterlein, J., Iten, J., Rixon, G., Roberson, T., Polizzi, A., ... & Noble, J. (2019). PermiAM: Porous additively manufactured L-PBF flow property characterization for rocket engines. In *AIAA Propulsion and Energy 2019 Forum* (p. 4308).
- [149] Z. Wu, S.P. Narra, A. Rollett, Exploring the fabrication limits of thin-wall structures in a laser powder bed fusion process, *Int. J. Adv. Manuf. Technol.* 110 (1–2) (2020) 191–207
- [150] Ni, J., Ling, H., Zhang, S., Wang, Z., Peng, Z., Benyshek, C., ... & Khademhosseini, A. (2019). Three-dimensional printing of metals for biomedical applications. *Materials Today Bio*, 3, 100024.
- [151] Meena, V. K., Kumar, P., Kalra, P., & Sinha, R. K. (2021). Additive manufacturing for metallic spinal implants: A systematic review. *Annals of 3D Printed Medicine*, 3, 100021.
- [152] Matos, G. R. M. (2021). Surface roughness of dental implant and osseointegration. *Journal of Maxillofacial and Oral Surgery*, 20, 1-4.
- [153] Elias, C. N., & Meirelles, L. (2010). Improving osseointegration of dental implants. *Expert review of medical devices*, 7(2), 241-256

- [154] Albrektsson, T., & Wennerberg, A. (2019). On osseointegration in relation to implant surfaces. *Clinical implant dentistry and related research*, 21, 4-7.
- [155] Alla, R. K., Ginjupalli, K., Upadhyaya, N., Shammash, M., Ravi, R. K., & Sekhar, R. (2011). Surface roughness of implants: a review. *Trends in Biomaterials and Artificial Organs*, 25(3), 112-118.
- [156] https://www.odtmag.com/issues/2017-08-01/view_features/manufacturing-in-layers-3d-printings-impact-on-orthopedics/
- [157] <https://www.keyence.com/ss/products/microscope/roughness/surface/parameters.jsp>
- [158] [https://www.olympus-ims.com/en/metrology/surface-roughness-measurement-portal/evaluating-parameters/#!cms\[focus\]=01](https://www.olympus-ims.com/en/metrology/surface-roughness-measurement-portal/evaluating-parameters/#!cms[focus]=01)
- [159] Gadelmawla, E. S., Koura, M. M., Maksoud, T. M., Elewa, I. M., & Soliman, H. H. (2002). Roughness parameters. *Journal of materials processing Technology*, 123(1), 133-145.
- [160] Black, J. T., & Kohser, R. A. (2020). DeGarmo's materials and processes in manufacturing. John Wiley & Sons. Chapter 32-Surface integrity and finishing processes. Page 705-729.
- [161] ASME B46.1-2009 (Revision of ASME B46.1-2002) Surface Texture (Surface Roughness, Waviness, and Lay)
- [162] Choudhury, S. K., & Chinchani, S. (2016). 1.3 finish machining of hardened steel. *Comprehensive Materials Finishing*, 29, Pages 47-92.
- [163] Hong, M. H., Min, B. K., & Kwon, T. Y. (2016). The influence of process parameters on the surface roughness of a 3D-printed Co-Cr dental alloy produced via selective laser melting. *Applied Sciences*, 6(12), 401.
- [164] Charles, A., Elkaseer, A., Thijs, L., Hagenmeyer, V., & Scholz, S. (2019). Effect of process parameters on the generated surface roughness of down-facing surfaces in selective laser melting. *Applied Sciences*, 9(6), 1256.
- [165] Tian, Y., Tomus, D., Rometsch, P., & Wu, X. (2017). Influences of processing parameters on surface roughness of Hastelloy X produced by selective laser melting. *Additive Manufacturing*, 13, 103-112.
- [166] Baci, M. A., Baci, E. R., Bejinariu, C., Toma, S. L., Danila, A., & Baci, C. (2018, June). Influence of selective laser melting processing parameters of Co-Cr-W powders on the roughness of exterior surfaces. In *IOP Conference Series: Materials Science and Engineering* (Vol. 374, No. 1, p. 012010). IOP Publishing.

- [167] Wang, D., Liu, Y., Yang, Y., & Xiao, D. (2016). Theoretical and experimental study on surface roughness of 316L stainless steel metal parts obtained through selective laser melting. *Rapid Prototyping Journal*
- [168] Chen, Z., Wu, X., Tomus, D., & Davies, C. H. (2018). Surface roughness of selective laser melted Ti-6Al-4V alloy components. *Additive Manufacturing*, 21, 91-103.
- [169] Yadroitsev, I., & Smurov, I. (2011). Surface morphology in selective laser melting of metal powders. *Physics Procedia*, 12, 264-270.
- [170] Chen, Z., Cao, S., Wu, X., & Davies, C. H. (2019). Surface roughness and fatigue properties of selective laser melted Ti-6Al-4V alloy. In *Additive manufacturing for the aerospace industry* (pp. 283-299). Elsevier.
- [171] Mumtaz, K., & Hopkinson, N. (2009). Top surface and side roughness of Inconel 625 parts processed using selective laser melting. *Rapid Prototyping Journal*.
- [172] Spierings, A. B., Herres, N., & Levy, G. (2011). Influence of the particle size distribution on surface quality and mechanical properties in AM steel parts. *Rapid Prototyping Journal*, 17(3), 195-202.
- [173] Cheng, B.; Shrestha, S.; Chou, K. Stress and deformation evaluations of scanning strategy effect in selective laser melting. *Addit.Manuf.* 2016, 12, 240–251.
- [174] Paraschiv, A., Matache, G., Constantin, N., & Vladut, M. (2022). Investigation of Scanning Strategies and Laser Remelting Effects on Top Surface Deformation of Additively Manufactured IN 625. *Materials*, 15(9), 3198.
- [175] Matache, G.; Vladut, M.; Paraschiv, A.; Condruz, R.M. Edge and corner effects in selective laser melting of IN 625 alloy. *Manuf. Rev.* 2020, 7, 8.
- [176] Sames, W. J., List, F. A., Pannala, S., Dehoff, R. R., & Babu, S. S. (2016). The metallurgy and processing science of metal additive manufacturing. *International materials reviews*, 61(5), 315-360.
- [177] Yonehara, M., Kato, C., Ikeshoji, T. T., Takeshita, K., & Kyogoku, H. (2021). Correlation between surface texture and internal defects in laser powder-bed fusion additive manufacturing. *Scientific Reports*, 11(1), 22874.
- [178] Schneidau, K. (2020). An investigation of the effect of contour process parameters on the surface roughness and dimensionality of overhanging features in 17-4 stainless steel.

- [179] Wang, D., Lv, J., Wei, X., Lu, D., & Chen, C. (2023). Study on Surface Roughness Improvement of Selective Laser Melted Ti6Al4V Alloy. *Crystals*, 13(2), 306.
- [180] Deng, Y., Mao, Z., Yang, N., Niu, X., & Lu, X. (2020). Collaborative optimization of density and surface roughness of 316L stainless steel in selective laser melting. *Materials*, 13(7), 1601.
- [chapter 6-oxides reference]
- [181] Yang, X., Tang, F., Hao, X., & Li, Z. (2021). Oxide evolution during the solidification of 316L stainless steel from additive manufacturing powders with different oxygen contents. *Metallurgical and Materials Transactions B*, 52(4), 2253-2262
- [182] Kim, Y. K., Baek, M. S., Yang, S., & Lee, K. A. (2021). In-situ formed oxide enables extraordinary high-cycle fatigue resistance in additively manufactured CoCrFeMnNi high-entropy alloy. *Additive Manufacturing*, 38, 101832.
- [183] Artzt, K., Mishurova, T., Bauer, P. P., Gussone, J., Barriobero-Vila, P., Evsevlev, S., ... & Haubrich, J. (2020). Pandora's box—influence of contour parameters on roughness and subsurface residual stresses in laser powder bed fusion of Ti-6Al-4V. *Materials*, 13(15), 3348.
- [184] Louw, D. F., & Pistorius, P. G. H. (2019). The effect of scan speed and hatch distance on prior-beta grain size in laser powder bed fused Ti-6Al-4V. *The International Journal of Advanced Manufacturing Technology*, 103, 2277-2286.
- [185] Baci, A. M., Bejinariu, C., Corăbieru, A., Mihalache, E., Lupu-Poliac, M., Baci, C., & Baci, E. R. (2019, July). Influence of process parameters for Selective Laser Melting on the roughness of 3D printed surfaces in Co-Cr dental alloy powder. In *IOP Conference Series: Materials Science and Engineering* (Vol. 572, No. 1, p. 012054). IOP Publishing.
- [186] Mohammad, A., Al-Ahmari, A. M., AlFaify, A., & Mohammed, M. K. (2017). Effect of melt parameters on density and surface roughness in electron beam melting of gamma titanium aluminide alloy. *Rapid Prototyping Journal*, 23(3), 474-485.
- [187] Chen, H., Gu, D., Xiong, J., & Xia, M. (2017). Improving additive manufacturing processability of hard-to-process overhanging structure by selective laser melting. *Journal of Materials Processing Technology*, 250, 99-108.

- [188] Conlon, M. J., & Azari, K. (2018). Impact of powder size, size distribution and morphology on additive manufacturing. *Advances in Powder Metallurgy and Particulate Materials*, 745-754.
- [189] Balbaa, M. A., Ghasemi, A., Fereiduni, E., Elbestawi, M. A., Jadhav, S. D., & Kruth, J. P. (2021). Role of powder particle size on laser powder bed fusion processability of AlSi10Mg alloy. *Additive manufacturing*, 37, 101630.
- [190] Liu, Z., Wang, X., Kim, H., Zhou, Y., Cong, W., & Zhang, H. (2018). Investigations of energy density effects on forming accuracy and mechanical properties of Inconel 718 fabricated by LENS process. *Procedia Manufacturing*, 26, 731-739.
- [191] Bean, G. E., Witkin, D. B., McLouth, T. D., Patel, D. N., & Zaldivar, R. J. (2018). Effect of laser focus shift on surface quality and density of Inconel 718 parts produced via selective laser melting. *Additive Manufacturing*, 22, 207-215.
- [192] Yasa, E., Deckers, J., & Kruth, J. P. (2011). The investigation of the influence of laser re-melting on density, surface quality and microstructure of selective laser melting parts. *Rapid Prototyping Journal*, 17(5), 312-327.
- [193] Oter, Z. C., & Coskun, M. (2021). Effect of building platform position on the surface quality, dimensional accuracy, and geometrical precision of direct metal laser sintering (DMLS) parts. *Dimensional Accuracy, and Geometrical Precision of Direct Metal Laser Sintering (DMLS) Parts* (February 15, 2021).
- [194]. Jarfors, A.E.W.; Shashidhar, A.C.G.H.; Yepur, H.K.; Steggo, J.; Andersson, N.-E.; Stolt, R. Build Strategy and Impact Strength of SLM Produced Maraging Steel (1.2709). *Metals* 2021, 11, 51.
- [195]. Kruth, J.-P.; Badrossamay, M.; Yasa, E.; Deckers, J.; Thijs, L.; Van Humbeeck, J. Part and material properties in selective laser melting of metals. In *Proceedings of the 16th International Symposium on Electromachining (ISEM XVI)*, Shanghai, China, 19–23 April 2010.
- [196] Robinson, J. H., Ashton, I. R. T., Jones, E., Fox, P., & Sutcliffe, C. (2018). The effect of hatch angle rotation on parts manufactured using selective laser melting. *Rapid Prototyping Journal*, 25(2), 289-298.
- [197] Yasa, E.; Deckers, J.; Craeghs, T.; Badrossamay, M.; Kruth, J.-P. Investigation on occurrence of elevated edges in selective laser melting. In *Proceedings of the Twentieth Annual International Solid Freeform Fabrication Symposium*, Austin, TX, USA, 3–5 August 2009.

- [198] Jiang, J., Chen, J., Ren, Z., Mao, Z., Ma, X., & Zhang, D. Z. (2020). The influence of process parameters and scanning strategy on lower surface quality of TA15 parts fabricated by selective laser melting. *Metals*, 10(9), 1228.
- [199] Giganto, S., Martínez-Pellitero, S., Barreiro, J., Leo, P., & Castro-Sastre, M. Á. (2022). Impact of the laser scanning strategy on the quality of 17-4PH stainless steel parts manufactured by selective laser melting. *Journal of Materials Research and Technology*, 20, 2734-2747.
- [200] Miao, X., Liu, X., Lu, P., Han, J., Duan, W., & Wu, M. (2020). Influence of scanning strategy on the performances of GO-reinforced Ti6Al4V nanocomposites manufactured by SLM. *Metals*, 10(10), 1379.
- [201] Zhu, Y., Zou, J., & Yang, H. Y. (2018). Wear performance of metal parts fabricated by selective laser melting: a literature review. *Journal of Zhejiang University-SCIENCE A*, 19(2), 95-110.
- [202] Sun, Y., Moroz, A., & Alrbaey, K. (2014). Sliding wear characteristics and corrosion behaviour of selective laser melted 316L stainless steel. *Journal of materials engineering and performance*, 23, 518-526.
- [203] H. Lia, M. Ramezania, M. Li, C. Ma, J. Wang Tribological performance of selective laser melted 316L stainless steel *Tribol Int*, 128 (2018), pp. 121-129.
- [204] Kazemipour, M., Mohammadi, M., Mfoumou, E., & Nasiri, A. M. (2019). Microstructure and corrosion characteristics of selective laser-melted 316L stainless steel: the impact of process-induced porosities. *Jom*, 71, 3230-3240.
- [205] Rausch, A.M., Markl, M. and Körner, C., 2019. Predictive simulation of process windows for powder bed fusion additive manufacturing: Influence of the powder size distribution. *Computers & Mathematics with Applications*, 78(7), pp.2351-2359.
- [206] Kaji, F. and Barari, A., 2015. Evaluation of the surface roughness of additive manufacturing parts based on the modelling of cusp geometry. *IFAC-PapersOnLine*, 48(3), pp.658-663.
- [207] Taufik, M., & Jain, P. K. (2016). A study of build edge profile for prediction of surface roughness in fused deposition modeling. *Journal of Manufacturing Science and Engineering*, 138(6).
- [208] Özel, T., Altay, A., Kaftanoğlu, B., Leach, R., Senin, N., & Donmez, A. (2020). Focus Variation Measurement and Prediction of Surface Texture Parameters Using Machine Learning in Laser Powder Bed Fusion. *Journal of Manufacturing Science and Engineering*, 142(1).

- [209] Chen, Z., Wu, X., & Davies, C. H. (2021). Process variation in Laser Powder Bed Fusion of Ti-6Al-4V. *Additive Manufacturing*, 101987.
- [210] Delfs, P., Tows, M., & Schmid, H. J. (2016). Optimized build orientation of additive manufactured parts for improved surface quality and build time. *Additive Manufacturing*, 12, 314-320.
- [211] Rott, S., Ladewig, A., Friedberger, K., Casper, J., Full, M., & Schleifenbaum, J. H. (2020). Surface roughness in laser powder bed fusion—Interdependency of surface orientation and laser incidence. *Additive Manufacturing*, 36, 101437.
- [212] Galati, M., Rizza, G., Defanti, S., & Denti, L. (2021). Surface roughness prediction model for Electron Beam Melting (EBM) processing Ti6Al4V. *Precision Engineering*, 69, 19-28.
- [213] Bacchewar, P. B., Singhal, S. K., and Pandey, P. M., 2007, “Statistical Modelling and Optimization of Surface Roughness in the Selective Laser Sintering Process,”*Proc. Inst. Mech. Eng. B*, 221(1), pp. 35–52.
- [214] Campbell, R. I., Martorelli, M., and Lee, H. S., 2002, “Surface Roughness Visualization for Rapid Prototyping Models,” *Comput.-Aided Des.*, 34(10), pp. 717–725.
- [215] Strano, G., Hao, L., Everson, R. M., and Evans, K. E., 2013, “Surface Roughness Analysis,
- [216] British Standard: BS EN ISO 4288:1998, Geometrical Product Specifications (GPS)—Surface Texture: Profile Method—Rules and Procedures for the Assessment of Surface Texture.
- [217] ISO 25178-3,2012, Geometrical Product Specifications (GPS)—Surface Texture: Areal Part 3: Specification Operators
- [218] Cabanettes, F., Joubert, A., Chardon, G., Dumas, V., Rech, J., Grosjean, C. and Dimkovski, Z., 2018. Topography of as built surfaces generated in metal additive manufacturing: a multi scale analysis from form to roughness. *Precision Engineering*, 52, pp.249-265.
- [219] Newton, L., Senin, N., Chatzivagiannis, E., Smith, B. and Leach, R., 2020. Feature-based characterisation of Ti6Al4V electron beam powder bed fusion surfaces fabricated at different surface orientations. *Additive Manufacturing*, p.101273.
- [220] Thomas.T.R . "Characterization of surface roughness." *Precision Engineering* 3, no. 2 (1981): 97-104.
- [221] Chiffre. L. De, Lonardo. P, Trumpold. H, Lucca. D.A, Goch. G, Brown. C.A, Raja. J, and Hansen. H. N. "Quantitative characterization of surface texture." *CIRP Annals* 49, no. 2

- [222] Geometrical product specifications (GPS) — Surface texture: Profile method — Rules and procedures for the assessment of surface texture (ISO 4288:1996)
- [223] Tato, W., Blunt, L., Llavori, I., Aginagalde, A., Townsend, A., & Zabala, A. (2020). Surface integrity of additive manufacturing parts: a comparison between optical topography measuring techniques. *Procedia CIRP*, 87, 403-408.
- [224] Zhou, Y., Ning, F., Zhang, P., & Sharma, A. (2021). Geometrical, microstructural, and mechanical properties of curved-surface AlSi10Mg parts fabricated by powder bed fusion additive manufacturing. *Materials & Design*, 198, 109360.
- [225] Kozior, T., & Bochnia, J. (2020). The influence of printing orientation on surface texture parameters in powder bed fusion technology with 316L steel. *Micromachines*, 11(7), 639.
- [226] Snyder, J. C., Stimpson, C. K., Thole, K. A., & Mongillo, D. (2016). Build direction effects on additively manufactured channels. *Journal of Turbomachinery*, 138(5).
- [227] Gui, Y., Aoyagi, K., Bian, H., & Chiba, A. (2022). Detection, classification and prediction of internal defects from surface morphology data of metal parts fabricated by powder bed fusion type additive manufacturing using an electron beam. *Additive Manufacturing*, 54, 102736.
- [228] Sidambe, A.T., 2017. Three-dimensional surface topography characterization of the electron beam melted Ti6Al4V. *Metal powder report*, 72(3), pp.200-205.
- [229] Ullah, R., Akmal, J.S., Laakso, S.V. and Niemi, E., 2020. Anisotropy of additively manufactured AlSi10Mg: threads and surface integrity. *The International Journal of Advanced Manufacturing Technology*, pp.1-18.
- [230] Alfieri, V., Argenio, P., Caiazzo, F., & Sergi, V. (2016). Reduction of surface roughness by means of laser processing over additive manufacturing metal parts. *Materials*, 10(1), 30.
- [231] Wan, H. Y., Luo, Y. W., Zhang, B., Song, Z. M., Wang, L. Y., Zhou, Z. J., ... & Zhang, G. P. (2020). Effects of surface roughness and build thickness on fatigue properties of selective laser melted Inconel 718 at 650° C. *International Journal of Fatigue*, 137, 105654.
- [232] Yan, X., Gao, S., Chang, C., Huang, J., Khanlari, K., Dong, D., ... & Liu, M. (2021). Effect of building directions on the surface roughness, microstructure, and tribological properties of selective laser melted Inconel 625. *Journal of Materials Processing Technology*, 288, 116878.
- [233] Udrioiu, R., Braga, I. C., & Nedelcu, A. (2019). Evaluating the quality surface performance of additive manufacturing systems: Methodology and a material jetting case study. *Materials*, 12(6), 995.

- [234] Dalgarno, K. Materials research to support high-performance RM parts. At Rapid manufacturing 2nd international conference, Loughborough University
- [235] D. N. Aqilah, Y. Farazila, D. Y. Suleiman, M. A. N. Amira, & W. B. W. N. Izzati, (2018). Effects of process parameters on the surface roughness of stainless steel 316L parts produced by selective laser melting. *Journal of Testing and Evaluation*, 46(4), 1673-1683.
- [236] Tian, Y., Tomus, D., Huang, A., & Wu, X. (2019). Experimental and statistical analysis on process parameters and surface roughness relationship for selective laser melting of Hastelloy X. *Rapid Prototyping Journal*.
- [237] Cao, L., Li, J., Hu, J., Liu, H., Wu, Y., & Zhou, Q. (2021). Optimization of surface roughness and dimensional accuracy in LPBF additive manufacturing. *Optics & Laser Technology*, 142, 107246.
- [238] Zhu, Z., Lou, S., & Majewski, C. (2020). Characterisation and correlation of areal surface texture with processing parameters and porosity of High-Speed Sintered parts. *Additive Manufacturing*, 36, 101402.
- [239] Vilaro, T., Colin, C., & Bartout, J. D. (2011). As-fabricated and heat-treated microstructures of the Ti-6Al-4V alloy processed by selective laser melting. *Metallurgical and materials transactions A*, 42(10), 3190-3199.
- [240] Gong, H., Rafi, K., Gu, H., Starr, T., & Stucker, B. (2014). Analysis of defect generation in Ti-6Al-4V parts made using powder bed fusion additive manufacturing processes. *Additive Manufacturing*, 1, 87-98.
- [241] Cherry, J. A., Davies, H. M., Mehmood, S., Lavery, N. P., Brown, S. G. R., & Sienz, J. (2015). Investigation into the effect of process parameters on microstructural and physical properties of 316L stainless steel parts by selective laser melting. *The International Journal of Advanced Manufacturing Technology*, 76(5), 869-879.
- [242] Haboudou, A., Peyre, P., Vannes, A. B., & Peix, G. (2003). Reduction of porosity content generated during Nd: YAG laser welding of A356 and AA5083 aluminium alloys. *Materials Science and Engineering: A*, 363(1-2), 40-52.
- [243] Qingsong, Z. S. G. U. I. R. W. E., & Yusheng, S. H. I. (2013). Cracking behavior and formation mechanism of TC4 alloy formed by selective laser melting. *Journal of Mechanical Engineering*, 49(23), 23.

- [244] Li, R., Shi, Y., Wang, Z., Wang, L., Liu, J., & Jiang, W. (2010). Densification behavior of gas and water atomized 316L stainless steel powder during selective laser melting. *Applied surface science*, 256(13), 4350-4356.
- [245] Gu, D., & Shen, Y. (2009). Balling phenomena in direct laser sintering of stainless-steel powder: Metallurgical mechanisms and control methods. *Materials & Design*, 30(8), 2903-2910.
- [246] G. Dursun, S. Ibekwe, G. Li, P. Mensah, G. Joshi and D. Jerro, "Influence of laser processing parameters on the surface characteristics of 316L stainless steel manufactured by selective laser melting." *Materials Today: Proceedings* 26 (2020): 387-393.
- [247] Karimi, P., Raza, T., Andersson, J., & Svensson, L. E. (2018). Influence of laser exposure time and point distance on 75- μ m-thick layer of selective laser melted Alloy 718. *The International Journal of Advanced Manufacturing Technology*, 94(5), 2199-2207.
- [248] Sinico, M., Metelkova, J., Dalemans, T., Thijs, L., & Van Hooreweder, B. (2022). High speed laser powder bed fusion of M789 tool steel with an optimized 120 μ m layer thickness approach. *Procedia CIRP*, 111, 162-165.
- [249] Qiu, C., Ward, M., Basoalto, H. C., Brooks, J. W., & Attallah, M. M. (2015). On the role of melt flow into the surface structure and porosity development during selective laser melting. *Acta Materialia*, 96, 72-79.
- [250] Montgomery, D. C. (2017). *Design and analysis of experiments*. John Wiley & sons.
- [251] Camposeco-Negrete, C. (2013). Optimization of cutting parameters for minimizing energy consumption in turning of AISI 6061 T6 using Taguchi methodology and ANOVA. *Journal of Cleaner Production*, 53, 195-203.
- [252] <https://www.investopedia.com/terms/a/anova.asp#:~:text=Analysis%20of%20variance%2C%20or%20ANOVA,the%20dependent%20and%20independent%20variables.>
- [253] <https://www.simplypsychology.org/anova.html>
- [254] Q. Zhang, H. Xue, Q. Tang, S. Pan, M. Rettenmayr, M. Zhu, "Microstructural evolution during temperature gradient zone melting: Cellular automaton simulation and experiment." *Computational Materials Science* 146 (2018): 204-212.
- [255] Tan, C., Zhou, K., Kuang, M., Ma, W., & Kuang, T. (2018). Microstructural characterization and properties of selective laser melted maraging steel with different build directions. *Science and technology of advanced materials*, 19(1), 746-758.

- [256] C.Tan, K. Zhou, W. Ma, P.Zhang, M. Liu, T. Kuang. Microstructural evolution, nanoprecipitation behavior and mechanical properties of selective laser melted high-performance grade 300 maraging steel. *Materials and Design* 134 (2017) 23–34.
- [257] Barrionuevo, G. O., Ramos-Grez, J. A., Walczak, M., Sánchez-Sánchez, X., Guerra, C., Debut, A., & Haro, E. (2022). Microstructure simulation and experimental evaluation of the anisotropy of 316 L stainless steel manufactured by laser powder bed fusion. *Rapid Prototyping Journal*, (ahead-of-print).
- [258] J. Boes, A. Röttger, C. Mutke, C. Escher, W. Theisen. Microstructure and mechanical properties of X65MoCrWV3-2 cold-work tool steel produced by Selective laser melting, *Additive Manufacturing* 23 (2018) 170–180
- [259] T. Kurzynowski, K. Gruber, W. Stopyra, B. Kuźnicka, E. Chlebus, Correlation between process parameters, microstructure and properties of 316 L stainless steel processed by Selective laser melting, *Materials Science & Engineering A* 718 (2018) 64–73
- [260] Y.M. Wang, T. Voisin, J.T. McKeown, J. Ye, N.P. Calta, Z. Li, Z. Zeng, Y. Zhang, W. Chen, T.T. Roehling, R.T. Ott, M.K. Santala, P.J. Depond, M.J. Matthews, A. V. Hamza, T. Zhu, additively manufactured hierarchical stainless steels with high strength and ductility, *Nat. Mater.* 17 (2018) 63–70.
- [261] K.P. Davidson, S.B. Singamneni. Metallographic evaluation of duplex stainless-steel powders processed by Selective laser melting", *Rapid Prototyping Journal*, Vol. 23(2017), pp.1146-1163.
- [262] F. Feuerhahna, A. Schulzb, T. Seefeldt, F. Vollertsena. Microstructure and properties of selective laser melted high hardness tool steel *Physics Procedia* 41 (2013) 843 – 848
- [263] M. Wei, S. Chen, L. Xi, J. Liang, C. Liu S. Selective laser melting of 24CrNiMo steel for brake disc: Fabrication efficiency, microstructure evolution, and properties. *Optics and Laser Technology* 107 (2018) 99–109
- [264] R. Casati, M. Coduri, N. Lecis, C. Andrianopoli, M. Vedani. Microstructure and mechanical behavior of hot-work tool steels processed by Selective laser melting. *Materials Characterization* 137 (2018) 50–57
- [265] E. Yasa, J.P Kruth. Microstructural investigation of Selective laser melting 316L stainless steel parts exposed to laser re-melting., *Procedia Engineering* 19 (2011) 389 – 395.

- [266] H. Yu, J. Yang, J. Yin, Z. Wang, X. Zeng, Comparison on mechanical anisotropies of selective laser melted Ti-6Al-4V alloy and 304 stainless steel, *Mater. Sci. Eng. A* 695 (2017) 92–100.
- [267] J. Suryawanshi, K.G. Prashanth, U. Ramamurty, Mechanical behavior of selective laser melted 316L stainless steel, *Mater. Sci. Eng. A* 696 (2017) 113–121
- [268] Y. Zhong, L. Liu, S. Wikman, D. Cui, Z. Shen, Intragranular cellular segregation network structure strengthening 316L stainless steel prepared by Selective laser melting, *J. Nucl. Mater.* 470 (2016) 170–178,
- [269] P.G.E. Jerrard, L. Hao, K.E. Evans, Experimental investigation into Selective laser melting of austenitic and martensitic stainless-steel powder mixtures, *Proc. Inst. Mech. Eng. B J. Eng. Manuf.* 223 (2009) 1409–1416,
- [270] K. Abd-Elghany, D.L. Bourell, Property evaluation of 304L stainless steel fabricated by Selective laser melting, *Rapid Prototyp. J.* 18 (2012) 420–428.
- [271] T. Niendorf, S. Leuders, A. Riemer, H.A. Richard, T. Troster, D. Schwarze, highly anisotropic steel processed by Selective laser melting, *Metall. Mater. Trans. B* 44 (2013) 794–796,
- [272] S. Gorsse, C. Hutchinson, M. Goune, R. Banerjee, Additive manufacturing of metals: a brief review of the characteristic microstructures and properties of steels, Ti-6Al-4V and high-entropy alloys, *Sci. Technol. Adv. Mater.* 18 (2017) 584–610.
- [273] Z. Sun, X. Tan, S.B. Tor, C.K. Chua, Simultaneously enhanced strength and ductility for 3D-printed stainless steel 316L by Selective laser melting, *NPG Asia Mater.* 10 (2018) 127–136,
- [274] S.-H. Sun, T. Ishimoto, K. Hagihara, Y. Tsutsumi, T. Hanawa, T. Nakano, Excellent mechanical and corrosion properties of austenitic stainless steel with a unique crystallographic lamellar microstructure via Selective laser melting, *Scr. Mater.* 159 (2019) 89–93
- [275] M. Shamsujjoha, S.R. Agnew, J.M. Fitz-Gerald, W.R. Moore, T.A. Newman, High strength and ductility of additively manufactured 316L stainless steel explained, *Metall. Mater. Trans. A* 49 (2018) 3011–3027,
- [276] E.A. Jagle, Z. Sheng, P. Kürsteiner, S. Oclok, A. Weisheit, D. Raabe, Comparison of maraging steel micro- and nanostructure produced conventionally and by Laser Additive Manufacturing, *Materials* 10 (2017),
- [277] W. Sha, Z. Guo, *Maraging Steels: Modelling of Microstructure, Properties and Applications*, CRC Press, New York, 2009,

- [278] B. Ren, D. Lu, R. Zhou, Z. Li, J. Guan, Preparation and mechanical properties of selective laser melted H13 steel, *J. Mater. Res.* (2019) 1–11
- [279] L. Facchini, N. Vicente, I. Lonardelli, E. Magalini, P. Robotti, A. Molinari, Metastable Austenite in 17-4 precipitation-hardening stainless steel produced by Selective laser melting, *Adv. Eng. Mater.* 12 (2010) 184–188.
- [280] B. Clausen, D.W. Brown, J.S. Carpenter, K.D. Clarke, A.J. Clarke, S.C. Vogel, J. D. Bernardin, D. Spornjak, J.M. Thompson, Deformation behavior of additively manufactured GP1 stainless steel, *Mater. Sci. Eng. A* (2017),
- [281] Y. Sun, R.J. Hebert, M. Aindow, Effect of heat treatments on microstructural evolution of additively manufactured and wrought 17-4PH stainless steel, *Mater. Des.* 156 (2018) 429–440,
- [282] C. Haase, J. Bültmann, J. Hof, S. Ziegler, S. Bremen, C. Hinke, A. Schwedt, U. Prah, W. Bleck, C. Haase, J. Bültmann, J. Hof, S. Ziegler, S. Bremen, C. Hinke, A. Schwedt, U. Prah, W. Bleck, exploiting process-related advantages of Selective laser melting for the production of high-manganese steel, *Materials* 10 (2017) 56,
- [283] J.C. Walker, K.M. Berggreen, A.R. Jones, C.J. Sutcliffe, Fabrication of Fe-Cr-Al oxide dispersion strengthened PM2000 alloy using Selective laser melting, *Adv. Eng. Mater.* 11 (2009) 541–546,
- [284] T. Boegelein, S.N. Dryepont, A. Pandey, K. Dawson, G.J. Tatlock, Mechanical response and deformation mechanisms of ferritic oxide dispersion strengthened steel structures produced by Selective laser melting, *Acta Mater.* 87 (2015) 201–215.
- [285] G.J. Tatlock, K. Dawson, T. Boegelein, K. Moustoukas, A.R. Jones, High resolution microstructural studies of the evolution of nano-scale, yttrium-rich oxides in ODS steels subjected to ball milling, Selective laser melting or friction stir welding, *Mater. Today Proc.* 3 (2016) 3086–3093,
- [286] R.M. Hunt, K.J. Kramer, B. El-dasher, Selective laser sintering of MA956 oxide dispersion strengthened steel, *J. Nucl. Mater.* 464 (2015) 80–85,
- [287] E. Vasqueza, P.F. Giroux, F. Lomello, A. Chniouel, H. Maskrotb, F. Schuster, P. Castanyd. Elaboration of oxide dispersion strengthened Fe-14Cr stainless steel by Selective laser melting. *Journal of Materials Processing Tech.* 267 (2019) 403–413

- [288] I. Yadroitseva, P. Krakhmalev, I. Yadroitsava, S. Johansson, I. Smurov. Energy input effect on morphology and microstructure of Selective laser melting single track from metallic powder *Journal of Materials Processing Technology* 213 (2013) 606– 613
- [289] A.Yadollahi ,N. Shamsaei, S.M Thompson , A Elwany ,L. Bian . Effects of building orientation and heat treatment on fatigue behavior of selective laser melted 17-4 PH stainless steel. *Int J Fatigue* 94(2017):218–235.
- [290] Y.J. Yin, J.Q. Sun, J. Guo, X.F. Kan, D.C. Yang, Mechanism of high yield strength and yield ratio of 316 L stainless steel by additive manufacturing, *Mater. Sci. Eng. A* 744 (2019) 773–777,
- [291] K. Saeidi, X. Gao, Y. Zhong, Z.J.J. Shen, Hardened austenite steel with columnar sub-grain structure formed by laser melting, *Mater. Sci. Eng. A* 625 (2014) 221–229,
- [292] K. Guan, Z. Wang, M. Gao, X. Li, X. Zeng, Effects of processing parameters on tensile properties of selective laser melted 304 stainless steel, *Mater. Des.* 50 (2013) 581–586,
- [293] J.J. Lewandowski, M. Seifi, Metal additive manufacturing: a review of mechanical properties, *Annu. Rev. Mater. Res.* 4614 (2016).
- [294] X. Lou, P.L. Andresen, R.B. Rebak, Oxide inclusions in laser additive manufactured stainless steel and their effects on impact toughness and stress corrosion cracking behavior, *J. Nucl. Mater.* 499 (2018) 182–190,
- [295] H.D. Carlton, A. Haboub, G.F. Gallegos, D.Y. Parkinson, A.A. MacDowell, Damage evolution and failure mechanisms in additively manufactured stainless steel, *Mater. Sci. Eng. A* 651 (2016) 406–414,
- [296] K. Saeidi, S. Alvi, F. Lofaj, V.I. Petkov, F. Akhtar, Advanced mechanical strength in post heat treated SLM 2507 at room and high temperature promoted by hard/ ductile sigma precipitates, *Metals* 9 (2019) 199
- [297] S.D. Meredith, J.S. Zuback, J.S. Keist, T.A. Palmer, Impact of composition on the heat treatment response of additively manufactured 17–4 PH grade stainless steel, *Mater. Sci. Eng. A* 738 (2018) 44–56,
- [298] Sabooni, S., Chabok, A., Feng, S. C., Blaauw, H., Pijper, T. C., Yang, H. J., & Pei, Y. T. (2021). Laser powder bed fusion of 17–4 PH stainless steel: A comparative study on the effect of heat treatment on the microstructure evolution and mechanical properties. *Additive Manufacturing*, 46, 102176.

- [299] Z. Guo, J.T. Kindt, Partitioning of size-mismatched impurities to grain boundaries in 2d solid hard-sphere monolayers, *Langmuir* 34 (2018) 12947–12956
- [300] K. Kempen, E. Yasa, L. Thijs, J.-P. Kruth, J. Van Humbeeck. Microstructure and mechanical properties of selective laser melted 18Ni-300 steel, *Phys. Procedia* 12(2011) 255–263.
- [301] T. Becker, D. Dimitrov, the achievable mechanical properties of SLM produced Maraging Steel 300 components, *Rapid Prototyp. J.* 22 (2016) 487–494.
- [302] J. Safka, M. Ackermann, L. Voleský, Structural properties of H13 tool steel parts produced with use of Selective laser melting technology, *J. Phys. Conf. Ser.* 709 (2016).
- [303] B. Ren, D. Lu, R. Zhou, Z. Li, J. Guan, Preparation and mechanical properties of selective laser melted H13 steel, *J. Mater. Res.* (2019) 1–11.
- [304] R. Dorfert, J. Zhang, B. Clausen, H. Freiße, J. Schumacher, F. Vollertsen, Comparison of the fatigue strength between additively and conventionally fabricated tool steel 1.2344, *Addit. Manuf.* 27 (2019) 217–223.
- [305] R.Mertens, B. Vrancken, N. Holmstock, Y. Kinds, J.-P. Kruth, J. Van Humbeeck. Influence of powder bed preheating on microstructure and mechanical properties of H13 tool steel SLM parts, *Phys. Procedia* 83 (2016) 882–890
- [306] M. Mazur, P. Brincat, M. Leary, M. Brandt, Numerical and experimental evaluation of a conformally cooled H13 steel injection mould manufactured with Selective laser melting, *Int. J. Adv. Manuf. Technol.* 93 (2017) 881–900,
- [307] M.J. Holzweissig, A. Taube, F. Brenne, M. Schaper, T. Niendorf, Microstructural characterization and mechanical performance of hot work tool steel processed by Selective laser melting, *Metall. Mater. Trans. B Process Metall. Mater. Process. Sci.* 46 (2015) 545–549,
- [308] M. L Montero-Sistiaga, M.Godino-Martinez, K. Boschmans, J-P Kruth, J.V Humbeeck, K. Vanmeensel. Microstructure evolution of 316L produced by HP-SLM (high power Selective laser melting, *Additive Manufacturing* 23 (2018) 402–410
- [309] M. Mahmoudi, A. Elwany, A. Yadollahi, S. M. Thompson, L. Bian, N. Shamsaei, "Mechanical properties and microstructural characterization of selective laser melted 17-4 PH stainless steel", *Rapid Prototyping Journal* 23(2017) pp.280-294

- [310] X. Yan, C. Chen, R. Zhao, W. Ma, R. Bolot, J. Wang, Z. Ren, H. Liao, M. Liu. "Selective laser melting of WC reinforced maraging steel 300: Microstructure characterization and tribological performance." *Surface and Coatings Technology* 371 (2019): 355-365.
- [311] S. Pasebani, M. Ghayoor, S. Badwe, H. Irrinki, S.V. Atre Effects of atomizing media and post processing on mechanical properties of 17-4 PH stainless steel manufactured via Selective laser melting, *Additive Manufacturing* 22 (2018) 127–137
- [312] Y. Zhu, T. Peng, G. Jia, H. Zhang, S. Xu, H. Yang. Electrical energy consumption and mechanical properties of selectivelaser-melting-produced 316L stainless steel samples using various processing parameters, *Journal of Cleaner Production* 208 (2019) 77-85
- [313] M S I N Kamariah, W S W Harun, N Z Khalil, F Ahmad, M H Ismail, S.Sharif .Effect of heat treatment on mechanical properties and microstructure of Selective laser melting 316L stainless steel *Materials Science and Engineering* 257 (2017) 012021
- [314] Y. Zhai, B. Huang, X. Mao, M.Zheng. Effect of hot isostatic pressing on microstructure and mechanical properties of CLAM steel produced by Selective laser melting, *Journal of Nuclear Materials* 515 (2019) 111-121
- [315] O.O. Salmana, C. Gammerb, A.K. Chaubeyc, J. Eckertb,d, S. Scudino Effect of heat treatment on microstructure and mechanical properties of 316L steel synthesized by Selective laser melting, , *Materials Science & Engineering A* 748 (2019) 205–212
- [316] H. Azizi, R. Ghiaasiaan, R. Prager, M.H. Ghoncheh, Khaled Abu Samk, Ante Lausic, Wes Byleveld, A.B. Phillion Metallurgical and Mechanical Assessment of Hybrid Additively-Manufactured Maraging Tool Steels via Selective laser melting.
- [317] J-P. Kruth, P. Mercelis, J. Van Vaerenbergh, L. Froyen, M. Rombouts, "Binding mechanisms in selective laser sintering and Selective laser melting", *Rapid Prototyping Journal*.11 (2005), pp.26-36
- [318] P. Miroslav, T. Pavlína,H. Jana, S. Pavel, K. Boivie . A study of Selective laser melting technology on the ultra-high strength tool steel use—quality, mechanical properties and fatigue. *Applied mechanics, behavior of materials, and engineering systems*, El- Qued. 2016
- [319] TS Srivatsan, TS Sudarshan. *Additive manufacturing: innovations, advances, and applications*. New York: CRC Press; 2015

- [320] H.A Stoffregen, K. Butterweck, E Abele. Fatigue analysis in Selective laser melting: review and investigation of thin-walled actuator housings. Proceedings of the 25th solid freeform fabrication symposium, Austin. 2014.
- [321] J Lai, H Huang, W Busing. Effects of microstructure and surface roughness on the fatigue strength of high-strength steels. *Procedia Struct Integrity* 2(2016):1213–1220.
- [322] E Uhlmann, C Fleck, G Gerlitzky, F Faltin. Dynamical fatigue behavior of additive manufactured products for a fundamental life cycle approach. *Procedia CIRP* 61 (2017) 588 – 593.
- [323] A.B. Spierings, T.L. Starr, K. Wegener. Fatigue performance of additive manufactured metallic parts. *Rapid Prototyping Journal*, 19(2013) 88-94.
- [324] A. Riemer, S Leuders, M Thöne, H.A Richard, T Tröster, T Niendorf. On the fatigue crack growth behavior in 316L stainless steel manufactured by Selective laser melting. *Eng Fract Mech* 120(2014)15–25.
- [325] J Suryawanshi, K.G Prashanth, U Ramamurty. Tensile, fracture, and fatigue crack growth properties of a 3d printed maraging steel through Selective laser melting. *J Alloys Compd* 725(2017) 355–364.
- [326] G. Ziółkowski, E. Chlebus, P. Szymczyk, J. Kurzac. Application of X-ray CT method for discontinuity and porosity detection in 316L stainless steel parts produced with SLM technology. *Archiv Civ Mech Eng* 14((2014):608–614.
- [327] R. Shrestha, J. Simsiriwong, N. Shamsaei, S.M Thompson, L. Bian. Effect of build orientation on the fatigue behavior of stainless steel 316L manufactured via laser powder bed fusion process. 27th Annual solid freeform fabrication symposium proceedings, Austin. 2016.
- [328] B Blinn, M. Klein, C. Gläßner, M. Smaga, JC Aurich, T Beck. An investigation of the microstructure and fatigue behavior of additively manufactured AISI 316L stainless steel with regard to the influence of heat treatment. *Metals* 8(4) (2018)1–23.
- [329] B. Blinn, M. Klein, T. Beck. Determination of the anisotropic fatigue behaviour of additively manufactured structures with short-time procedure PhyBal. *MATEC web of conferences*. 2018
- [330] L. Carneiro, B. Jalalahmadi, A. Ashtekar, Y. Jiang, Cyclic deformation and fatigue behavior of additively manufactured 17–4 PH stainless steel, *Int. J. Fatigue* 123 (2019) 22–30,
- [331] P.D. Nezhadfar, R. Shrestha, N. Phan, N. Shamsaei, Fatigue behavior of additively manufactured 17-4 PH stainless steel: synergistic effects of surface roughness and heat treatment, *Int. J. Fatigue* 124 (2019) 188–204.

- [332] P.D. Nezhadfar, E. Burford, K. Anderson-Wedge, B. Zhang, S. Shao, S. R. Daniewicz, N. Shamsaei, Fatigue crack growth behavior of additively manufactured 17-4 PH stainless steel: effects of build orientation and microstructure, *Int. J. Fatigue* (2019),
- [333] D. Croccolo, M. De Agostinis, S. Fini, G. Olmi, A. Vranic, S. Ciric-Kostic, Influence of the build orientation on the fatigue strength of EOS maraging steel produced by additive metal machine, *Fatigue Fract. Eng. Mater. Struct.* 39 (2016) 637–647.
- [334] G.Q. Yin, X. Kang, G.P. Zhao, Fatigue properties of the ultra-high strength steel TM210A, *Materials* 10 (2017),
- [335] Q. Chen, T. Nagano, Y. Nakamura, Y. Maeda, N. Kawagoishi, Initiation and propagation behavior of a fatigue crack of maraging steel in high humidity, in: 13th Int. Conf. Fract., 2013
- [336] M. Zhang, C.N Sun, X. Zhang, P.C Goh, J. Wei, H. Li, et al. Elucidating the relations between monotonic and fatigue properties of laser powder bed fusion stainless steel 316L. *JOM* 70(3) (2018):390–5.
- [337] M. Zhang, C.N Sun, X. Zhang, P.C Goh, J. Wei, D. Hardacre, et al. Fatigue and fracture behaviour of laser powder bed fusion stainless steel 316L: influence of processing parameters. *Mater Sci Eng, A* 703 (2017)251–261.
- [338] Tullis, R., Dunn, A., Young, D., Klingbeil, N., & Gockel, J. (2023). Additive Manufacturing Bulk Parameter's Influence on Surface Roughness, Microstructure, and Fatigue. *JOM*, 75(6), 1975-1981.
- [339] Shrestha, R., Simsiriwong, J., Shamsaei, N., Thompson, S. M., & Bian, L. (2016). Effect of build orientation on the fatigue behavior of stainless steel 316L manufactured via a laser-powder bed fusion process. In 2016 International Solid Freeform Fabrication Symposium. University of Texas at Austin.
- [340] Crenn, M. J., Benoit, A., Rohman, G., Guilbert, T., Fromentin, O., Attal, J. P., & Bardet, C. (2022). Selective laser melted titanium alloy for transgingival components: influence of surface condition on fibroblast cell behaviour. *Journal of Prosthodontics*, 31(1), 50-58.
- [341] Liang, X., Hor, A., Robert, C., Salem, M., Lin, F., & Morel, F. (2022). High cycle fatigue behavior of 316L steel fabricated by laser powder bed fusion: Effects of surface defect and loading mode. *International Journal of Fatigue*, 160, 106843.

- [342] S. Bodziak, K. S. Al-Rubaie, L. D Valentina, F.H Lafratta, E.C Santos, A.M Zanatta, Y.Chen
Precipitation in 300 grade maraging steel built by Selective laser melting: Aging at 510 °C for 2
h, *Materials Characterization* 151 (2019) 73–83
- [343] F.F Conde, J. D. Escobar, J.P. Oliveira, M. Béreš, A.L. Jardini, W.W. Bose, J.A. Avila.
Effect of thermal cycling and aging stages on the microstructure and bending strength of a selective
laser melted 300-grade maraging steel
- [344] S. Yin, C. Chen, X. Yan, X Feng, R. Jenkins, P. O'Reilly, M. Liu, H. Li, R. Lupoi. The
influence of aging temperature and aging time on the mechanical and tribological properties of
selective laser melted maraging 18Ni-300 steel. *Additive Manufacturing* 22 (2018) 592–600
- [345] Y. Kaynak, O. Kitay. The effect of post-processing operations on surface characteristics of
316L stainless steel produced by Selective laser melting, *Additive Manufacturing* 26 (2019) 84–
93
- [346] B. Song, S. Dong, Q. Liu, H. Liao, C. Coddet. Vacuum heat treatment of iron parts produced
by Selective laser melting: Microstructure, residual stress and tensile behavior. *Materials and
Design* 54 (2014) 727–733
- [347] C. Elangeswaran, A. Cutolo, G. K Muralidharan, C. de Formanoir, F. Berto, K. Vanmeensel,
B. V. Hooreweder. Effect of post-treatments on the fatigue behaviour of 316L stainless steel
manufactured by laser powder bed fusion, *International Journal of Fatigue* 123 (2019) 31–39.
- [348] Haghdadi, N., Laleh, M., Moyle, M., & Primig, S. (2021). Additive manufacturing of steels:
a review of achievements and challenges. *Journal of Materials Science*, 56(1), 64-107.
- [349] Brenne, F., Taube, A., Pröbstle, M., Neumeier, S., Schwarze, D., Schaper, M., & Niendorf,
T. (2016). Microstructural design of Ni-base alloys for high-temperature applications: impact of
heat treatment on microstructure and mechanical properties after selective laser melting. *Progress
in Additive Manufacturing*, 1(3), 141-151.
- [350] Teo, A. Q. A., Yan, L., Chaudhari, A., & O'Neill, G. K. (2021). Post-processing and surface
characterization of additively manufactured stainless steel 316l lattice: Implications for biomedical
use. *Materials*, 14(6), 1376.
- [351] Denti, L., & Sola, A. (2019). On the effectiveness of different surface finishing techniques
on A357. 0 parts produced by laser-based powder bed fusion: surface roughness and fatigue
strength. *Metals*, 9(12), 1284.

- [352] Melia, M. A., Duran, J. G., Koepke, J. R., Saiz, D. J., Jared, B. H., & Schindelholz, E. J. (2020). How build angle and post-processing impact roughness and corrosion of additively manufactured 316L stainless steel. *npj Materials Degradation*, 4(1), 21.
- [353] <https://resources.renishaw.com/en/details/data-sheet-ss-316l-0407-powder-for-additive-manufacturing--90802>
- [354] Metelkova, J.; de Formanoir, C.; Haitjema, H; Witvrouw, A.; Pfleging, W.; Hooreweder, B.V. Elevated edges of metal parts produced by laser powder bed fusion: Characterisation and post-process correction. In *Proceedings of the Joint Special Interest Group Meeting between Euspen and ASPE Advancing Precision in Additive Manufacturing*, Nantes, France, 21–23 September 2019.
- [355] Yasa, E., & Kruth, J. P. (2011). Microstructural investigation of Selective Laser Melting 316L stainless steel parts exposed to laser re-melting. *Procedia Engineering*, 19, 389-395.
- [356] Yasa, E., Kruth, J. P., & Deckers, J. (2011). Manufacturing by combining selective laser melting and selective laser erosion/laser re-melting. *CIRP annals*, 60(1), 263-266.
- [356] Ukar, E., Lamikiz, A., Lopez De Lacalle, L. N., Del Pozo, D., Liebana, F., & Sanchez, A. (2010). Laser polishing parameter optimisation on selective laser sintered parts. *International Journal of Machining and Machinability of Materials*, 8(3-4), 417-432.
- [358] Kruth, J. P., Badrossamay, M., Yasa, E., Deckers, J., Thijs, L., & Van Humbeeck, J. (2010). Part and material properties in selective laser melting of metals. In *Proceedings of the 16th International Symposium on Electromachining (ISEM XVI)* (pp. 3-14). Shanghai Jiao Tong Univ Press.
- [359] Kruth, J. P., Deckers, J., & Yasa, E. (2008). Experimental investigation of laser surface remelting for the improvement of selective laser melting process. In *Proceedings of the 19th Solid Freeform Fabrication Symposium* (pp. 321-332).
- [360] Liu, D.; Yue, W.; Kang, J.; Wang, C. Effect of Laser Remelting Strategy on the Forming Ability of Cemented Carbide Fabricated by Laser Powder Bed Fusion (L-PBF). *Materials* 2022, 15, 2380.
- [361] <https://www.alicon.com/en>
- [362] <https://www.alicon.com/en/technologies/focus-variation>
- [363] [58] <https://www.digitalsurf.com/software-solutions/profilometry/>

- [364] Lou, S., Jiang, X., Sun, W., Zeng, W., Pagani, L. and Scott, P.J., 2019. Characterization methods for powder bed fusion processed surface topography. *Precision Engineering*, 57, pp.1-15.
- [365] Reeves, P.E. and Cobb, R.C., 1995. Surface deviation modeling of LMT Processes—a comparative analysis. In *Proceedings of Fifth European Conference on Rapid Prototyping and Manufacturing*.
- [366] F. Blateyron, Chapter-2 “Characterization of areal surface texture”. Springer Science & Business Media, 2013. pp.15-43.
- [367] Lou, S., Zhu, Z., Zeng, W., Majewski, C., Scott P.J., Jiang, X., “Material Ratio Curve of 3D Surface Topography of Additively Manufactured Parts: An Attempt to Characterise Open Surface Pores”, *Surface Topography: Metrology and Properties* (2021) (manuscript under review).
- [368] Rosa, B., Brient, A., Samper, S. and Hascoët, J.Y., 2016. Influence of additive laser manufacturing parameters on surface using density of partially melted particles. *Surface Topography: Metrology and Properties*, 4(4), p.045002
- [369] Buchholz, M., Gruber, S., Selbmann, A., Marquardt, A., Meier, L., Müller, M., ... & Bach, C. (2022). Flow rate improvements in additively manufactured flow channels suitable for rocket engine application. *CEAS Space Journal*, 1-14.
- [370] Liu, W., Chen, X., Zeng, W., Sun, W., Jiang, X., Scott, P., & Lou, S. (2021, September). FVM and XCT Measurement of Surface Texture of Additively Manufactured Parts. In *2021 26th International Conference on Automation and Computing (ICAC)* (pp. 1-6). IEEE.
- [371] Sendino, S., Gardon, M., Lartategui, F., Martinez, S., & Lamikiz, A. (2020). The effect of the laser incidence angle in the surface of l-pbf processed parts. *Coatings*, 10(11), 1024.
- [372] Kleszczynski, S., Ladewig, A., Friedberger, K., Zur Jacobsmühlen, J., Merhof, D., & Witt, G. (2015). Position dependency of surface roughness in parts from laser beam melting systems. In *2015 International Solid Freeform Fabrication Symposium*. University of Texas at Austin.
- [373] <https://www.renishaw.com/en/additive-manufacturing-feature-articles--41148>
- [374] <https://michmet.com/3d-s-height-parameters-sasq.htm#:~:text=Nonetheless%2C%20once%20a%20surface%20type,is%20used%20for%20machined%20surfaces.>
- [375] Fernandez, A. G., Tarhini, H., Grottke, S. T., & Emmelmann, C. (2020). In-Situ Quality Assurance of Surface Roughness Using an On-axis Photodiode. In *Fraunhofer Direct Digital Manufacturing Conference DDMC* (p. 032059)

- [376] Galati, M., Minetola, P., & Rizza, G. (2019). Surface roughness characterization and analysis of the electron beam melting (EBM) process. *Materials*, 12(13), 2211.
- [377] Gibson, B. T., & Lowden, R. A. (2018). Process Development for Selective Laser Melting of Molybdenum (No. ORNL/SPR-2018/1045). Oak Ridge National Lab. (ORNL), Oak Ridge, TN (United States).
- [378] Ye, D., Fuh, J. Y. H., Zhang, Y., Hong, G. S., & Zhu, K. (2018). In situ monitoring of selective laser melting using plume and spatter signatures by deep belief networks. *ISA transactions*, 81, 96-104
- [379] Sahoo, A. K., & Pradhan, S. (2013). Modeling and optimization of Al/SiCp MMC machining using Taguchi approach. *Measurement*, 46(9), 3064-3072.
- [380] https://www.astm.org/e0008_e0008m-22.html
- [381] Shrestha, R., Simsiriwong, J., & Shamsaei, N. (2021). Fatigue behavior of additive manufactured 316L stainless steel under axial versus rotating-bending loading: Synergistic effects of stress gradient, surface roughness, and volumetric defects. *International Journal of Fatigue*, 144, 106063.